TOPEX Dual Frequency Altimeter Studies: Ionospheric Corrections and Ocean Surface Measurements

Thesis submitted for the degree of
Doctor of Philosophy
at the University of Leicester

Jonathan Price Angell
Department of Physics and Astronomy
University of Leicester

July 1997

This thesis is dedicated to Mum, Dad and Emma

When he established the force of the wind and measured out the waters,
when he made a decree for the rain and a path for the thunderstorm,
then he looked at wisdom and appraised it; he confirmed it and tested it.

Job 28:25-27

TOPEX Dual Frequency Altimeter Studies: Ionospheric Corrections and Ocean Surface Measurements

Jonathan Price Angell

Abstract

The TOPEX/Poseidon altimetry mission was developed as a NASA/CNES collaboration to provide accurate sea surface height (SSH) measurements. The TOPEX mission's altimeter is the first, and so far only, dual frequency system in space. The use of two frequencies allows a correction to be made for the radar pulse delay imposed by the Earth's ionosphere which would otherwise lead to an underestimation of SSH. Not only does TOPEX/Poseidon provide the most accurate SSH measurements yet from space, it also provides the first ever quasi-global measure of the integrated electron content (IEC) of the ionosphere. This thesis utilises TOPEX/Poseidon data in a combined study of both the oceans and the ionosphere. Firstly a study of the dependence of the IEC on geomagnetic disturbances, and the spatial coherence scale of the IEC is performed by comparison with the International Reference Ionosphere, an empirical ionospheric model. A systematic dependence of IEC with geomagnetic disturbance is found, and the first ever quasi-global maps of IEC spatial coherence distance are produced. This investigation may lead to an improvement in the accuracy of the model, and hence also that of single frequency altimeter systems, which must rely on such empirical models for their correction to the ionospheric delay. Secondly the tropical Pacific Ocean is studied, in particular the characteristics of large scale wave activity in relation to the devastating climatic/oceanic phenomena known as El Niño. Kelvin, Rossby and tropical instability waves are identified, and their interactions and possible mechanisms related to El Niño are investigated. Evidence for both western and eastern boundary reflections are presented, and their significance to the delayed oscillator mechanism is discussed. The study illustrates the necessity for highly accurate SSH measurements.

Acknowledgements

I am extremely grateful to the following people:

Professor Tudor Jones for allowing me the opportunity to work in the Department of Physics and Astronomy at Leicester University.

Professor Terry Robinson for his supervision, support, questions and comments.

Professors Stan Cowley and Tudor Jones for their good stewardship of the Radio and Space Plasma Physics Group during my studies.

Dr. Ricky Beard for all the invaluable help and guidance.

Dr. Sean Lawrence for his expert advice whilst dipping my toes in unknown oceans.

Nigel Wade, Chris Thomas and Julian Thornhill for keeping the computers running.

All the staff at the AVISO data centre for the unending flood of CD Roms.

The University of Leicester for providing me with funding for my postgraduate studies.

All the members of the Radio and Space Plasma Physics Group, both past and present, in particular I would like to single out a few individuals for keeping me sane by their insanity: Darren Wright for all his Yorkshireness, Alan "music man" Stocker for keeping my feet tapping, Brian Shand (my finest squash tutee), Ricky Beard for all his furniture, Mark Lester for working so hard in goal, Pete, Stuart and Mick for all their repair work, Eric and Paul for showing me what being fit means, the Jackie-Steve-Gabby monster for being so consistent, my new office mates Hina, Jon and Jon for letting me get in first, and last but not least Jon Bob and Giles for making this line fit.

A special thanks to all my friends at Holy Trinity for all their support and love.

My Mum and Dad for always being there for me and helping me through.

My wife, Emma, for her love, and for bringing light to my life.

Contents

8 Conclusions and Future Work

References

Chapter 1: Introduction

1.1 Overview

Satellite altimetry has become an increasingly important technique for measuring oceanographic parameters, providing a quasi-global and accurate data source. The accuracy of altimetric measurements is determined by a number of factors, not least of which is the group path delay introduced by the ionosphere. Accurate altimetric measurements of sea surface height (SSH) are vital for the global monitoring of ocean currents and large scale waves, which in turn play important roles in the Earth's climate system. Altimeters which utilise models to correct for the ionospheric delay risk imposing the morphology of the ionosphere onto that of the sea surface. The global nature of both ionospheric and oceanic features makes them ideal for study using a satellite system such as TOPEX/Poseidon.

The dual frequency altimeter flown on the TOPEX mission is the first and, so far, only such system capable of directly estimating the ionospheric path delay, which is directly proportional to the ionospheric electron content (IEC). This project aims to exploit the unprecedented accuracy of TOPEX SSH measurements for the study of large scale ocean waves, and also to use the ionospheric electron content data produced by the dual frequency measurements to provide means of improving empirical ionospheric models. Such improvements would lead to an increase in the accuracy of SSH measurements made by single frequency altimeter systems.

Figures 1 and 2 illustrate the spatial scales of both ionospheric electron content and equatorial ocean features respectively. Figure 1 reveals the correction necessary to the altimeter range measurement to account for the ionospheric delay. Figure 2 presents a global picture of the sea level anomaly in the equatorial oceans. Not only are the longitudinal and latitudinal extent of features very similar, but the ionospheric range correction is of the same order as the sea level anomaly measurements. Were the ionospheric delay on the radar pulse not corrected for, then ionospheric features would become confused with ocean features.

1.2 The Ionosphere

The Earth's upper atmosphere is weakly ionised by solar extreme-ultraviolet and X-ray radiation to form a quasi-neutral plasma. This plasma production mechanism is balanced by loss mechanisms such as recombination and attachment. Below approximately 60 km the loss mechanisms strongly dominate due to sufficiently high atmospheric density. However above 60 km free electrons can exist for significant periods of time. The ionosphere is the region of the atmosphere where photoionisation by the sun's radiation produces a sufficiently high electron density to affect radio wave propagation. It is a highly variable region in terms of height, thickness, electron density and structure, but may be defined as extending from approximately 60 km to over 800 km altitude. Being under solar control, the ionosphere is subject to diurnal, seasonal and solar cycle variations. The efficiency of plasma production by solar radiation of a given frequency is controlled by the power of the solar radiation at that frequency, the density of the atmosphere, and the ionisation cross-sections of the individual atmospheric species present.

Due to the varying ionisation cross-sections and stratification of atmospheric constituents, and also plasma transport effects, the electron density of the ionosphere varies with height, forming several distinct ionospheric regions - the D, E and F regions. Typical mid-latitude electron density profiles are illustrated in Figure 3.

The D-region is generated by hard X-rays, and as a result only exists during the daytime. It extends from 60 km to 90 km, and has low electron densities (10^{10} electrons/m^3), with no maximum of electron density. The E-region extends from 90 km to 120 km with daytime electron densities of 10^{11} electrons/m^3. The E-region varies in a regular way with solar illumination, being generated by soft X-ray and euv radiation, with production and loss mechanisms in quasi-equilibrium and a peak in electron density around 105 km. Finally the F-region lies above 120 km. Maximum electron densities occur in this region. During the daytime in the summer the region can split into two parts, the F1 and F2 regions. The F1 region is a daytime feature with a production maximum between 160 km and 180 km, caused by the most heavily absorbed part of the euv spectrum. The F2 region has a production maximum anywhere between 200 km and 600 km, typical altitudes being near to 250 km during the daytime. In contrast to the E and F1 regions, there is no production maximum to account for the F2-region peak. The increase in density in the bottomside of the layer is explained by the recombination rate falling off more quickly than the production rate as the altitude increases. At even greater altitudes vertical diffusion dominates the loss rate, and the increase in electron density is halted and reversed. The overwhelming proportion of atmospheric partial plasma population is encompassed within the F2 region. The F2 region persists throughout the night at a higher altitude, with reduced electron densities, due to the action of thermospheric winds.

Although the ionosphere is subject to control by solar radiation, it is still a highly variable region of the atmosphere due to a variety of mechanisms, including geomagnetic control, neutral winds, instabilities etc. A representation of mid-latitude ionospheric temporal variations is depicted in Figure 4, where the ratio of the maximum to minimum electron density is plotted for a seven decade range of periods (after Georges, 1968). The solar control of the ionosphere is readily evident in this plot by the larger amplitude fluctuations at the solar, seasonal and diurnal periods. The irregular variations of the ionosphere due to geomagnetic storms and wave motions are also apparent. The spatial variations associated with the Travelling Ionospheric Disturbances (TIDs) on Figure 4 range from hundreds of kilometres for medium scale waves (periods around 15 minutes) to thousands of kilometres for large scale waves (periods around 30 minutes). The electron density varies spatially with both longitude and latitude as a result of its strong dependence on solar radiation (e.g. Figure 1), with typical length scales of hundreds to thousands of kilometres.

An important parameter for satellite altimetric corrections is the ionospheric electron content (IEC). The IEC can be calculated by the height integration of the vertical electron density profile, and represents the number of free electrons in a column of one square metre cross-section. It is subject to diurnal, seasonal and solar cycle variations, and is an important quantity influencing trans-ionospheric radio wave propagation. Two maps of ionospheric correction data are presented in Figure 1. The two maps depict the dual frequency correction for both universal and local time. The dual frequency correction is directly proportional to IEC, 1 mm correction corresponding to approximately 2.3×10^{15} electrons m^{-2}. The spatial and temporal structure of IEC, to first order due to solar control, is apparent. Enhancements in IEC either side of the equator are apparent, these being due to the equatorial anomaly (discussed in Chapter 5).

Both regular and irregular fluctuations of electron density create an imprint on the IEC. Indeed the IEC and maximum electron density of the ionosphere are very well correlated (Houminer and Soicher, 1996). The results pertaining to IEC in this research may thus be extended to *fo*F2 (which is an important parameter in oblique HF radio wave communication systems, defining the maximum (or "critical") frequency of a radio wave which will reflect from the F2 layer).

1.3 The Pacific Ocean

The Pacific Ocean plays a significant role in controlling the Earth's climate system. An indicator of its importance is given by the phenomenon known as El Niño, which is associated with both ecological and economic disasters. Figure 5 presents a view of the worldwide effects of El Niño on the climate. During an El Niño year, warm water from the western Pacific basin 'surges' eastward towards the cooler eastern Pacific (see section 4.3 for a fuller description). From an oceanographic point of view this surge is initiated by a weakening of the easterly trade winds. One form of oceanic response to atmospheric changes is by large scale internal waves, such as Kelvin and Rossby waves (discussed next). It has been suggested that Kelvin and Rossby waves play a vital role in the initiation and termination of the El Niño phenomenon (Kessler 1990). Rossby waves are fundamentally important to modern large scale ocean circulation models, providing the means for westward intensification of circulation gyres and the adjustment to large scale atmospheric forcing. The spectral characteristics and mechanisms involved in their production are needed in order to properly examine their role in the El Niño phenomenon.

When the density of a fluid is a function of pressure only, the isobaric (constant pressure) and isopycnal (constant density) surfaces are parallel to each other. This is known as the barotropic field. However, when density is a function of other parameters as well as pressure, such as temperature and salinity, then the isobaric and isopycnal surfaces may be inclined to each other. This is known as the baroclinic field, and occurs in the upper oceans, where temperature, salinity and pressure all have large effects on the sea water density. The Kelvin and Rossby waves of interest to this study are baroclinic waves - the baroclinic field supports their propagation as internal waves between boundaries of water of differing density.

Rossby waves exist due to the principle of conservation of potential vorticity. Vorticity is the tendancy of a parcel of water to rotate, and can be seen as equivalent to angular momentum. The conservation of potential vorticity is defined as:

$$\frac{d}{dt}\left(\frac{\xi + f}{d}\right) = 0$$

where ξ is the relative vorticity (the spin of the parcel relative to the Earth), f is the planetary vorticity (the spin of the parcel due to the Earth), and d is the water depth.

The planetary vorticity is zero at the equator, and increases as a function of latitude to a maximum at the poles ($f = 2\Omega \sin\phi$, where Ω is the angular frequency of the Earth, and ϕ is the latitude in degrees). If one imagines displacing a parcel of water northwards in the northern hemisphere (as in Figure 6), it can be seen that the planetary vorticity will increase, but as a consequence of the conservation law the relative vorticity must decrease. This is achieved by the parcel of water circulating relatively clockwise. Now the coriolis force will be greater at the poleward side of the water parcel than the equatorward side, and the net effect will be a force directed equatorwards, hence providing a restoring force. The parcel of water will then overshoot it's equilibrium position, and the opposite will happen i.e. the relative vorticity will increase, and the net coriolis force will be northwards. Hence the parcel of water will oscillate in a wavelike manner. This mechanism is the basis for Rossby wave propagation. Solutions of the equations of motion for the ocean reveal that Rossby waves must have westward phase speeds relative to the background flow. Since the background flow in the oceans is never strong enough in the eastward direction, oceanic Rossby waves will always be observed to propagate westwards.

Kelvin waves are a special boundary solution to the equations of motion. The boundary can either be physical, such as a coastline, but may also be found at the equator, where the coriolis force is zero. Figure 7 depicts the mechanism for Kelvin wave propagation. Considering the equatorial case, westward travelling water is deflected to the right in the northern hemisphere, and to the left in the southern hemisphere by the coriolis force. At the equator, where the coriolis force is zero, the water piles up. A balance is formed between the coriolis force forcing the water towards the equator, and the resulting pressure force created by the sloping waters. This balance of forces leads to geostophic flow eastwards along the equator. Hence Kelvin waves can only propagate eastwards at the equator (in general Kelvin waves will propagate with the boundary on the right in the northern hemisphere, and the left in the southern hemisphere).

To a very simple approximation the temperature distribution in the oceans can be viewed as a cold body of water with a thin layer of warmer water on the surface. The upper warm layer has a fairly uniform temperature, below which there is a region of rapidly decreasing temperature, separating the upper warm layer from the lower cold body of water. The surface layer may be referred to as the mixed layer, and the boundary of rapidly decreasing temperature is known as the *thermocline*. A typical temperature depth curve for the tropical oceans is depicted in Figure 8. Rossby and Kelvin waves affect the thermocline depth, and hence the ocean's temperature profile, as well as the sea surface height. The waves can either raise or lower the thermocline, leading to a decrease or increase, respectively, in the sea surface height. A lowering of the thermocline leads to a warming effect in the region of the disturbance, since the cooler water under the thermocline is forced down and replaced by warmer water. The opposite is true for a raising of the thermocline i.e. there is a cooling associated with an upwelling event. For the first-baroclinic mode, variations in sea surface height are inversely mirrored in the thermocline depth, with approximately three orders of magnitude greater amplitude (Gill, 1982). A one centimetre sea level rise will thus correspond to a ten metre thermocline depression, and a significant variation in the upper-ocean thermal structure.

Kelvin and Rossby waves in the ocean have previously been difficult to observe because of their small sea surface amplitudes, slow propagation speeds and long wavelengths. The TOPEX/Poseidon satellite, launched in August 1992, is the first satellite able to measure with sufficient accuracy to distinguish these waves. Previous missions (e.g. GEOS-3, SEASAT and GEOSAT) were not able to observe these waves due to either insufficient accuracy, or because of inappropriate orbit configurations which aliased tidal errors into frequencies difficult to distinguish from annual-period Rossby waves.

1.4 The Present Study

This project aims to bring together the two distinct topics of ionospheric physics and oceanography via the mutually important technique of dual frequency satellite altimetry. The first part of this thesis utilises TOPEX altimeter data to study the ionosphere. As previously mentioned, the ionospheric path delay is an important consideration in the accuracy of single frequency altimeter measured SSH. TOPEX provides the first ever opportunity to study ionospheric electron content in a quasi-global way. The research aims to provide a way to improve current empirical ionospheric models by means of a global study of the IEC variability dependence on geomagnetic activity. The first ever quasi-global maps of IEC coherence distance are produced to provide scale lengths for the inclusion of data into adaptive ionospheric models. Whilst being useful for the application of such adaptive models, this research is also of direct interest for the study of the ionosphere and its characteristics.

The second topic consists of the study of large scale wave activity in the equatorial Pacific ocean using TOPEX/Poseidon sea level anomaly data. Kelvin, Rossby, and tropical instability waves are identified, and their propagation characteristics calculated. Possible generation mechanisms for the waves are investigated. The study of such waves is crucial to provide a deeper understanding of the El Niño/Southern Oscillation phenomenon, which has a major effect on the world's climate system.

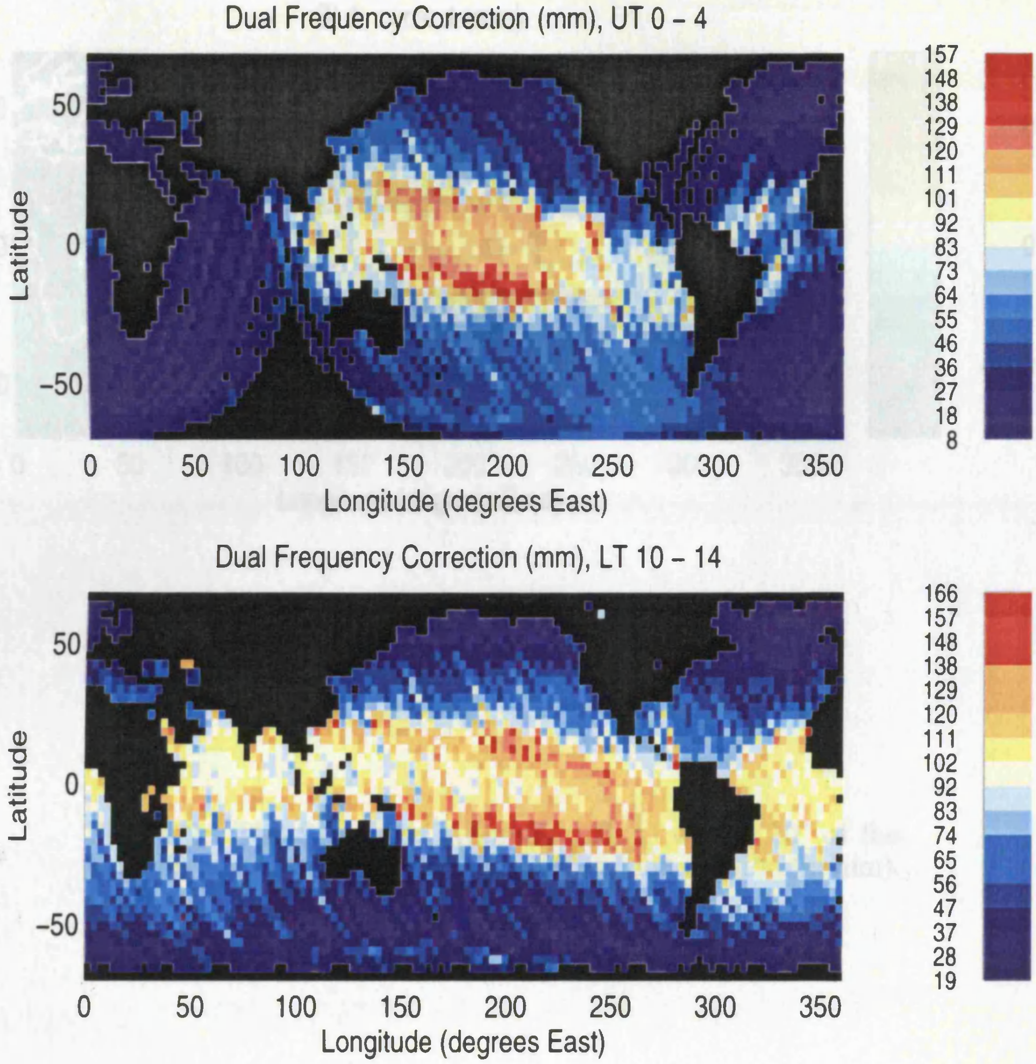

Figure 1: The correction to the ionospheric delay, which is directly proportional to the electron content along the ray path) as estimated by the TOPEX dual frequency altimeter (in mm). The data are taken over 4 cycles (approximately 40 days). Top panel: over 4 hours of universal time, Bottom panel: over 4 hours of local time.

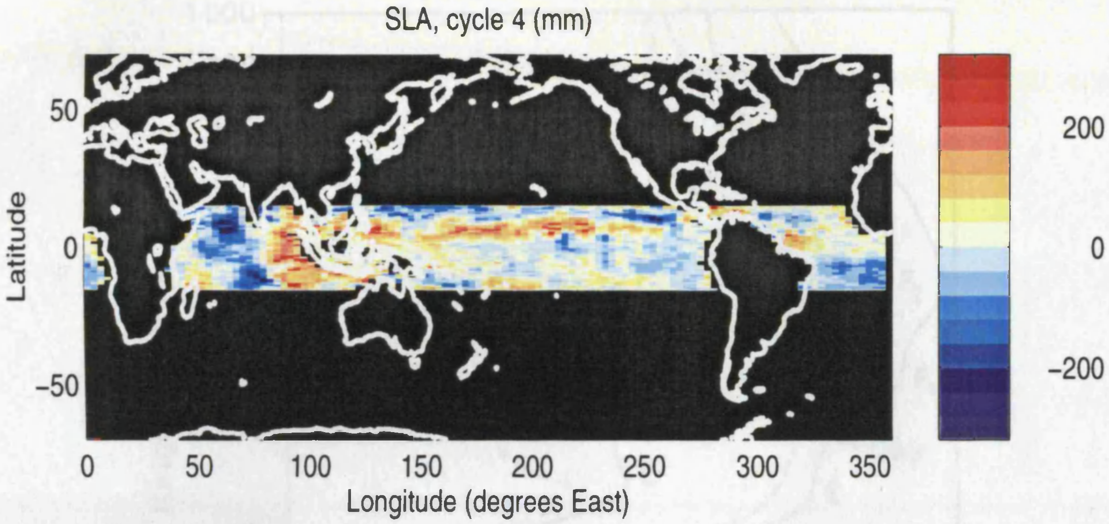

Figure 2: The Sea Level Anomaly (SLA) within 20° of the equator, as measured by the TOPEX/Poseidon mission (in mm).

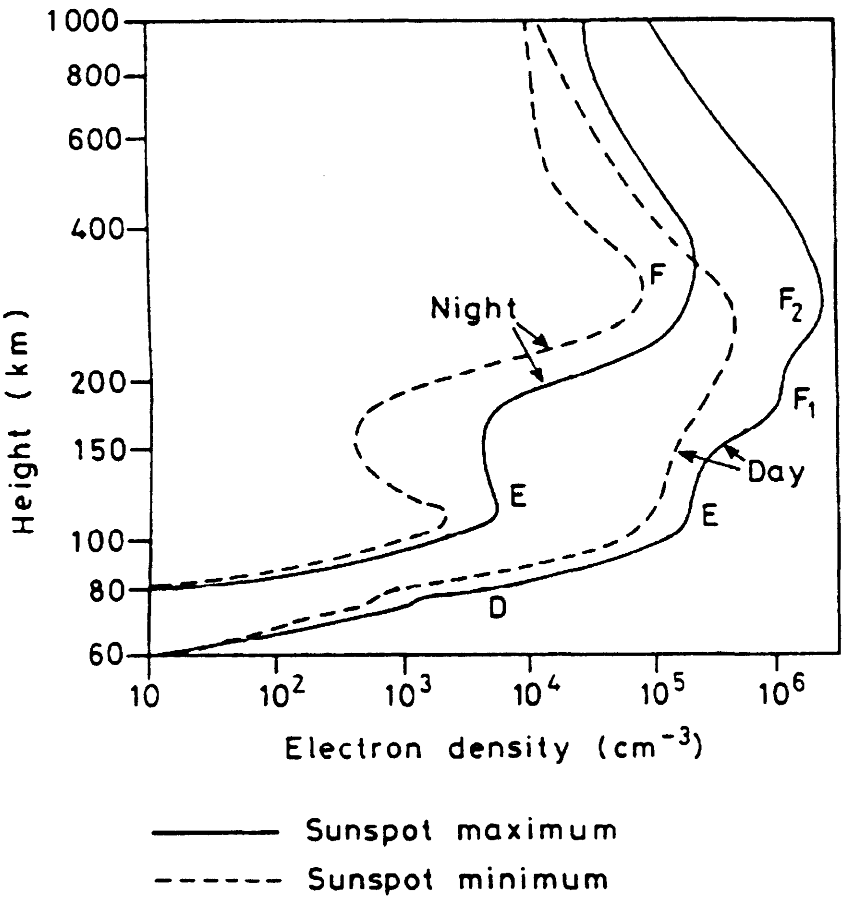

Figure 3: Schematic diagram of typical mid-latitude electron density with altitude, for night and day at solar maximum and minimum. (From Hargreaves, 1995).

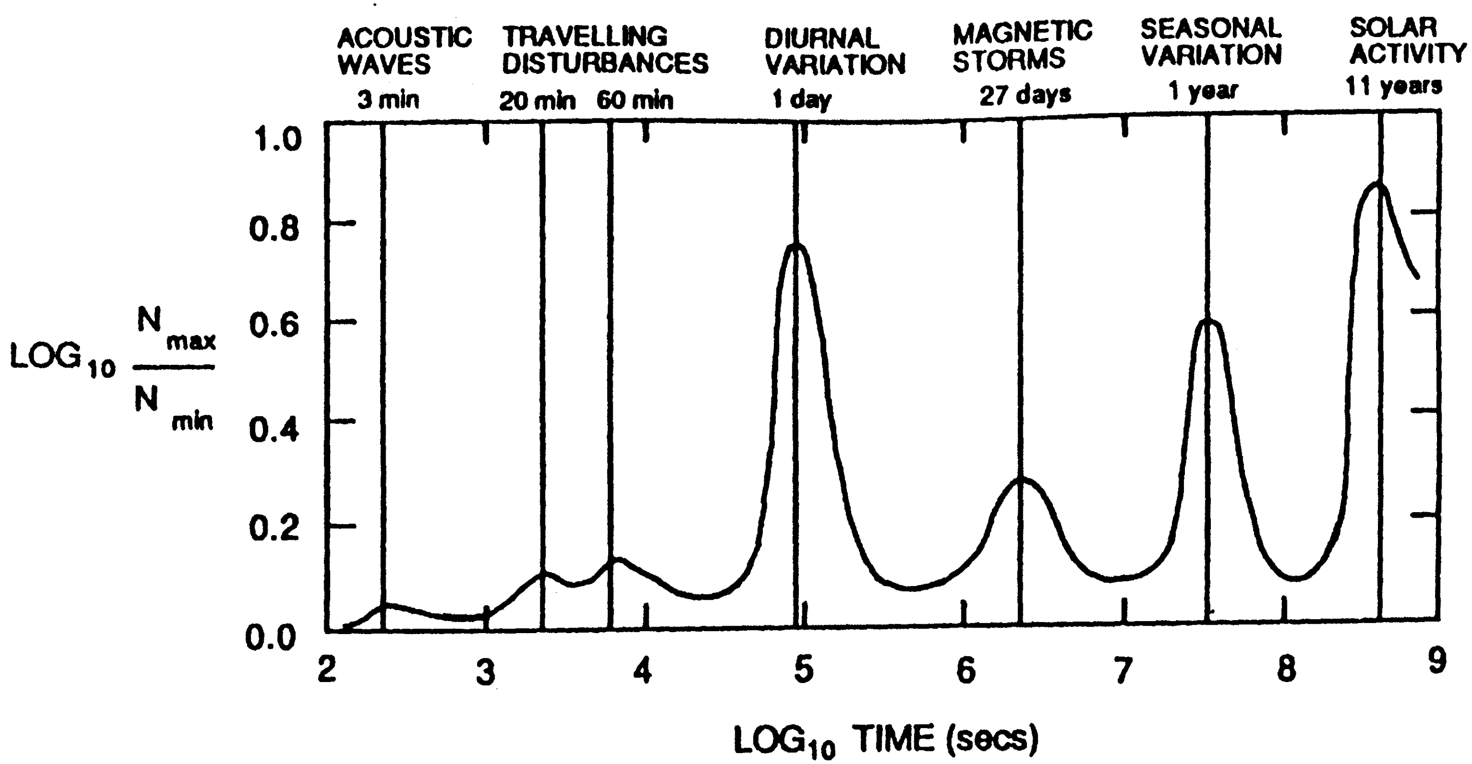

Figure 4: Schematic illustration of the temporal power spectrum of electron density (after Georges, 1968).

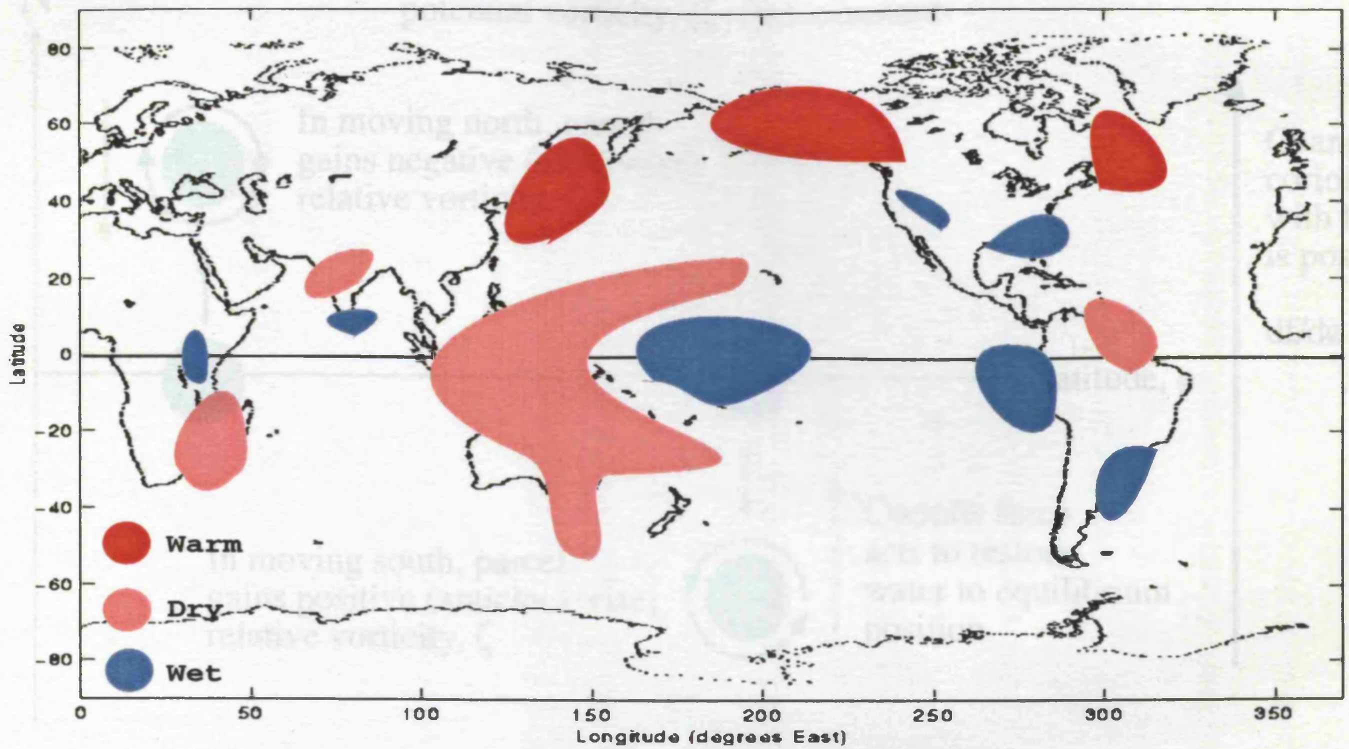

Figure 5: Schematic of the far reaching climatic effects of an El Nino, indicating anomalously warm, dry and wet regions. (After Ropelewski and Halpert (1987).

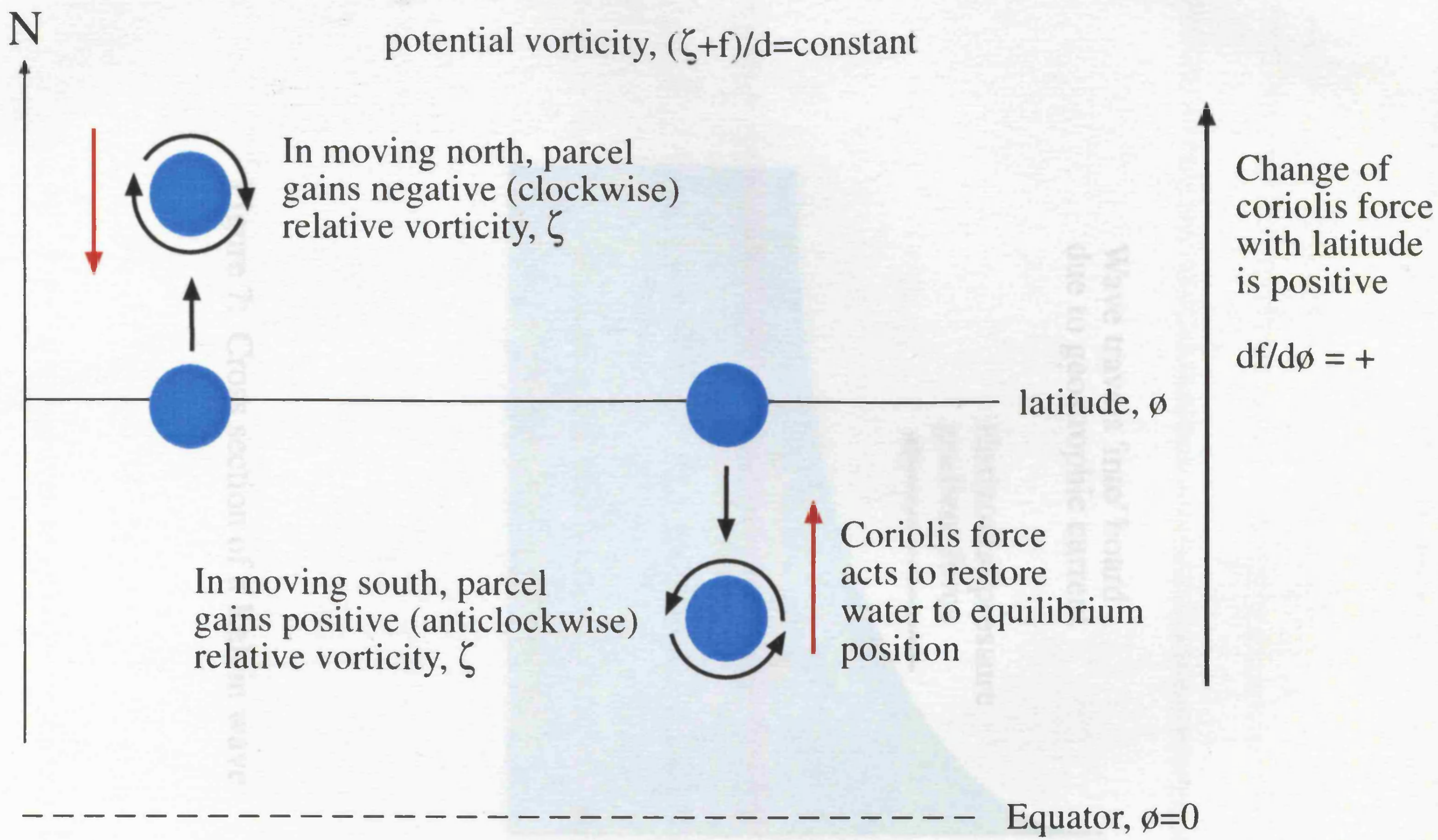

Figure 6: Rossby wave restoring force mechanism

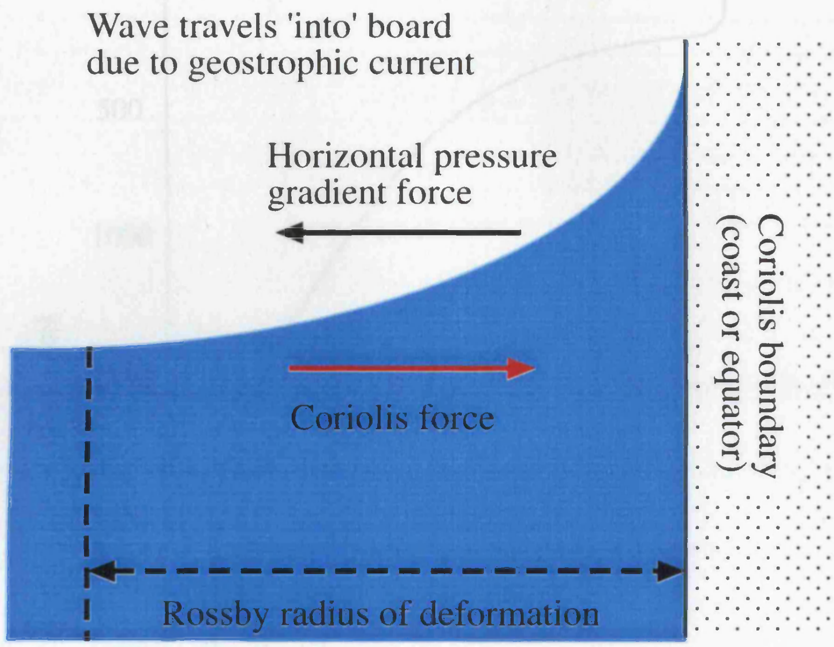

Figure 7: Cross section of a Kelvin wave

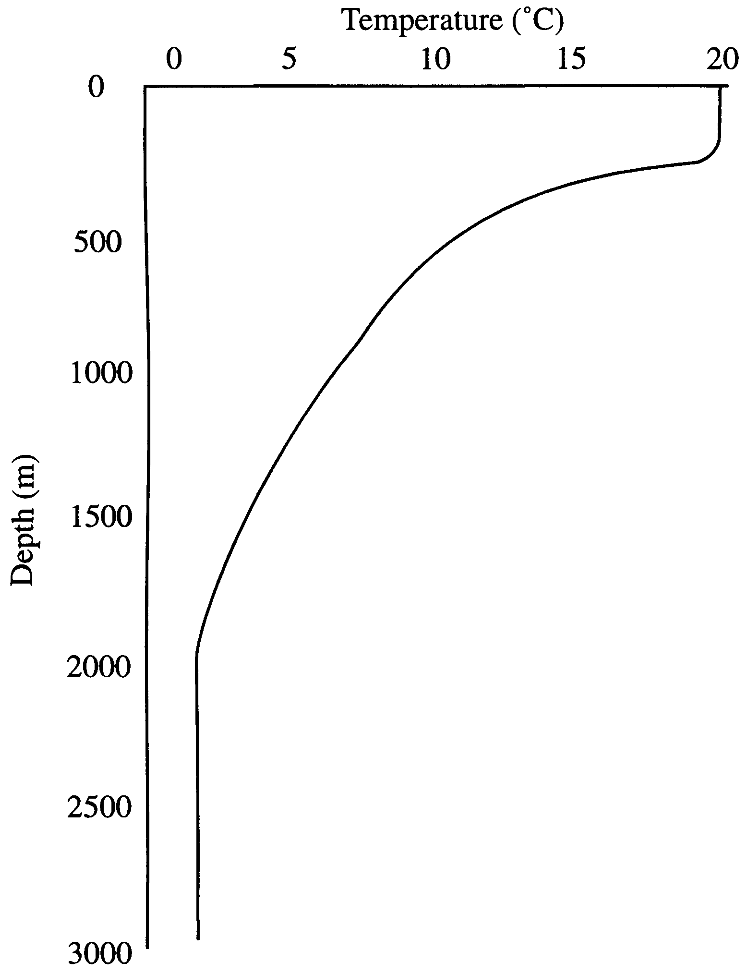

Figure 8: A typical temperature depth curve for the tropical ocean

Mean Classical Orbit Elements	
Semi-major axis	7 714.43 km
Eccentricity	0.000095
Inclination	66.04 °
Auxiliary Data	
Reference Altitude	1 336 km
Repeat Period	9.9156 days
Number of revolutions per cycle	127
Equatorial cross-track separation	315 km
Orbital Speed	7.2 km/s

Table 1: TOPEX/Poseidon orbit characteristics

Error Source	**/cm**
Instrument noise (TOPEX,1 second average)	1.7
(Poseidon,1 second average)	2.0
Sea state bias	2.0
Dry Troposphere	0.7
Wet Troposphere	1.2
Ionosphere	0.5 (NRA dual frequency measurements)
Ionosphere	1.7 (from DORIS)
Orbit	3.5 (from CNES DODG or NASA POD)

Table 2: TOPEX/Poseidon error budget

Chapter 2 Satellite Radar Altimetry

2.1 Introduction

Since the 1960s the development of space programs has had an enormous impact on a variety of scientific fields, and in particular on the understanding of the Earth's environment. Remote sensing satellites have developed as an important tool in the study of the Earth's land, ocean, and atmospheric environments, complementing conventional ground based measurement techniques. The satellites' advantages derive from their repetitive and continuous coverage of the Earth on global scales, as well as providing access to normally remote or inaccessible areas. This is particularly true for the oceans, which cover three quarters of the Earth's surface and play a dominant role in the behaviour of the climate system. Many of the important measurable phenomena of the oceans have cycles of the order of hours to years, and these are constrained to a large extent to the upper layers of the oceans. Hence satellite systems are ideally suited to obtaining such measurements.

Satellite altimetry was developed for the study of the oceans. Ocean circulation, sea surface topography, ocean tides, wind and wave measurements are just a few of the research aims for such missions. Since the inclination of the sea surface across a current system can be as little as 100 cm over 100 km, accurate ocean height measurements are required for more accurate climate models and predictions.

The basic principle of satellite radar altimetry (Figure 1) involves a nadir-directed radar pulse emitted from the satellite above an incoherently scattering locally planar surface (for example the ocean). The pulse is scattered from the surface, and is received by the altimeter. The time delay between the transmission and reception of the pulse is measured and, in principle, the distance from the satellite to the surface can be calculated. Then from accurate orbit determination of the satellite and a knowledge of the Earth's geoid (the iso-potential surface that the oceans would assume if at rest), the ocean height can be calculated. The requirements for the TOPEX/Poseidon satellite altimetry mission are that sea level measurements have a precision of ±2.4 cm and an accuracy of ±14 cm for typical oceanic conditions (precision being defined in this case as the ability to determine sea level changes over distances of 20 km, and accuracy is the uncertainty of each sea level measurement expressed in geocentric coordinates) (AVISO 1992). These requirements have been met, and exceeded, with single pass accuracy being quoted as 5 cm (Fu et al, 1994), and even 2 cm when sea level measurements are avereaged over a few hundred kilometres (Cheney et al, 1994).

However, this calculation is complicated due to various delays and errors introduced by the atmosphere onto the pulse propagation. Typical atmospheric range errors are recorded in Table 1. These errors are caused by refraction through, for example, water vapour in the troposphere and plasma in the ionosphere. Refraction delays lead to an underestimation of ocean height if not corrected. Corrections can be quite accurately made for most of the delays, as their values are well known from measurements or models. For example the dry tropospheric correction is quite predictable and produces height errors of approximately 2.3m; the water vapour content is more variable and corrections can range from 6-30 cm; this error is corrected for by brightness temperature measurements at 18, 21 and 37 GHz - the water vapour signal being sensed by the 21 GHz channel, whilst the 18 GHz is used to remove the surface emission, and the 37 GHz to remove cloud cover influence. These delays are not very variable, and hence do not introduce large errors into the altimeter measurement, However the ionospheric delay is highly variable, and current models used to predict the ionospheric electron content, and hence propagation delay, can have fairly substantial errors when compared to experimental results. These errors can be of the order of a few tens of centimetres.

Since the aim of altimeter systems is to be able to measure the ocean height to a few cm precision, the ionosphere is therefore a problem for single frequency altimeters (e.g. SEASAT, GEOSAT, ERS-1). This may be overcome by the use of a dual frequency system, such as the TOPEX altimeter. Since the ionospheric path delay is inversely proportional to the frequency squared, an altimeter operating at two frequencies will allow the error to be accurately estimated and hence removed. This error measurement provides a direct estimate of the IEC.

The following sections will present an overview of the TOPEX/Poseidon altimetry mission.

2.2 The TOPEX/Poseidon Mission

TOPEX/Poseidon is a joint mission conducted by the United States' National Aeronautics and Space Administration (NASA) and the French Space Agency, Centre National d'Etudes Spatiales (CNES). The TOPEX/Poseidon satellite was launched on August 10, 1992. The mission aims were to provide a specific altimetric satellite mission to substantially increase the understanding of global ocean dynamics by making accurate observations of sea level.

The TOPEX project consists of the NASA Radar Altimeter (NRA), and the Poseidon project concerns the French Solid State Altimeter (SSALT).

2.2.1 The Satellite

The satellite (Figure 2) is comprised of the Multimission Modular Spacecraft (MMS) bus and the Instrument Module (IM) which houses the sensors. The MMS provides all house keeping functions including propulsion, electrical power, command and data handling, and attitude control.

2.2.2 Sensors

The satellite carries six sensors to carry out the science and mission goals. Four of these were produced by NASA, the other two were produced by CNES. A brief overview of five of the sensors relevant to the current project follows. A more detailed description of the NRA may be found in Section 2.3.

i) Dual-frequency Ku/C band NASA Radar Altimeter (NRA)

The NRA is the first ever space borne dual frequency altimeter. It operates simultaneously at 13.6 GHz (Ku band) and 5.3 GHz (C band), allowing the ionospheric delay on the radar pulse to be directly estimated. The altimeter measures the satellite height above the sea (satellite range), the wind speed, the wave height and the ionospheric correction.

ii) Three-Frequency TOPEX Microwave Radiometer (TMR)

Water vapour content in the troposphere will cause the radar pulse to be delayed, and hence cause an error in the satellite range if uncorrected. The TMR provides the total water vapour content in the troposphere by measuring the sea surface brightness temperature at three frequencies (18 GHz, 21 GHz and 37 GHz). The 21 GHz channel is the main channel for water vapour content estimation. The 18 GHz channel is used to remove the effects of wind speed, and the 37 GHz to remove the effects of cloud cover in the water vapour measurements. The three channels' data are processed and combined by CNES to provide the correction to the delay.

iii) The Laser Retroreflector Array (LRA)

The LRA can be used to calibrate the NRA bias by reflecting signals from a network of ~15 satellite laser tracking stations. It is also used to provide the baseline tracking data for NASA precise orbit determination.

iv) Dual-frequency Doppler tracking system receiver (DORIS)
DORIS provides all weather global tracking of the satellite for CNES precise orbit determination. It uses a two-channel receiver (1401.25 MHz and 2036.25 MHz) on the satellite to observe the Doppler signal from a network of 40 to 50 ground transmitting stations. DORIS also provides an estimate for the ionospheric correction.

v) Single Frequency Ku band Solid State Altimeter (SSALT)
The SSALT is an experimental sensor, to test the technology of a low-power, light-weight altimeter for future Earth observing missions. It uses the same antenna as the NRA, and hence only one altimeter will operate at any one time. The altimeter measures the satellite height above the sea (satellite range), the wind speed and the wave height. Being a single-frequency sensor, an external correction for the ionosphere must be supplied (generally by DORIS).

2.2.3 Orbit

The mean classical orbit elements for the TOPEX/Poseidon mission are presented in Table 2. The orbit is not sun-synchronous. It is a high orbit to minimise the atmospheric drag and hence increase the precision of the orbit determination. The TOPEX/Poseidon mean orbit altitude of 1365 km compares with a mean altitude of 785 km for ERS-1. It provides a broad coverage of the ice-free oceans as frequently as possible without aliasing the tides to unacceptable frequencies. The ground track of one cycle of TOPEX/Poseidon is plotted in Figure 3.

Periodic manoeuvres are necessary to keep the satellite in its orbit, to counteract orbit decay due to atmospheric drag, solar radiation pressure, and the inhomogenous gravity field of the Earth. Manoeuvres are performed every 40 to 200 days. Manoeuvres take approximately 20 to 60 minutes, during which time no scientific data is taken.

2.2.4 Antenna Sharing

Since the NRA and SSALT (which will now be referred to as TOPEX and Poseidon respectively) operate using the same antenna, only one may be active at any one time. There is a time share between the altimeters which means that TOPEX will operate 90% of the time, with Poseidon taking the remaining 10%. TOPEX is the primary concern for the current study, due to its ability to not only measure sea surface heights but also to provide direct estimates of IEC. A functional description of the altimeter follows, a more detailed account may be found in Marth et al (1993).

2.3 The NASA Radar Altimeter

As previously stated the TOPEX altimeter operates at two frequencies, 13.6 GHz (Ku-band) and 5.3 GHz (C-band). Linear-FM (chirp) pulse waveforms are generated by the altimeter with a bandwidth of 320 MHz and a duration of 102.4 μs for both Ku and C-bands. The pulse repetition frequency is ~4500 Hz for the Ku-band channel, and ~1200 Hz for the C-band channel.

The antenna is a 1.5 m diameter parabolic receiver. The beamwidth of the antenna (~1.1° for Ku-band) covers an area on the surface of the Earth that has a diameter of over 20 km. However the pulse limited operation of the altimeter leads to a diameter on the surface of 2 km for a flat sea surface, or 7 km for a 5 m significant wave height (SWH) surface.

Precise details of pulse generation and transmission timing may be found in Marth et al (1993). Transmission of the pulses occurs in "bursts", each burst consisting of 38 Ku-band and 10 C-band pulses. Six bursts are grouped together to form what is referred to as one "track interval". This corresponds to 228 pulses for Ku-band and 60 pulses for C-band. This track interval corresponds to about 53 ms of data, and is the smallest time scale over which the signal processor interprets the waveform.

Each pulse received by the altimeter undergoes processing whereby the pulse is dechirped, lowpass filtered and digitised at a 1.25 MHz rate. This digitisation produces 128 complex samples from the 102.4 μs pulse. After further processing the square magnitude of the complex Fourier transform is taken. This represents the waveform for the altimeter pulse. Each of the 128 points in this waveform can be interpreted as the amount of power scattered back to the altimeter from a given range.

2.3.1 Waveform Noise

The main source of noise on the waveform is speckle noise. This noise results from the received power being the coherent sum of backscatter from many independently phased facets on the ocean surface. At any one time the facets could act constructively or destructively, and hence the received power will fluctuate. The confidence in waveform values derived from a single pulse is very low (Marth et al, 1993).

The waveform will also contain white noise that is dependent on the thermal noise from the amplification processes in the receiver. The importance of this noise is dependent on the antenna gain, the power of the transmitted signal, and other such factors. The speckle noise is not dependent on the altimeter system, however. To minimise the effect of speckle noise the waveforms from many pulses are averaged together to form a single "tracker" waveform. Six bursts are used to form this track interval, as described previously.

The following sections briefly describe the orbital models used by TOPEX/Poseidon, as well as the relevant errors to the altimeter range, and the corrections applied.

2.4 TOPEX/Poseidon Orbital Accuracy

The TOPEX/Poseidon mission uses two precision orbit determination programs, one computed by CNES and one by NASA. The CNES program uses the Schwiderski ocean tide model, and the NASA program uses the devoted JGM2 ocean tide model.

The differences between the two orbits is ~2 cm RMS radially, and below 10 cm RMS in the cross-track and along-track directions. The radial accuracy is expected to be below 5 cm RMS (AVISO, 1992).

2.5 Corrections for Environmental Effects

2.5.1 Tropospheric Delay

If hydrostatic equilibrium and the ideal gas law are assumed, then the range error due to the dry tropospheric term is a function of the surface pressure only. There is no straightforward way of measuring the nadir surface pressure from a satellite, however, and so it is determined from numerical model outputs received every six hours from the European Centre for Medium Range Weather Forecasting (ECMWF). The uncertainty in the dry tropospheric correction is ~ 0.7 cm for 1000 - 3000 km scales.

The correction applied for the delay due to the water vapour in the troposphere has already been outlined. Using the TMR the uncertainty in the correction is ~1.2 cm for 100-2000 km scales. The ECMWF model also calculates a value for the wet tropospheric delay, and this is placed in the TOPEX/Poseidon data as a backup to the TMR. The model result is used when sun glint, land contamination or anomalous sensor behaviour make the TMR data unusable.

2.5.2 Ionospheric Delay

The phase refractive index of the ionosphere is of great importance when studying transionospheric radio wave propagation. This is described in full by the Appleton

Equation (Appleton 1932); however for frequencies in the SHF band, such as the NRA uses, the phase refractive index, n, can be simplified and approximated by equation 1:

$$n^2 = 1 - \frac{\omega_N^{\ 2}}{\omega^2} \qquad 1$$

ω_N=angular plasma frequency

ω=angular frequency of electromagnetic wave

The group refractive index, r_g, at these high frequencies is just a function of electron density and wave frequency and is defined by equation 2:

$$r_g = \frac{c}{v} = c\frac{\partial\kappa}{\partial\omega} = \frac{\partial(n\omega)}{\partial\omega} \qquad 2$$

r_g=group refractive index v=group velocity

κ=electromagnetic wave number n=phase refractive index

c=speed of light in free space

Hence substituting equation 1 into equation 2 gives r_g as:

$$r_g^2 = (1 - \frac{\omega_N^2}{\omega^2})^{-1} \qquad 3$$

The time taken for an electromagnetic signal to pass through the ionosphere is greater than the free-space propagation time for the same distance. This ionospheric time delay may be used to study electron content. The time delay, τ, is given by equation 4:

$$\tau = \int_p \frac{r_g}{c} dp - \int_p \frac{1}{c} dp \qquad 4$$

which leads to equation 5:

$$\tau = \frac{40.3}{cf^2} E \qquad 5$$

f=frequency of electromagnetic wave

E=Integrated electron content (electrons m^{-2})

p=path distance

From these equations it is easy to show how a dual frequency system makes the ionospheric correction. If the measured return times for frequencies f_1 and f_2 are T_1

and T_2 respectively, where T_1 =(T+ τ_1) and T_2 =(T+ τ_2) then we have equation 6 for the integrated electron content:

$$E = \frac{cT_D}{40.3(f_1^{-2} - f_2^{-2})} \qquad 6$$

$T_D = T_1 - T_2$, the difference in received times from the two frequencies.

Then using equation 5 the pulse delay can be calculated and T , the 'delay free time' can be found.

The ionospheric delay is estimated directly by the dual frequency altimeter, and also by the DORIS system. The first method is only applicable to TOPEX, whilst the DORIS correction is applicable to both TOPEX and Poseidon. The Bent ionospheric model (Bent et al, 1972) prediction is also included in the data as a backup. The typical accuracy for the dual frequency estimate is 0.5 cm over 150-2000 km scales.

A technique for the evaluation of IEC by use of the Global Positioning Satellite (GPS) system has fairly recently been developed (Mannucci et al, 1993). Dual frequency signals from the satellites are measured at slant paths, and are then fitted to vertical assuming that the ionosphere can be modelled by a thin shell at 350 km altitude. A comparative study has only just been made by Ho et al (1997), between IEC measurements from GPS, TOPEX, and the Bent model. Taking TOPEX as "ground truth", the authors found an *average* difference of only 1.5 electron content units (1 ecu = 10^{16} el/m^2) between GPS maps and TOPEX, within 1500 km of a GPS ground station. The authors selected the ionospheric shell height based on the best results after comparison with TOPEX measurements. The maps are produced by essentially using a form of adaptive model with the Bent model. The average difference of 1.5 ecu compares with RMS differences up to 12 ecu. The errors become worse further from the GPS ground station, with a significant increase at around 2000 km away (an interesting point to note is that this is of the same scale as the coherence distances calculated in Chapter 5). Errors may be up to 30 ecu (corresponding to 15 cm path correction) or more at 3000 km. Again, whilst the essentially climatological GPS maps do provide an improvement over the Bent model, their use in point to point measurements of IEC is still dubious. Indeed the method of calculating the shell height using TOPEX data, which has been taken as "ground truth", obscures the accuracy of the maps in their own right. For instance if the TOPEX altimeter were to fail, then the GPS map accuracy would be degraded.

2.5.3 Ocean Wave Influence or sea state bias (SSB)

The SSB is made up of two components, the electromagnetic bias (EMB) and the instrumental bias (INB). Theoretical understanding of these biases is limited, and hence the most accurate SSB estimates are obtained using empirical models derived from analysis of the altimeter data itself. The BM4 model is used to estimate the SSB of both TOPEX and Poseidon Ku-band measurements, based on the results of Gaspar et al (1994) and Chelton (1994).

2.5.4 The Inverse Barometer Effect

The sea surface tends to respond to atmospheric pressure increases and decreases. A 1 mbar increase in atmospheric pressure will depress the sea surface by about 1 cm. The inverse barometer effect is corrected for by scaling the surface atmospheric pressure available from numerical models provided by the ECMWF. The correction applied for this effect is given as:

$$Inv\_Bar = -9.948 * (P\_atm - 1013.3)$$

where Inv-Bar is the correction applied in mm, and P-atm is the surface atmospheric pressure in mbar.

2.6 Summary

Although satellite altimeter systems are subject to many different sources of errors, accuracies of the order of cm are currently sought and achieved. Most of these potential errors (e.g. orbital error) may be corrected for effectively by the use of measurements and models. Many of the environmental errors have a low variability (see AVISO, 1992, for more information), and are quite predictable. However it has been demonstrated by various authors (e.g.Dulong, 1977, Beard and Robinson, 1994) that the variability of IEC around median ionospheric model predictions is very high (of the order of 25%). These residual errors in the ionospheric correction may introduce a considerable unwanted signal (of the order of tens of cm) into the analysis of ocean heights.

Two ways to reduce these residual errors are by the direct measurement of the IEC, or secondly by the use of an adaptive model. The TOPEX mission relies on the direct estimation of IEC by making measurements at two frequencies, leading to the unprecedented precision of ± 2.4 cm for range measurements.

The TOPEX/Poseidon mission hence provides an excellent instrument firstly for the study of ocean dynamics, and secondly for the study of the ionospheric integrated electron content. This global ionospheric study is the first of its kind, and provides a good opportunity to further increase the accuracy of both adaptive and empirical ionospheric models, which would in turn increase the accuracy of sea surface height measurements made using single frequency altimeter systems.

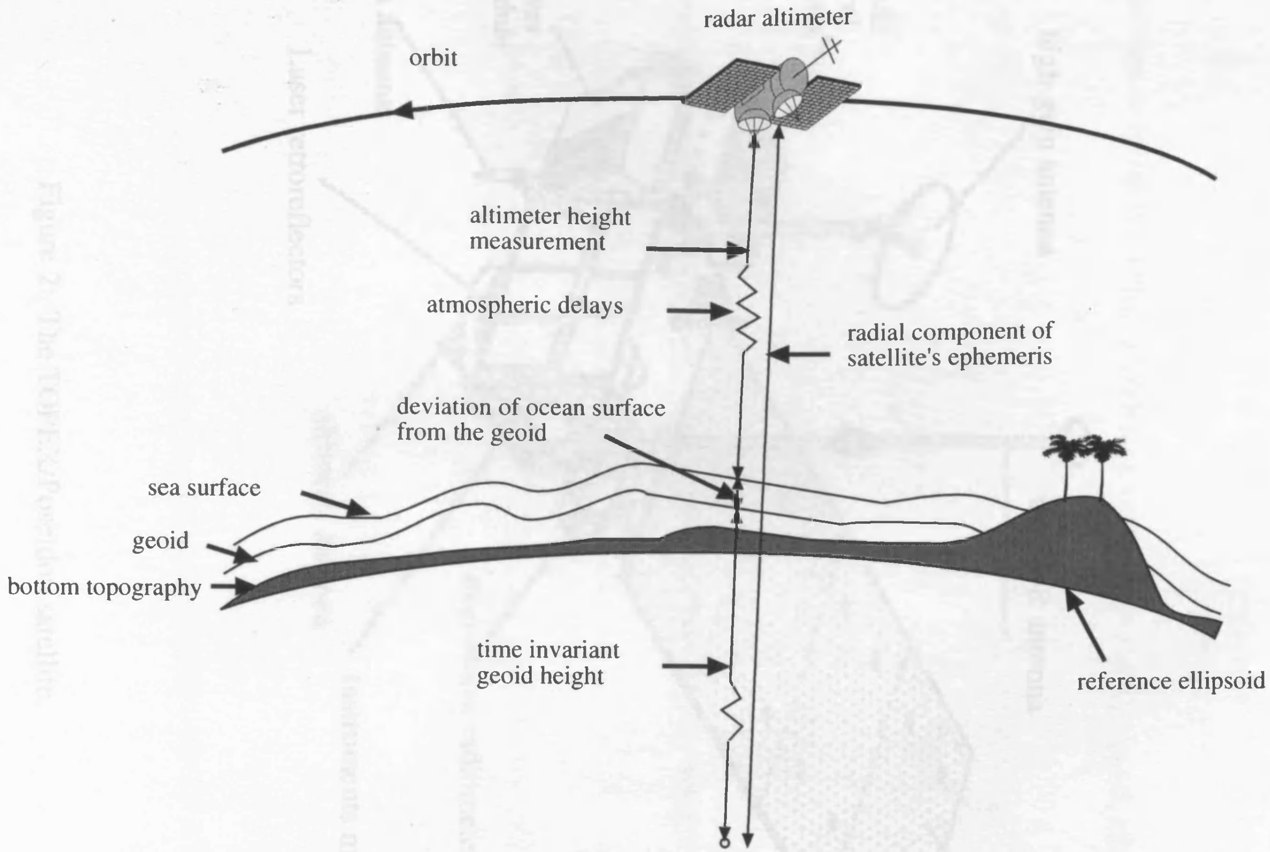

Figure 1: A schematic of the sea surface height measurement from a satellite radar altimeter.

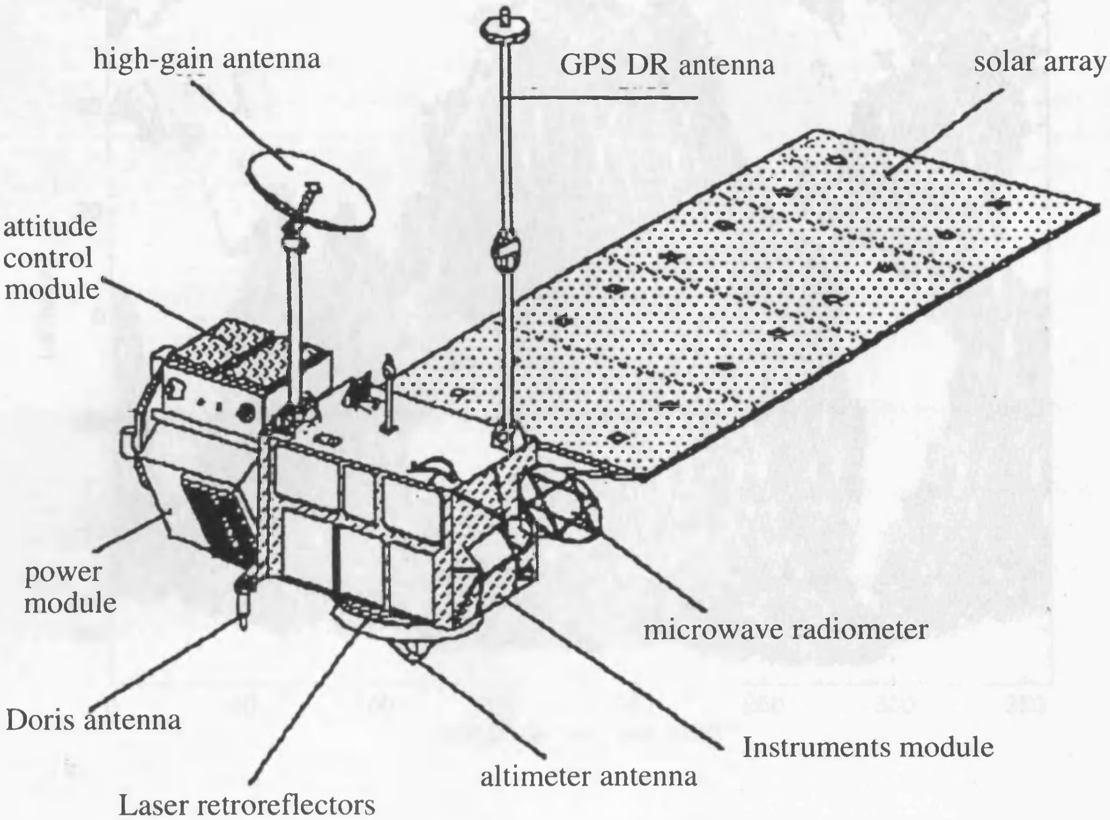

Figure 2: The TOPEX/Poseidon satellite

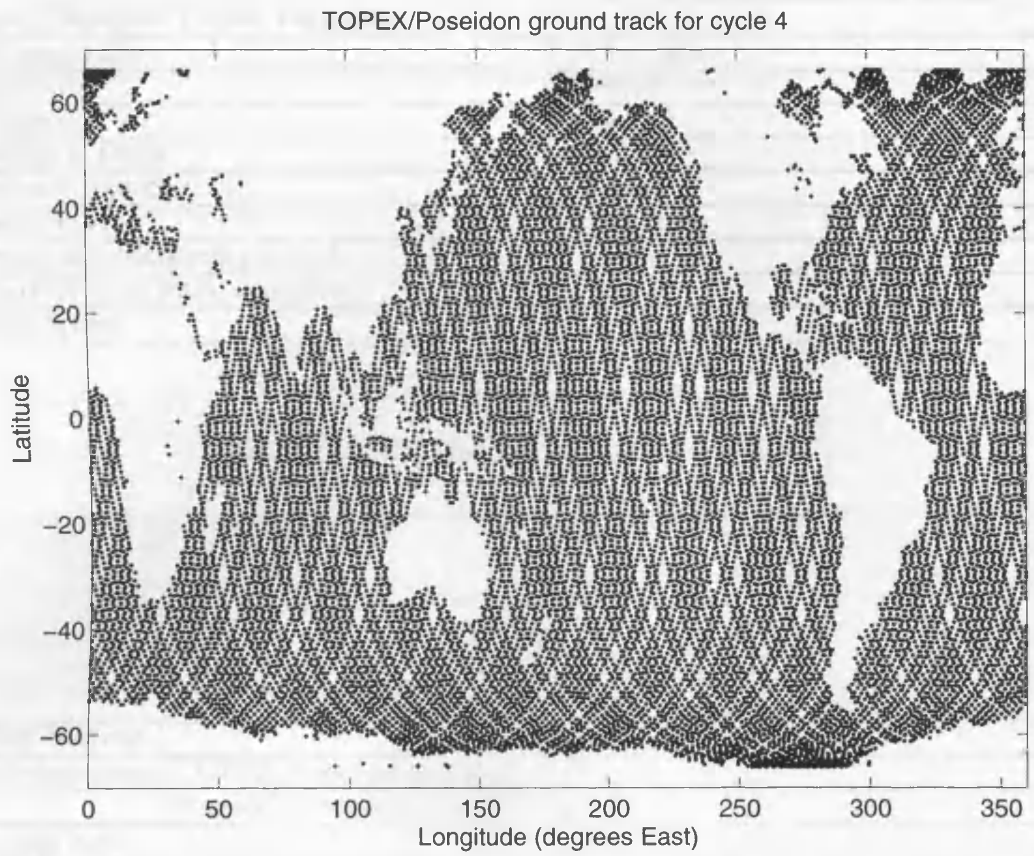

Figure 3: The TOPEX/Poseidon ground track for cycle 4.

Mean Classical Orbit Elements	
Semi-major axis	7 714.43 km
Eccentricity	0.000095
Inclination	66.04 °
Auxiliary Data	
Reference Altitude	1 336 km
Repeat Period	9.9156 days
Number of revolutions per cycle	127
Equatorial cross-track separation	315 km
Orbital Speed	7.2 km/s

Table 1: TOPEX/Poseidon orbit characteristics

Error Source	**/cm**
Instrument noise (TOPEX,1 second average)	1.7
(Poseidon,1 second average)	2.0
Sea state bias	2.0
Dry Troposphere	0.7
Wet Troposphere	1.2
Ionosphere	0.5 (NRA dual frequency measurements)
Ionosphere	1.7 (from DORIS)
Orbit	3.5 (from CNES DODG or NASA POD)

Table 2: TOPEX/Poseidon error budget

Chapter 3: Review of Previous Ionospheric Electron Content Coherence Distance Studies

3.1 Introduction

The inclusion of measurements of ionospheric electron content can increase the accuracy of model estimates for a particular point by providing information on local ionospheric conditions. The data must be collected sufficiently close to that point in both space and time in order to produce such an improvement. Such updating of a model is known as adaptive modelling (e.g. see Katz et al, 1978). This chapter reviews some previous work, carried out using ground based methods, whose aims were to find the spatial or temporal extent whereby the inclusion of such measurements would produce a significant improvement on model estimate accuracy. The current study, using TOPEX data, has concentrated on providing estimates for the spatial scale. TOPEX is not limited to a single ground point and provides a quasi-global data set.

The spatial and temporal scales can be determined from the coherence of electron content. The spatial correlation is a measure of how well a deviation at one point is mirrored at a remote point, and the temporal correlation is a measure of the persistence of a deviation from its mean level with time. Perfectly correlated data will have correlation coefficients equal to 1, dropping to 0 for no correlation between the data, and -1 for perfect anti-correlation. Following on from previous studies (e.g. Gautier and Zacharisen, 1965, Klobuchar and Johanson, 1978 and Leigh ,1989), the coherence distance is defined as the distance where the spatial correlation coefficient has dropped to 0.7. If the correlation of electron content can be taken to be linear, then the coherence distance will define the spatial coherence function.

3.2 Measurement of IEC

The principle technique for the measurement of the electron content is by Faraday rotation. Faraday rotation is a consequence of the geomagnetic field causing the ionosphere to be birefringent at radio frequencies. A radio wave entering the ionosphere will be split into two characteristic waves known as the ordinary and extraordinary waves (o- and x-modes). But the phase velocity of the o-mode is greater than that of the x-mode, and hence as the resultant wave propagates its angle of polarisation rotates in the same sense as the o-mode. This phenomenon is known as Faraday rotation. The extraction of the rotation angle requires weighting by the altitude profile of the geomagnetic field; this can be replaced by the field-factor, its value at a mean field height (Yeh and Gonzales 1960). This mean field height is usually taken to be 420 km (Titheridge 1972). The Faraday rotation angle of a signal leads to an estimate of the electron content of the ionosphere.

The electron content can also be measured by a dual frequency radar altimeter; the advantages of this sort of system over Faraday rotation include improved accuracy (because no magnetic weighting term is involved) , as well as coverage over the oceans - whereas Faraday rotation techniques require land-based receivers, the satellite borne radar altimeter can give almost continuous coverage over the sea surface.

Another global source of information available on ionospheric electron content are empirical models, such as the International Reference Ionosphere (IRI). Such models use actual peak F-layer electron density measurements combined with a number of Chapman layers and other terms to construct an electron density profile. These models are limited by the relatively small coverage of ground stations providing data, which are restricted to land masses, the majority of which are in the northern hemisphere. Whilst producing accurate monthly mean predictions of electron content, the models cannot allow for the day to day variability of the ionosphere, and discrepancies arise between model predictions and measurements.

3.3 Adaptive Modelling

The inclusion of electron content measurements sufficiently close to a model prediction point in space and time can improve the accuracy of this estimate by allowing for local disturbances in the ionosphere (Leigh et al, 1988). This method of model updating is known as adaptive modelling, which is based on least mean square estimation. However, unless data is taken within a restricted space-time cell, no significant improvement can be achieved over the normal model prediction. The spatial and temporal extent of this cell must therefore be determined, in order to ascertain over what scale adaptive modelling would improve the accuracy of a particular model prediction. The boundaries of this cell are defined by the coherence of the integrated electron content variability. That is, in this case, the coherence of the offset between TOPEX measurement and IRI model prediction.

3.4 Definition of Coherence

The coherence calculation and definition of coherence in this study is as used by Leigh et al (1988), based on Papoulis (1965). Temporal coherence times have not been extracted from the satellite data as yet, but will be quoted from previous ground based studies by Feen (1975), Dulong (1977), Donatelli et al (1978) and Klobuchar (1980) as

180 minutes for solar maximum and between 180 and 60 minutes for solar minimum (temporal coherence being a measure of the persistence of a deviation from its mean level, and being defined as the time delay after which the temporal correlation coefficient falls to 0.7). The TOPEX data used in this study starts just after the last solar maximum, and finishes mid way between solar maximum and minimum. Therefore a value of 120 minutes will be taken as appropriate to represent our temporal coherence.

The spatial correlation gives a measure of how well a deviation at one point is mirrored at a point some distance away. The coherence distance used in this study is defined as the separation at which the spatial correlation coefficient falls to 0.7.

Gautier and Zacharisen (1965) pointed out that the percentage improvement, *PI*, in the prediction of the parameter $foF2$ (see section 1.2) is related to the correlation coefficient r by equation 1, assuming a Gaussian distribution..

$$\mathrm{PI} = 100[1-(1-\mathrm{r}^2)^{1/2}] \qquad 1$$

This same relation applies to the IEC uncertainty reduction. A correlation coefficient of 0.7 will result in an improvement of 29 percent in the prediction of IEC at one station using data from a second station.

The adaptive model is formed by investigating the statistical process of the deviation of total electron content from its mean level:

$$D(d,t) = IEC(d,t) - \langle IEC(d,t) \rangle \qquad 2$$

d = spatial co-ordinate

t = temporal co-ordinate

IEC(d,t) = IEC at position d, time t

<IEC(d,t)> = Monthly mean IEC at position d, time t

D(d,t) = deviation at position d, time t

Then the spatial covariance (Cs) is defined as the expectation (E) of the product of the deviations (D) at two points separated in space by σ (equation 3, where d and t are spatial and temporal co-ordinates, respectively)

$$Cs(d,\sigma,t) = E[D(d,t)D(d+\sigma,t)] \qquad 3$$

and the spatial correlation coefficient between two points is defined as the ratio of the covariance of the instantaneous electron content at the two positions to the square root of the product of the corresponding variances (equation 4), and ranges in value from +1 (perfectly correlated) to -1 (anti-correlated).

$$Rs(d,\sigma,t) = \frac{Cs(d,d+\sigma,t)}{(Cs(d,d,t)Cs(d+\sigma,d+\sigma,t))^{1/2}} \qquad 4$$

The integrated electron content (IEC) used in this study is provided by the dual frequency TOPEX radar altimeter. The mean value is provided by the International Reference Ionosphere (IRI). Hence the correlation coefficients calculated (and hence coherence distances) will refer to the correlation of the TOPEX estimated IEC minus the IRI predicted mean.

3.5 The International Reference Ionosphere

Single frequency altimeters use semi-empirical ionospheric models to provide corrections to the delay imposed on the radar pulse by the ionosphere. The International Reference Ionosphere (Rawer and Bilitza, 1989), or IRI, is one such semi-empirical model used to describe the electron density (as well as the electron temperature, ion temperature, and ion composition) in the altitude range 50 km to about 2000 km.

The IRI requires empirical data of the worldwide variation of peak electron density and the peak electron density height as inputs. These are provided by the Comité Consultatif International des Radiocommunications (CCIR) prediction program. The CCIR model maps of *fo*F2 and M(3000)F2 are based on monthly median values obtained by a worldwide network of ionosondes (about 150 stations) during 1954 to 1958, altogether amounting to approximately 10,000 station months of data. The peak density of the F2 region (NmF2) is directly proportional to *fo*F2 squared. M(3000)F2 is a propagation factor closely related to the height of the F2 peak. It is the highest frequency that can be received at a distance of 3000 km. Each station data set is first represented by a Fourier time series (in Universal Time), and then a worldwide development is applied in the form of Legendre functions performed on each Fourier coefficient. This spherical harmonic analysis is described in detail by Jones and Gallet (1962, 1965), but will not be discussed further here.

The IRI uses different mathematical expressions for the various ionospheric height ranges to build up the electron density profile (Figure 1). Height integration of the electron density profile gives the ionospheric integrated electron content (IEC), which is directly proportional to the ionospheric delay imposed on the altimeter radar pulse. The model provides monthly averages in the non-auroral ionosphere for magnetically quiet conditions.

3.5.1 Accuracy of the IRI

The accuracy of the IRI's IEC predictions, compared to those derived by TOPEX, was investigated by Robinson and Beard (1995). The offset between TOPEX and IRI values was found to exhibit considerable variability. Although both overestimation and underestimation by the IRI compared to TOPEX was evident, the mean values indicated a bias towards an underestimation close to 10 mm at all latitudes, with evidence of higher differences in the vicinity of the equatorial anomaly and polar regions. The small mean bias, which is approximately twice the system error, indicates good agreement between the IRI and TOPEX over yearly time scales. However the large variability indicates significant estimation errors if the IRI is used on time scales of a few days.

3.6 Review of IEC Spatial Coherence Distance

This section summarises previous work carried out in the field of coherence distance of both *fo*F2 and IEC.

Gautier and Zacharisen (1965) produced, in a seminal publication, some very important results in their study of the use of current observations to predict future values or their values at other locations. Although they investigated the critical frequency of the F layer, *fo*F2, the results are equally important to the correlation scales of IEC (Houminer and Soicher, 1996). The correlation coefficient fell below 0.7 at a spatial separation of approximately 1000 km, although the correlation coefficient was found to be 0.7 or higher at separations as great as 5400 km. The diurnal variations of the correlation coefficients between Washington and San Francisco (separation 3912 km) and Washington and Anchorage (separation 5424 km) are presented in Figure 2.

Kane (1975) studied the coherence distance of ionospheric electron content during a time of solar maximum. From observations made at six mid and low-latitude beacon satellite receiving stations, he calculated a coherence distance of electron content of approximately 1800 km. Kane suggested that the coherence distance of the ionospheric electron content may be determined by the scale size of ionospheric irregularities produced by convection cells in the neutral thermosphere.

Bent et al (1975) investigated updating predictions of foF2 (the F-region critical frequency). Bent et al suggested that data taken within 2000 km of an update point would be useful in updating monthly mean estimates, a figure in good agreement with Kane's (1975) value for the electron content coherence distance.

Rush (1976) also studied the updating of foF2 predictions. Data were obtained from thirtytwo ionosonde stations during the high solar activity period known as the International Geophysical Year. Correlation coefficients were found to be slightly higher for the midday period, and lowest for night-time in winter. Equinoctial values were found to be slightly greater than those for the summer or winter months. Rush was the first person to recognise that the coherence distance of electron content may vary between zonal and meridional values. The coherence distances found were 1150 km in the north-south direction, and 2300 km in the east-west direction.

Klobuchar and Johanson (1978) studied the correlation distance of mean daytime TEC using an array of monitoring stations ranging from Wales to the west coast of the USA. A daytime correlation distance of 2900 km was calculated for east-west, and 1800 km for north-south. No clear seasonal dependence was revealed, although there were seasonal differences between certain monitoring stations, generally revealed as an increased coherence in autumnal months. The stations used and the coherence between them are plotted against distance for both the north-south direction (latitudinal) and the east-west direction (longitudinal) in Figures 3 and 4 respectively.

Soicher (1978) examined the spatial correlation of electron content between two remote sites, one in New Jersey (37°N, 283°E), and the other in Florida (24°N, 278°E). The cross correlation coefficient between the two sites was found to be approximately 0.7 during equinoctial months, and slightly greater than this in winter months. Thus, assuming a linear correlation function, the coherence distance can be estimated to be 1800 km. The difference between winter and the equinoxes is the opposite to that found by Rush (1976), where equinoctial coherence was slightly greater than for summer or winter. Soicher also noticed an increase in correlation between the stations during a magnetic storm.

Nisbet et al (1981) used beacon satellite electron content data from a remote site to update model predictions. The data were found to be most useful if taken within 1000 km of the point to be updated. Beyond 3000 km the accuracy of the updated model was found to be no better than predictions made using the model alone. Nisbet et al concluded that to obtain more accurate predictions from models it would be necessary to include some measure of the ionosphere's day to day variability.

Huang (1983) used data collected during 1975 and 1976 from two sites, Aberystwyth and Hawick, to investigate the decorrelation of electron content with latitude. The north-south separation of the 420 km ionospheric points of the two sites was 900 km. High correlations were found between the two sites, the coefficients being calculated as approximately 0.9. Again, assuming a linear drop in correlation coefficients with distance, this translates to a coherence distance of 2700 km north-south.

Huang (1984) used Faraday rotation data from Lunping observatory (25°N, 121°E) and Kaohsiung (23°N, 122°E). These two equatorial sites lie near the equatorial anomaly crest, and the spatial correlation of electron content between them was studied from December 1981 to November 1982 (data from March and September were not available due to satellite eclipse). The sites were only separated by 280 km, and so high correlation coefficients were found. However, even though the sites were so close together, differences in electron content as large as 30 electron content units (ecu, equivalent to 1×10^{16} electrons m^{-2}) were found between the two stations. Huang tried correlating the maximum electron contents over each day, as well as values taken every 15 minutes. The correlations were found to be stronger between the data taken every 15 minutes. A seasonal difference was found by Huang. Assuming a linear correlation function, coherence distances can be inferred from the correlation coefficients quoted by Huang. The coherence distances are approximately north-south, and are 2000 km for summer, 1000 km for winter, and 500 km for the equinoxes. This result agrees with Soicher (1978) in that the equinoctial correlations are worse than the summer or winter values.

Soicher et al (1984) studied the spatial coherence of electron content at mid-latitudes. Data from Athens, Greece (37°N, 23°E), and Haifa, Israel (32°N, 35°E) were used in the study. An average of daily coherence distance was given as 1900 km. Soicher et al did not find any evidence for a seasonal trend, in contrast to other work (e.g. Soicher (1978), Huang (1984)), but did find a local time variation. Cross correlation coefficients calculated in the early morning were found to be approximately half those found during the remainder of the day.

Bhuyan et al (1984) used simultaneous signals from two geostationary satellites to investigate the spatial coherence distance. The data were collected during March and April 1979, the two ionospheric points being separated by 900 km. It was suggested

that there was a vague diurnal variation in the correlation coefficients, with the night-time values higher than the daytime values in March, and vice-versa in April. The average diurnal correlation coefficients were found to be just above 0.6, which corresponds to a coherence distance of approximately 700 km.
Bhuyan and Tyagi (1983) investigated the spatial variation of electron content in and around the equatorial anomaly crest, by using a chain of beacon satellite observatories. The decorrelation of electron content between stations in both the north-south and east-west directions was found to be stronger than for mid latitudes, i.e. the correlation distances were shorter at equatorial latitudes than mid latitudes. A similar study was made by Bhuyan and Tyagi (1986). Data were obtained around the equatorial anomaly crest by Faraday rotation of the ATS-6 satellite beacon. They calculated a north-south coherence distance of 900 km and an east-west distance of 1500 km. Over short scales (around 300 km) the correlation was found to be comparable at all latitudes. However for longer scales the correlation was found to be lower at low latitudes compared to mid latitudes. Figure 5 depicts the results for both north-south and east-west separations.

Bhuyan and Bhattacharyya (1993) investigated the effect of longitude separation on the correlation of electron content, using data collected from two mid latitude stations, Osan, Korea (37°N, 121°E), and Athens, Greece (37°N, 23°E), during January-December 1980. Correlations between the two stations' data were found to be around 0.4 (apart from early sunrise and early morning). This would correspond to coherence distances of up to 5000 km. A correlation of 0.4 was found to lead to a 20% improvement in the prediction estimate of electron content.

The coherence of electron content at Melbourne, Australia, was investigated by Essex (1978), by using data from two geostationary satellites whose ionospheric points were separated by 1400 km. For magnetically quiet days Essex found that the diurnal variations between the two points were small, and it was suggested that these differences were due to gravity waves. However for more magnetically active days, the differences at the two sites were larger with respect to the monthly mean, yet in the same sense as each other, and it was suggested that the coherence of electron content was stronger for times of magnetic activity, a result also discovered by Soicher (1978).

3.7 Review of IEC Temporal Coherence Time

A typical profile of IEC versus local time is depicted in Figure 6. The data were collected at a single ground station during both solar maximum and solar minimum. Figure 7 illustrates a similar profile produced from analysis of TOPEX dual frequency data, collected over 40 days. The increases and decreases due to solar zenith angle are apparent, with the rapid ionisation at sunrise (6 LT), IEC values reaching a peak after midday, and then decaying as the sun sets. Superimposed on top of this diurnal trend are fluctuations due to other atmospheric or geomagnetic processes. These fluctuations away from the mean behaviour pose a problem to accurate predictions of IEC at any time.

The coherence of these temporal fluctuations has been investigated by relatively few authors. As mentioned previously, a knowledge of the scale (in both spatial and temporal terms) over which data may be used to successfully adapt a model is required. Whilst a way to extract temporal coherence from the TOPEX data set has not yet been established, it is necessary to outline previous work in this field since it has implications for the study of spatial coherence carried out.

Gautier and Zacharisen (1965) produced, in their seminal work on the use of current observations to predict future values, a temporal coherence time of approximately 2 hours. This result was obtained by examination of the critical frequency of the F region. At 4 hours the correlation coefficients had dropped to 0.5. Figure 8 reveals the decrease in correlation with time at two groundstations, Washington and Anchorage.

Dulong (1977) attempted to predict the IEC several hours in advance, by updating monthly mean data using the variation of measurements from that mean. Adaptive adjustments more than three hours in advance did not produce any better results than the already known monthly mean. As the time separation between update and prediction time decreased, however, the residual error decreased, becoming acceptable for predictions no more than 60 minutes from an update.

Donatelli and Allen (1978) studied the effect of updating an ionospheric model by scaling the model predictions with measurements from calibration satellites taken in advance of the time of prediction. The data were obtained by means of Faraday rotation of the VHF beacon on the ATS-3 satellite. During solar maximum conditions most of the benefit of daytime updates was lost after three hours. In contrast during solar minimum updates only less than an hour long were found to be useful. A 70-80% reduction in residual error was quoted for the updated predictions as opposed to simply using the model mean prediction.

Johanson et al (1978) investigated the variability of ionospheric time delay, in order to outline the errors which would result when only monthly average time delay values, without updating, were available to precise ranging systems (e.g.the Global Positioning System). Figure 6 reproduces their results, indicating the variability of IEC about the mean predicted value.

Klobuchar (1980) carried out a similar study, suggesting a coherence time of less than three hours at solar maximum and less than one hour at solar minimum for dayside electron content, in order to obtain a 50% reduction in prediction error.

3.8 Brief Review of Ionospheric Phenomena, with Relation to IEC

This section briefly outlines some previous research into ionospheric phenomena which may induce a positive or negative ionospheric electron content response to geomagnetic disturbances. Whilst the current project does not attempt to investigate these mechanisms, a basic understanding of them is required in order to interpret results in Chapters 5 and 6.

3.8.1 Atmospheric Composition Change

The negative phase of the ionospheric response to geomagnetic disturbance (i.e. the depletion in plasma population) is contributed to by an increase in the loss rate of O^+ brought about by a molecularly enriched atmosphere (Chandra and Herman, 1969, Risbeth, 1975).

The atmosphere is molecularly enriched due to the large scale thermospheric circulation generated by auroral zone heating (Babcock and Evans, 1979, Richmond, 1979, and Goel and Rao, 1981). This influx of energy produces a modification of the high latitude wind pattern, consisting of an upwelling of lower altitude molecularly rich atmosphere (Rishbeth et al, 1987) due to the heating and the flows necessary to compensate for the divergence of the horizontal storm-time wind patterns. As a result the composition at F-region altitudes becomes more molecular (an increase in the ratio N2/O). This composition change leads to a higher recombination rate, and hence lowers the ionisation density and the IEC. The effect occurs initially throughout the auroral oval, but then propagates down to mid-latitudes in the midnight sector, and is then carried to all time sectors by the rotation of the Earth (Prölss, 1993).

Measurements of these large compositional changes have been made by various methods (Prolss, 1980, Torr et al, 1982, and Okano and Kim, 1986). Goel and Rao (1981) quantitatively estimated the changes in the ionospheric composition and temperature during geomagnetic storms at Delhi, a low latitude station. They found that

O^+, H_e^+, and H^+ ions, all important to the F-region and above, increased and decreased in phase with the concentration changes of atomic oxygen (when there was no change in total neutral density).

3.8.2 Mid latitude Trough

Another mechanism for producing a negative phase at mid latitudes is the equatorward movement of the mid-latitude trough. The mid-latitude trough is a depletion in the F-region electron density at the equatorward edge of the nightside auroral oval. The mid-latitude trough forms due to the stagnation of ionospheric plasma, trapped between a region of eastward (corotating) plasma drift equatorwards of the auroral zone, and a region of westward drift in the auroral zone (Spiro et al, 1978). The stagnation of the plasma allows chemical recombination to reduce the ion concentration. Solar illumination causes the trough to fill, and hence it is generally a night-time phenomenon. The leading edge of the daytime trough (LEDT) can, however, extend into the dayside during periods of increased geomagnetic activity (Whalen, 1987). Under quiet geomagnetic condition, the plasmasphere of the Earth extends to L = 4 - 5, corresponding to geomagnetic latitudes in the range of 60 - 64 degrees. However, during geomagnetic storms, the plasmasphere is compressed and the mid latitude trough moves to lower latitudes. The LEDT expands equatorward and rotates clockwise to earlier local time with increasing geomagnetic activity, as depicted in Figure 16. Low density plasma is convected westward (sunward) to produce a depleted dayside trough. The magnitude of the equatorward expansion observed by Whalen (1987), between the highest and lowest activity in his data, was 20° geomagnetic latitude. Such a movement of the trough will result in a significant drop in IEC at mid latitudes. Experimental evidence for this mechanism was also provided by Mendillo et al (1974), who observed five cases of large and rapid drops in TEC near sunset, which were interpreted as being due to the contraction of the plasmasphere to L-values less than 3. This equatorwards movement of the trough away from high latitudes would also provide an enhancement in IEC in the region previously occupied by the trough.

3.8.3 Lifting of the Ionospheric Plasma

An important mechanism, leading to positive ionospheric responses, is the lifting of ionospheric plasma to higher altitudes. The response created is positive since the recombination rates are lower at higher altitudes. The vertical lifting occurs due to equatorward neutral winds associated with the stormtime circulation (Jones and Risbeth, 1975, Babcok and Evans, 1979) and the eastward stormtime electric field

(Tanaka and Kirao, 1973, Fejer et al, 1979). The neutral wind is most effective at lifting at high latitudes, and the electric field is most effective at low latitudes.

3.8.4 Equatorial Anomaly Response

The equatorial anomaly can undergo drastic modification due to geomagnetic disturbance effects (Abdu et al, 1991). This modification manifests itself as the occurrence of the equatorial anomaly at local times away from its normal quiet time position, and also as the inhibition or enhancement of the anomaly at its quiet time positions. Tanaka (1981) studied the variations of *fo*F2 at two stations, following a geomagnetic storm in 1980. One station, Okinawa, was located near the equatorial anomaly crest, whilst the other station, Manila, was situated in the anomaly's trough. An enhancement in the anomaly was visible around 18 LT of the first day, where the Okinawa readings increased and the Manila readings decreased i.e. the crest increased and the trough deepened. The following two days revealed an inhibition of the trough, with the *fo*F2 readings from both stations being comparable i.e. there was no discernible trough or crest during these times.

The changes in the dynamics and morphology of the equatorial anomaly are caused by the direct penetration to equatorial latitudes of the magnetospheric electric fields and the thermospheric disturbances involving winds, electric fields and composition changes. A good review of this subject is provided by Abdu et al (1991), but is outside the scope of the current study.

3.9 Summary

This chapter has summarised previous work in the area of ionospheric electron content coherence (both spatial and temporal), as well as briefly describing the International Reference Ionosphere and the concept of adaptive modelling. All of the aforementioned studies have been limited by their ground based nature. These limitations may be transmitted to any models which rely on such ground data.

A brief review of mechanisms which may lead to both positive and negative electron density responses to geomagnetic disturbances has been presented. Although these mechanisms themselves are not investigated in this work, an understanding of the processes is important in being able to interpret the results of Chapter 6 especially.

The data available for this study from the TOPEX mission should provide a valuable insight into the global structure of IEC, which in turn will provide a means for the validation or adaptation of current empirical ionospheric models. Such models are curently used in single frequency altimeter systems to provide a correction to the delay imposed on the radar pulse by the ionosphere. Whilst an adaptive model will still not provide a completely error free system, it could greatly improve the delay estimate. This would in turn improve, at the very least, single pass estimates of ocean height.

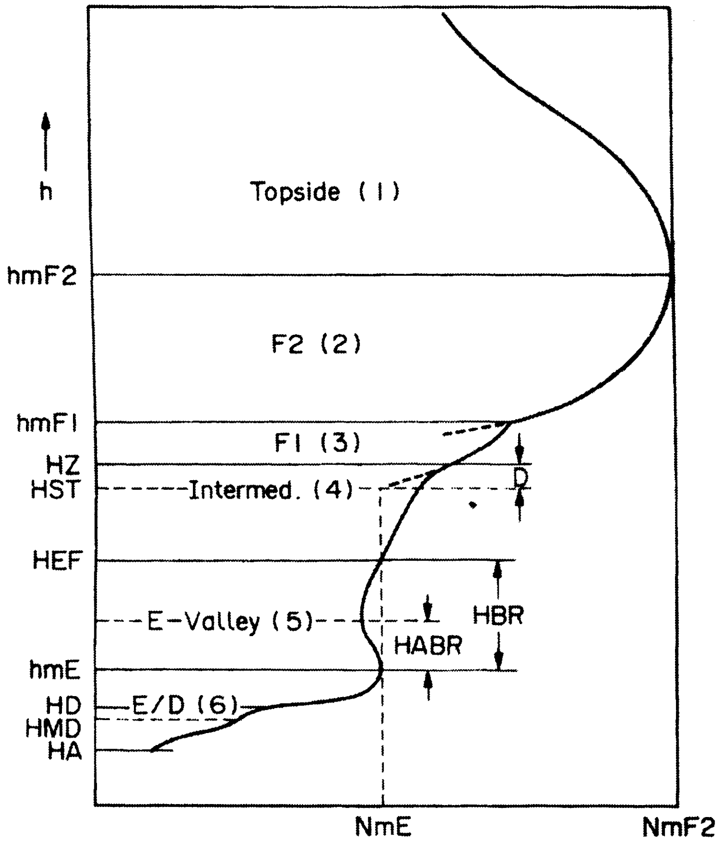

Figure 1: The layer-by-layer profile as used by the IRI (from Rawer and Bilitza, 1989).

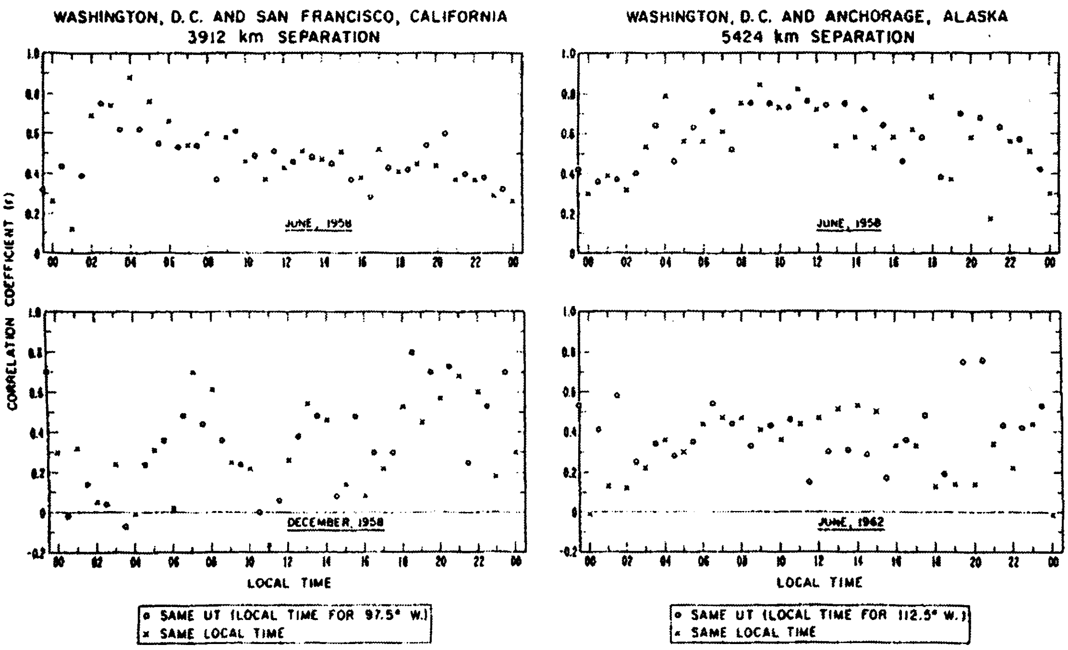

Figure 2: The diurnal variation of the correlation coefficients between Washington and San Francisco (separation 3912 km) and Washington and Anchorage (separation 5424 km) (top panels represents solar maximum conditions, bottom panels solar minimum) (after Gautier and Zacharisen, 1965).

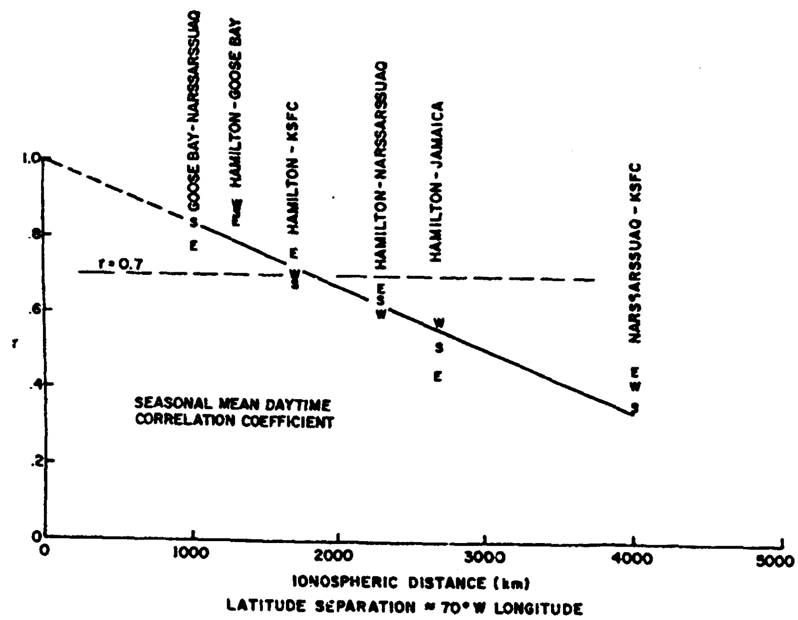

Figure 3: Correlation coefficient vs station latitude separation in km (from Klobuchar and Johanson, 1977).

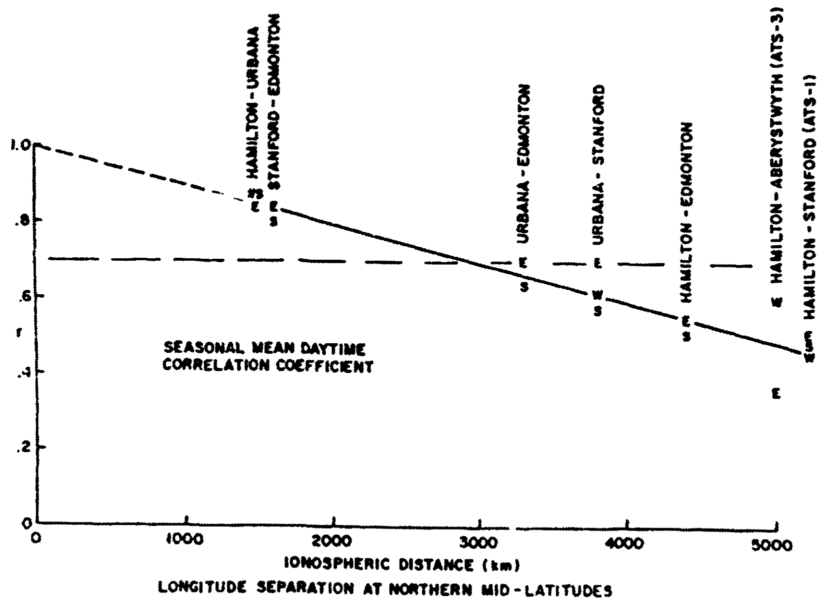

Figure 4: Correlation coefficient vs station longitude separation in km (from Klobuchar and Johanson, 1977).

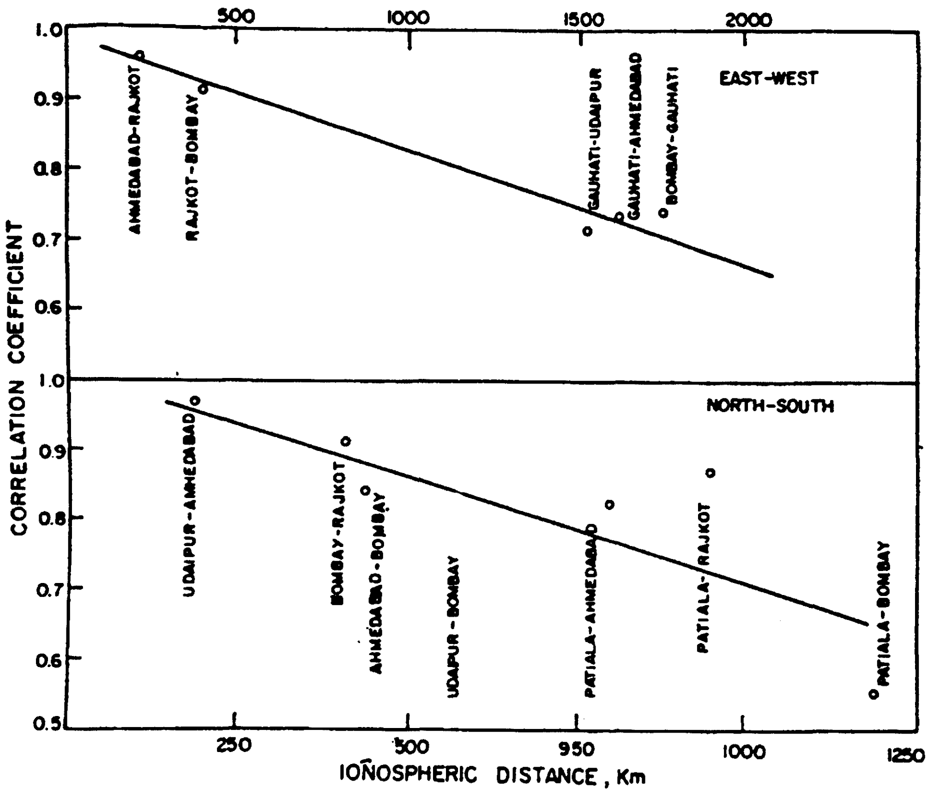

Figure 5: Correlation coefficient versus (top) longitude, and (bottom) latitude separation of station pairs (from Bhuyan and Tyagi, 1986).

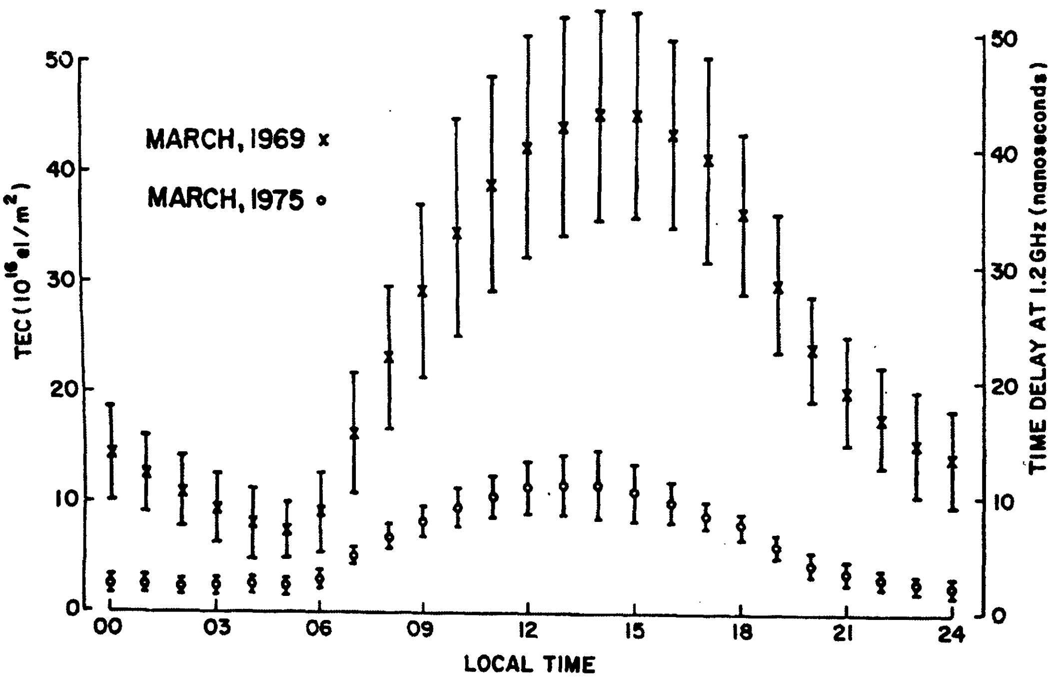

Figure 6: The diurnal variation of IEC for solar maximum (1969) and solar minimum (1975). The bars represent the standard deviation of the data (Johanson et al, 1978).

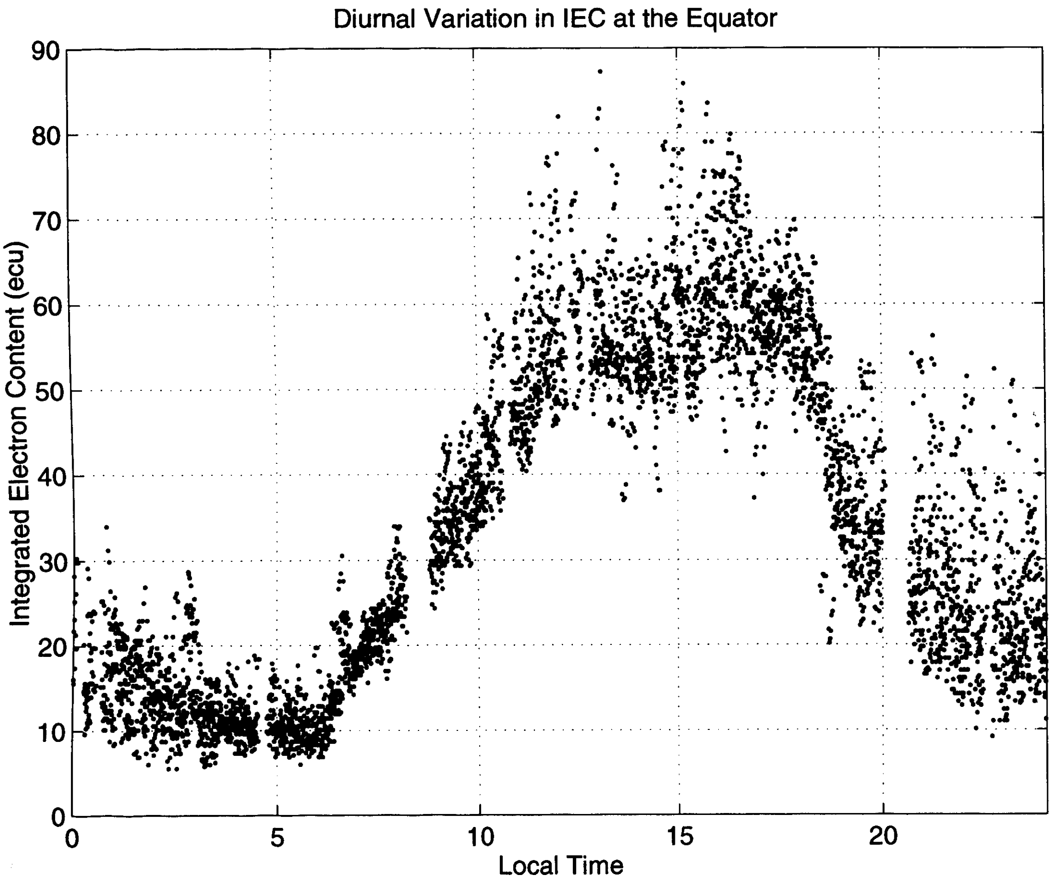

Figure 7: The diurnal variation in IEC at the equator as measured by the TOPEX dual frequency altimeter.

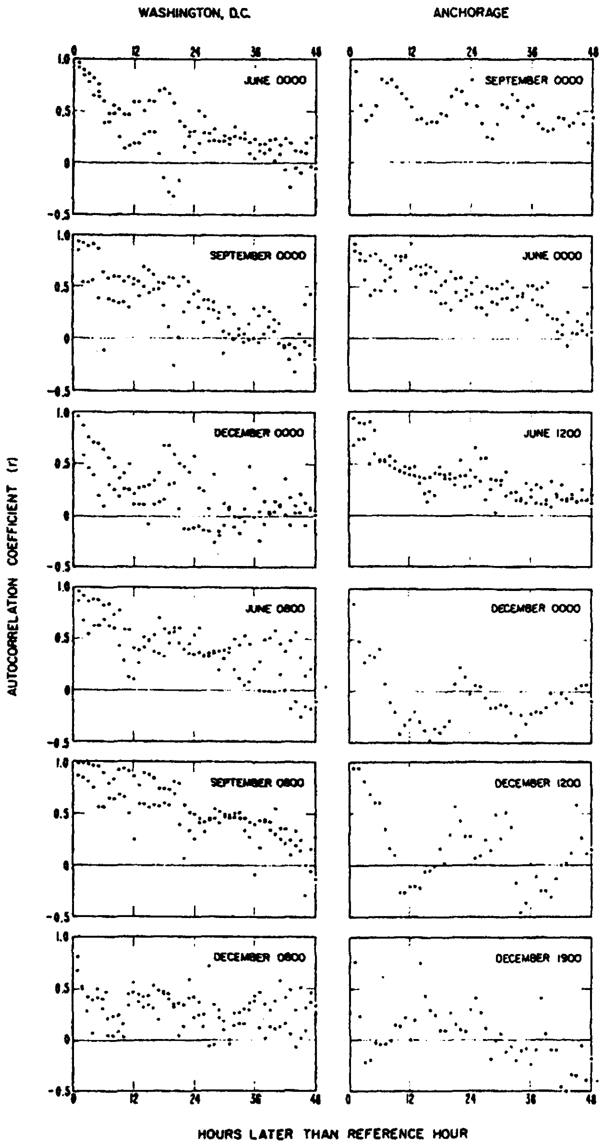

Figure 8: The decrease in correlation coefficient with time at two separate stations (from Gautier and Zacharisen, 1965).

Chapter 4: Review of the Equatorial Pacific with Regard to El Niño, Rossby, Kelvin, and Tropical Instability Waves

4.1 Introduction

The ocean-atmosphere system involves highly complex feedback mechanisms, which are not fully understood. The Pacific ocean is the largest expanse of water on the Earth, and consequently plays an important role in the ocean-atmosphere system. As a result the Pacific region has been extensively studied by both oceanographers and atmospheric scientists. The area under investigation in this study consists of the tropical Pacific region, and is depicted in Figure 1.

This chapter presents a review of previous work on the tropical Pacific, in particular the study of equatorial Kelvin, Rossby, and instability waves.

4.2 Sea Level Anomaly

Studies of propagating ocean features are complicated by the mean background topography of the sea surface. The upper layers of the solid Earth are neither perfectly spheroidal nor uniformly dense, so that an equipotential surface will have a topography with a horizontal scale of tens to thousands of kilometres, and a relief of up to 200m. Hypothetically, if the ocean were allowed to be at rest on the Earth, then its surface features would mimic that of the equipotential surface (allowing for the effects of the Earth's rotation). This surface is known as the Earth's marine geoid, and would complicate observations of spatial ocean topography if not removed. Normally the other major complicating factor in studying propagating ocean features are the tides. The orbit of TOPEX/Poseidon has been specifically chosen to avoid tidal aliasing for this reason.

When this background is removed, the resulting quantity will be the fluctuation from the mean ocean surface. The mean sea surface is a good approximation to the marine geoid because even in regions where there are strong and relatively steady currents (e.g. the Gulf Stream) the contribution to the topography from current flow is only about one-hundredth of that resulting from variations in the underlying solid crust. This fluctuation from the mean surface is called the sea level anomaly (SLA).

4.3 The El Niño - Southern Oscillation (ENSO)

The tropical regions are noted for the large interannual (time scales greater than one year) variations in weather, as well as seasonal changes. Many of the interannual variations are coherent (e.g. sea-level atmospheric pressure, air temperature, sea-surface temperature, precipitation, and sea level) over large distances, and the atmospheric coherent changes are called the Southern Oscillation (SO) (Walker 1924, 1928). This term does not refer to the southern hemisphere, but was coined to avoid confusion with two "northern oscillations" (the coherent variability associated with the changes in strength of the Icelandic low - and of the Aleutian low-pressure centres). From time-series of such variations (usually including pressure at Darwin or Djakarta), a southern oscillation index (SOI) can be constructed. The SOI for the years 1948 to 1979 is plotted on Figure 2. This index is either positive or negative depending on the relative change of e.g. surface pressure, across the Pacific. Figure 3 depicts the correlated relationship between the position of the eastern edge of the Pacific warm pool and the SOI.

The first suggestion that there may be a link between El Niño events and the Southern Oscillation (SO) was made by Bjerknes (1969, 1972). The prevailing winds over the equatorial Pacific are the South-East Trades and North-East Trades (though the convergence zone of the two wind fields lies north of the equator). Their strength depends on the difference in surface atmospheric pressure between the subtropical high pressure region in the eastern South Pacific, and the low pressure region over Indonesia. A positive SOI corresponds to easterly surface wind anomalies in the western central Pacific, and anomalously cold surface water in the eastern central tropical Pacific. However when the SOI is negative then there is usually a westerly surface wind anomaly in the western central Pacific, and the surface water is warmer than normal in the eastern tropical Pacific. Already the complex nature of the problem can be seen, whereby anomalous surface winds modulate, and are modulated by, SST changes.

The warm phase of the oceanic component is known as El Niño. The cold phase has only, relatively, recently been studied and named anti-El Niño or La Niña (Philander, 1985). The ocean-atmosphere interaction which links the SO, El Niño, and La Niña together is known as the El Niño-Southern Oscillation (ENSO). The effects of El Niño tend to be more devastating than La Niña (Canby, 1984), and hence El Niño has been more extensively studied. The phases of an ENSO event are depicted in the SST plots of Figure 4, showing SSTs expected for normal, El Niño, and La Niña conditions.

The main signature of El Niño is the transfer of warm water from the western Pacific warm pool (typically surface water warmer than 28-29°C) to the eastern Pacific. Wyrtki (1975) was the first to suggest that the appearance of warm water in the eastern Pacific was the result of westerly wind anomalies in the central western Pacific which generate equatorial *downwelling* Kelvin waves. Kelvin waves are now acknowledged as an integral part in the ENSO system (McCreary, 1976, Busalacchi *et al*, 1983, Miller *et al*, 1988, Kessler *et al*, 1995).

Gill (1983) used linear equatorial wave theory to suggest that the zonal displacements of the warm pool are due to anomalous advection of warm water. He found that anomalous advection during 1972-1973 was the result of anomalous wind forcing producing a succession of equatorial Kelvin waves and Rossby waves. This idea of winds causing remote forcing via large scale ocean waves has been corroborated by various studies, some of which will be discussed shortly.

The method by which the central Pacific becomes warmer is uncertain at present. Modelling studies have suggested that horizontal advection is important (Battisti, 1988, Seager, 1989, Harrison and Graig, 1993). Vertical advection due to *downwelling* Kelvin waves may also be important in warming the Eastern Pacific. Kelvin waves depress the thermocline, and inhibit the mean *upwelling* of cold, dense water. Hayes *et al* (1991) demonstrated that zonal and meridional advection and vertical mixing could not be dismissed either.

During a strong El Niño, zonal advection may produce a slowly "propagating" eastward displacement of anomalous SST all the way to the eastern Pacific. Usually, though, El Niño starts with warm SST anomalies near the date line (180°E), which expand into the eastern equatorial Pacific.

4.3.1 The Delayed Action Oscillator Theory

Several hypotheses have been developed to explain ENSO. Anderson and McCreary (1985) and Neelin (1990) investigated the slow "propagative" SST anomalies using coupled models. Neelin's (1991) definition of the slow SST mode contrasted with an alternative hypothesis called the delayed action oscillator mechanism (Schopf and Suarez, 1988, Battisti, 1988, and Cane, 1992). The slow SST mode comes from unstable basin-wide coupled ocean-atmosphere modes, and equatorial ocean waves are unimportant. In contrast the delayed action oscillator involves local ocean-atmosphere interaction in the central eastern part of the basin, and ocean waves are essential

(Boulanger and Menkes, 1995). In this mechanism a warm event is initiated as a central to eastern Pacific SST anomaly. As a result westerly wind anomalies are generated to the west of the SST anomalies. These winds then force eastward propagating *downwelling* Kelvin waves, and westward propagating *upwelling* Rossby waves. The Rossby waves advect warm water from the western Pacific to enhance the pre-existing SST anomalies. The cooling effect of the Rossby waves, as they upwell deeper and colder water, also acts to increase the relative difference between the region of anomalously warm water and the waters to the west of that region. The Kelvin waves advect water to the east, and deepen the thermocline as they propagate. The deepening of the thermocline further enhances the warm SST anomalies, by suppressing the *upwelling* cooling effect which would otherwise exist. The reinforcement of the initial warm SST anomalies thus instigates an even larger response from the atmosphere, and stronger westerly winds are generated. Hence the ocean-atmosphere system is coupled in a positive feedback loop. This process would grow indefinitely if left unchecked. However the theory proposes that the westward propagating *upwelling* Rossby waves reach the Pacific western boundary, where they are reflected as *upwelling* Kelvin waves which propagate back towards the initial area of warm SST anomaly. The *upwelling* Kelvin waves act to erode and eventually reverse the warm anomalies. The system then enters a cold phase (La Niña), roughly opposite to the warm phase (El Niño). The delayed action oscillator has been supported from results by Zou and Latif (1994). However Delcroix *et al* (1994) and Picaut and Delcroix (1995) have demonstrated their results to be inconsistent with the hypothesis. Boulanger and Menkes (1995) concluded that although some features of their data were consistent with the mechanism (i.e. the appearance of an *upwelling* Kelvin wave simultaneous with the weakening of the 1991-1993 ENSO), others were not (i.e. the Kelvin wave appeared to be forced by strong easterly wind anomalies in the western Pacific, rather than by reflection of an *upwelling* Rossby wave).

4.4 Equatorial Waves

Ocean equatorial waves have only recently been identified in observational data, mainly due to the advent of satellite altimeters (e.g.Geosat, TOPEX/Poseidon), and also due to the deployment of the Tropical Ocean and Global Atmosphere-Tropical Atmosphere Ocean (TOGA-TAO) array of moorings in the equatorial Pacific. TOGA-TAO was developed especially to monitor El Niño, and consists of approximately 70 bouys deployed across the tropical Pacific, measuring *in situ* currents, temperatures and winds. These observations are important as they allow the role of equatorial waves in the transfer of heat and mass to be assessed (e.g.Delcroix *et al*, 1991), as well as their role in the slow eastward displacement of the western Pacific warm pool (Kessler *et al*, 1995).

4.4.1 Kelvin Wave Observations

Equatorial Kelvin waves were observed before equatorial Rossby waves. They were suspected owing to the meridional shape of their sea level signature at the Galapagos Islands by Ripa and Hayes (1981), detected by Knox and Halpern (1982) as an eastward propagating pulse in zonal near-surface current, and observed by Eriksen *et al* (1983) and Lukas *et al* (1984) from sea level changes. As with Rossby waves, Kelvin waves have been observed much more readily since the advent of satellite altimetry. Numerous authors have observed equatorially trapped Kelvin waves in the Pacific using a variety of instruments, a variety of processing techniques, and several have provided varying phase speed estimates via differing analysis methods. Delcroix *et al* (1991) used a time-lag correlation method on Geosat data to give a Kelvin wave phase speed of 2.82±0.96 m/s, and a least squares fit of SLA meridional structures to theoretical Kelvin wave shape to give a phase speed of 2.26±1.02 m/s. The Geosat derived Kelvin waves are apparent at the end of 1986 and during August 1987 on Figure 5. Zou and Latif (1994) applied the technique of principal oscillation analysis on Geosat data to produce a phase speed of ~2.5 m/s. Boulanger and Menkes (1995) used the more accurate TOPEX/Poseidon data, along with TOGA-TAO data; a time-lag correlation gave a phase speed of 2.7±0.9 m/s from the TOPEX/Poseidon data, and 2.3±0.3 m/s from the TOGA-TAO data set. Kessler *et al* (1995) concentrated on the TOGA-TAO 20°C depth data which revealed Kelvin wave speeds of 2 - 3 m/s; a value of 2.4 m/s was obtained for the Kelvin wave phase speed by correlation with zonal wind. Chelton and Schlax (1996) obtained a Kelvin wave phase speed of 2.70 m/s from an empirical version of the Radon transform (or 'slant stack').

4.4.2 Rossby Wave Observations

The first observations of Rossby waves in the tropical Pacific were made by Emery and Magaard (1976), White (1977), and Meyers (1979). These, however, were off-equatorial waves, with White (1977) examining the annual cycle of the subsurface thermal structure in the eastern Pacific in the latitude range 10° to 20°N. White (1983) went on to find westward propagating interannual signals travelling at Rossby wave speeds from 6°N to 30°N. The ocean was severely under sampled, and unambiguous interpretation of Rossby wave signals in the thermal measurements was difficult except in a few locations. The observational evidence for equatorial Rossby waves was limited to either the Rossby waves' zonal propagation between a few locations (Lukas *et al*, 1984) or to their meridional structure measured along one longitude (Lukas and Firing, 1985).

Equatorial Rossby waves were not comprehensively observed until the advent of satellite altimetry and the Geosat mission. Delcroix *et al* (1991) used the Geosat 17 day exact repeat orbit (November 8, 1986 to November 8, 1987) to make the first such observation of an equatorial Rossby wave. The wave showed up as a severe drop in SLA (~12 cm) propagating westward along 4°N and 4°S at an estimated speed of 1.02±0.37 m/s, which roughly corresponds to the theoretical phase speed of a first mode equatorial Rossby wave. This result is reproduced in Figure 6, which shows a contour time-longitude plot of Geosat SLA along the latitude 4°N.

Equatorial Rossby waves have since been observed by numerous authors in varying data sets including Penhoat *et al* (1992, Geosat/linear model forced by FSU wind stress intercomparison), White and Tai (1992, Geosat), Zou and Latif (1994, Geosat data and principle oscillation patterns technique (POP)), Delcroix *et al* (1994, Geosat), Zheng *et al* (1995, Geosat), Boulanger and Fu (1996, TOPEX/Poseidon), and Chelton and Schlax (1996, TOPEX/Poseidon). Estimates of the phase speed of the first mode equatorial Rossby wave have been made by Delcroix *et al* (1991), 1.02±0.37 m/s as previously mentioned, and also by Zou and Latif (1994), ~0.5 m/s at 6°N and 6°S (second mode Rossby wave), Boulanger and Menkes (1995), 1.0±0.2 m/s (TOPEX/Poseidon) and 1.1±0.2 m/s (TOGA-TAO), and Chelton and Schlax (1996), 1.0 m/s. Widely different methods of data processing and interpretation have been used by all of the authors.

It should also be noted that the Rossby phase speeds reported are mainly faster than those given by standard linear theory (Chelton and Schlax, 1996). Recent work by Kilworth et al (1997) has revealed a possible mechanism for this discrepancy. It is argued that the major part of the discrepancy is caused by the presence of baroclinic east-west flows, which modify the potential vorticity gradient. This has obvious implications for Rossby waves since the restoring force is provided by the conservation of potential vorticity (section 1.3).

4.4.3 Wind Forcing of Equatorial Waves

A review on pre-satellite altimetry observations of ocean response to wind forcing was provided by Knox (1986). The wind field in the western Pacific exhibits events of anomalous westerly wind which are localised (both spatially and temporally) events. These anomalous winds are known as "westerly wind bursts". The role of these wind bursts in generating Kelvin and Rossby wave modes was studied using a theoretical approach by Gill and Clarke (1974), which revealed that zonal winds over a restricted time and space region could excite an ocean response, expressible as an eastward propagating Kelvin wave.

The first attempt to describe the spatial and temporal shape of a forcing event and response from observational data, was made by Knox and Halpern (1982). A pulse forced by a wind event, noted in April 1980, was observed as an increase in eastward current near 152°W, later at 110°W, and finally as a rise in sea level at the Galapagos Islands. The propagation speed measured was higher than that computed for a first mode Kelvin wave, but Doppler shifting due to mean eastward currents was suggested as an explanation for the extra speed. Eriksen *et al* (1983) correlated several distinct westerley wind bursts measured at three islands of the Gilbert Group with increased sea level at five near-equatorial islands during 1977-1981. These studies concentrated on near-equatorial sea level data as a measure of response, which would exclude the possibility of observing Rossby waves. Eriksen (1985) used equatorial current meter moorings, and found low-mode Rossby wave as well as Kelvin wave responses to wind forcing.

Delcroix *et al* (1991), using Geosat and FSU (Florida State University) wind stress analysis data, noticed good time agreement between Kelvin wave appearance and the existence of notable zonal wind stress anomalies. They suggested that the anomalous wind may be the local generating mechanism for Kelvin waves. They did, however, advise that this hypothesis be treated with caution, since not all such wind events produce observable waves. This was also noted by Kessler *et al* (1995) using the TOGA-TAO network of buoys. Boulanger and Fu (1996) have also recently reported an incidence of a strong *downwelling* Kelvin wave apparently not fully explained by local wind forcing. They stress an important point that, except during three periods of their data where western boundary reflection was demonstrated, the Kelvin wave amplitude in the western Pacific was explained neither by reflection nor by wind forcing.

Giese and Harrison (1991) used linear theory and an ocean general circulation model to conclude that three types of westerly wind are able to induce an eastern Pacific response by forcing equatorial waves. The three types were named as the C-type (centred on the equator), the S-type (south of the equator), and the N-type (north of the equator) (Figure 7). The C-type was seen to excite Kelvin waves that subsequently altered the SST in the central and eastern Pacific. S-type events had similar effects to the C-type, but lower in amplitude. The N-type westerly wind type only excited a very weak eastern Pacific response.

Kelvin waves are an important contributor to climate variability. A connection between intraseasonal Kelvin waves in the equatorial Pacific and the Madden-Julian oscillation has recently been made by Zou and Latif (1994) and Kessler *et al* (1995). The Madden-Julian oscillation, or MJO, (Madden and Julian, 1972) consists of planetary scale, eastward propagating intraseasonal convection fluctuations in the tropical atmosphere. Westerly wind bursts are a feature of the MJO. A good review of recent atmospheric work investigating the MJO is given by Kessler *et al* (1995). The atmospheric oscillation has a period of between 30 to 100 days, whilst the intraseasonal Kelvin waves have periods nearer 90 days. Kessler *et al* (1995) suggested that this discrepancy can be attributed to the oceanic response to forcing whose fetch is similar to the wavelength of a Kelvin wave at intraseasonal frequencies.

4.5 Tropical Instability Wave Observations

Instability waves in equatorial current and temperature fields are a universal feature of the world's oceans. The oscillations are narrow-band in frequency and wavenumber, with time and zonal length scales centred around three weeks and 1000 km. The waves appear to be seasonally modulated in time. Their phase speed is westward, but their apparent energy flux is eastward. They are thought to exist due to shear instabilities in the equatorial surface current system (Philander, 1978), and serve as a dissipative mechanism for these.

The waves were first discovered in the Atlantic by Duing (1975). The first observations of such waves in the Pacific were made using *in-situ* data from bottom-mounted current meters by Harvey and Patzert (1976). They reported a 25 day oscillation of 1000 km wavelength, with a phase speed of 50 cm/s. Further observations were made using satellite SST data (Advanced Very High Resolution Radiometer data (AVHRR)) during boreal autumn and winter 1975 by Legeckis (1977). Legeckis (1977) reported wavelengths of 800-1200 km, periods around 20-30 days, and phase speed estimates of 40 cm/s. The tropical instability wave (TIW) signatures in the AVHRR data are presented in Figure 8, and their signatures in moored current meter data in Figure 9. Busalacchi *et al* (1994) described the waves as having periods between 20-30 days, and a westward phase speed of ~45 cm/s. Giese *et al* (1994) reported westward propagating waves centred around 6°N with phase speeds of 46 cm/s at 30 to 40 day periods, although they admitted considerable uncertainty in these estimates due to the method they used (a 'by eye' straight line fit). Both authors used TOPEX/Poseidon data. Qiao and Weisberg (1995) used velocity measurements from an array of acoustic Doppler current profilers, finding a period of 500 hours, wavelength 1060 km, and a phase speed of 59 cm/s. McPhaden (1996) recorded a very broad band period of 15-50 days, with phase speeds of 30-40 cm/s and a zonal wavelength of 750-1150 km.

Lawrence *et al* (1994) and Allen *et al* (1995) compared TIW activity in data from the Along-Track Scanning Radiometer (ATSR), on the ERS-1 satellite, and from TOGA-TAO with TIWs generated by an ocean general circulation model. They found a correspondence between the phases and phase-speeds of the model and observed TIWs greater than would be expected if the TIWs were formed from pure instabilities. This then led Allen *et al* (1995) to conclude that the TIWs structure must be controlled to some extent by external wind forcing. One plausible hypothesis considered involves wind forcing of Kelvin waves leading to the generation of Rossby waves via eastern boundary reflection. The Rossby waves could then control the phase of individual TIWs through their effect on the current shear. Recent modelling work by Lawrence *et al* (1997) provides new evidence in support of this hypothesis.

4.6 Western Boundary Reflection

The question of whether ENSO could be driven by extra-equatorial Rossby waves was investigated by Kessler (1991) using ship of opportunity vertical temperature profiles, in the light of coupled model work which had shown that ENSO-like behaviour could be simulated without extra-equatorial input (Battisti, 1989, Anderson and McCreary, 1985). Kessler concluded that the net zonal flows associated with observed extra-equatorial (further than 8° latitude from the equator) Rossby waves in the northern Pacific do not provide a net transport which could make a significant contribution to equatorial Kelvin waves.

White and Tai (1992) used data from the Geosat exact repeat mission to investigate reflection of interannual Rossby waves at the western boundary of the tropical Pacific over a 2.7 year period. They observed Rossby waves reflecting and consequently generating Kelvin waves in the equatorial wave guide. Using linear theory they concluded that the first-mode Rossby wave accounts for 70-80% of the Kelvin wave amplitude. However Zou and Latif (1994), again using Geosat data, found no evidence for annual western boundary Rossby wave reflection. Boulanger and Menkes (1995) also studied the western boundary, but using both the TOPEX/Poseidon and TOGA-

TAO data sets. They concluded that wind forcing, rather than boundary reflection, is the main trigger for Kelvin wave propagation from the western to eastern Pacific. A case study made by Boulanger and Menkes (1995) of an *upwelling* Kelvin wave propagating from the western Pacific in September 1993 to the eastern Pacific in November 1993, simultaneous with the weakening of the extended 1991-1993 ENSO event revealed that whilst the action of the Kelvin wave was consistent with the predictions of the delayed oscillator mechanism, the way in which the Kelvin wave was forced was inconsistent with the delayed action oscillator i.e. the Kelvin wave appeared to be forced by a strong easterly wind anomaly in the western Pacific, rather than by reflection of an *upwelling* Rossby wave. Boulanger and Fu (1996), however, evidenced reflection at the western boundary, again using TOPEX/Poseidon (data from November 1992 to May 1995); in contrast to their observations at the eastern boundary, where reflection of Kelvin waves into first mode Rossby waves was observed throughout their entire data set, the reflection of Rossby waves at the western boundary was seen during three specific periods: April-August 1993, January-June 1994, and December 1994 to February 1995.

A recent paper by Chelton and Schlax (1996) concluded that the issue of whether the Kelvin waves could be produced by a purely oceanic process (i.e. by the reflection of Rossby waves from the western boundary) or by an air-sea interaction (i.e. by wind variations in response to changes in SST induced by the Rossby waves) was a controversial subject, and that the continued coverage of the region by TOPEX/Poseidon is likely to provide important insight into this dynamical process.

4.7 Eastern Boundary Reflection

The question of whether Kelvin waves could reflect from the eastern boundary as Rossby waves was investigated by Delcroix *et al* (1991) using the Geosat 17 day repeat orbit. They suggested that the equatorial *upwelling* Rossby wave observed in January 1987 in the eastern Pacific was due to the reflection of an *upwelling* Kelvin wave. They tested this hypothesis using a first baroclinic linear model. When forced with Florida State University (FSU) wind stress anomaly, both up and *downwelling* Kelvin waves were produced, in agreement with the Geosat observations. An *upwelling* Rossby wave was also observed reflecting from the eastern boundary in the model results, although *downwelling* Rossby waves were not produced. They repeated the analysis excluding the contribution of the locally forced Rossby wave. A *downwelling* Rossby wave, and a reduced amplitude *upwelling* Rossby wave, were produced. They concluded that the local response of the wind weakens the reflected *downwelling*

Rossby wave, whilst enhancing the *upwelling* Rossby wave - in other words the local wind forcing is responsible for the absence of a reflected *downwelling* Rossby wave. Kessler (1995), using TOGA-TAO data, concluded that eastern boundary reflection did not occur, since the observed Rossby waves were almost 180° out of phase with that expected if they were reflected waves (Figure 10).

Penhoat *et al* (1992) went on to compare a linear model forced by FSU wind stress with the Geosat data in more detail, examining the 1986-1987 El Niño. They found that the *upwelling* Rossby wave in the eastern Pacific was mainly due to Ekman pumping anomalies (Ekman pumping being the upwelling or downwelling of water to compensate for divergences and convergences of overlying water) generated directly by a favourable wind forcing, and that the reflection process was of minor importance, although it reinforced the Ekman pumping effect. The Ekman pumping was also attributed to cancelling out the sea level rise due to the *downwelling* Rossby wave issued by a reflection from the eastern boundary. The reflection process was said to be important in contributing to the Rossby wave signal, making it visible all the way from the eastern to the western side of the Pacific. It was noted that although the Kelvin wave and reflected Rossby wave are part of the annual cycle, in El Niño years they have larger amplitudes. Boulanger and Menkes (1995) used the TOPEX/Poseidon and TOGA-TAO data sets to investigate reflection at the eastern boundary. Eastern boundary reflection was not deemed to play a significant role in the generation of Rossby waves in the period studied (1992-1993 El Niño), most of the signal from incoming Kelvin waves either being counteracted by unfavourable wind forcing, or strongly reinforced by the wind forcing. Boulanger and Fu (1996), using the TOPEX/Poseidon data set alone, observed eastern boundary reflection of Kelvin waves into first-mode Rossby waves during the entire period of their data (November 1992 - May 1995). The efficiency estimated of the reflection process was 80% of that expected from an infinite meridional wall.

4.8 Summary

The El Niño Southern Oscillation, or ENSO, is a phenomenon which can have huge consequences for the Earth's ocean-atmosphere and climate system. Large scale waves, known as Kelvin waves, are acknowledged as an integral part of the ENSO system (e.g. McCreary, 1976, Busalacchi *et al*, 1983, Miller *et al*, 1988, Kessler *et al*, 1995). Although several hypotheses have been proposed to explain ENSO, there is not one definitive theory. The question of whether western or eastern boundary reflection of large scale waves can affect the system is still a controversial one, with several contradicting studies, and the role of tropical instability waves in the dynamics of ENSO still requires further investigation. The advent of satellite altimetry missions providing data of unprecedented accuracy and coverage has presented the opportunity to study the propagation characteristics of large scale oceanic waves with much more confidence, facilitating the study of ENSO. The TOPEX/Poseidon data in this study will be examined for possible reflection events.

Chapter 7 details the work done in this study, using TOPEX/Poseidon data, which identifies the important waves and their characteristics, and provides a detailed examination of the wave dynamics and processes during the period October 1992 - October 1994.

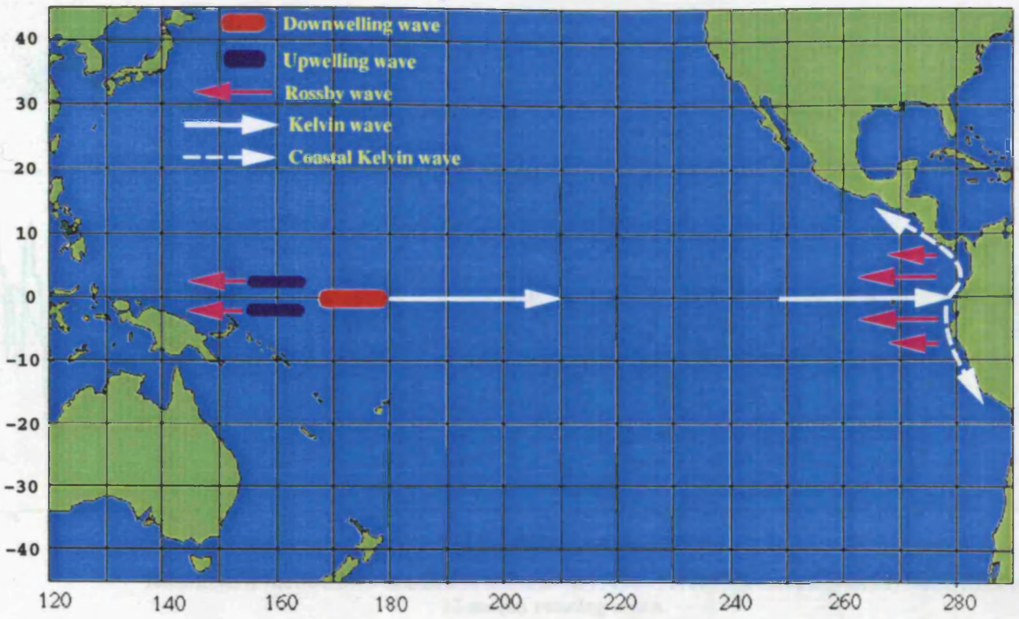

Figure 1: Schematic of Kelvin and Rossby wave activity in the Pacific region

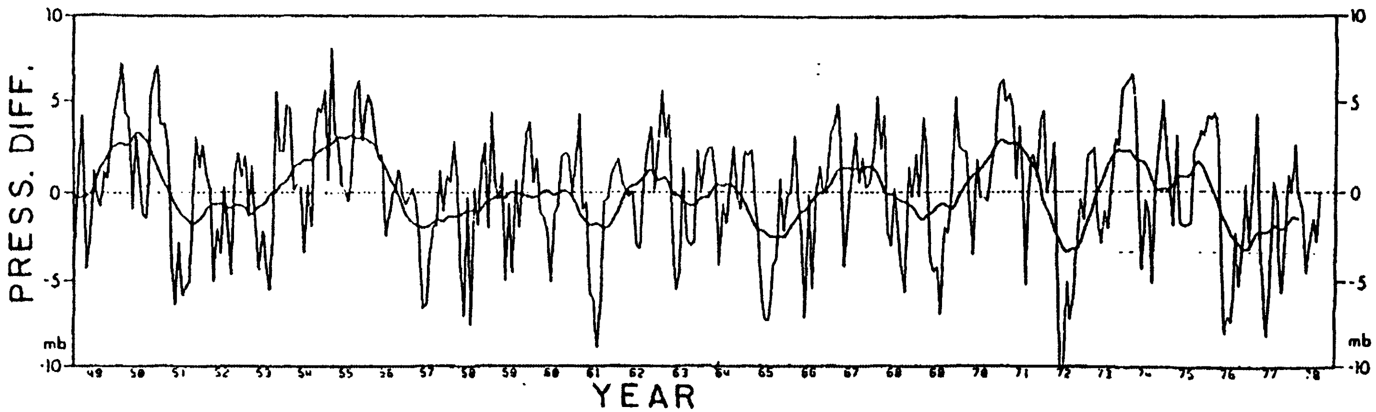

Time-series of the Southern Oscillation Index from 1949 to 1978. Thin curve is monthly mean, thick curve is 12 month running mean.

Figure 2: The Southern Oscillation Index (SOI) from 1949 to 1978. The thin curve is the monthly mean, the thick curve is the 12 month running mean. (From Pickard and Emery).

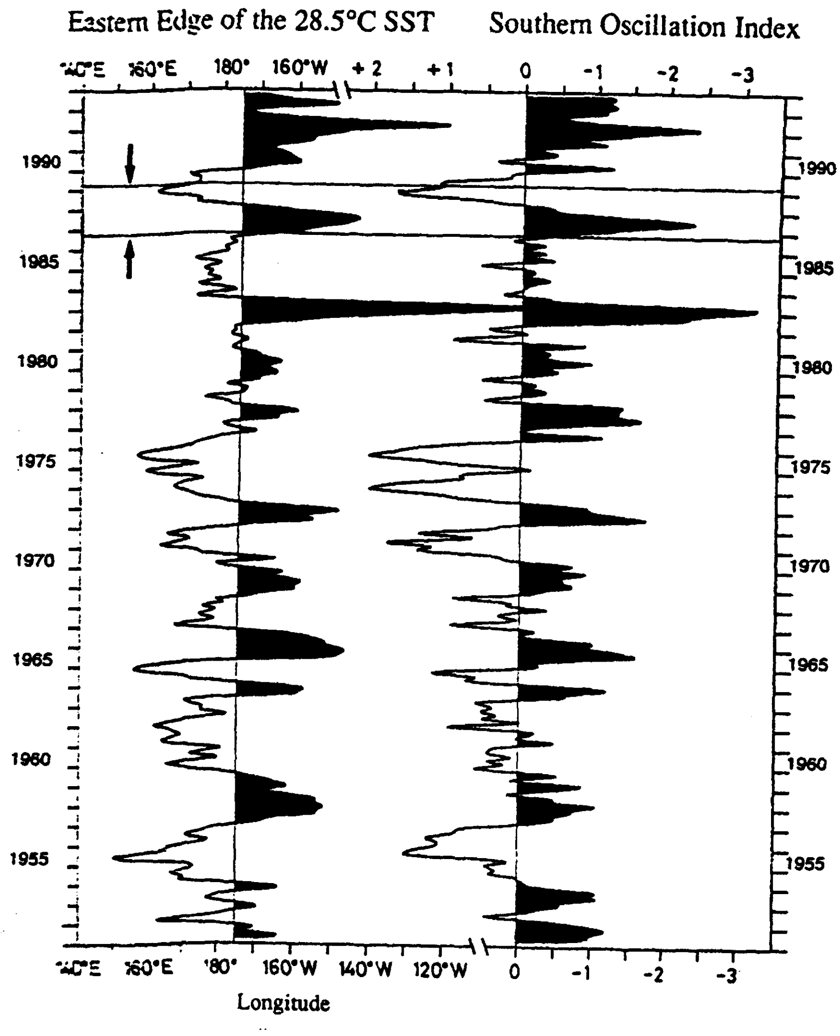

Figure 3: The correlated relationship between the position of the eastern edge of the Pacific warm pool and the SOI.
(From Picaut and Delcroix, 1995).

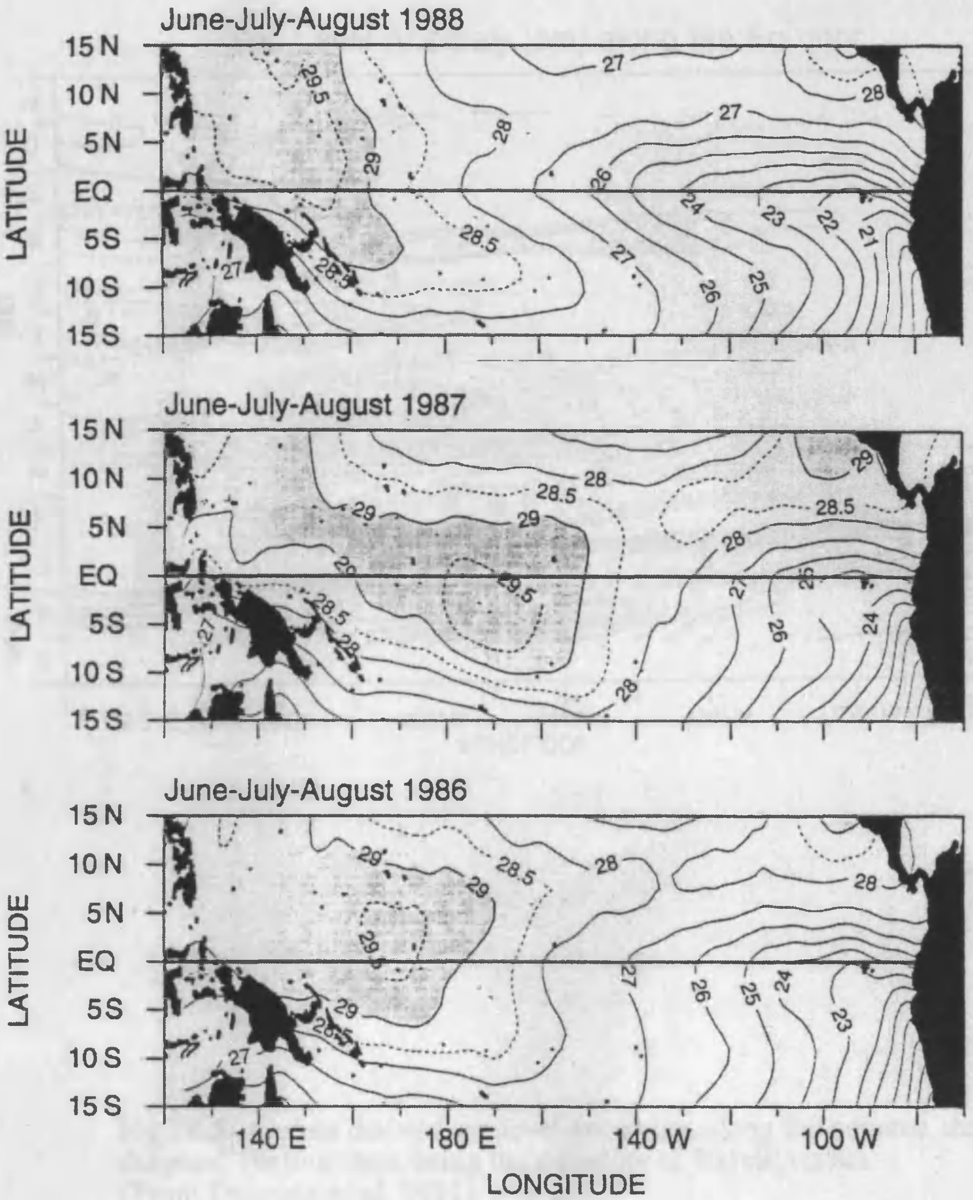

Figure 4: SST fields in the tropical Pacific during June-August 1988 (top, La Niña), 1987 (middle, El Niño), and 1986 (bottom, "normal"). SST warmer than 29°C is shaded. (From Picaut and Delcroix, 1995)

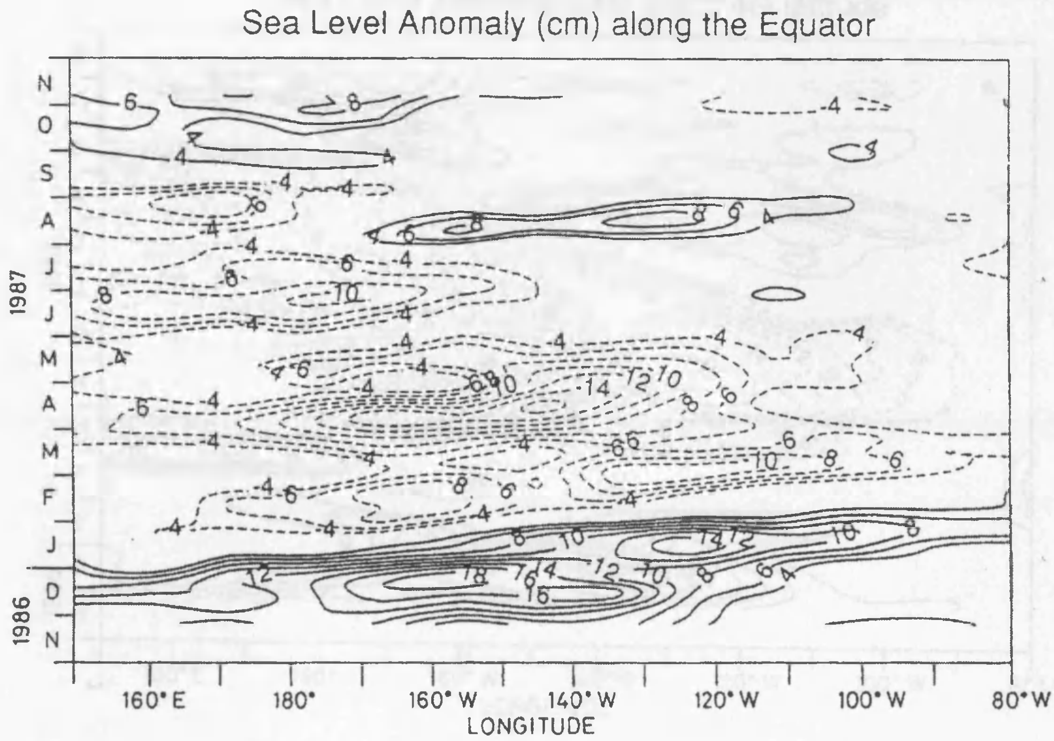

Figure 5: Geosat derived sea level anomalies along the equator, the diagonal contour lines being the signature of Kelvin waves.
(From Delcroix *et al*, 1991)

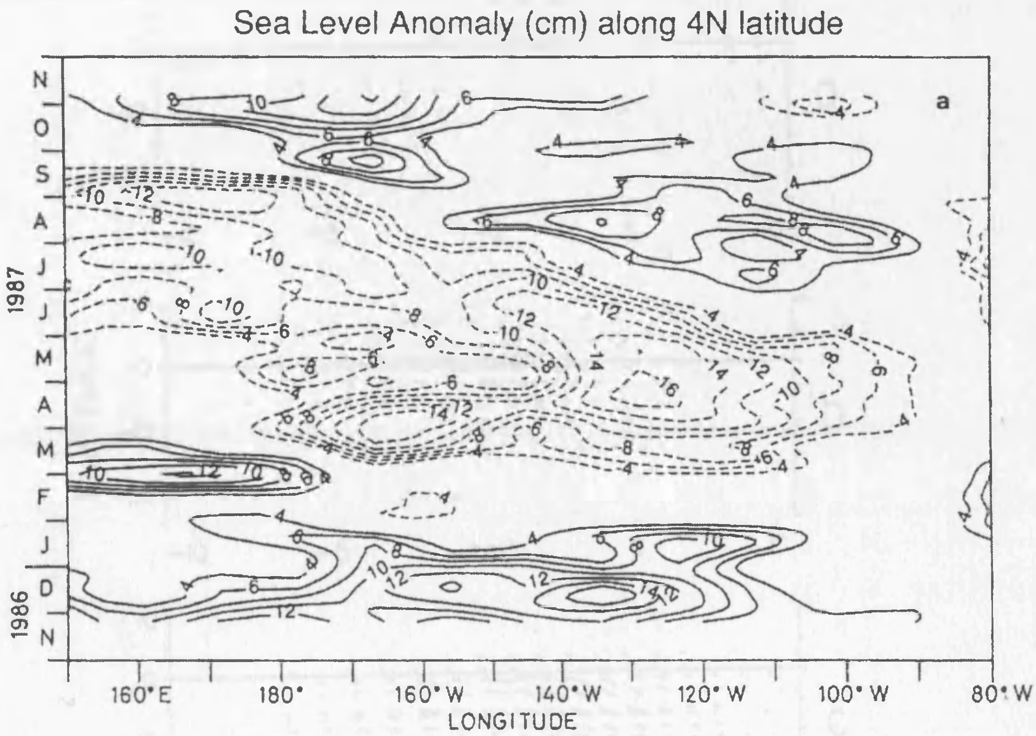

Figure 6: Geosat derived sea level anomalies along 4°N, the diagonal contour lines being the signature of Rossby waves. (From Delcroix *et al*, 1991).

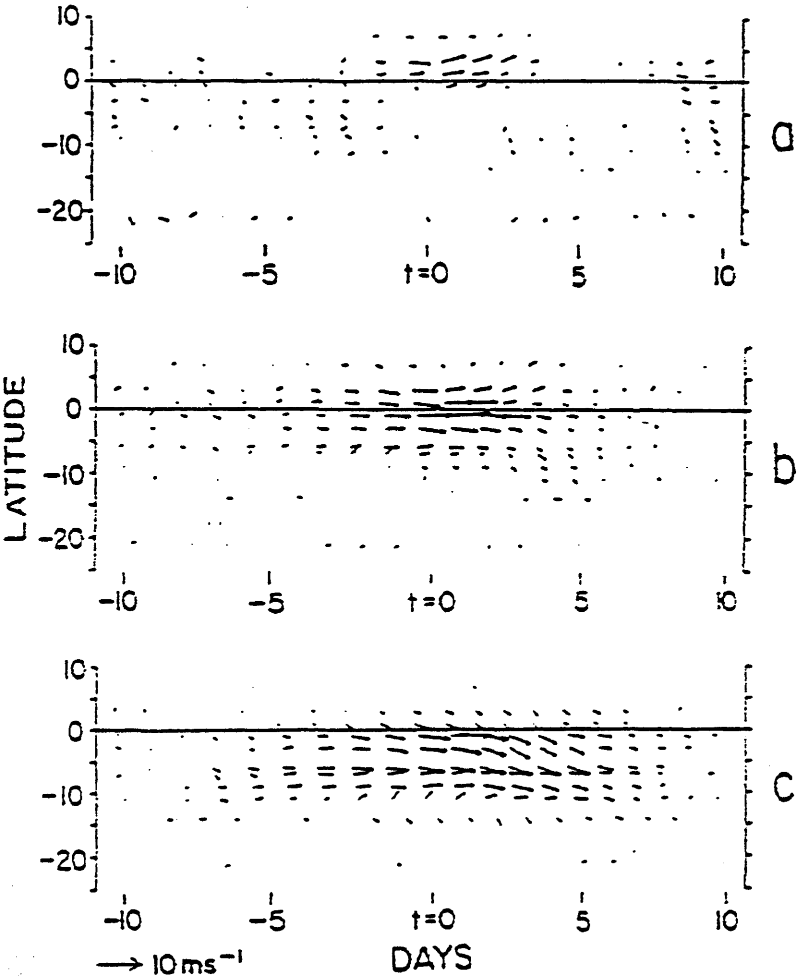

Figure 7: Three composite westerly wind bursts, as described by Harrison and Giese (1991) a) The composite anomalous N-types, b) C-type, and c) S-type events.

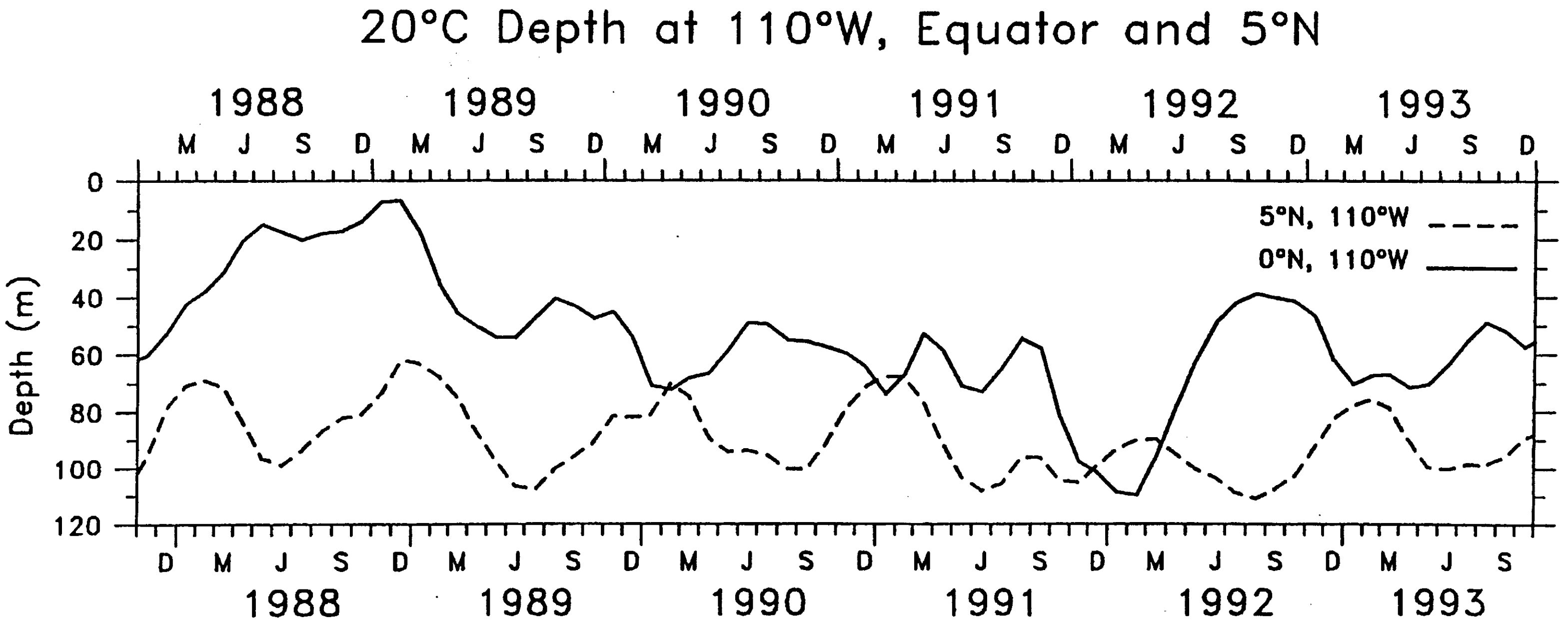

Figure 8: 20°C depth at longitude 110°W, and latitudes 0° and 5°N. The solid line represents Kelvin wave activity, the dashed line Rossby wave activity (equatorial time series lagged 2 months to account for wave propagation)

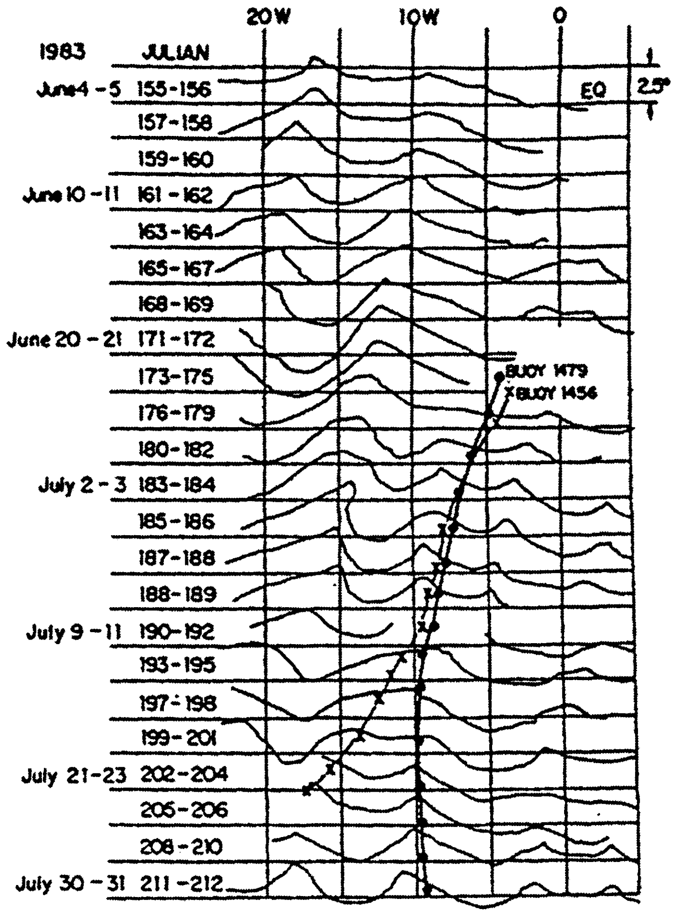

Figure 9: Tropical instability wave signatures in the near equatorial SST front from satellite AVHRR data (from Legeckis and Reverdin , 1986).

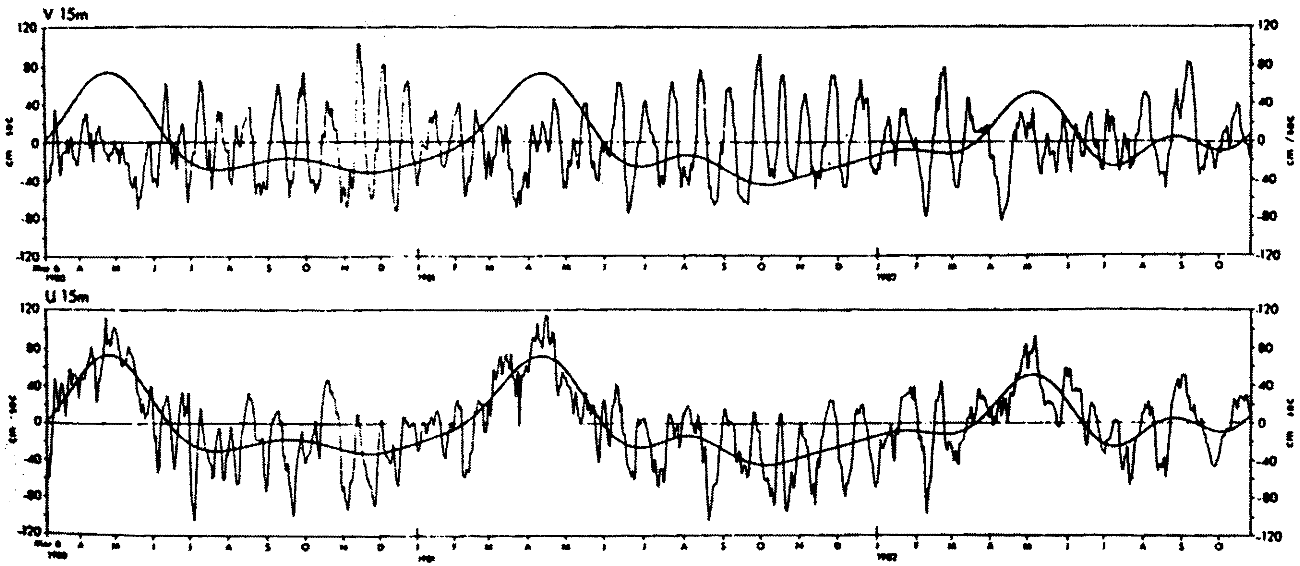

Figure 10: Meridional (v) and zonal (u) velocity fluctuations at a depth of 15 m on the equator at 110°W. The superimposed curve is the low-pass filtered zonal current. The 3-week oscillations (TIWs) are most energetic when the mean current is westward (u < 0). (From Philander *et al*, 1985).

Chapter 5: An Investigation of Spatial Coherence Scales of Ionospheric Electron Content Variability around Monthly and Local conditions

This chapter deals with the extraction of a spatial coherence scale for the offset between measured ionospheric electron content (IEC) and predictions of mean monthly IEC. The scale characterises the variability of the IEC away from the monthly mean, and has uses in radio propagation prediction models.

Adaptive models are used to correct monthly mean parameters estimated by predictive models, by allowing for conditions in the local ionosphere. Since single frequency altimeter systems, such as ERS-1, rely on predictive models to provide corrections to the path delay imposed by the ionosphere on the altimeter pulse, such adaptive models could, in principal, be used to improve the accuracy of altimeter measurements of sea surface height.

Coherence distances have been calculated, using TOPEX dual frequency estimates of the IEC, over a range of geographic latitude, from 45°S to 45°N (corresponding to 60°N to 60°S geomagnetic latitude), and over all local times. These calculations have provided the first ever 'world wide' maps (quasi-global) of IEC coherence distance.

5.1 Introduction

Current models used to predict the ionospheric electron content, and hence propagation delay, can have fairly substantial errors when compared to experimental results. The ionospheric correction applied to altimeter sea surface height typically ranges from 1 - 20 cm, but the errors in model mean monthly predictions, when compared to instantaneous measurements, can also be of the order of 20 cm. Such large errors should be unacceptable to modern altimeter missions which try to achieve accuracies around 5 cm or better.

All satellite radar altimeters to date, other than TOPEX, have been single frequency systems e.g. ERS-1, SEASAT, and GEOSAT These missions have relied on semi-empirical models, such as the International Reference Ionosphere (IRI), to correct for the ionospheric delay imposed on the radar pulse's propagation time. Such models use peak F-layer electron density measurements combined with a number of Chapman layers and other terms to construct an electron density profile. They are limited by the relatively small coverage of their ground stations, which are restricted to land masses, the majority of which are in the northern hemisphere. Predictions are made on a monthly basis, and so do not allow for unexpected disturbances in the ionosphere which could be caused by, for example, a magnetic storm.

Figure 1 illustrates the discrepancy between the IRI model predictions and the actual measurements of IEC from TOPEX for one pass of the satellite. Variations of the order of cm are evident, which is the order of the sea surface height accuracy required by modern oceanographic altimeter missions. The offset is largest, for this pass, around geomagnetic latitude 18°N, corresponding to the northern arm of an ionospheric phenomenon known as the equatorial anomaly (discussed in section 5.6.3).

Figure 2 illustrates this offset on a global basis. The data are taken over approximately 1 month (3 TOPEX/Poseidon cycles). The offset is strongest at around 20 degrees north and south of the equator, and follows the form of the magnetic equator. This again corresponds to the equatorial anomaly region, where the ionosphere is likely to be disturbed by irregularities.

5.2 Data Processing

The TOPEX data used in this study were provided on CD ROM format from the AVISO Altimetry multi-satellite data bank in France. The data on the CD ROM are referred to as the raw data. The raw data consists of various geophysical parameters which are provided at a sampling rate of one reading per second. The raw data contains all the geophysical parameters returned by the altimeter, and comprises a very large data set; for each CD ROM there are approximately 2 million separate readings of 130 parameters, giving 2.2×10^8 records (approximately 200 Mb). After allowing for certain flags and conditions the data required for this study were extracted from the raw data. The flags make sure that the parameter being extracted is within acceptable physical bounds, and the conditions check for such things as the TOPEX altimeter being switched on and that the reading was taken over liquid water etc. This new set is known as the reduced data. The reduced data removes physically impossible and otherwise unreliable readings. However spurious values of other types can still remain, and these are removed by the use of median filtering (Beard et al, 1995) to produce one per 20 second records.

5.3 Coherence of Ionospheric Electron Content Variability

The research has concentrated on obtaining spatial coherence distances of the offset between instantaneous measurement and model mean monthly predictions. This spatial coherence gives a measure of the variability of the ionosphere from the monthly mean, and provides a scale over which adaptive modelling techniques can be used. A more detailed account of spatial coherence can be found in section 3.4.

Previous coherence studies of the ionosphere have utilised ground station data, which have certain limitations in the study of spatial correlation scales. A detailed high resolution picture of the spatial coherence is not possible with the low spatial sampling afforded by the location and number of ground stations. Hence such studies must rely on assuming a linear decorrelation in calculations of coherence distances. The TOPEX altimeter provides the first opportunity to investigate the spatial coherence of the ionosphere on a more quasi-global basis, without the need for interpolation of results.

Ground based studies are fixed to a geographic location, and the coherence calculations are performed on ionospheric data which are restricted to being collected over this set geographic position. Even though the TOPEX/Poseidon satellite does pass over the same geographic location approximately every ten days, there is no reason to gather data over the same restricted geographic region. Therefore the data sets used for this coherence study will come from consecutive passes of TOPEX i.e. differing geographic locations. Each consecutive ascending pass is 57 seconds later in local time than the preceding pass, and so we are essentially sampling the 'same' ionosphere (in terms of local time) between each pass.

5.4 Data Preparation

Data have been extracted from cycles 10 to 88 and processed to remove spurious readings by taking a twenty point along track median. Cycles 2-9 have not been used due to possible problems created by an antenna mispointing error. It was feared that such mispointing errors may introduce incorrect correlations in the data. Each cycle is split into ascending and descending passes, using a simple algorithm. The values of IEC from both ascending and descending passes, and the corresponding offset from the monthly mean, can then be extracted from each pass. The data are binned into along track one degree geomagnetic latitude ranges. The equatorial local crossing time of each pass is calculated and recorded. This is to allow the coherence scales to be binned with respect to local time later on in the processing. Next the parameters for each cycle are concatenated together to form large pseudo-continuous matrices of data. These large data matrices are used to produce quasi-global maps of spatial coherence distances. The quasi-global maps cover all local time and a region between ±45° geographic latitude (corresponding to ±60° geomagnetic latitude). Each stage towards the production of such maps is discussed in the following section.

5.5 Production of Quasi-Global Spatial Coherence Maps

The correlation calculations are performed on the data matrices described in the previous section. Each of the 50 passes in a matrix consists of 120 latitude ranges (+60° to -60°, 1° steps). Hence for any one latitude range there are 50 readings (one per pass) of IEC offset from the monthly mean. These readings form a spatial series of offset for the latitude in question.

The correlation of data from a particular latitude range with itself will obviously produce a correlation coefficient of one. However the correlation coefficient will generally decrease with increasing latitude from the range in question. The correlation coefficients are calculated between every range for each data matrix. A mean local equatorial crossing time is recorded for the coherence distances thus calculated. Taking 50 consecutive passes produces a mean equatorial crossing local time ± 20 minutes . The spread of local time across 50 consecutive passes is depicted in Figure 3.

Figure 4 depicts the correlation coefficients of all latitudes with respect to the equatorial latitude range. Such a plot will be called the correlation coefficient profile for a range. The spatial coherence distance, as previously defined, has also been plotted on Figure 4 at the 0.7 coefficient level. Examination of Figure 4 reveals that the coherence distance to the north of the equatorial range is different from that to the south. Hence two coherence distances must be measured. The coherence distances will be referred to as north and south, indicating the direction of the measurement along the satellite track (which has an inclination of 66°).

An important point to note is that the variation of local time across a pass from 45°S to 45°N geographic latitude is quite large. Whilst the satellite only takes approximately 50 minutes to complete a track from 45°S to 45°N, the local time difference between 45°S to 45°N is approximately 3.5 hours, as depicted in Figure 3. Correlation coefficients between the extremes of the pass would be affected not only by the spatial variation of IEC, but also by its temporal variation. This would pose a problem for all the latitude ranges if the spatial coherence scales were large enough to introduce a significant local time bias. Fortunately this is not the case, as local features in the ionosphere constrict the spatial coherence scales to the order of thousands of kilometres, over which distance the local time variation is only around 0.5 hours. The temporal correlation coefficient is very high (~0.98) over a time period this short. Hence this time difference along track will not significantly reduce the estimates of spatial coherence distance.

The spatial correlation coefficients for the whole range of geomagnetic latitudes of such a set of offset data may be visualised in the form of a 'butterfly' graph. The butterfly graph plots the correlation coefficient profile for every latitude range. Figure 5 presents the butterfly plot for one example data matrix. The x and y-axes show the latitudes compared, and the colour scale represents the correlation between any two latitudes. The 0.7 correlation coefficients have been marked on the figure, and also the coherence distances north and south at the geomagnetic equator. The discrepancy between northwards and southwards coherence distance can be seen in this plot. The coherence distances are extracted from the butterfly matrices using a simple algorithm to find the 0.7 correlation coefficient distance by linear interpolation.

It might have been expected, in a simple system, that the correlation coefficient would fall off in some linear fashion with distance from the range in question. This is generally the case up to the 0.7 correlation coefficient. However past this point the linearity is lost due to areas of enhanced correlation and decorrelation. The variation of the coherence distance with latitude is also apparent from this figure. Of note are the correlation coefficients associated with the latitudes 10°N and 10°S. The correlation coefficient falls with increasing distance from these latitude ranges (as expected) decreasing to 0.7 within about 8° from 10°N or 10°S. This is the scale recorded as the coherence distance. However the correlation does not continue to fall. Using the 10°N range as an example, the southwards correlation coefficient falls to 0.7 by approximately 2°N, yet increases back up to 0.7 by 10°S. That is the two latitude regions, 10°N and 10°S, are well correlated with each other. Since these latitudes will typically be heavily influenced by the equatorial anomaly, the high correlation is simply an indication of the symmetry of the fountain effect (which causes the equatorial anomaly). The fountain effect is discussed in more detail in section 5.6.3. A similar feature can be seen on Figure 5 around 45°N and 45°S. A possible explanation for this anomalously high coherence between two such distant points could be that it is caused by the mid-latitude trough (see section 6.6.2 for a discussion of this feature).

Using the mean equatorial crossing local times calculated with each correlation coefficient profile it is possible to build up quasi-global maps of coherence distance. The local time data is processed by extracting full 24 hour coverage periods. To cover 24 hours of local time requires 120 days of TOPEX data. Out of the 78 cycles of TOPEX data available for this study, six such 24 hour periods are extractable.

The mean equatorial crossing times, and the coherence distance associated with each latitude, are averaged into 1/2 hour by 1° geomagnetic latitude bins. For each 1/2 hour bin this will produce a strip of coherence distance running from approximately 60°N to 60°S geomagnetic latitude.

As previously mentioned, the actual local time along a strip will vary by up to 3.5 hours, so a time shift algorithm is applied in order to force each strip onto a latitude by local time matrix. This results in the top part of an ascending track being shifted negatively along the local time axis, and the bottom part being shifted positively along the local time axis. The opposite is true for a descending pass. In this way six resulting global maps can be produced.

The maps are averaged to form a mean yearly quasi-global coherence distance map. The resulting mean yearly map for the northwards coherence distance is presented in Figure 6. The matrix can also be plotted as a three-dimensional surface (as in Figure 7), to aid the identification of features. The corresponding global maps for the coherence distance to the South have also been calculated and are plotted in Figures 8 and 9 respectively. The maps and their features will be discussed in the following sections.

5.6 Discussion of Global Maps

The main features of the maps are indicated on Figure 10, to which reference will be made in the following discussion.

5.6.1 Coherence Pattern

The striking feature of both the northwards and southwards coherence maps is the well defined pattern of high coherence distances (see Figures 6, 7, 8, 9), which will be referred to as the coherence pattern The coherence distances northwards and southwards are different, as previously noted, although their gross features are very similar. The northwards coherence pattern is shifted southwards with respect to the equator, and the southwards coherence pattern is shifted northwards with respect to the equator. This asymmetry may be expected since the ionospheric conditions to the north and south of a point will not be exactly the same. Since the main features of both coherence patterns are similar, the following description will be applicable to both distances. It should be remembered that the coherence distance being discussed relates to the offset of an instantaneous IEC measurement from a monthly mean value. The coherence distances are a measure of the predictability of this variance around the mean. High values indicate a well correlated anomaly, whereas low values indicate more random fluctuations from the monthly mean value.

5.6.2 Sunrise

The apex of the coherence pattern (middle of feature "a" on Figure 10) starts to form at 05:00 local time, rapidly increasing at 06:00. The start of the pattern (feature "a") is actually quite flattened, the region of enhanced coherence distance stretching from 40N to 40S. This increase in coherence distance is coincident with the ionosphere becoming illuminated with solar radiation, i.e. local sunrise. The coherence distance grows rapidly from low night-time values of approximately 350 km up to high values around 1500 km (depending on latitude) in less than 1.5 hours.

The coherence distance would, if just dependent upon solar illumination, increase and decrease according to solar zenith angle. This is not the case, as is apparent from Figure 6. Indeed, the coherence distances close to the equator at sunrise are in fact smaller than those further away from the equator. As mentioned, the coherence distance does indeed increase initially, but only remains high along two bands of latitude (features "b" on Figure 10). These two mid-latitude bands are approximately 15° wide in geomagnetic latitude, and are offset from the equator on either side by around 30 degrees.

5.6.3 Equatorial Region

In-between the two mid-latitude bands the coherence distance does not remain at the initial high sunrise values, but falls to between 300 and 1000 km, the lower range being comparable to night time values. There is a great deal of structure to the coherence distance in this region, chiefly characterised by two bands of relatively high coherence distances up to 800 km (features "d" on Figure 10) stretching across a trough of low coherence distances of around 300 km magnitude (features "c" on Figure 10). This forms an alternating pattern of low and high values. These features are clearly observable in the three dimensional surface plots. The central dip is offset northwards from the equator by about 8 degrees.

The equatorial structure is a consequence of an ionospheric phenomenon known as the equatorial anomaly, which is produced by the *fountain effect*. The fountain effect arises due to equatorial electrodynamics. The zonal electric field at the magnetic equator is eastward during the day, resulting in a steady upward $\boldsymbol{ExB/B^2}$ plasma drift (Martyn, 1953), where $\boldsymbol{E}$ is the eastward electric field, and $\boldsymbol{B}$ the Earth's magnetic field. The dense equatorial plasma rises until gravitational and pressure forces balance the $\boldsymbol{ExB}$ drift. The plasma then sinks, guided by magnetic field lines, towards the tropical ionosphere (Sterling *et al*, 1969). This creates regions of depleted and enhanced plasma density. A schematic of the forces acting on the plasma in this region is presented in Figure 11. The locations of the bands of high coherence distance (feature "d" on Figure 10) correspond well to the latitudes of the enhanced regions produced by the fountain effect. The equatorial anomaly is visible in the TOPEX IEC measurements depicted in Figure 1 (see also Chapter 1, Figure 1).

Just after sunset this eastward electric field is enhanced, and the F-region plasma can drift to very high altitudes. This enhancement can be explained by F-region dynamo action (Rishbeth, 1971) or as a natural consequence of E-region dynamo theory (Walton and Bowhill, 1979).

5.6.4 Sunset

An interesting feature of the maps occurs at sunset, approximately 17:00 local time. There is a fast drop in the coherence distance of the mid-latitude bands. This decrease is not as rapid as the corresponding increase in coherence at sun rise. The coherence structure due to the equatorial anomaly is still present at least 6 hours later, although at slightly reduced amplitudes (approximately 700 km as opposed to 1000 km before sunset).

The persistence of the equatorial features is explained by the mechanism of the fountain effect. The ionospheric plasma is raised by the ***ExB*** drift to altitudes where recombination (and hence electron content reduction) is low, thus prolonging the existence of the plasma relative to its life expectancy at lower altitudes.

Another notable feature is the increase in coherence distance seemingly across all latitudes in the 1-2 hours preceding sunset. This increase is possibly due to a cessation in the strength of the fountain effect, as solar zenith angle decreases. A relaxation of the fountain effect would allow the redistribution of plasma across the equator.

5.6.5 "Seasonal" Structure

The six global maps mentioned in Section 5.5 may be selectively combined to form three averaged maps. The three resulting maps correspond to the dates 11 March - 9 July (Figure 12), 10 July - 6 November (Figure 13), and 7 November - 10 March (Figure 14). The sections correspond approximately to boreal spring/summer, summer/autumn and winter, respectively.

A comparison of the three maps with each other reveals differences in the coherence distance. These differences are to be expected due to the changing solar zenith angle with season. The asymmetry between the spring/summer and winter sections is clear (Figures 12 and 14), with the hemisphere experiencing summer having a much more persistent band of high coherence distance, stretching around 22 hours of local time. That is the northern hemisphere in Figure 12 and the southern hemisphere in Figure 14. This asymmetry is due to the higher solar zenith angle in the summer months compared to winter months.

The second section, however, is approximately evenly distributed around the autumnal equinox. The levels of solar illumination, once averaged over this time period, should be approximately equal for both hemispheres. Indeed the two hemispheres in Figure 13 exhibit very similar magnitudes and distributions of coherence distance to each other. As may be expected, the peak coherence distances are higher for these 'seasonal' maps than for the yearly average, with values up to and over 2000 km in certain regions.

5.6.6 Night-time Enhancements

The IEC is expected to decrease after sunset, as electron/ion recombination processes start to dominate production processes. It might be expected, therefore, that the coherence distance of the IEC might also decrease, since (as has been demonstrated previously) it is largely dependent on solar illumination.

The coherence distances do decrease at sunset. However in the hemisphere experiencing summer (northern hemisphere in Figure 12, southern hemisphere in Figure 14) the coherence distance undergoes an enhancement after this initial decrease. This enhancement occurs from 21:00 to 02:00 local time, drifting slowly equatorwards.

Winter-night enhancements of IEC have been observed in mid-latitudes. The enhancements occur on magnetically quiet days, and cover large geographical areas (Mendillo et al, 1977, Huang, 1983). The ATS-6 radio beacon has provided evidence that this effect is also present during other seasons (Davies, 1990), although it is obscured by the decline in IEC at sunset (the diurnal decline). Two peaks were present in the IEC, one near midnight and the other near 03:00 LT.

In contrast our enhancement in coherence distance occurs during summer, not winter, and appears anti-correlated with the enhancement in IEC at mid latitudes. An explanation for this apparent discrepancy is that the low coherence distances during winter night-time, apparent from the maps, are caused by a decrease in coherence rather than being the 'normal' night-time values i.e. even though the IEC is enhanced in magnitude, the enhancement is not a uniform one, and so the correlation between the plasma *decreases,* hence coherence distances decrease. The apparent "enhancements" in summer night-time may then be viewed as the expected normal values for night-time.

5.6.7 Southern Mid-latitude Trough

The summer/autumn and winter maps both exhibit a trough-like structure in coherence distance at southern mid-latitudes. The southern mid-latitude band consists of two peaks in coherence, one centred at 35°S and the other at 50°S, between 12:00 and 17:00 local time, with a reduction in coherence distance in-between. One possible explanation for this feature may be the ionospheric phenomenon known as the *mid-latitude trough.* The mid-latitude trough is a depletion in the F region electron density at the equatorward edge of the night-side auroral oval. However, previous observations and model calculations have placed the trough no earlier than 16:00 local time (e.g. Quegan et al, 1984, Sojka and Schunk, 1989). The trough in coherence distance may be a precursor to an F-region electron density depletion.

5.7 Unexplained Features

i) An increase in coherence distance occurs around 20:00 local time in the southern hemisphere around 35°S. The increased coherence distance has a small temporal and spatial extent, covering only a few degrees latitude and a couple of hours local time. The feature is apparent in all of the 'seasonal' plots (and hence also in the yearly average). The explanation for this feature is unclear at present.

ii) A latitude band of low coherence distance exists in the region of 10-15°S and is apparent at almost all local times. The only enhancement of correlation in this band occurs just before sunset (feature "e" on Figure 10), as described in section 5.6.4.

5.8 Comparison with Previous Studies

The spatial coherence distance for the offset varies between ~200 km to ~1600 km over the global maps. These distances compare well with the results obtained for the north-south coherence by Rush (1976) of 1150 km, Klobuchar and Johanson (1978) 1800 km, Soicher (1978) 1800 km, Nisbet et al (1981) 1000 km, Bhuyan and Tyagi (1983) 900 km, Soicher (1984) 1900 km, and Bhuyan et al (1984) 700 km. Huang (1984) reported coherence distances for the equatorial anomaly crest region of 2000 km for summer, 1000 km for winter, and 500 km for the equinoxes. The wide variation in coherence distances is quite expected, and is well presented by the seasonal coherence maps discussed in section 5.6.5.

The variations in spatial scales reported by previous authors may be attributed to the very latitude dependent nature of the IEC coherence.

5.9 Summary

The first ever quasi-global maps of coherence distance of the offset between measurements and model values of IEC are achievable using TOPEX data. The offset coherence distance maps must be used in conjunction with ground based studies of temporal coherence distance in order to construct the space-time cell necessary for adaptive modelling.

The maps exhibit a large variation in spatial coherence distance with latitude and local time, which has previously been unobservable on such a global basis. The results of the present study compare well with previous ground based techniques.

These maps will help lead to an improvement in current semi-empirical models by providing a means of producing adaptive models. More reliable models would provide an increase in the accuracy of sea surface height measurements made by single frequency altimeters. This is vital if accurate estimates of current speed are to be made, since this is calculated from relative slopes of the sea surface.

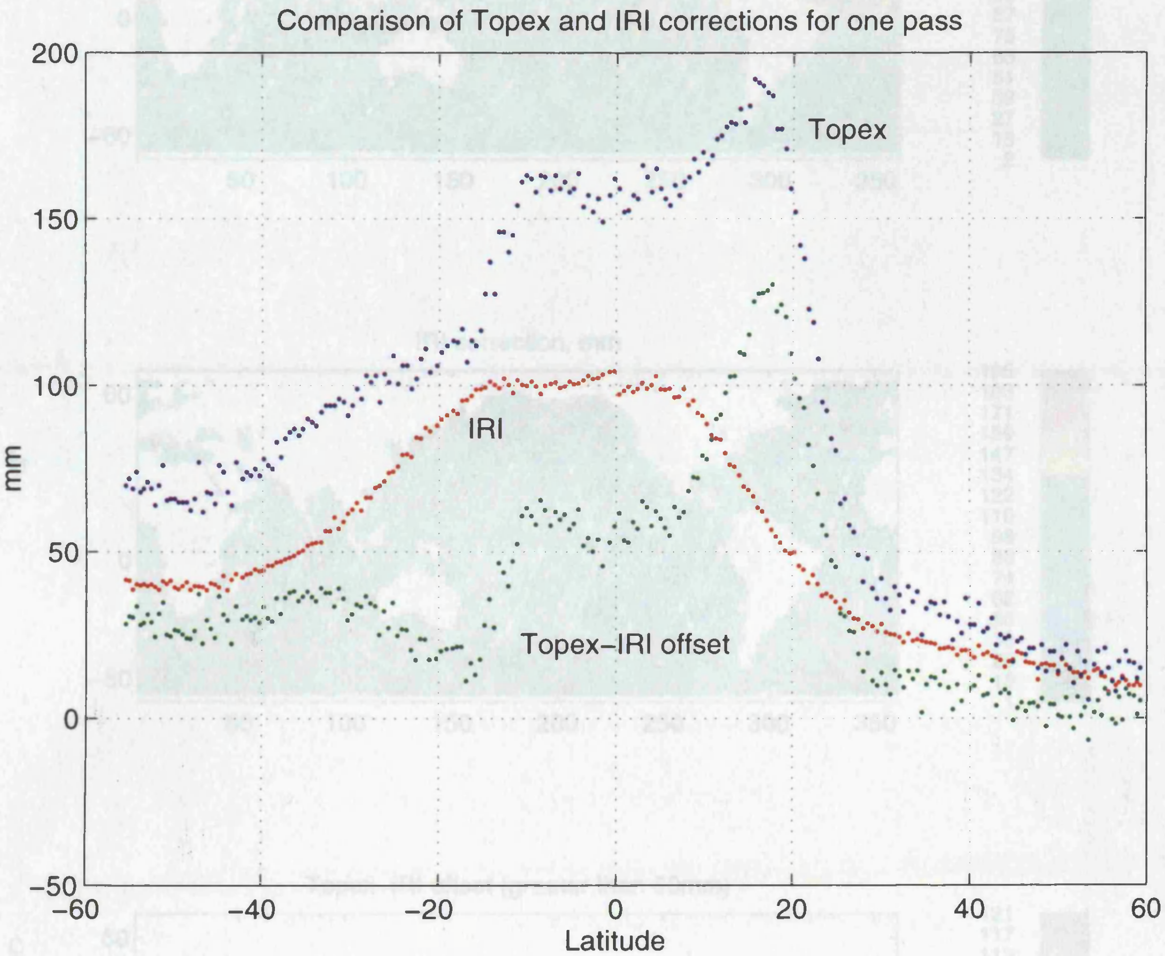

Figure 1: Discrepancy between Topex measurement of ionospheric correction and the IRI predictions for one satellite pass

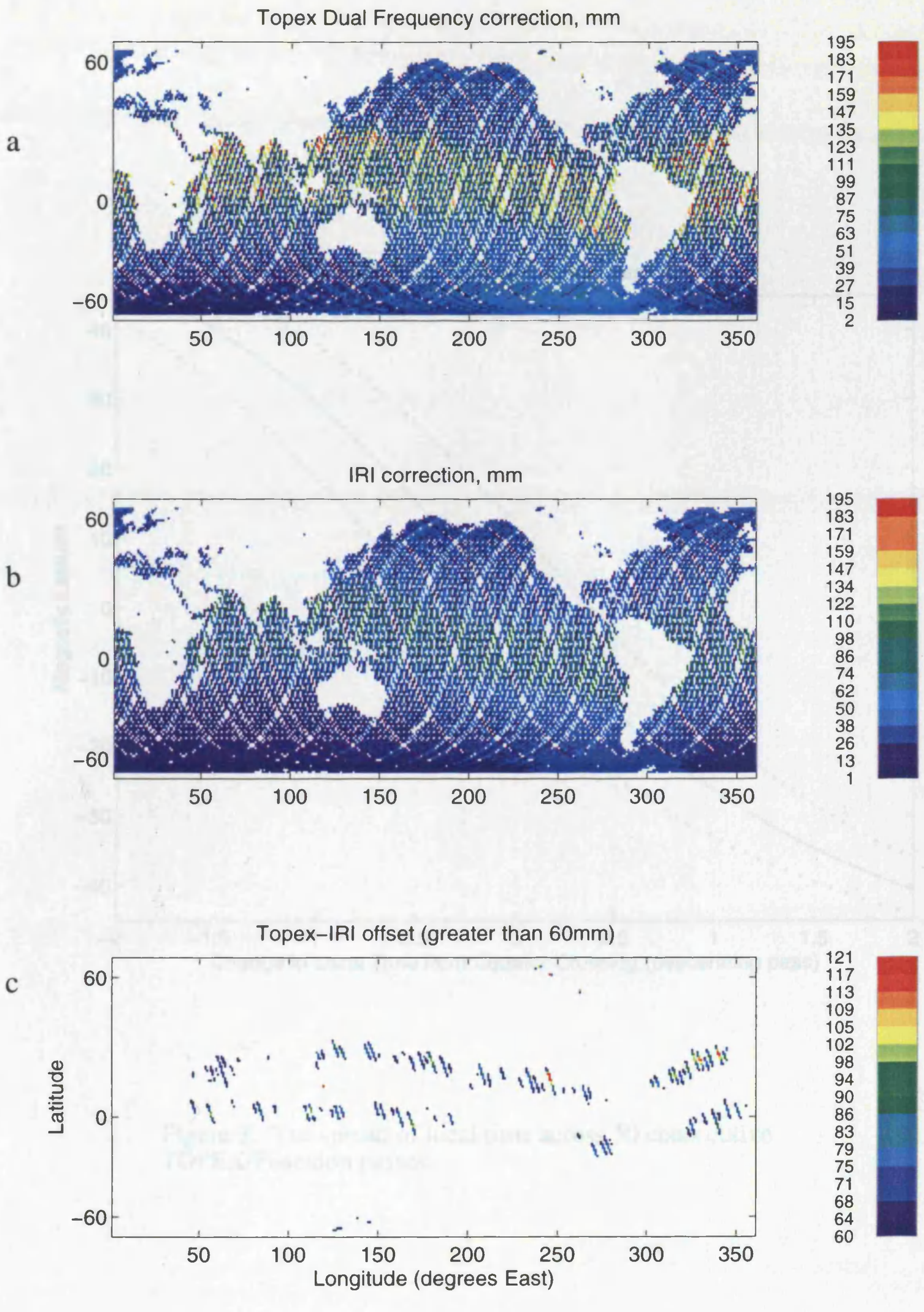

Figure 2 a) Topex ionospheric correction (mm), b) corresponding IRI predictions and c) the offset between Topex measurement and the IRI (greater than 60 mm)

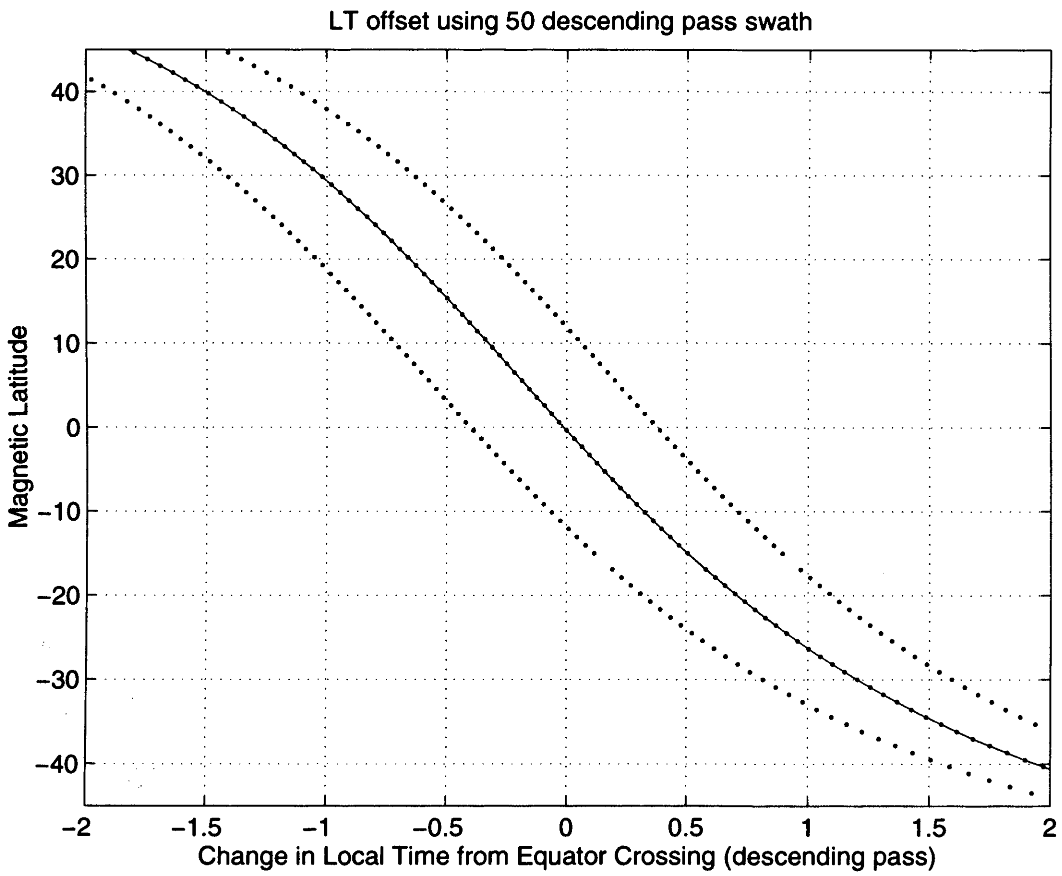

Figure 3: The spread of local time across 50 consecutive TOPEX/Poseidon passes

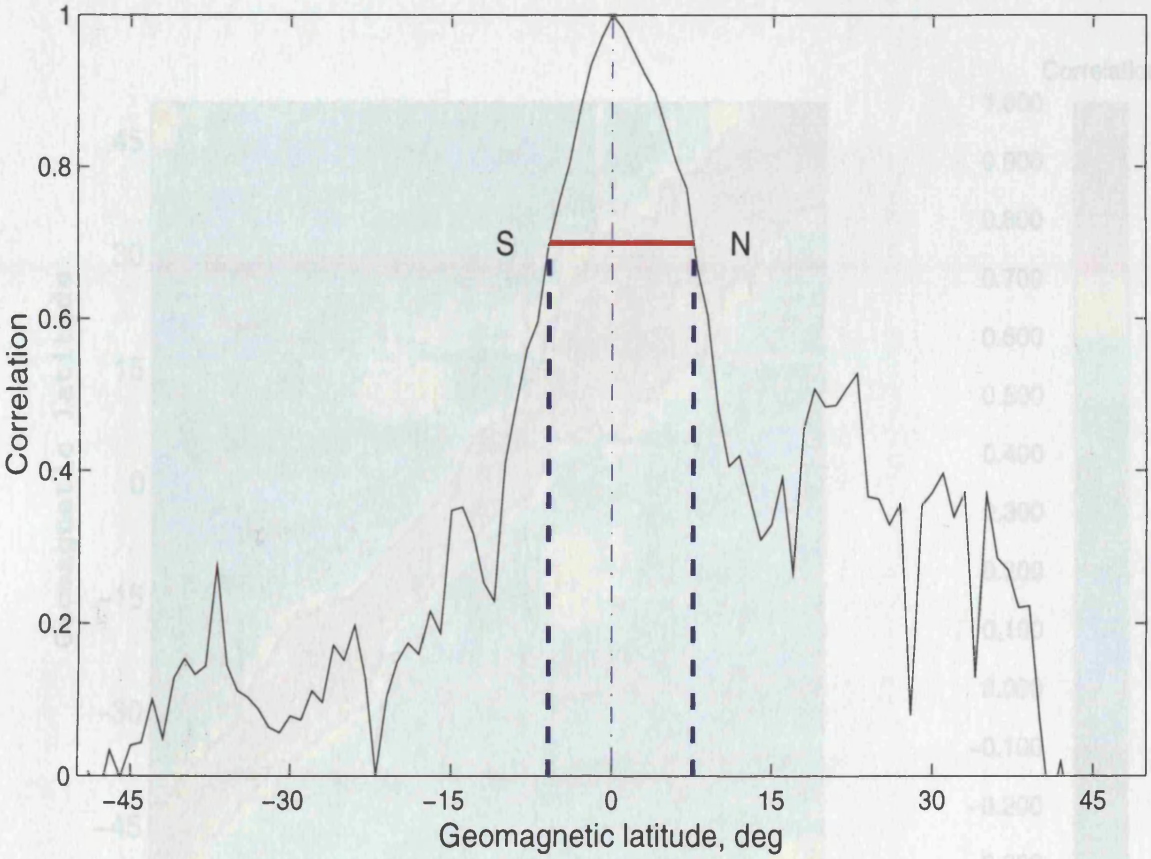

Figure 4: Correlation Profile for the equatorial latitude range, 0°. The coherence distances north and south have been marked at the 0.7 correlation point level.

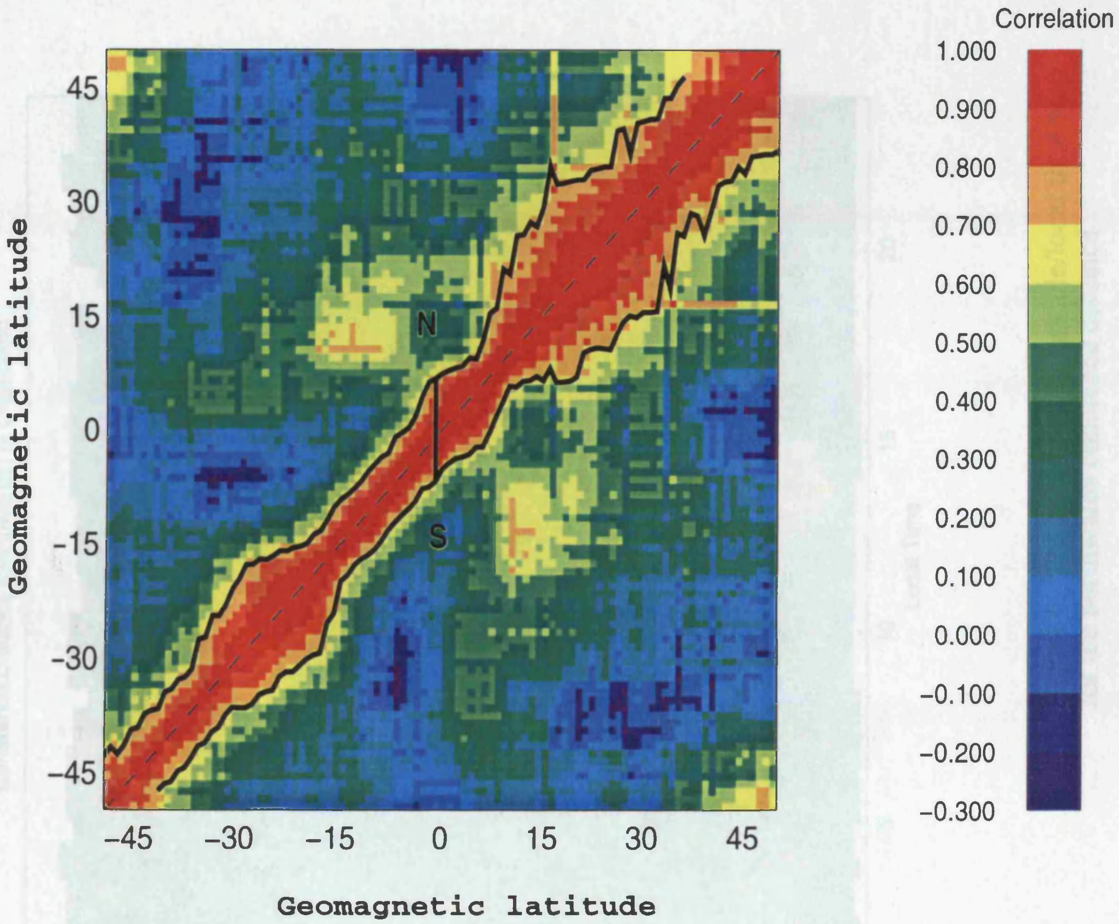

Figure 5: Butterfly plot for the correlation profiles calculated from one data matrix. The dashed line marks perfect correlation. The diagonal black lines indicate the first 0.7 correlation contour away from maximum correlation. The vertical black lines indicate the coherence distance north and south from the centre dashed line.

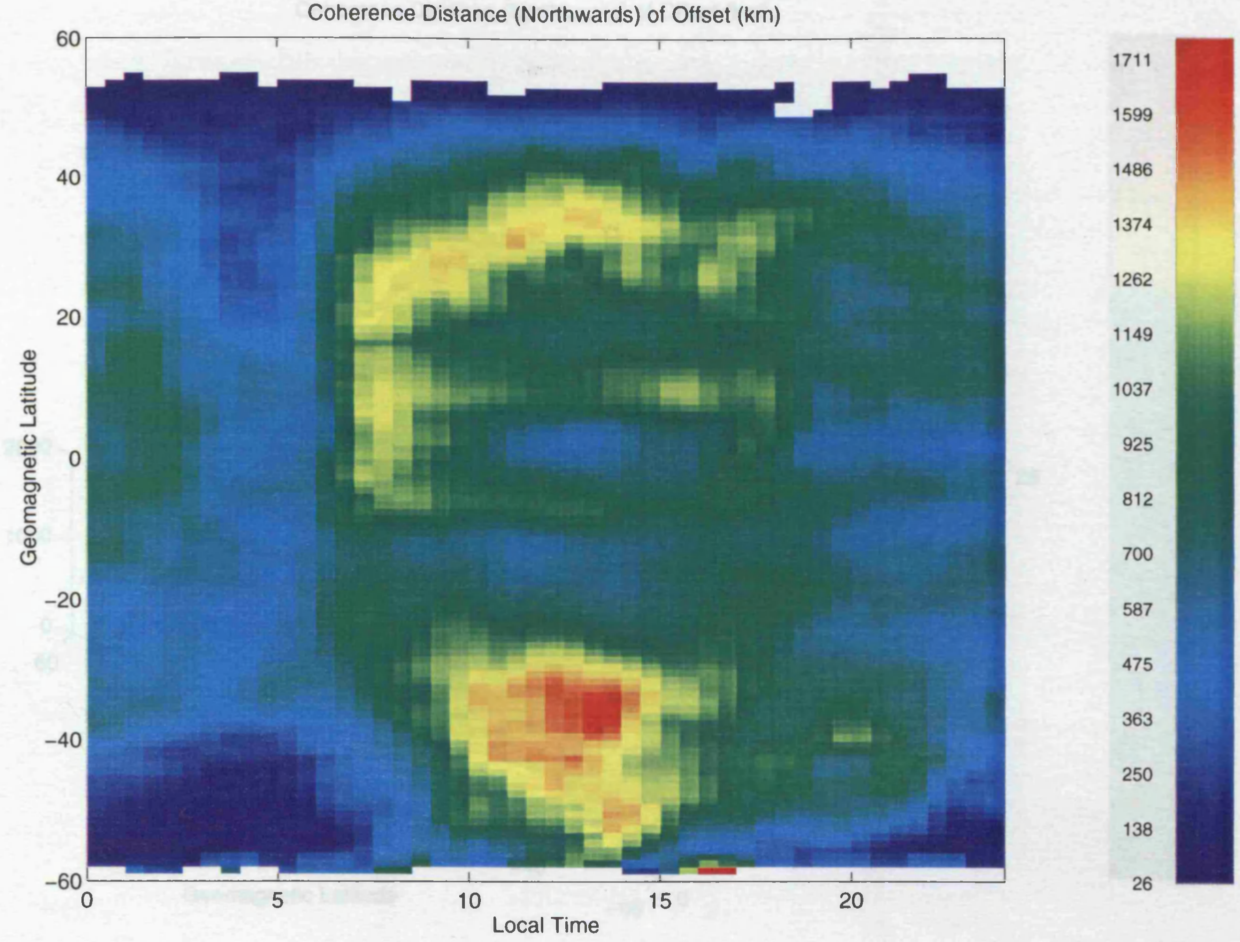

Figure 6: The mean yearly latitude/local time map for the northwards coherence distance

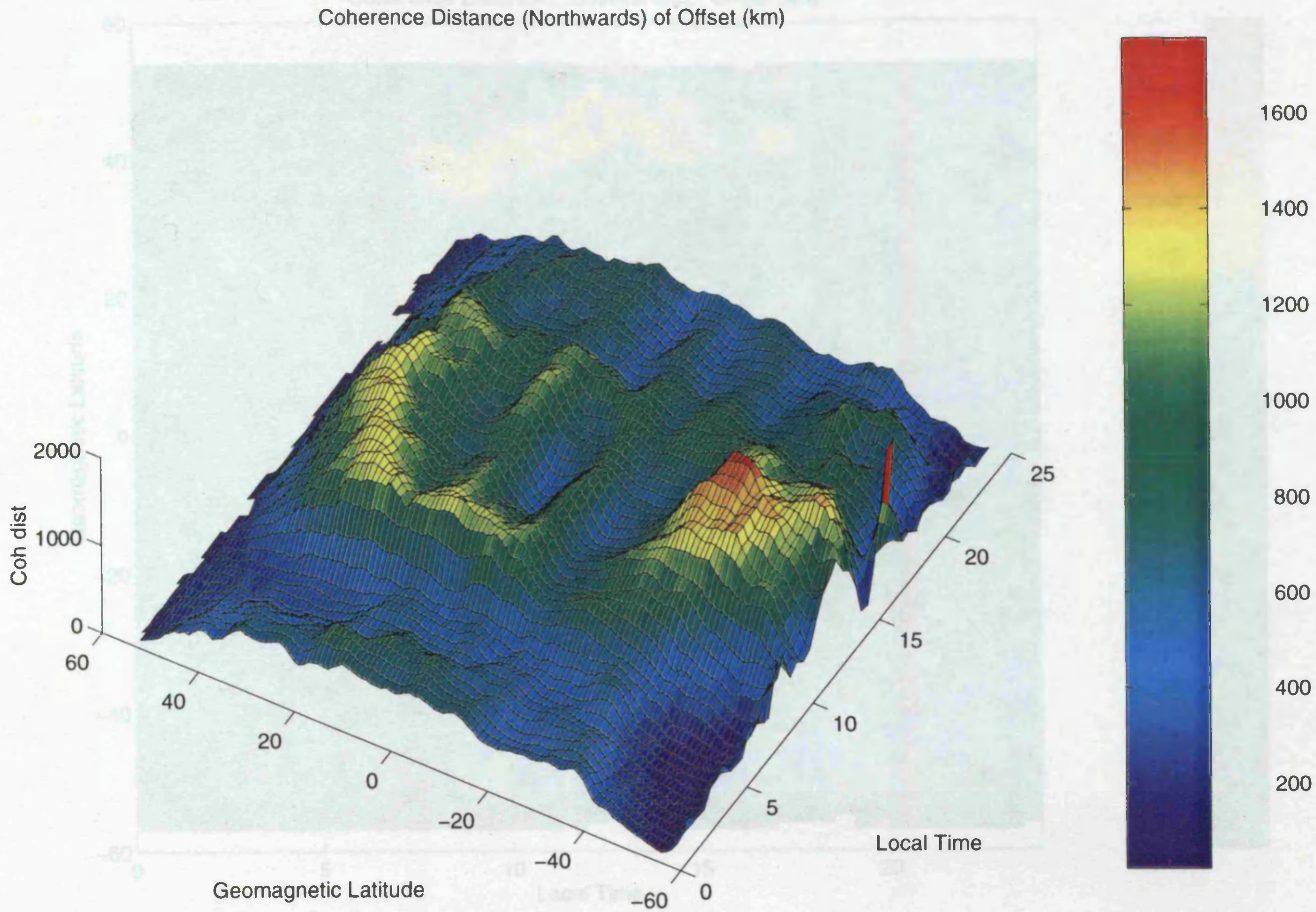

Figure 7: The mean yearly latitude/local time map for the northwards coherence distance (both colour and height indicate magnitude of coherence distance).

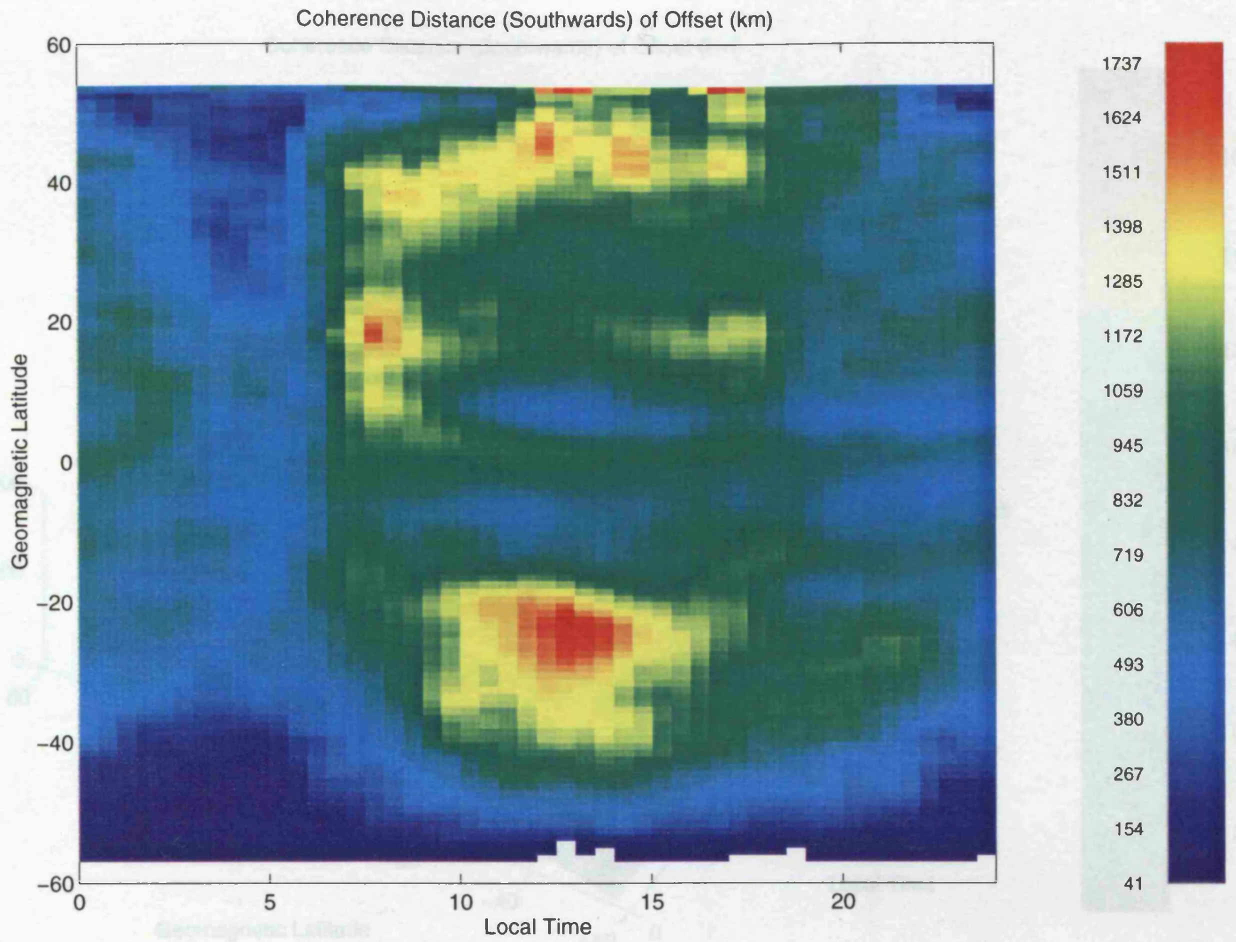

Figure 8: The mean yearly latitude/local time map for the southwards coherence distance.

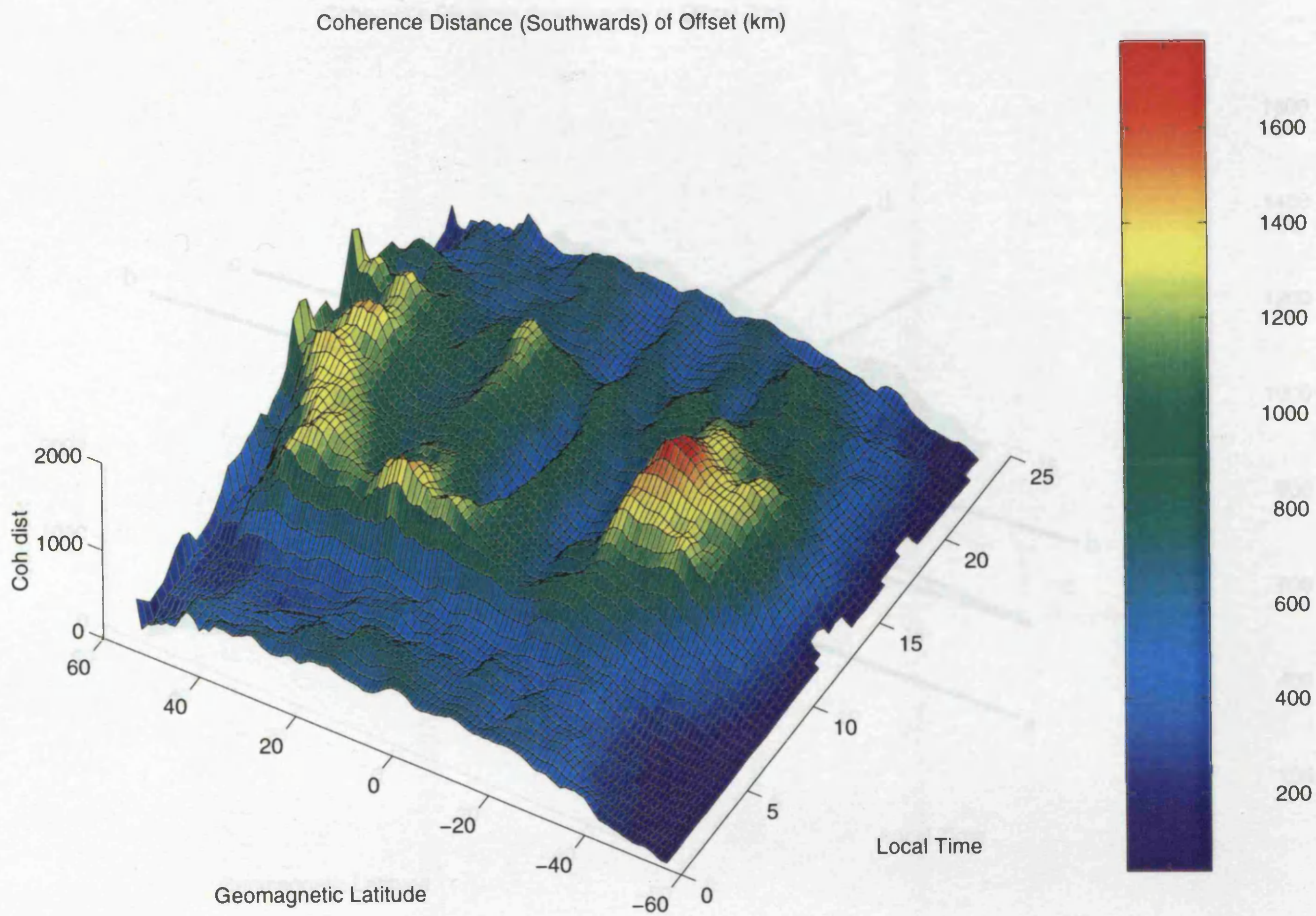

Figure 9: The mean yearly latitude/local time map for the southwards coherence distance (both colour and height indicate magnitude of coherence distance).

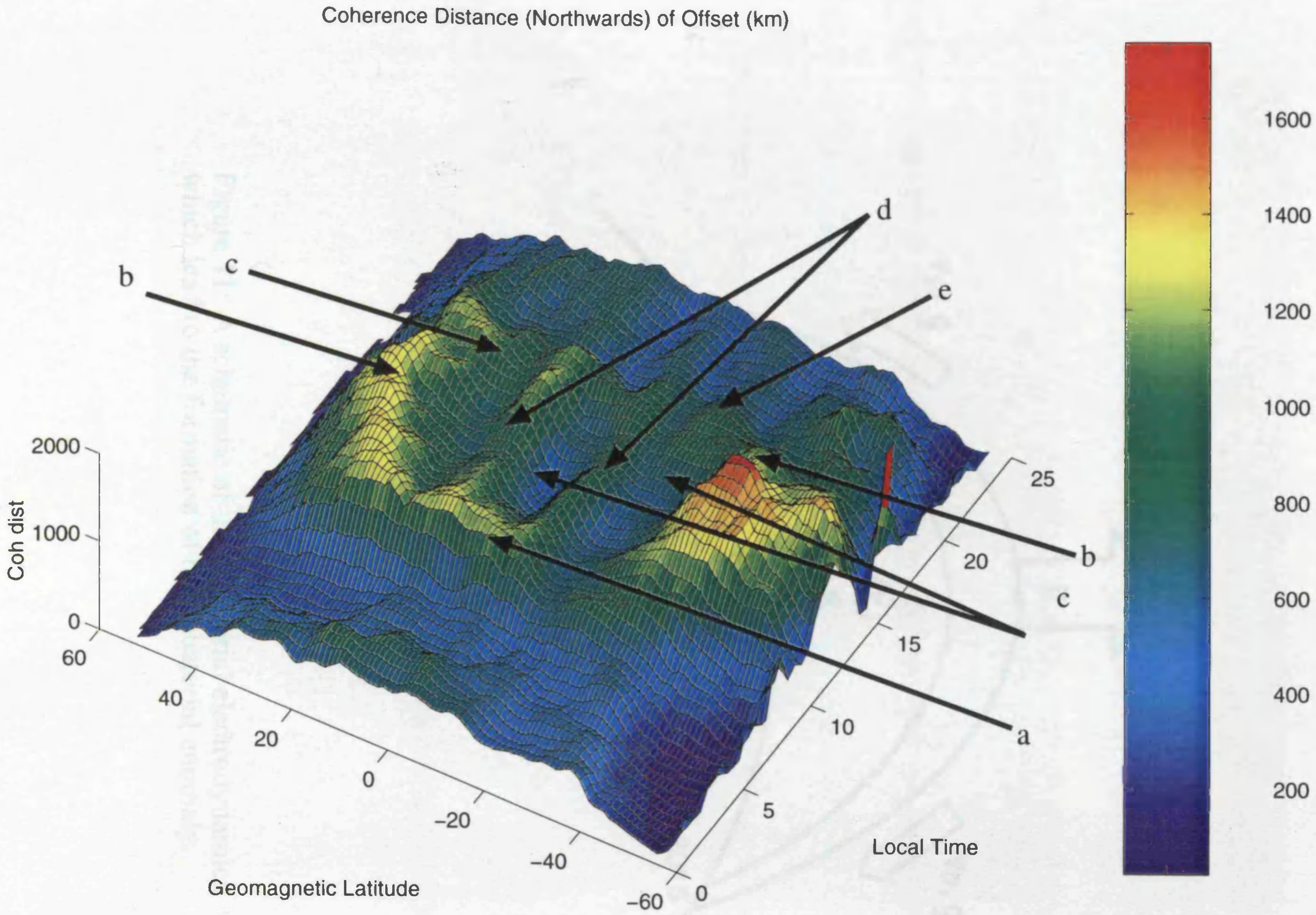

Figure 10: Key features on coherence maps (referred to in text).

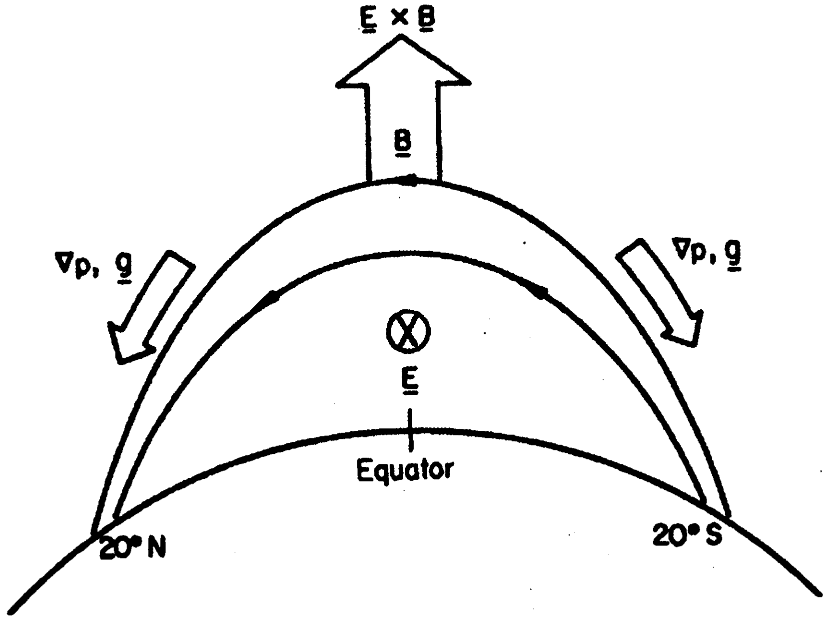

Figure 11: A schematic of the equatorial electrodynamics which lead to the formation of the equatorial anomaly.

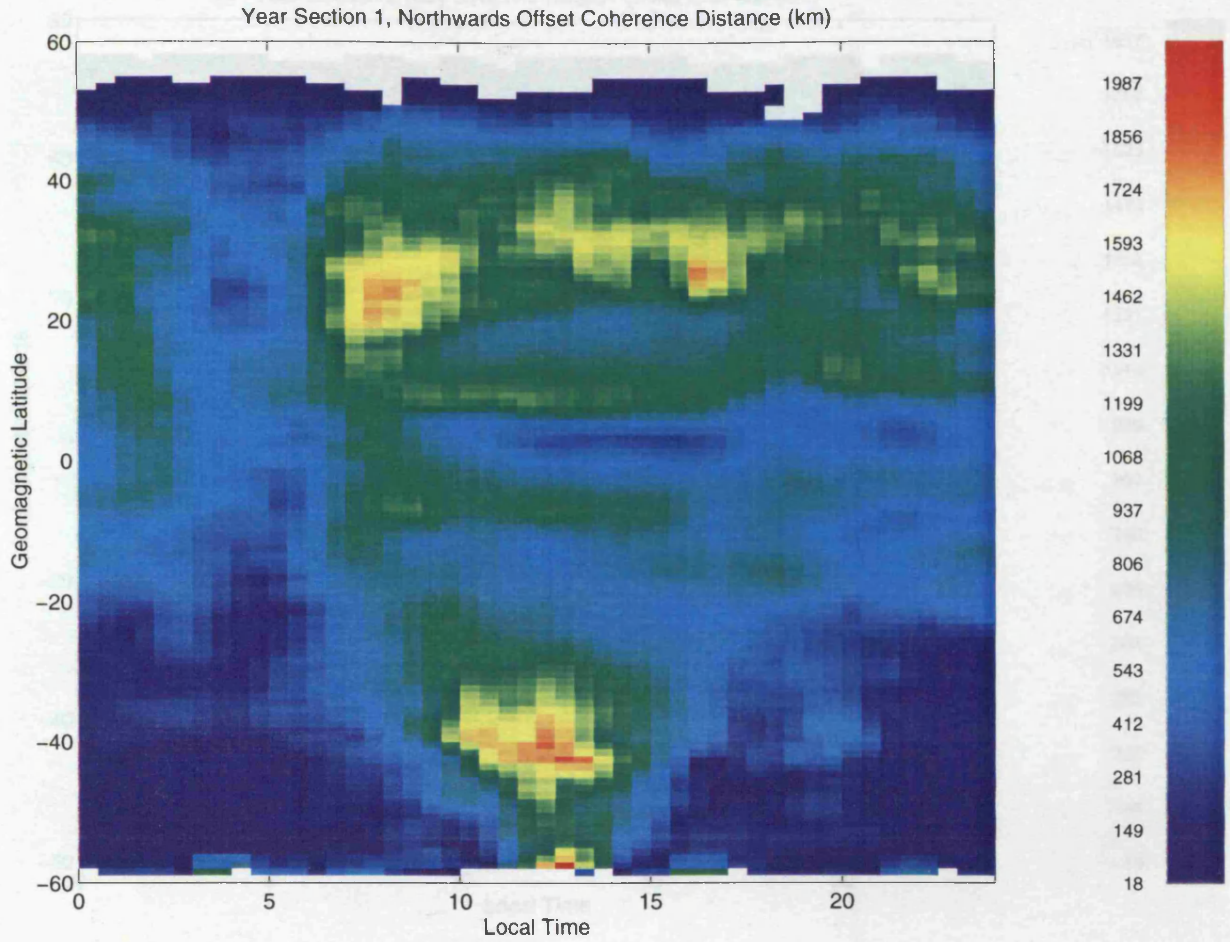

Figure 12: Northwards coherence distance map for March - July
The colour scale runs to the maximum coherence distance, which is ~2000km

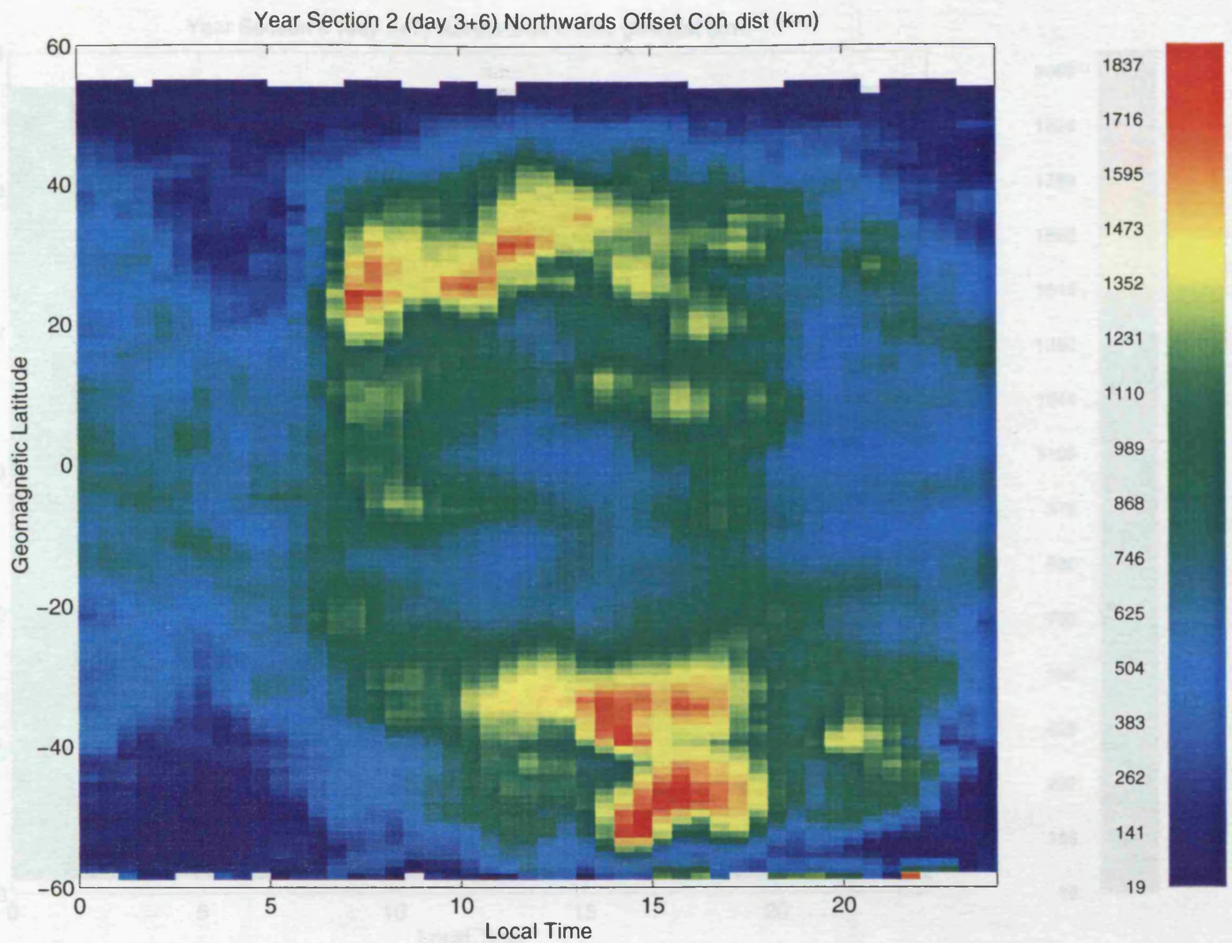

Figure 13: Northwards coherence distance map for July - November
Note that the colour scale runs up to ~1800km. This is less than for Figures 12 or 14.

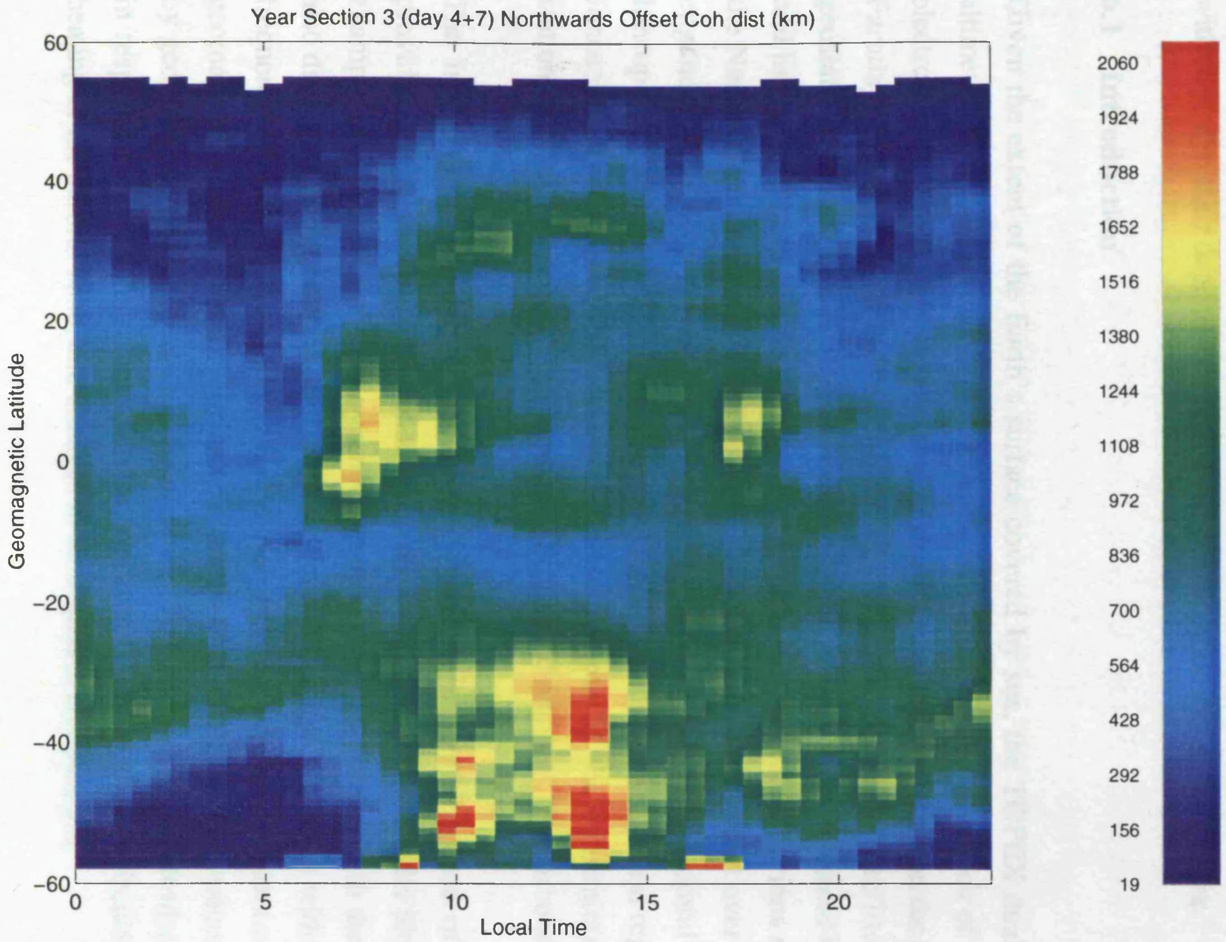

Figure 14: Northwards coherence distance map for November - March
The maximum coherence distance is highest for this period, with values over 2000 km.

Chapter 6: Geomagnetic Dependence Of The TOPEX-IRI Ionospheric Electron Content Offset

In this chapter the offset between the estimate of ionospheric electron content (IEC) made with the TOPEX dual frequency altimeter, and the predicted ionospheric IEC from height integration of electron density profiles from the IRI model are compared with regard to their dependence on the Kp geomagnetic disturbance index.

6.1 Introduction

Given the extent of the Earth's surface covered by sea, the TOPEX dual frequency altimeter constitutes an excellent instrument for the testing and validation of ionospheric electron density models. Previous studies of IEC have largely relied on the principle of Faraday rotation of transionospheric radio links between satellites (usually geostationary) and ground stations. Data collected in such a way is biased by the fixed and limited nature of ground stations (e.g. the majority of ground stations are based in the Northern hemisphere). These ground stations are of course absent over the oceans, engendering a considerable bias in models such as the International Reference Ionosphere (IRI). TOPEX, however, provides IEC measurements from regions of the ionosphere lying above the oceans, and is unhindered by the constraints of ground station location, and hence provides widely distributed readings from around the globe.

The International Reference Ionosphere is studied in detail because of its role in providing the correction to the ionospheric error for other satellite radar altimeters, for example ERS-1 and ERS-2. Any improvement which can be made to the IRI would also directly improve on the accuracy of sea level measurements made with such single frequency altimeters. The IRI model does not presently take into account any affect of geomagnetic activity on IEC. However it is well known that the ionosphere is affected by geomagnetic disturbances (e.g. Sojka et al, 1990), producing electrodynamic drifts in response to stormtime electric fields, enhanced thermospheric circulation due to heating of the auroral zone, and changes in atmospheric composition.

The IRI model provides a good estimate of monthly mean IEC. However, significant errors can be introduced into the model's predictions for day to day variability (Beard et al, 1994). Increasing geomagnetic disturbance might be expected to increase the variability of the day to day IEC values, but not change the underlying median IEC value, yet a systematic trend of IEC with Kp has been found in the data. This suggests that an addition of a Kp dependence factor in the IRI model would improve prediction accuracy.

6.2 Data used in the Study

The Kp data for this study are obtained from the World Data Centre A, at Boulder, by means of a File Transfer Protocol (FTP) process. The planetary magnetic index, Kp, is calculated by studying the variation of magnetic records within 3-hour periods of the day (00-03 UT, 00-06 UT etc.). The records are provided by up to twelve selected magnetic observatories. The Kp value is obtained after local weighting and averaging, and lies on a scale from 0 (for 'very quiet') to 9 (for 'very disturbed'). The scale is quasi-logarithmic, and is divided into thirds by use of the symbols + and -, i.e. 2, 2+, 3-, 3 etc. The downloaded data is processed into the correct format for the Matlab routines that are used (i.e. replacing the + and - signs with numerical values so that 3+ becomes $3.\dot{3}$ etc.). Kp values corresponding to the periods of available TOPEX data are extracted.

TOPEX IEC data are studied from the period October 1992 to October 1995. This corresponds to approximately 80 million data points (at one reading per second). To reduce the volume of data, and also to remove spurious readings, twenty point along track medians are taken. The IEC data set thus consists of 1 reading per 20 seconds.

The corresponding IRI predictions of IEC for each of the medianed data points, and the offset between the TOPEX estimate and the IRI prediction are calculated (this offset will be referred to as "the TOPEX-IRI offset", or simply "the offset"). This produces a global data set consisting of 1 reading per 20 seconds of latitude, longitude, UT, and offset, over the 3 years studied.

This global data set is then binned into 3 hour UT sections, in line with the binning of the magnetic disturbance index, Kp. Due to the nature of the satellite orbit, each 3 hour UT section of data will include measurements from all latitudes covered by TOPEX.

The data is then further binned and averaged into 5 degree geomagnetic latitude ranges. Geomagnetic latitude differs from geographical latitude in that the geomagnetic pole is offset from the geographic pole, producing a shift in the coordinate axis (the geographic position of the dipole axis are 11.018° latitude and -70.905° east longitude). TOPEX data is available from ~80°S to ~80°N geomagnetic latitude (corresponding to ±66° geographic latitude), although the number of data points at the extremes of the geomagnetic latitude range is relatively low. Hence the final data set consists of 3-hour time series of data for each 5 degree geomagnetic latitude range covered by TOPEX during the period October 1992 to October 1995. This data set will be referred to as the global data set.

6.3 Data Analysis

6.3.1 Global Analysis

The first stage of the analysis involved plotting the global data set of the TOPEX-IRI offset against the Kp index, in order to establish whether there is an overall global effect on IEC due to the level of geomagnetic disturbance.

The global data was binned into 5 mm offset ranges for each Kp value. The resulting pseudo colour plot is displayed in Figure 1, where the colour scale represents the number of data points per bin. Most readings lie between Kp 1 and 4-. Data above Kp 6 are relatively few in number. A simple first order least squares linear regression to the global data was performed up to Kp value 5 (for reasons discussed in Section 6.4), minimising the squares of the deviation of the TOPEX-IRI offset from the expected value. The resulting line has also been plotted on Figure 1. Although there is a large spread of values around the mean, the variance is relatively small due to the large concentration of points close to the mean. This simple linear regression reveals a very weak trend to the data, indicating an increase in the TOPEX-IRI offset with increasing geomagnetic disturbance. If the model's mean monthly predictions are taken to be reliable (Beard et al, 1995), then this latitudinal profile may be indicating a depletion of plasma at the high latitudes, and a corresponding increase at low latitudes. Whether this simultaneous increase/decrease is due to an equatorward movement of plasma is unclear.

This increase in offset can equivalently be seen as an increase in IEC measured by TOPEX relative to the monthly mean. It should be noted that for some regions the offset will be positive at very low Kp (IRI underestimating IEC), and negative at high Kp (IRI overestimating IEC). Thus to talk about an increase in offset may not necessarily be meaningful. A positive dependency will be taken as an increase in IEC measured by TOPEX *relative* to the monthly mean, and a negative dependency will be taken as a decrease *relative* to the monthly mean.

6.3.2 High Latitude Analysis

The same procedure as applied to the global data was then used to analyse data from a high latitude region (geomagnetic latitude range 70 to 75° N), to ascertain whether the strength of the global trend between Kp and offset differed at high latitudes. The resultant graph is plotted in Figure 2. The linear regression again reveals a trend in the data, but this time the trend is the opposite to that seen in the global data set. This result implies that as the Kp index (i.e. geomagnetic disturbance) increases the TOPEX IEC values decrease relative to the monthly mean. The IRI apparently underestimates IEC over all Kp values at this latitude range.

6.3.3 Low Latitude Analysis

A repeat of the analysis on a low latitude region (geomagnetic latitude range 0 to 5° N) again revealed a trend between Kp index and offset. The resultant graph is plotted in Figure 3. The trend is stronger than, and has the same sense as, the global trend. The trend has apparently reversed from the high latitude to the low latitude region. Figure 3 reveals that the IRI is overestimating IEC at low Kp, whilst underestimating at high Kp.

6.3.4 Analysis over all Latitudes

To ascertain how significant this change in dependence is, similar graphs were plotted for each 5 degree geomagnetic latitude range, resulting in graphs from 80°S to 80°N. The resulting plots are presented in Figure 4, starting with 80°S in the top left corner of the plot running through to 80°N in the bottom right. The analysis reveals a tendency for increasing geomagnetic disturbance to decrease electron content at high latitudes, but to increase electron content at low latitudes. If the dependency was not significant, and just due to some random fluctuation, then the gradient of the linear regression lines would be expected to fluctuate randomly across the globe. However this is not the case as the dependency varies systematically across the globe - it reverses sign gradually from high to low latitudes, indicating that the result is significant, and not due to random fluctuations. The gradients of the linear regressions are plotted in Figure 5 to show the progression of the dependency with latitude more clearly. An example plot to depict the profile expected if the data were random is presented in Figure 6. The random data were generated to be normally distributed, and were processed with respect to real Kp data used in the previous analysis to provide a realistic distribution of Kp values. As is apparent from Figure 6, there is no coherent trend from high to low latitudes, reinforcing that the result in Figure 5 is significant.

The correlation coefficients (a value of 1 meaning the data are perfectly correlated and -1 meaning that the data are perfectly anti-correlated) have been calculated between the offset and Kp values for all data corresponding to Kp ≤ 5, and are plotted as a latitude profile in Figure 7. The offset data is weakly correlated with Kp, the correlation being negative at high latitudes and positive at low latitudes, as expected from the linear regression analysis. The latitude profile exhibits a lot of well defined structure, the most prominent feature of which is the enhancement in correlation at the equator.

There is also a tendency for the IRI to consistently either underestimate or overestimate IEC at certain latitudes and certain values of Kp. The TOPEX-IRI offset is plotted across all latitude ranges for each value of Kp in Figure 8. A tendency can be seen for the IRI to overestimate IEC at very low latitudes by around 10 mm, and underestimate IEC at high latitudes again by around 10 mm. This "v" shaped profile becomes more flattened with increasing Kp, indicating that the IRI predicts low latitude IEC values more efficiently at higher geomagnetic disturbance.

6.4 Switch from Low to High Kp Linear Dependence

In the previous section the linear regression was only performed up to Kp value 5. The pseudo colour plots so far presented, whilst being informative, do not emphasise the median value of the offset in each bin. To reveal this information, the median value for each Kp bin has been calculated, along with the standard deviation of the data in each bin and are plotted in Figure 9 The linear regressions to these median values have also been plotted on the graphs. The standard deviations are small compared to the spread of data exhibited in Figure 1. The plot reveals the importance in taking the linear regression to only Kp 5, and also the different dependency past this point.

The slope of the linear regression to the median values, up to Kp 5, for each latitude bin is plotted in Figure 5. The dependency changes from negative at high latitudes to weakly positive at mid-latitudes, and strongly positive at low latitudes.

The reason for taking the linear regression only to Kp value ≤ 5 now becomes apparent from Figure 9. Up to Kp 5 the median values exhibit a linear trend, but at Kp values greater than 5 the data strays from the initial linear relationship. Above Kp 5 the amount of data available is quite low. This fact, coupled with the increased geomagnetic activity, generates more widely distributed data at high Kp. Whilst a linear trend above Kp 5 is clearly discernible at many latitudes, caution should be advised since at some latitudes the data appears fairly randomly spread.

The correlation coefficients have been calculated between the median offset and Kp, for all data corresponding to Kp ≤ 5 and also for Kp > 5. These are presented in Figure 10. The variation with latitude is very pronounced for both profiles. The correlation coefficients exhibited for low Kp are very strong, ranging from almost perfectly anticorrelated at high latitudes (coefficients close to -1) to almost perfectly correlated (coefficients close to 1) at low latitudes. The latitude profile exhibits similar structure to that for the entire data set, although the features are more exaggerated. The correlation is lower for high Kp as opposed to low Kp.

6.5 Seasonal Dependence

The next stage in the analysis of the offset variation with geomagnetic disturbance is to investigate whether the trends seen in the global data set remain constant throughout the year. The data set is now further processed by binning into seasons. The seasons are defined here as Spring (March, April, May), Summer (June, July, August), Autumn (September, October, November), and Winter (December, January, February). These are the boreal (northern hemisphere) definitions of season. When referring to a season, e.g. spring, we are referring to boreal spring yet austral (southern hemisphere) autumn.

The same analysis applied to the global data set is used on each season. The median offsets have been calculated and the linear regression analysis applied. The linear regression slopes for each season have been plotted versus latitude on one plot, Figure 11, to allow comparison of the dependency between seasons.

6.5.1 Low-Kp Dependence

The profiles in Figure 11 for the equinox months show a pronounced enhancement in positive dependency at low latitudes. The dependency changes to a negative one at high latitudes for the spring months, but only at northern high latitudes for the autumn months.

In comparison the profiles for the summer and winter months are much flatter and the dependencies exhibited are also much lower. In the northern hemisphere both summer and winter regression slopes are close to zero. However in the southern hemisphere the regression profiles of the two seasons diverge, the summer profile becoming consistently positive, and the winter profile being consistently negative.

6.5.2 Switch from Low to High-Kp Dependence

The linear regression slopes for both Kp ≤ 5 and Kp > 5 have been plotted on individual graphs for each season (Figures 12, 13, 14, 15), where the solid line represents the low-Kp dependency, and the dashed line the high-Kp dependency. The switch between the two regimes is apparent for each of the seasons.

There is evidence that the equatorial anomaly may be enhanced, especially in the spring and autumn months, with the dependencies increasing greatly at approximately 20° north and south of the equator, coincident with the peaks in plasma density associated with the fountain effect. This correlates well with the fact that the ring current shows very strong semi-annual variations, with two peaks near the equinoxes (Kivelson and Russell, 1996). An explanation of the process by Russell and McPherron (1973), based on magnetic activity occuring preferentially when the Interplanetary Magnetic Field (IMF, the field carried by the solar wind) is southward relative to the dipole axis is now accepted. There are also some equatorial effects during the winter months, with a large enhancement at the equator, and with enhancements either side of the equator. The summer months do not appear to be significantly affected at equatorial latitudes, but experience a large enhancement in positive dependency in the northern hemisphere.

6.6 Discussion

6.6.1 Positive and Negative Phase Resonses

As discussed in chapter 3, there are several processes which might contribute to the variations observed in the IEC associated with geomagnetic disturbances. The ionospheric density exhibits both positive and negative phase responses to magnetospheric storms. It is, however, difficult to establish the efficacy of each mechanism in affecting the IEC in the data used in this study, due to the necessary averaging of the data as explained in section 6.2.

The latitudinal profile, for Kp < 5, whereby the offset change is negative at hgh latitudes and positive at low latitudes, may be explainable by the geographic dependence of the negative and positive responses of the ionosphere to geomagnetic disturbance. As discussed in section 3.8.1, atmospheric composition changes due to a molecularly enriched atmosphere occurs initially throughout the auroral oval (i.e.high latitudes). This produces a negative phase, and may be directly responsible for the negative offset that is apparent in the TOPEX data with increasing disturbance.

The lifting of the plasma to higher altitudes may be one of the important mechanisms for the enhancement in ionospheric plasma at the equator. An example of the enhancement of the equatorial anomaly following a geomagnetic storm, as seen by Tanaka (1981), is reproduced in Figure 17. Again, the geographical coincidence of the positive response of the ionosphere at the equator may explain the positive offset response discernable in the TOPEX data. Whilst it is not proposed that for every geomagnetic storm there is a set pattern of response, the essentially climatological study provided by the averaged TOPEX data indicates a preference for enhancement at the equator, and depletion at the high latitudes.

6.6.2 Effect of Ionospheric Coherence Distance on the IRI

An important point to note is that the accuracy of the IRI is dependent on the original ionospheric data input. It is not only dependent on the accuracy of this data, but also on the amount and distribution of the ground stations collecting the data. Figure 18 presents a geographical map of the ionospheric sounding stations used to produce data to be input into the model. The map also indicates the locations of stations where data were predicted from previous recordings made at the stations. The crosses on the map indicate 'screen points', whereby data is extrapolated onto these purely imaginary stations. This extrapolation is based on the assumption that although there may be a large latitudinal variation in ionospheric parameters, the longitudinal variation of the strong latitudinal trend is relatively small (Jones and Gallet, 1965).

The majority of the ground stations lie in the northern hemisphere, with large regions of the southern hemisphere having to be interpolated by screen points. The same is true of the equatorial region which, although being highly structured in nature, contains extremely few ground stations. This lack of measurement data, in the equatorial zone especially, produces inaccuracies in the IRI predictions, as evidenced by Figure 8.

The interesting point to note is that the scale size of the derivative of the offset is approximately the same as that for the coherence distances of the ionosphere discussed in Chapter 5 (that is of the order of thousands of kilometres). If one can imagine fitting a bell curve to Chapter 5 Figure 4, the resulting graph would appear very similar to the graphs presented on Figure 8 of the latitudinal profile of the offset between the IRI and TOPEX measurements. The proposal being made is that the IRI is limited by the amount and location of ground stations, with the interpolation of the data being limited by the coherence scale of the ionosphere. This hypothesis is supported by the variation of the offset with Kp. Figure 8 indicates that the errors in the IRI predictions become more uniform over latitude with increasing Kp, that is increasing geomagnetic disturbance. It is proposed that increasing geomagnetic activity increases the coherence distance of the ionosphere, in a way analagous to the increase of coherence time with solar activity as measured by Klobuchar (1980). This increase in ionospheric coherence hence explains the more uniform distribution of offset with latitude with increasing Kp.

6.7 Summary and Conclusions

The offset between TOPEX measurements of IEC and the monthly mean predictions produced by the IRI has been demonstrated to be partly dependent on the prevailing level of geomagnetic activity. The dependency may be split into two regimes, a low-Kp dependency ($Kp \leq 5$) and a high-Kp dependency ($Kp > 5$), which both exhibit latitudinal and seasonal structure. The level of dependency is highest for the equinoctial seasons.

A proposed link between the IEC coherence distance and magnetic activity has been made. The suggestion is that as magnetic activity increases the coherence distance also increases.

Predicting the ionospheric response to a geomagnetic storm is not a simple task. The response will consist of many mechanisms, both positive and negative, some of which have been discussed in Section 6.6. Due to the superposition of these mechanisms, it is not possible to quantitatively examine their effect on the dependencies of the IEC offset on Kp, observed in the TOPEX data. However these dependencies appear significant, and as such could be used in future ionospheric models to allow for the geomagnetic effect on the IEC.

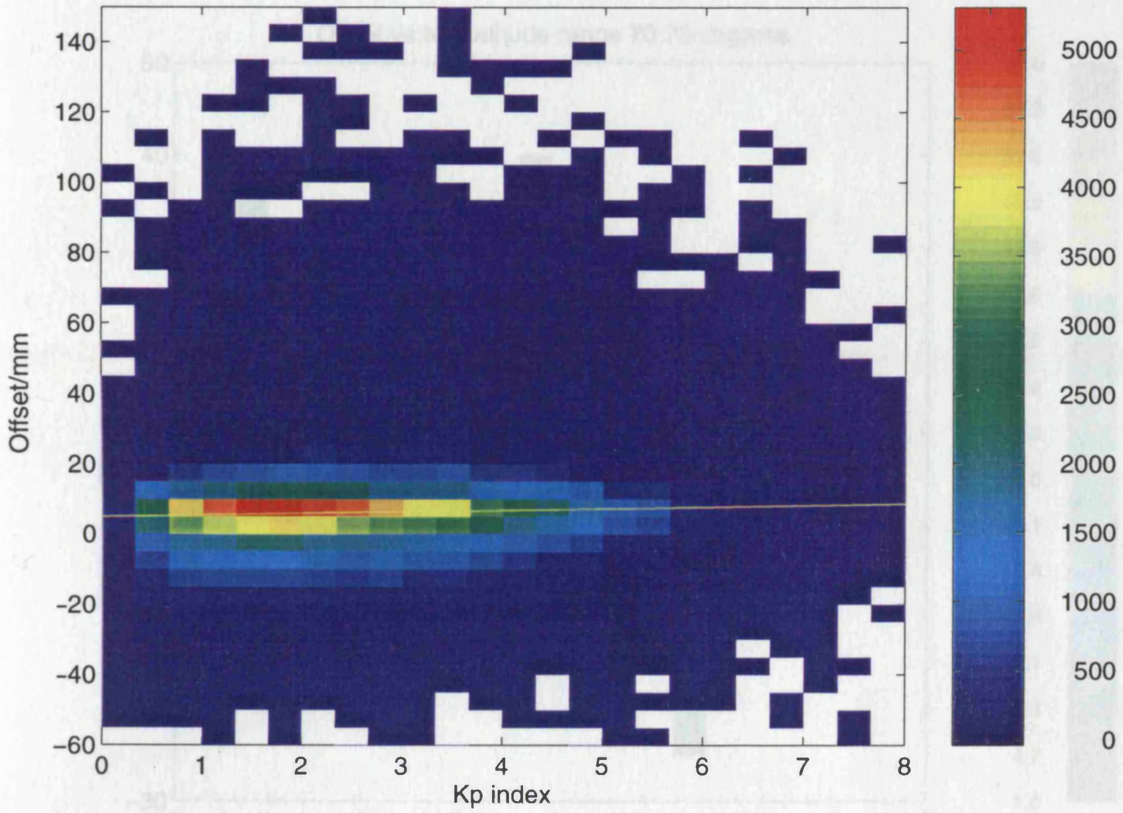

Figure 1: Plot of offset versus Kp index, averaged over all data. The yellow line represents a linear regression fit to the data, revealing a weak trend to the data.

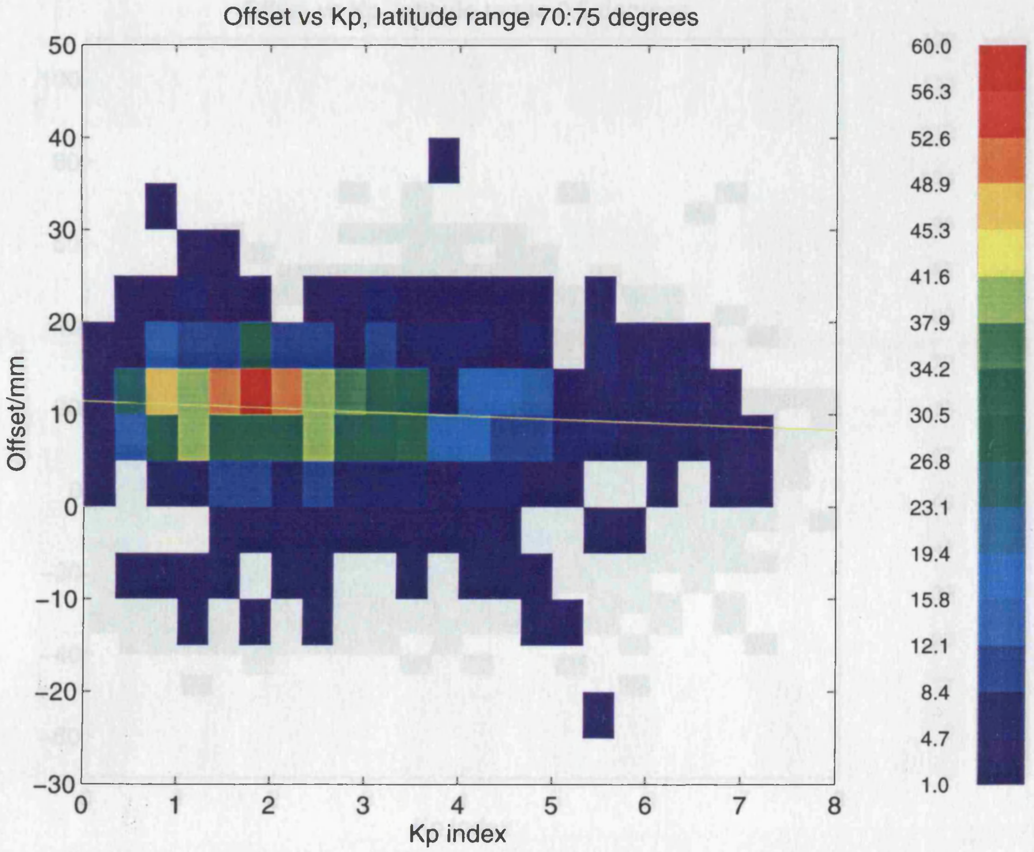

Figure 2: Plot of offset versus Kp index, for the latitude range 70°N to 75°N. The yellow line represents the linear regression to the data.

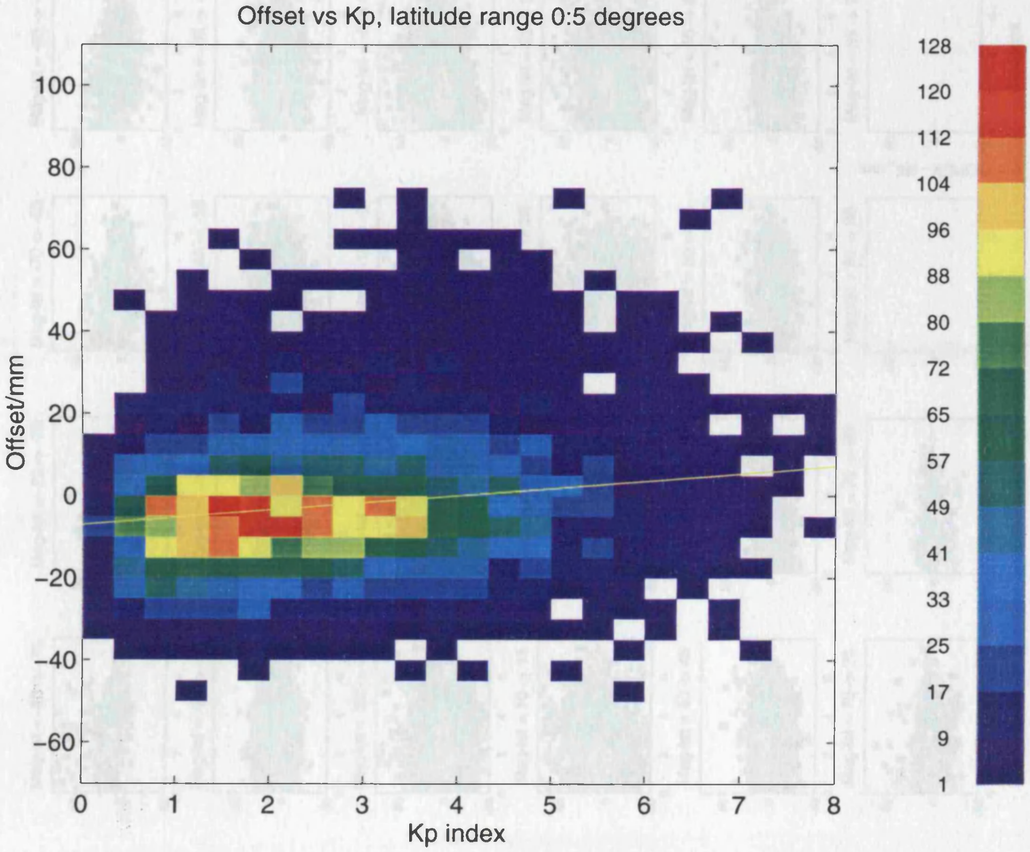

Figure 3: Plot of offset versus Kp index, for the latitude range 0° to 5°N. The yellow line represents the linear regression to the data.

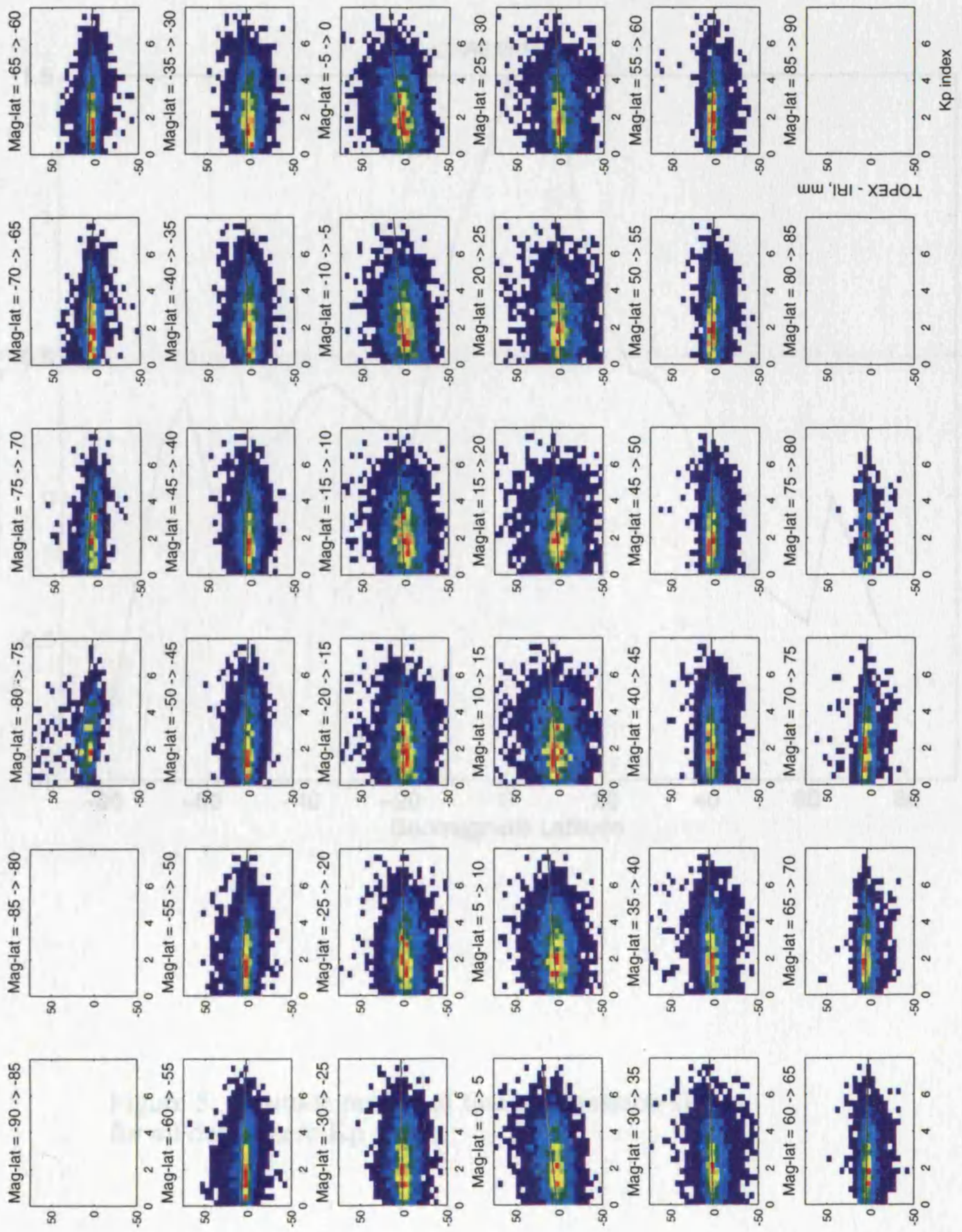

Figure 4: Plots of offset versus Kp index, for all latitude ranges. The black lines represent the linear regression for each latitude range.

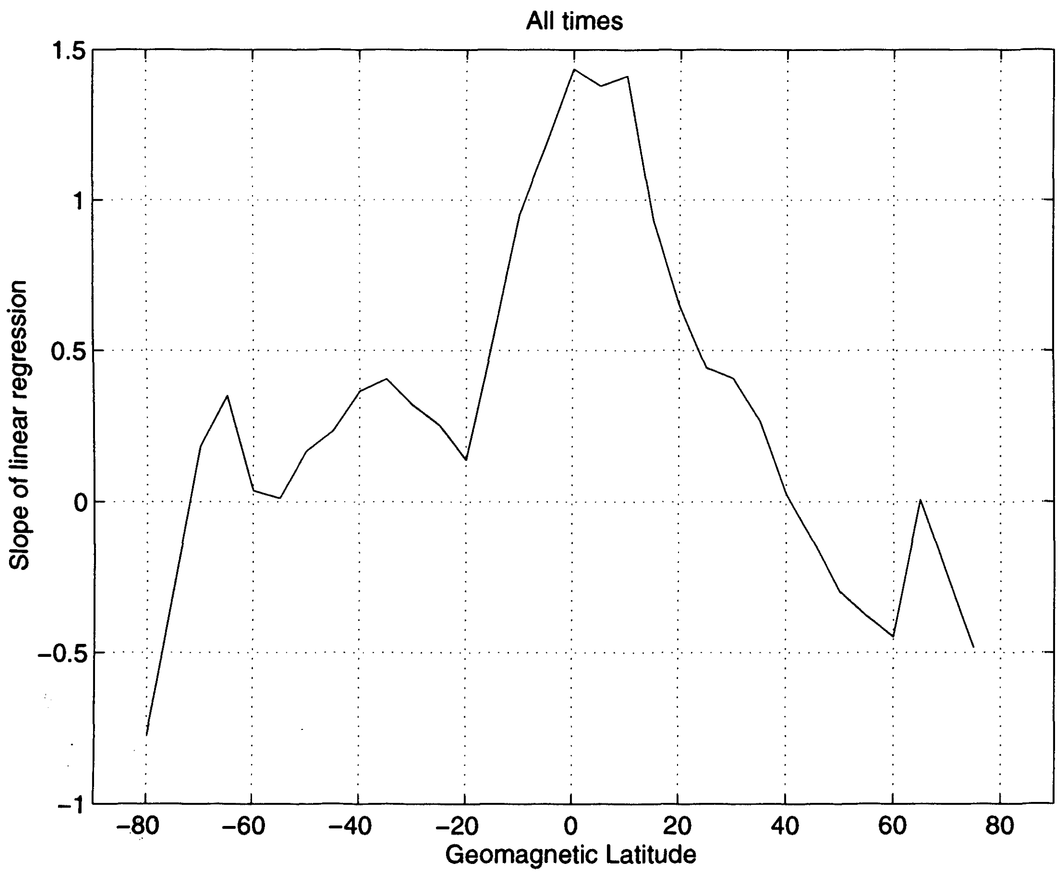

Figure 5: Latitude profile of linear regression slopes
for all data where Kp ≤ 5.

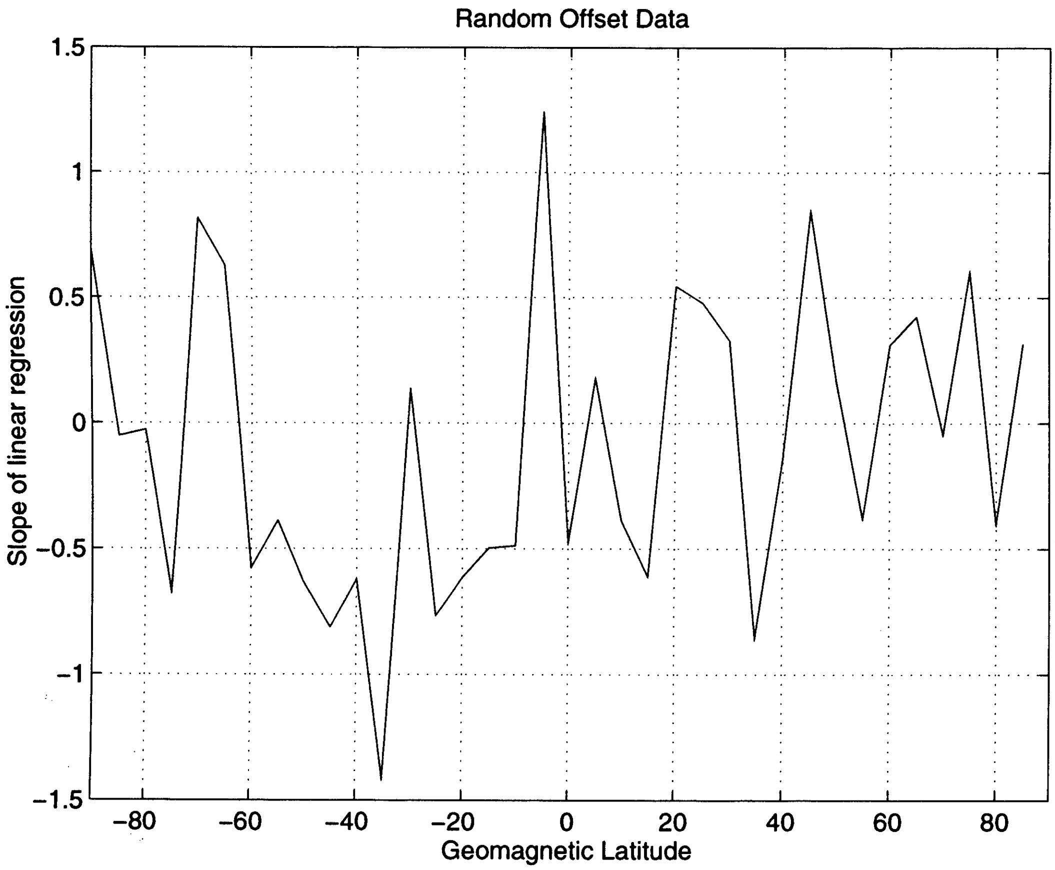

Figure 6: Latitude profiles of linear regression slope for random data generated with a realistic Kp < 5 distribution.

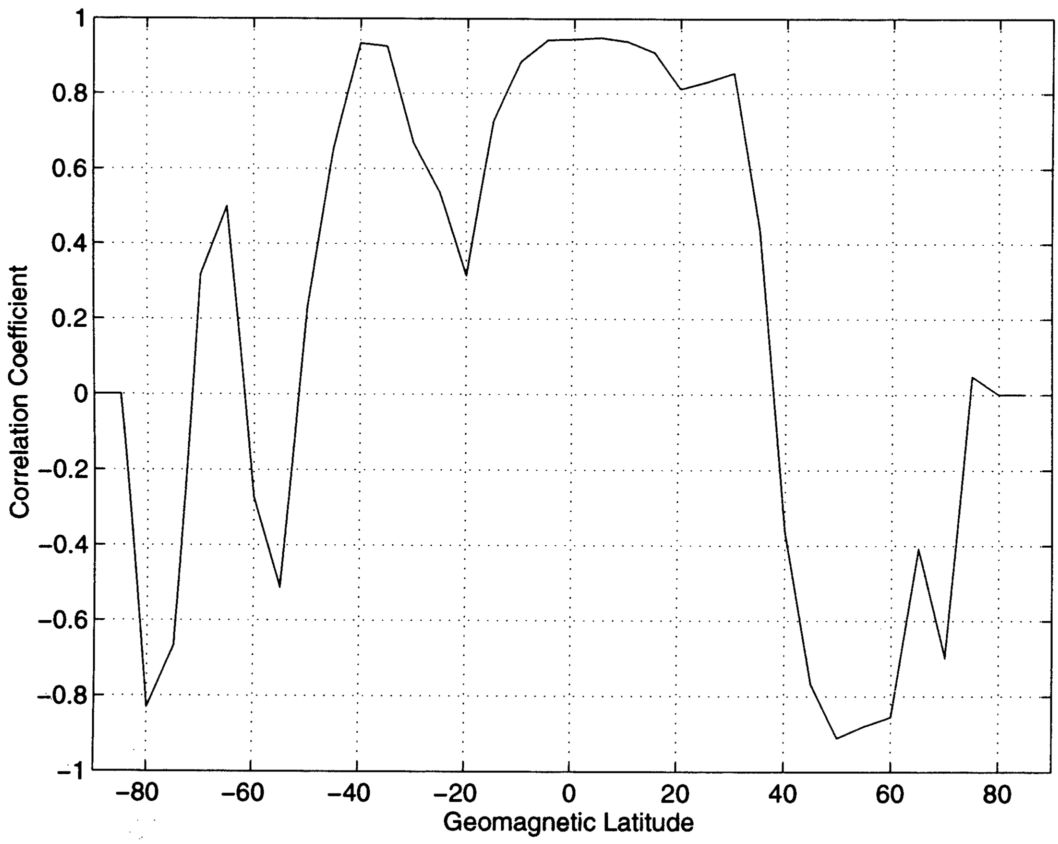

Figure 7: Latitude profile of correlation coefficients between offset and Kp index ≤ 5.

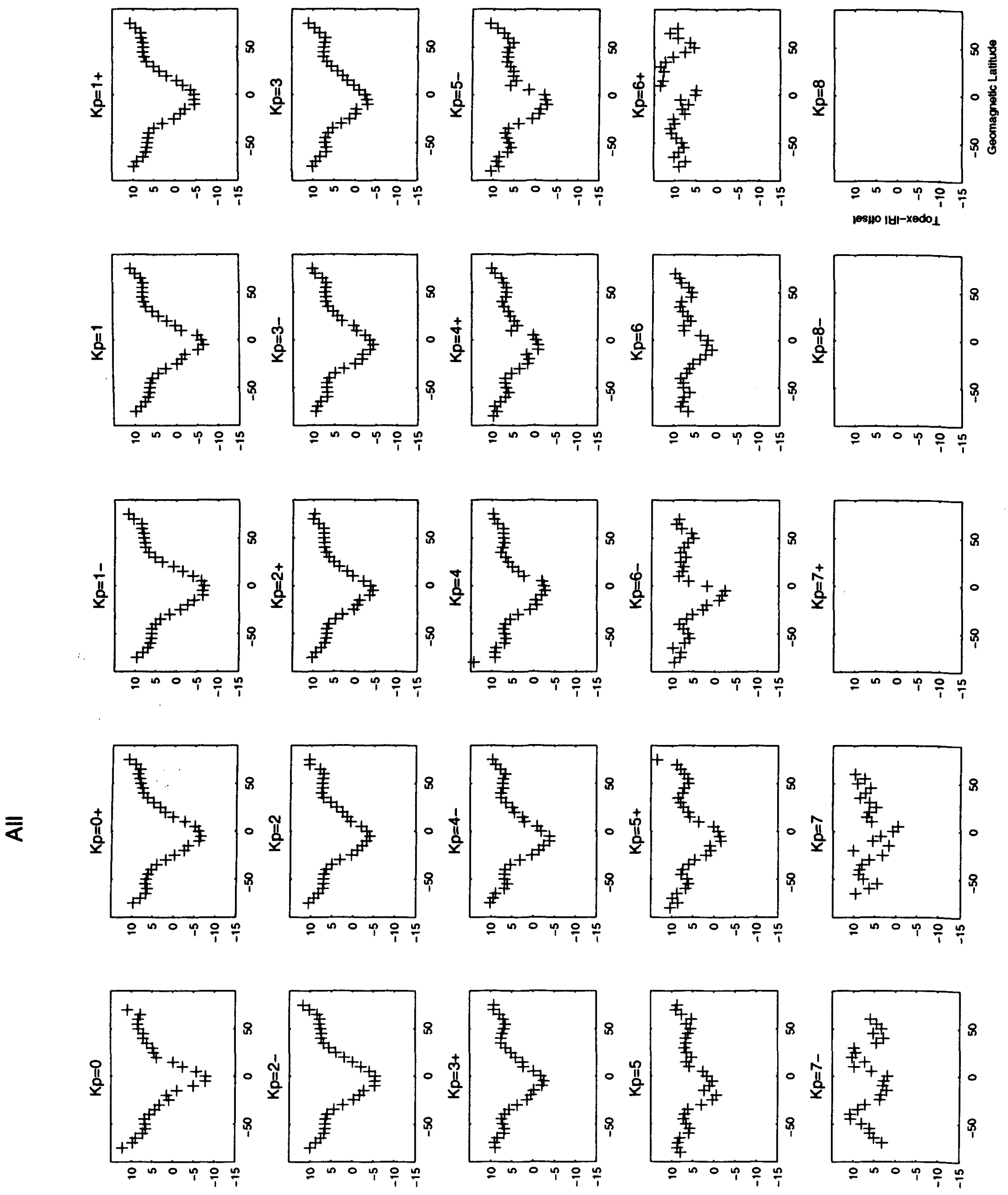

Figure 8: The Topex-IRI offset latitude profile for each value of Kp. The tendency of the IRI to overestimate at high latitudes and underestimate at low latitude is apparent.

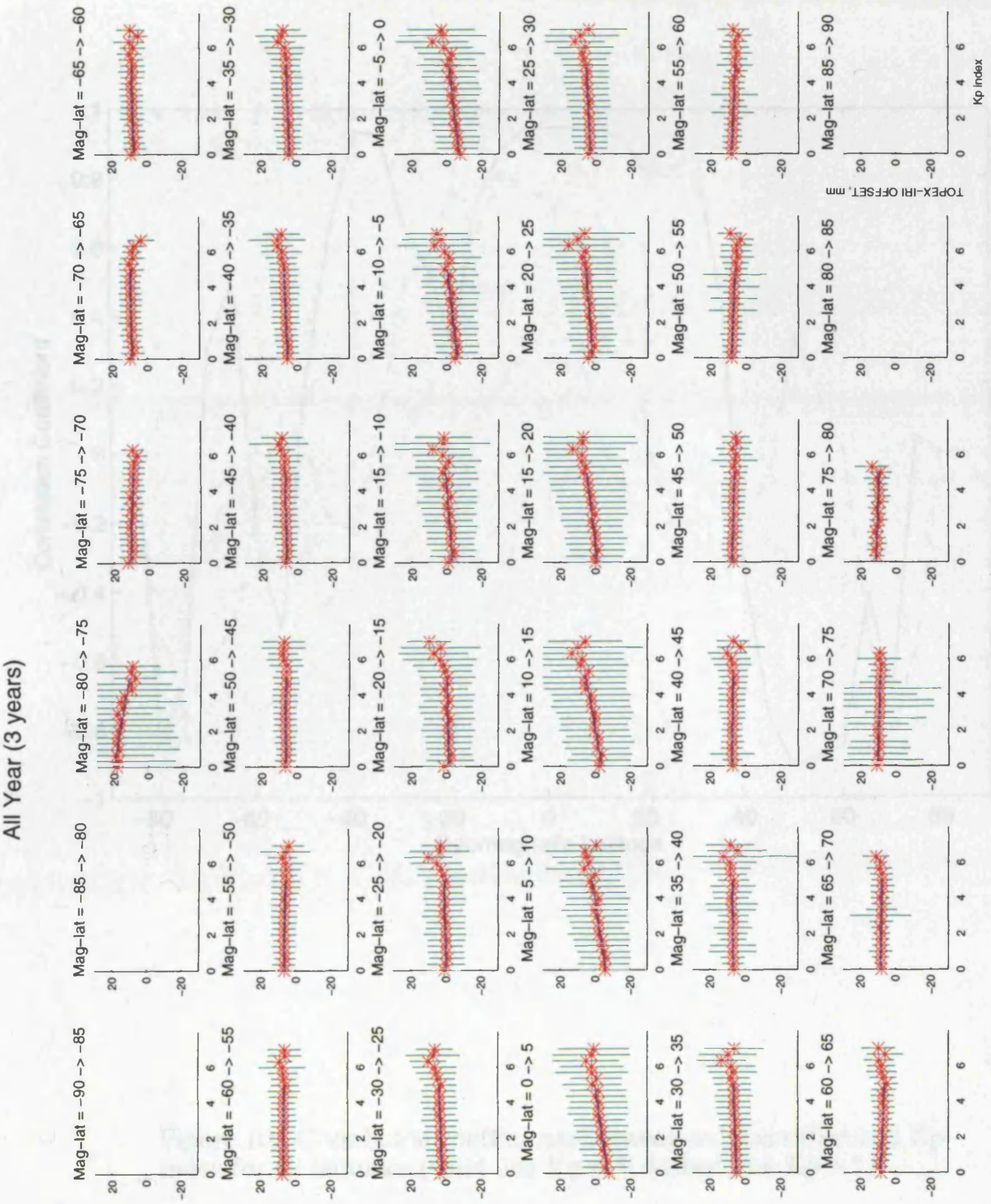

Figure 9: Median offset versus Kp index for all latitude ranges, with standard deviations (green bars) and linear regressions to Kp < 5 (black lines) also plotted.

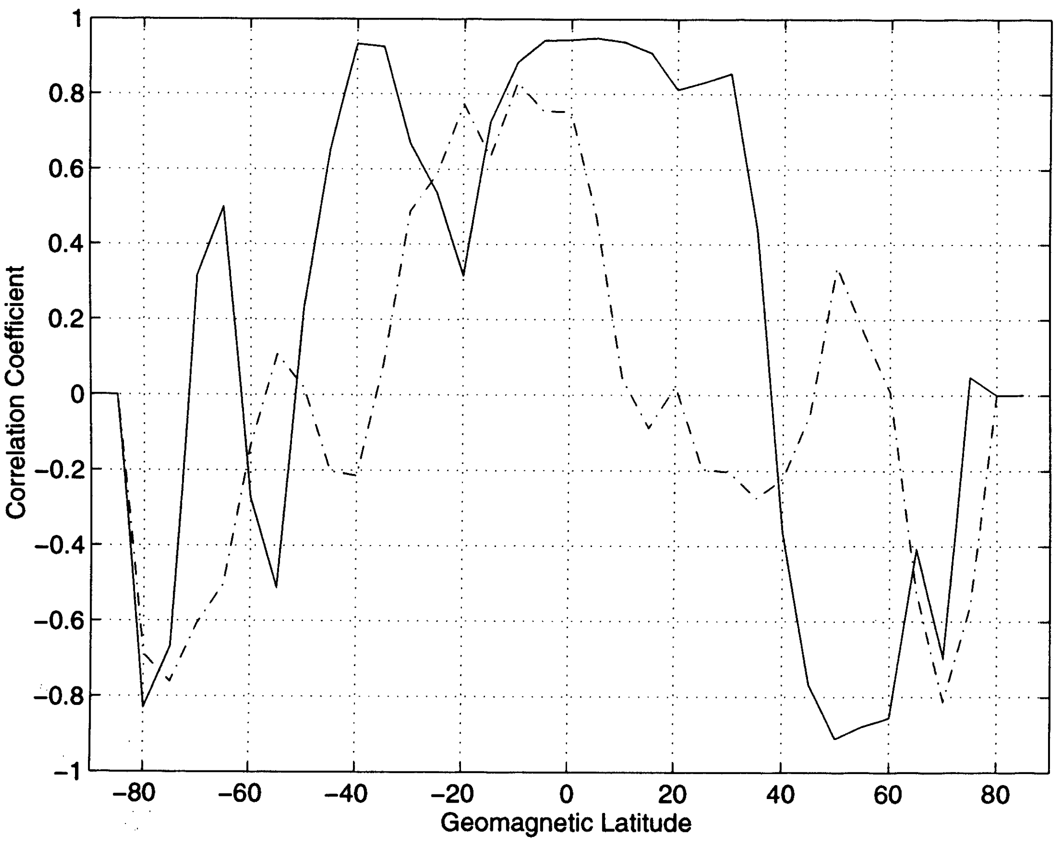

Figure 10: Correlation coefficients between mdeian offset and Kp index for all latitudes (solid line Kp ≤ 5, dashed line Kp > 5).

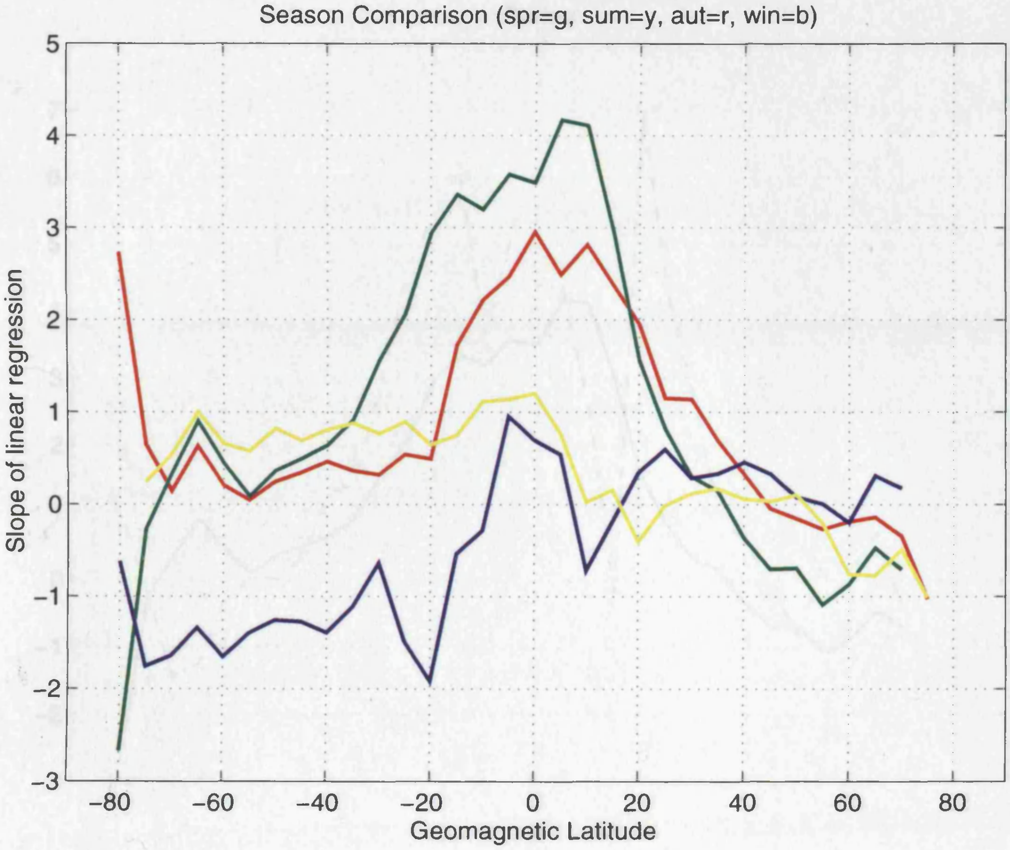

Figure 11: Latitude profiles of linear regression slope to the offset vs Kp < 5, for all seasons (green = spring, summer = yellow, autumn = red, winter = blue).

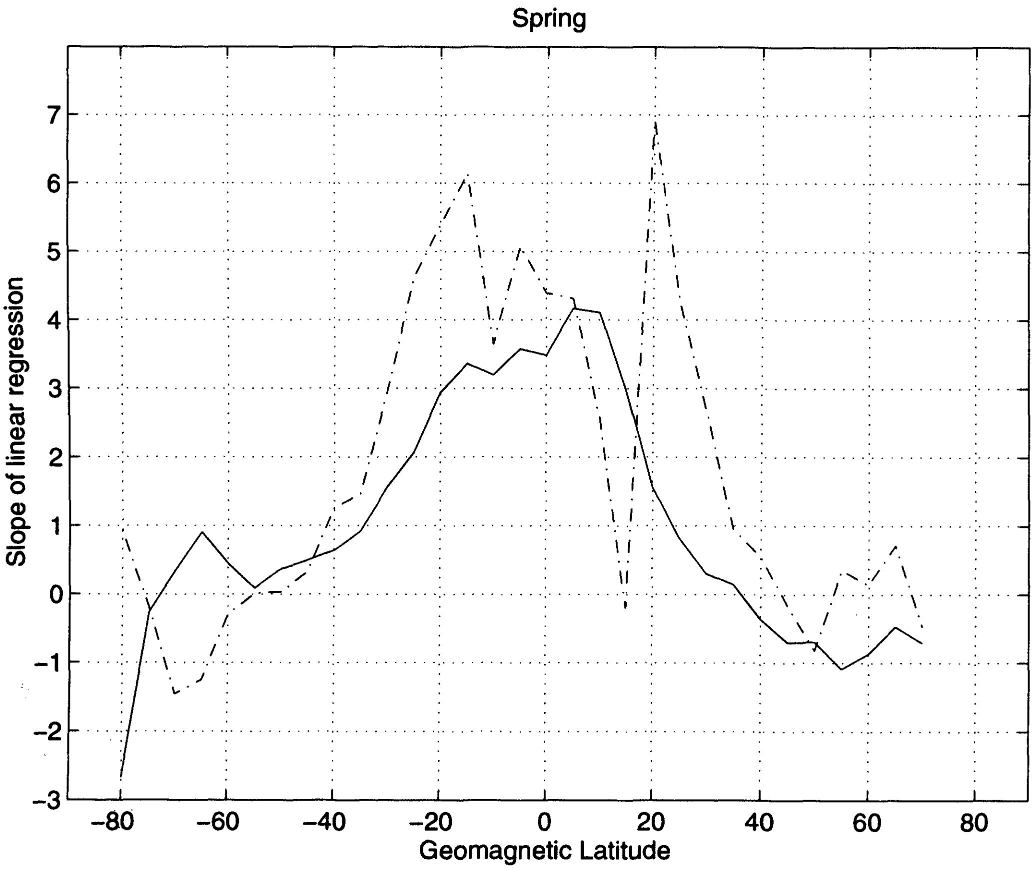

Figure 12: Latitude profile of linear regression slope of the offset vs Kp for spring (solid line Kp ≤ 5, dashed line Kp > 5).

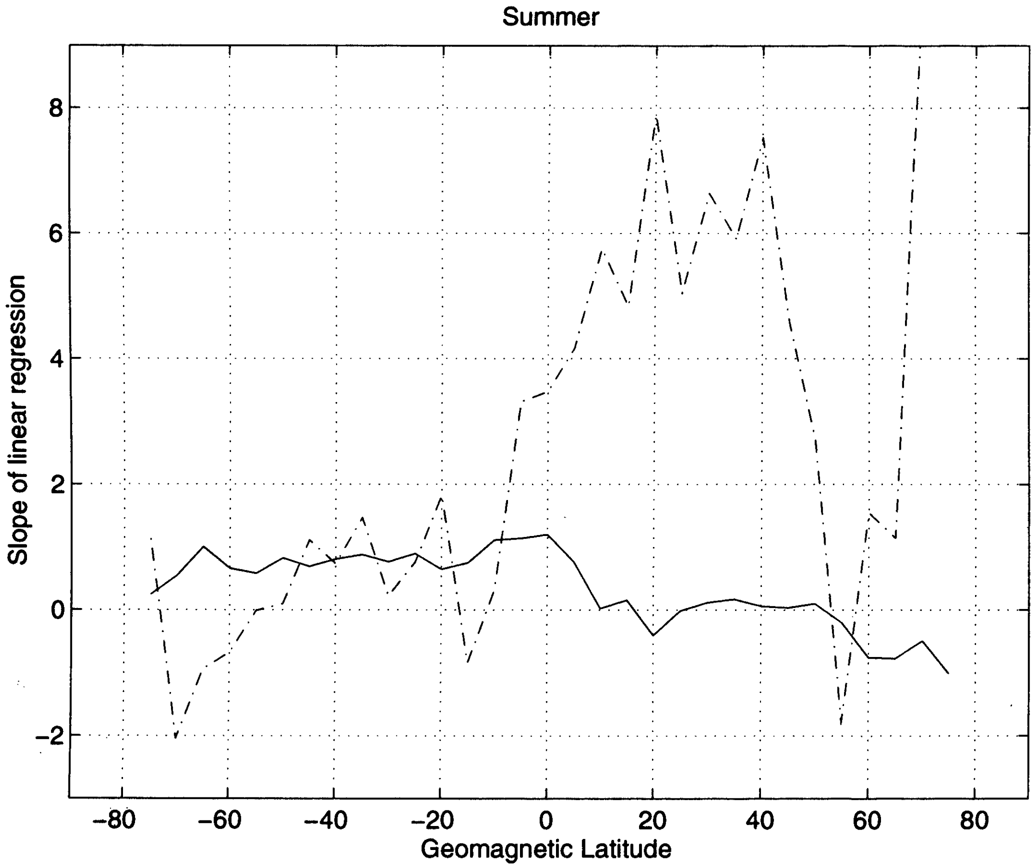

Figure 13: Latitude profile of linear regression slope of the offset vs Kp for summer (solid line Kp ≤ 5, dashed line Kp > 5).

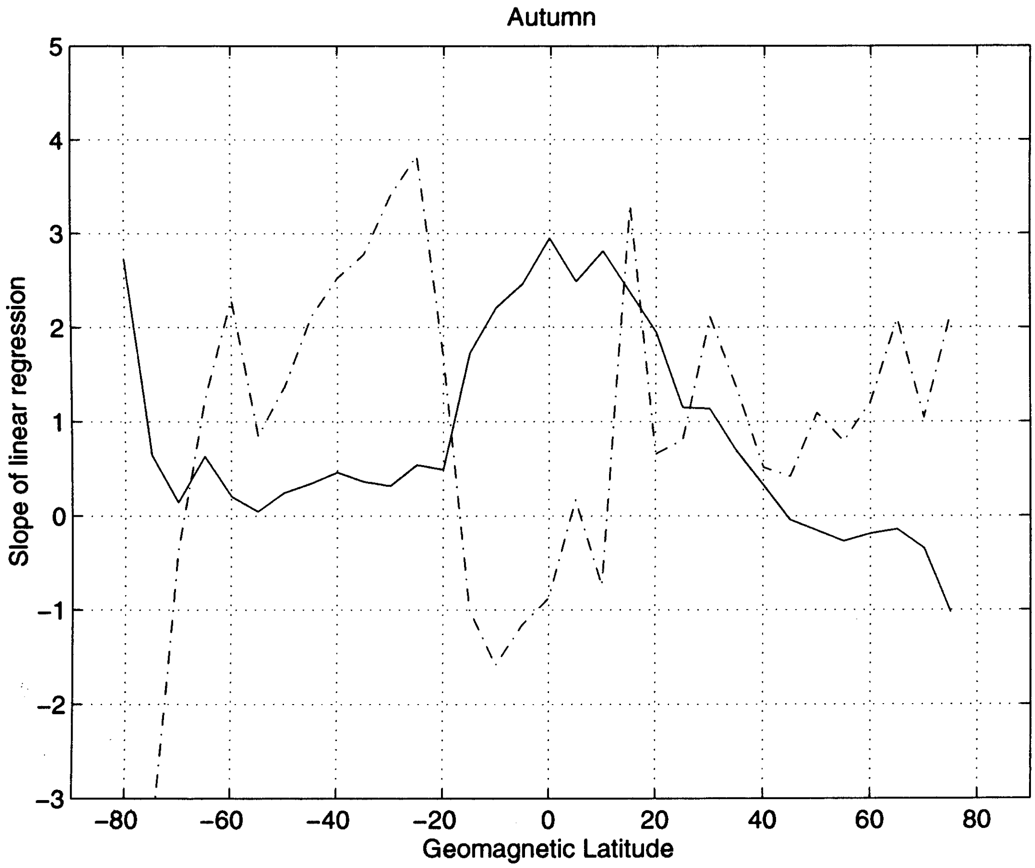

Figure 14: Latitude profile of linear regression slope of the offset vs Kp for autumn (solid line Kp ≤ 5, dashed line Kp > 5).

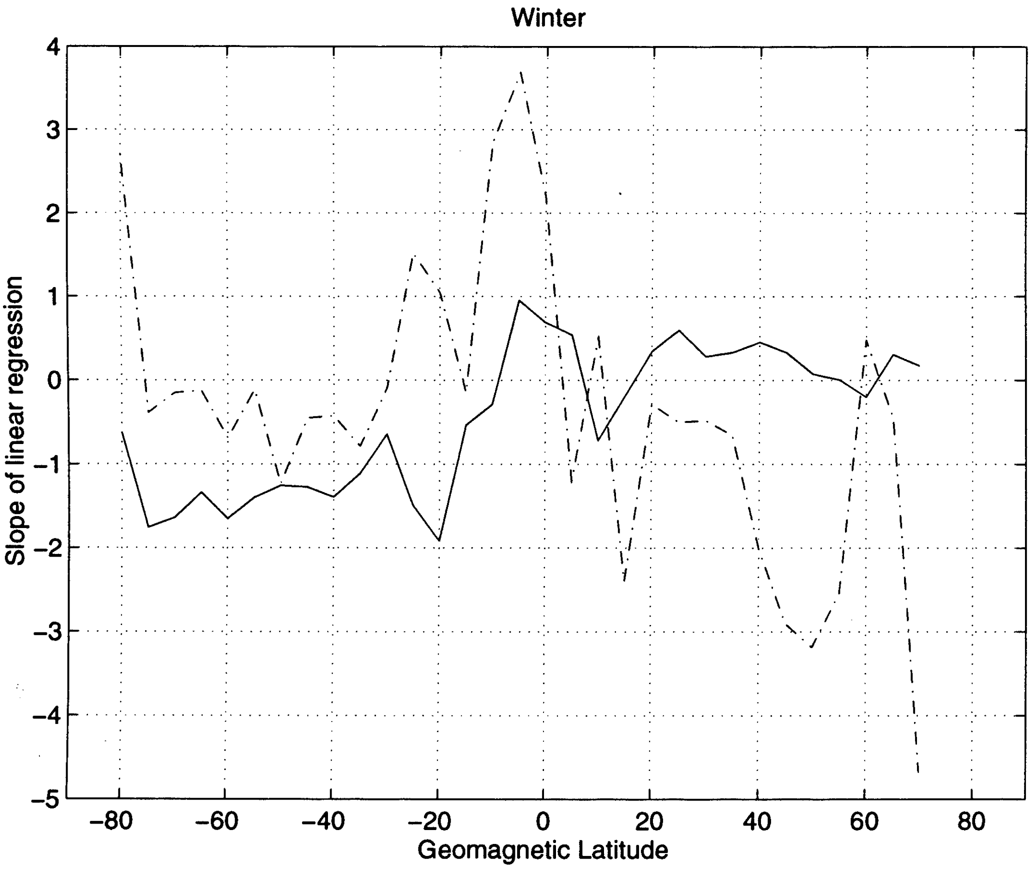

Figure 15: Latitude profile of linear regression slope of the offset vs Kp for winter (solid line Kp $\leq$ 5, dashed line Kp > 5).

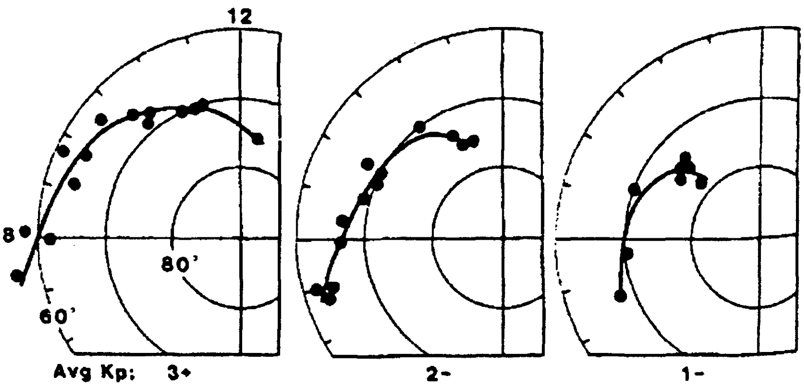

Figure 16: The LEDT position for 3 days, showing that as average Kp increases, the LEDT rotates clockwise and expands equatorward (from Whalen, 1987).

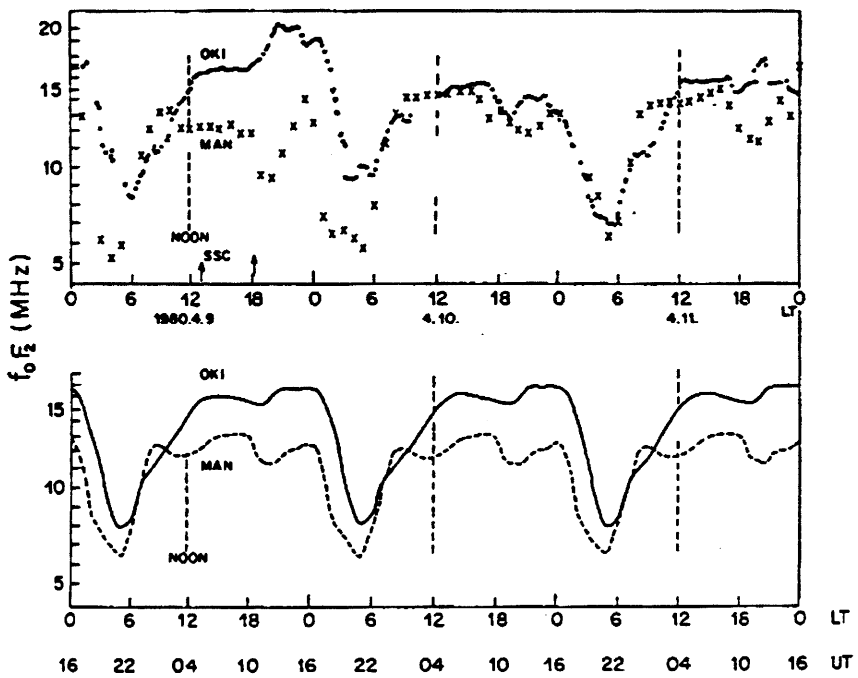

Figure 17: *fo*F2 variations (top frame), following the storm of 9 April 1980, over Okinawa located near the crest, and over Manila representing the trough. The lower frame shows the representative monthly mean variations in *fo*F2 over the two stations (from Tanaka, 1981).

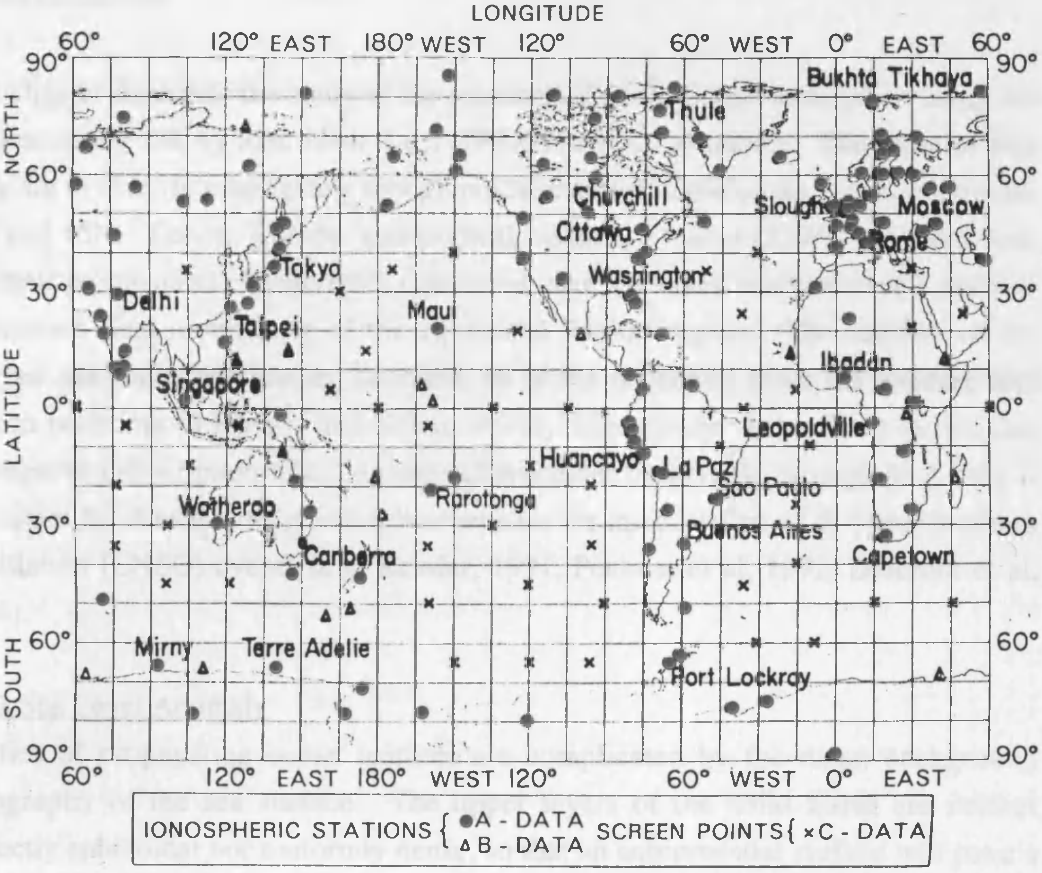

Figure 18: Map of ionospheric sounding stations used in the numerical analysis to produce the IRI. The red circles represent stations where data were recorded, the triangles mark ground stations where data were predicted from previous records, and the crosses indicate the locations of 'screen points'.

Chapter 7: TOPEX/Poseidon Sea Level Anomaly Studies of the Pacific Ocean, October 1992 - October 1994

7.1 Introduction

This chapter describes the study of the equatorial Pacific Ocean undertaken using sea level anomaly (SLA) data from the TOPEX/Poseidon altimeter. The aims of this work are to identify propagating topographical features of the ocean between latitudes 15S and 15N. Kelvin, Rossby, and tropical instability waves (TIWs) are identified, and their propagation charateristics calculated from a detailed study of over 2 years of continuous data monitoring of the equatorial Pacific region. The validity of the delayed oscillator mechanism is tested, as is the reflection from the western and eastern boundary of Rossby and Kelvin waves, respectively. It has been shown that an improved description of the dynamical processes observable through SLA data is important for determining possible mechanisms for the initiation of El Niño/Southern Oscillation (ENSO) events (e.g. Kessler, 1991, Penhoat et al, 1992, Delcroix et al, 1994).

7.1.1 Sea Level Anomaly

Studies of propagating ocean features are complicated by the mean background topography of the sea surface. The upper layers of the solid Earth are neither perfectly spheroidal nor uniformly dense, so that an equipotential surface will have a topography with a horizontal scale of tens to thousands of kilometres, and a relief of up to 200m. Hypothetically, if the ocean were allowed to be at rest on the Earth, then its surface features would mimic that of the equipotential surface (allowing for the effects of the Earth's rotation). This surface is known as the Earth's marine geoid, and would complicate observations of fluctuating ocean topography if not removed. Normally the other major complicating factor in studying propagating ocean features are the tides. The orbit of TOPEX/Poseidon has been specifically chosen to aviod tidal aliasing for this reason.

When this background is removed, the resulting quantity will be the fluctuation from the mean ocean surface. The mean sea surface is a good approximation to the marine geoid because even in regions where there are strong and relatively steady currents (e.g. the Gulf Stream) the contribution to the topography from current flow is only about one-hundredth of that resulting from variations in the underlying solid crust. This fluctuation from the mean surface is called the sea level anomaly (SLA).

7.2 Data Preparation

The SLA data used were pre-processed by the Collecte Localisation Satellites (CLS) Space Oceanography Group from AVISO GDR-Ms for TOPEX/Poseidon data. These data are provided periodically on CD-ROM by the AVISO multi satellite data bank, run by the French space agency, Centre National d'Etudes Spatiales (CNES). The processing of the data starts with a quality control and validation of the altimetric product and the geophysical corrections (this is part of the standard validation of the data provided by CLS for the TOPEX/Poseidon GDR-Ms). Based on analysis by Le Traon et al (1994), TOPEX data with sigma-*h* (the RMS of the range measurement over 1 s) greater than 10 cm are rejected; Poseidon data with sigma-*h* greater than 20 cm are rejected. Data were also rejected when there were less than 10 Poseidon or 5 TOPEX elementary data, and when the attitude was larger than 0.4 degrees (the attitude being measured directly from the altimeter waveform). The land and ice radiometer flags are used to reject altimeter data over land and ice, and data without tide corrections, with the TMR wet tropospheric correction greater than 50 cm, or with the significant wave height larger than 11 m are also rejected. Finally, to remove spurious spikes, an iterative process is used based on cubic spline functions (Le Traon et al, 1990). This only removes 0.01% of the data. The average value of rejected points (over the oceans) is about 10%. Non-valid data are concentrated (apart from in ice contaminated regions) in the tropical convergence zone, where rain is likely to occur, and in regions with very large significant wave height. Then the reduced GDRs are created. These contain sea surface height measurements corrected for all environmental errors and orbit errors.

CLS use conventional repeat-track analysis (Le Traon et al 1994) to calculate the sea level anomalies. This essentially involves taking the RMS difference between exact repeat track values of the sea surface height. Orbital errors are assumed to be negligible for TOPEX/Poseidon. Then the time varying part of the sea surface height signal can be ascertained. The data are then resampled every 7 Km using a cubic spline. The most complete profile is selected, and this is used to calculate the differences with respect to the other cycles. Data are then recentred relative to the mean of the data set to give the sea level anomaly.

For the present study data created by the CLS Space Oceanography Group has been taken from TOPEX cycles 2 to 75, covering a range of dates from approximately October 1992 to October 1994. Whilst there were reported mispointing errors during the first 9 cycles, the effect on SSH measurements is expected to be negligible, especially since the SLA data is averaged over a geographic scale of 1° latitude and 2.8° longitude.

7.3 Observations

7.3.1 Data Presentation

The area under investigation in this study, shown in Figure 1, covered a latitude range of 15S to 15N and a longitude range 120E to 280E. This region is relatively free of land contamination, and hence there are only a few data gaps. Data gaps are removed by using a simple mean interpolation function, where an average of the nearest neighbouring points is used to fill the gap. Two years of data were analysed, from October 1992 to October 1994 (cycles 2-75).

An important characteristic of the waves under study (primarily 1st mode baroclinic Rossby and Kelvin waves) is that they propagate zonally, that is they propagate essentially Westwards or Eastwards. A useful tool in the examination of such waves is provided in a time versus longitude plot for a particular latitudinal cross-section. Eastward/westward propagating features will then exhibit themselves as diagonal contours with positive/negative slope. The gradient of the line gives a measure of the phase speed of the wave. To generate a time-longitude plot, data from each ten day cycle of the altimeter (a ten day cycle giving full geographical coverage of the area) is averaged into 1° latitude strips by 2.8° longitude. These values have been chosen to give maximum resolution of the region under examination - attempts to produce higher resolution plots results in data gaps. Time runs up the y-axis, and longitude along the x-axis.

The SLA data can also be displayed as spatial plots on a latitude-longitude grid. Each spatial plot consists of data from a full TOPEX/Poseidon 10 day repeat cycle. The data can be viewed in the form of an animation of cycles, and propagating features to be described in sections 7.2.2, 7.2.3, 7.2.5 can be discerned in such animations. One frame from such an animation is presented in Figure 2, the spatial plot for the beginning of January 1993 (cycle 11). A full description of all the propagating events in the region under study is still complicated, due to the interaction of the waves with the wind, the bottom topography, and also other waves, as well as the variation of the thermocline depth across the Pacific altering the sea surface signature amplitude of the waves. To simplify this task, several latitude bands of interest have been identified. It is worth noting that any Kelvin or Rossby wave activity of concern to this study (i.e. 1st mode Kelvin waves, and 1st or 2nd mode Rossby waves) should be mirrored between the two hemispheres, allowing for thermocline variations, current structure, and bottom topography. Mirrored features in the Southern hemisphere are generally weaker than in the Northern hemisphere. Possible reasons for this discrepancy could be the differences in current systems between the two hemispheres, as well as the wind field assymetry (mentioned in section 4.3).

The latitudinal bands identified are (approximately) i) 3S-3N ii) 3N-7N iii) 9N-12N iv) 3S-10S, and will be referred to as E (for equatorial), N1, N2 and S respectively. Figure 3 depicts the bands overlaid on a spatial plot of cycle 7 (21/11/92 - 30/11/92), with the features of interest in each band identified. These bands are convenient when referring to a more theoretical framework. New Guinea is evident just below the equator near the western boundary, and South America lies in the far east of the plot. In this figure the N2 band's variability comes from an upwelling Rossby wave (as identified by way of a time-longitude plot method), the N1 band has evidence of a downwelling Rossby wave and tropical instability wave activity, the E band is dominated by Kelvin wave activity, and the S band exhibits a relatively weak Rossby wave signature. These bands seem to act as wave guides for the majority of the propagating features that are discernible in the data. It should be noted that these bands are not rigid, and many of the Rossby waves to be described initially appear to curve into a latitude band near the eastern boundary, and curve out of the band towards the western boundary. Due to the ten day time resolution of the spatial plots, there is the possibility of non-propagating features becoming confused with propagating features. The examination following will use a combination of spatial plot animations and time-longitude plots.

7.3.2 Kelvin Wave Observations

Kelvin waves should be apparent as lines of positive gradient in time-longitude plots. Large scale eastward travelling positive SLAs are observable in time-longitude plots of the two years of data analysed in which eastward propagating downwelling waves are represented as red stripes of positive gradient, and upwelling waves as blue stripes of positive gradient. Figure 4, the time-longitude plot for the latitude range 0:1N, reveals such propagating features. The phase speed of the features is given by their gradient in this figure. A simple graphical analysis of each pulse in Figure 4 reveals that they have approximately the same phase speed as predicted by linear theory for a 1st order baroclinic Kelvin wave (Pickard and Emery, 1990). Hence these pulses are believed to be separate upwelling and downwelling Kelvin waves.

The downwelling Kelvin waves appear to be excited in groups of three pulses. The time between the initiation of the first pulse and the initiation of the last pulse is approximately 150 days. A group of such Kelvin waves will be referred to as a Kelvin event. A separate pulse will be referred to as a Kelvin wave. The Kelvin event gives the impression of a general eastwards movement of positive SLA, taking around 220 days from initiation of the event to the last pulse reaching the western Pacific boundary. Kelvin waves take approximately 60 - 80 days to cross the entire Pacific basin.

The sea-surface height signature of Kelvin waves is apparent in the data between the latitude range 5S to 3N. Their amplitudes are typically around 10 cm. These amplitudes are easily resolvable by TOPEX (see Chapter 2). Seven downwelling Kelvin waves can be identified in the time longitude plots; there are also two upwelling Kelvin waves, although their speed is greater than the downwelling waves, and is more difficult to determine with the time resolution of the data. This discrepancy may be due to the difference in thermocline depth between upwelling and downwelling waves. Other features which may be indicative of Kelvin waves are difficult to definitely categorise due to their low amplitudes. The waves' characteristics were measured directly from the time-longitude plots. Initiation/termination dates and longitudes, amplitudes, spatial widths and phase speeds are recorded in Table 1 for four such Kelvin waves which have been identified.

7.3.3 Rossby Wave Observations

Rossby waves are apparent as lines of negative gradient on the time-longitude plots. The ease of identification is very dependent on the latitude range of the time-longitude plot being examined. Rossby waves are readily apparent from 7N to 15N in the eastern basin, and 9S to 15S in the western basin. The time-longitude plots for 9:10N and 9:10S are presented in Figures 5a and 5b, with the Rossby wave signatures indicated. The discrepancy between the Rossby phase speeds between 9:10N and 9:10S may be due to the differences in current structure, and hence east-west mean flows, modifying the potential vorticity gradient (Kilworth et al, 1997) as discussed in section 4.4.2 Between 8S and 6N the waves are less readily identifiable, due to instability waves (in the Northern hemisphere) and Kelvin waves complicating the time-longitude plots, and possibly modulating the Rossby wave signal. The higher phase speed of the Rossby waves at lower latitudes also complicates their identification, because their phase speeds then become very similar in magnitude to that of the seasonal signal i.e. the Rossby waves propagate at the same speed as the seasonal signal of high/low SLA.

The characteristics of these waves were measured directly from the time-longitude plots. Initiation/termination dates and longitudes, amplitudes, spatial widths and phase speeds are recorded, where possible, in Table 2 for each of the latitude ranges (one wave chosen per range). The phase speeds at the lower latitudes (8S to 6N) are subject to larger errors due to the problems mentioned previously.

It should be noted that the Rossby waves' phase speeds change as they propagate across the Pacific. The phase speed of a wave can either increase or decrease depending on the latitude at which the wave is propagating. The time-longitude plot for 3:4N is presented in Figure 6; the curved nature of the Rossby wave propagation is marked on the figure. The phase speed decreases from 1.05 ± 0.04 m/s in the eastern basin, to 0.35 ± 0.04 m/s in the western basin. In contrast the time-longitude plot for the latitude range 14:15N (Figure 7) reveals the phase speed of the Rossby waves increasing as they propagate westwards, from 0.12 ± 0.03 m/s in the eastern basin to 0.25 ± 0.03 m/s in the western basin. A change in thermocline depth across the Pacific may be responsible for the phase speed discrepancy (Kessler and McPhaden, 1995). If the thermocline deepens the waves would increase in speed, if it became more shallow the waves would decrease in speed. It has also been suggested that the topography of the sea floor may affect the phase speed of the waves (Cippolini et al, 1996).

The time-longitude plots from 7N to 15N also exhibit a yearly oscillation of positive and negative SLA. Diagonal tracks of positive SLA are clearly observable in these latitude ranges in the eastern basin, with amplitudes of up to 25cm. These are Rossby waves, and they are most obvious during the periods of positive SLA as in Figure 5a. Their signatures become less well defined as they propagate westwards across the basin, due to a decay in amplitude. These Rossby waves may not have the same source as the lower latitude Rossby waves. It has been suggested that they are generated by wind bursts over the Gulfs of Tehuantepec and Papagayo (Giese et al, 1994). Theses wind bursts occur around January, which is coincident with the initiation times of the Rossby waves observed in the TOPEX/Poseidon data.

The time-longitude plots from 9S to 15S are markedly different to those from 8N to 15N. The time-longitude plot for 9:10S (Figure 5b) does not show the yearly oscillation between periods of positive and negative SLA, which is seen in all ranges from 8N to 15N. Also, in contrast to the northern hemisphere, the Rossby wave signatures are strongest in the western basin of the southern hemisphere.

7.3.4 Comparison Between Rossby Phase Speed: Measurement and Extra-Tropical Theory

The standard theory for freely propagating, linear Rossby waves can be derived by a linearisation of the unforced equations for the large-scale, low-frequency motion about a state of rest (Gill, 1981). The dispersion relation for Rossby waves is given by:

$$\omega_n = -\frac{\beta k_x}{k^2 + f^2/gh_n}$$

where k_x is the x-component of the horizontal wave number $\boldsymbol{k}, f$ is the coriolis parameter ($f=2\Omega\sin\phi$ where Ω is the angular frequency of the Earth, and ϕ is the latitude) and $\beta = \delta f/\delta y$. The first baroclinic (internal) mode has $n=1$, h_n being the equivalent depth given by :

$$h_n = \frac{N^2 h^2}{gn^2\pi^2}$$

where g is the acceleration due to gravity, N is the Brunt-Väisälä frequency ($N^2 = -g\rho_o^{-1}\, d\rho_o/dz$, ρ_o being the unperturbed density and z being the vertical scale), and h is the depth of the open ocean. For purely westward flow, as we are investigating, the equation for the phase speed of the first baroclinic mode becomes:

$$C = -\frac{\beta k^2}{k^2 + f^2\pi^2/N^2h^2}$$

The Brunt-Väisälä (or buoyancy) frequency is dependent on the density profile of the water. It will vary across the Pacific. A frequency of 2×10^{-3} rad/s has been assumed in our simple model, and a value of 5000 m for h, after Pond and Pickard (1989). The angular frequency of the Earth, Ω, has been taken as 7.3×10^{-5} rad/s.

The resultant theoretical predictions, based on these assumptions, are plotted versus the measured Rossby wave phase speeds from this study in Figure 8. The measurements in the Southern hemisphere match the predicted values very well. The measurements in the Northern hemisphere are not matched so well with the assumed values of N and h. This may be due to the difference in density profile that exists between the two hemispheres. The results do, however, indicate good agreement in the general trend of the phase speeds with latitude.

It should be remembered that a recent paper by Kilworth et al (1997) has provided a means for adjusting the linear theory, taking into account mean westward flows (see section 4.4.2). The application of this new theory may well explain the discrepancy between the TOPEX/Poseidon derived phase speeds and linear theory presented here.

7.3.5 Instability Wave Observations

Instability waves are apparent as lines of negative gradient on the time-longitude plots. They are much more localised than the Rossby waves, only extending over a set range of latitude and longitude, and have a much finer, higher frequency structure. The waves are evident on time-longitude plots in the latitude range 1N through to 8N, extending over longitudes 195E - 255E. The fine structure of a TIW is indicated on Figure 9. The TIWs can also be discerned in spatial plots of the data, such as Figure 2. Unlike the Kelvin and Rossby waves which appear as single pulses of SLA, the instability waves create a wave pattern of crests and troughs in the SLA signal. This makes Fourier analysis ideal for estimating the wave's characteristics (section 7.3.6). There is one full instability wave event (defined as from when the waves are observed to be initiated to when they have decayed) in the two years of data. The event lasts from June 1993 to March 1994. The tail end of another instability wave event is apparent at the start of the data, from October 1992 to March 1993.

7.3.6 Fourier Analysis of the Instability Waves

The temporal-spatial region containing instability wave activity is selected from the time-longitude plots. This covered a temporal range from cycles 32:51 (198 days), and a spatial range from longitude 201W to 257W (6300Km), and is shown on Figure 10a. The two-dimensional (spatial and temporal) autocorrelation of the region was taken, to help reduce the noise in the signal (Figure 10b), from which a two-dimensional (spatial and temporal) Fast Fourier Transform (FFT) was calculated. The FFT reveals dominant frequencies as peaks in the relative power (Figure 10c). The wavelength, frequency and phase speed may be obtained from such two-dimensional FFTs. The instability waves have wavelengths of 1600 $\pm$ 100 km, periods of 33 $\pm$ 3 days, and phase speeds of 0.60 m/s. The phase speeds obtained in this manner were also verified by two other methods. Firstly the time-longitude plots were examined graphically, as in the case of Kelvin and Rossby waves; secondly the two-dimensional autocorrelation was examined graphically in the same way. The comparison of phase speeds is presented in Table 3. All three methods appear to be consistent and quite accurate, but we will use the FFT method as the most consistent wavelengths, periods and phase speeds are obtainable by this technique.

The two-dimensional FFTs also reveal the relative power of the instability waves between each latitude range, if the same sized area is chosen each time for analysis.

This was done for all 7 latitude ranges, and the relative powers are plotted on Figure 11. The powers have been fitted by a cubic spline interpolation, which gives a peak in power at just below 5N.

7.4 Generation of Downwelling Kelvin Waves - Westerly Wind Bursts or Western Boundary Reflection?

Wind stress data provided by the European Centre for Medium Range Weather Forecasting (ECMWF), at Reading, has been examined to confirm or otherwise the hypothesis that Kelvin waves are initiated by westerly wind bursts (as suggested by e.g.Delcroix et al, 1991, Kessler, 1995). The ECMWF wind stress data are generated by using observations and a numerical model of the atmosphere, and represent some of the most accurate data currently available.

7.4.1 Kelvin Wave Generation by a Westerly Wind Burst

A good example of a westerly wind burst occurred during the end of December 1992 and the beginning of January 1993. The wind stress vectors for the last few days of the burst are plotted on Figure 12. Australia is bottom left of this figure, with South America on the far right. The wind burst can be seen to consist of a cyclonic wind in the southern hemisphere (Figure 13). Westerly winds occur from the equator down to 14 S. The burst had a zonal extent from 150 E to 180 E (approximately 3500 km), and a meridional extent of approximately 1000 Km, the wind stress reaching almost 0.5 N/m^2 as opposed to the normal background level of 0.05 N/m^2. The zonal wind stress has been plotted on Figure 14 for the end of 1992 and the first 50 days of 1993. Red colours represent westerly winds, whilst blue colours represent easterly winds. The westerly wind burst lasted from 25 December 1992 to 6 January 1993. The signature of a downwelling Kelvin wave occurring coincidentally with this wind burst is visible on the time-longitude plot of Figure 4. The Kelvin wave signature is first visible in the time-longitude plot (for 0:1N) at 170 E, cycle 11 (31 December 1992). This is consistent with the Kelvin wave being initiated by the wind burst. The spatial extent of the Kelvin wave is displayed on Figure 2. The zonal wind stress record at 4°S is recorded in Figure 15, indicating that the vast majority of wind stress is easterly at this latitude, with only a few strong westerly wind bursts in the two years of data.

7.4.2 Western Boundary Reflection

In contrast to the Kelvin wave of cycle 11, the Kelvin wave initiated around the beginning of November 1992, cycle 5, (the first Kelvin wave on Figure 4) does not appear to have been initiated by any westerly wind burst. The wind stress record for the region in 1992 is presented in Figure 16. The beginning of November corresponds to day 304. Although there is evidence of some westerly winds, they are not anomalously strong. It is tentatively suggested that this Kelvin wave was initiated as a consequence of the reflection from the western boundary of a downwelling Rossby wave. It has been demonstrated by Du Penhoat and Cane (1991) that the chain of islands at the western boundary, can act as an efficient reflector (reflecting 80-90% of the incident Rossby wave energy as equatorial Kelvin waves) even though the boundary is not physically solid.

There is, however, also evidence that the Kelvin wave may have been initiated as far north as 10 N by westerly wind stress, the wave consequently propagating southwards as a coastal Kelvin wave from the Philipines, to New Guinea, and eventually reaching and being trapped by the equator. This mechanism was suggested by Boulanger and Fu (1995) as a potential source for Kelvin wave generation. The wind stress vectors are presented in Figure 17 for 22 October 1992. The spatial plots of cycle 2 to 7 are shown in Figure 18. An enhanced positive SLA is evident along the coastline of the Philipines (10 N, 130 E). Whether this is a coastal Kelvin wave or not is unclear. Data from the preceding month may clarify this situation, but unfortunately TOPEX/Poseidon was not operational then.

7.5 Eastern Boundary Reflection

A region of positive SLA, apparent on Figure 19, associated with a downwelling Kelvin wave, appears in the E band between latitudes 200E:270E at cycle 20 (beginning of April 1993). The wave has reached the coast of South America by cycle 21, and positive SLA continues to increase in magnitude around the coast over the next couple of cycles. The region of positive SLA grows, and by cycle 25 covers a region from 240E:280E in the S, E and N1 bands. There is evidence for coastal Kelvin waves propagating northwards and southwards away from the equator along the coast, reaching to ~12S and 7N, as indicated on Figure 19. By cycle 27 it is evident that two Westward propagating positive features have emerged from the region of positive SLA created by the Kelvin wave. The two features are Rossby waves; the Kelvin waves and subsequent Rossby waves are depicted in the spatial plots for cycles 20 to 28 in Figure 19. They move along the N1 and S bands, after having apparently followed a curved ray path starting near to the equator. The N1 Rossby wave reaches 150E by cycle 41; the S Rossby wave has a smaller SLA signature than the N1, and appears to propagate a couple of degrees latitude further away from the equator than the N1 Rossby wave. The S Rossby wave signature is negligible by cycle 35, by which time it has reached approximately 200E. However, the S Rossby wave reappears by cycle 45, mirroring the N1 Rossby wave again. The two Rossby waves continue to propagate Westwards; the N1 wave reaches 125E, whilst the S wave reaches 150E. The N2 band becomes excited with positive SLA during cycle 57, and the band appears to curve downwards into the N1 band, enlarging and sustaining a forming patch of positive SLA. A large horseshoe shape positive SLA region then grows centred around the equator, and remains until cycle 61, whereupon it starts to decay, disappearing by cycle 67.

Kessler and McPhaden (1991) used the Toga-Tao buoy array (Figure 20) to study the effect of oceanic waves on the 1991-1993 El-Nino. They could not specifically measure phase speeds or the scale of the waves using the buoy data, as the spatial sampling was too low, but used the data to study the influence of wind stresses on the waves, and to investigate any possible reflection mechanism at the boundaries. They found no evidence for an eastern boundary reflection of Kelvin waves. This contrasts with our evidence for such a reflection occurring during cycles 25-27 (20/5/93 - 7/6/93), where two Rossby waves emerge from near the coast of South America after a Kelvin wave has hit the boundary. Kessler and McPhaden (1991) tried correlating buoy time series of Rossby and Kelvin waves. If eastern boundary reflection was occurring, their two time series at 250E (3600 km away from the coast) should have been well correlated with a lag of around 2 months, to allow for the propagation of the Kelvin wave to the coast and then back as a Rossby wave. They found there was a lag between the equatorial signal and that at 5 N of almost 180 degrees out of phase with that needed to produce the Rossby waves by reflection (see Figure 21). However a similar time series analysis to that done by Kessler and McPhaden (1991) has been performed on our TOPEX/Poseidon data.

The results are presented in Figure 22, and do in fact show a two month lag between the Kelvin and Rossby wave event mentioned - consistent with eastern boundary reflection. The time series was analysed at 250 E, as was Kessler's. Although Kessler chose this longitude due to a lack of buoy data nearer the coast, it is a sensible position to chose for TOPEX/Poseidon data since close to the coast the wave interactions vastly complicate the Rossby and Kelvin signals. So this result, from TOPEX/Poseidon, is consistent with eastern boundary reflection. Eastern boundary reflection would be significant to the variability in the N1 and S bands. Indeed the reflected Rossby waves then continue to propagate across the entire Pacific basin.

7.6 Discussion of Results and Conclusions

Prior to satellite based measurements of the oceans, in-situ instruments were the only source of data available for studying large scale wave activity. Due to the nature of the waves, with amplitudes of the order of 10 cm spread over wavelengths of tens of thousands of kilometres, these in-situ measurements were not able to resolve features very satisfactorily. Our results can be compared to previous studies using in-situ data (Toga Tao), and satellite data (Geosat and TOPEX/Poseidon).
Our definition of the N1, N2 and S bands is consistent with the idea of a critical latitude and turning latitude for the Rossby waves (Philander 1990) (see Figure 23). Rossby waves are equatorially refracted, and are not able to penetrate the turning latitude, and become trapped along the critical latitude. These latitudes are determined by current shear structure. The curving that is apparent at either end of the N1, N2 and S bands may therefore be attributable to the structure of the current systems.

The lack of consistency between simple eastern boundary reflection theory and observations at 5N found by Kessler agrees with other studies by Delcroix et al (1991) and Penhoat et al (1992) using Geosat data. They did find some ambiguous examples of possible reflection, but they concluded that this was of secondary importance to wind forcing in the off-equatorial region. The lack of consistency may be due to a lack of data over appropriate times, or due to the more ambiguous data itself, provided by the Toga-Tao buoys and Geosat. Indeed the Geosat data may well be adversely affected by the use of an empirical model to provide the ionospheric correction to the single frequency altimeter measurements, as discussed in chapters 5 and 6.

Kessler and McPhaden (1995) did find evidence that upwelling Rossby waves reaching the western boundary in early 1992 were reflected as an upwelling Kelvin wave; a similar event to the one they described is seen in the TOPEX/Poseidon data during cycles 10-13 (21/12/92 - 20/1/93), where negative SLAs, associated with upwelling Rossby waves, reach the western boundary and are apparently reflected as an upwelling Kelvin wave, which decays rapidly after reaching 180 E. This is the only possible upwelling western boundary reflection in our two years of data, and tends to suggest that western boundary reflection of wind generated Rossby waves is not the major cause of equatorial variability. Kessler and McPhaden (1995) pointed out that this situation is to be expected, since if the wind anomaly which produced the Rossby wave in the first place still exists once the Rossby wave has reflected and returned as a Kelvin wave, then the winds will oppose the Kelvin wave. This would require wind anomalies lasting about 125 days for an equatorial wind signal at 200 E. Equatorial wind anomalies do commonly last this long (Kessler and McPhaden, 1995), and hence give an explanation as to our lack of clear reflected signals from the western boundary. The apparent western boundary reflection of the downwelling Rossby wave into a downwelling equatorial Kelvin wave observed around cycle 4 would not be inhibited by such unfavourable winds. The suggestion is that a Rossby wave may be generated by the reflection of a Kelvin wave at the eastern boundary, as in cycle 26, propagate across the entire Pacific (as is observed with the cycle 26 reflected Rossby wave), and be reflected at the western boundary to form a downwelling equatorial Kelvin wave. Although such a process has not been observed in full in the two years of data analysed, there is evidence that the important mechanisms involved (i.e. eastern boundary reflection, the subsequent cross basin propagation of Rossby waves, and western boundary reflection) can occur.

The definition given of the N1 band having high variability agrees with Kessler and McPhaden's (1995) observations of the most prominent Rossby wave variability occurring at 5N and 5S, which they describe as due to the annual Rossby wave. Much of the variability observed in our data is indeed due to what we have identified as Rossby waves. Indeed, the latitudinal structure of sea level associated with the first mode baroclinic tropical Rossby waves is known from linear theory to have a local minimum at the equator with symmetric maxima at about 4 N and 4 S (Chelton and Schlax, 1996, Boulanger and Menkes, 1995).

Toga-Tao also revealed a mirroring of the Northern hemisphere signal at 5N with one at 5S with a weaker SLA signature. The TOPEX data has also revealed this mirrored weaker signal. Kessler and McPhaden (1995) suggest that this difference is due to the extra contribution of forcing in the Northern hemisphere associated with the annual migration of the ITCZ (Inter Tropical Convergence Zone) in the Northern hemisphere.

The results of the analysis of the Kelvin wave phase speeds (giving $V_p = 2.93 \pm 0.40$) correspond well with those obtained by Delcroix et al (1991) using Geosat data, and also model results produced by Lawrence et al (1997). They performed a time-lag correlation matrix analysis as well as a least squares fit of the SLA meridional structures to theoretical Kelvin wave shape, in order to obtain phase speeds of 2.82 ± 0.96 m/s and 2.26 ± 1.02 m/s for each of the analysis methods respectively. Chelton and Schlax (1996), using TOPEX/Poseidon data, obtained an objective estimate for the phase speed from an empirical version of the Radon transform (commonly referred to as a "slant stack" in seismological literature); their estimate of 2.70 m/s again agrees well with the results presented from the current study. Chelton and Schlax (1996) also noticed two of the larger, more slowly eastward propagating positive SLA, which we have called a Kelvin event. These events are coincident with the second and third pulses of the 1991-1993 El Nino event (Trenberth and Hoar, 1996). Because the propagation speed of the Kelvin events is only around a third that of the Kelvin waves, Chelton and Schlax define these events to be likely coupled atmosphere-ocean phenomena, rather than freely propagating waves. This is consistent with our reference to the events as Kelvin events. Essentially the event may be triggered by an initial Westerly wind burst, possibly produced by a downwelling Rossby wave piling warmer water into the western basin. The resulting Kelvin wave propagating eastwards takes with it a pulse of warm water, and because of this more westerly winds form to the west of the wave, triggering another Kelvin wave, and so on. The time for the Kelvin event to cross the Pacific therefore depends on a scale-time of ocean-atmosphere coupling. Whether the event can be described as the ocean controlling and feeding off the atmospheric winds, or vice-versa, is not clear. Previous authors have not quoted wavelengths (or more appropriately spatial scales) precisely for the Kelvin waves, most probably because the scale of each wave tends to vary, and because any estimate will have large errors due to the difficulty in extracting a clean signal from the background.

The Rossby wave phase speeds obtained using the TOPEX data are also in agreement with previous studies. Delcroix et al (1991) only analysed the Rossby phase speed at 4N and 4S. They obtained a value of 1.02 ± 0.37 m/s through time-lag correlation matrix analysis. The TOPEX/Poseidon data is too noisy (due to wave-wave interactions) in the Northern hemisphere to obtain a reliable estimate at these latitudes, although the value compares to our estimate of 0.75 ± 0.20 in the Southern hemisphere. Chelton and Schlax (1996) performed a more detailed study using TOPEX/Poseidon. The results from our analysis are in good agreement with their results (see Figure 24). Busalacchi et al (1994) computed a mean phase speed for 5N of 0.84 ± 0.36 m/s for TOPEX, and 0.89 ± 0.29 m/s for TAO, which our value agrees well with.

The investigation of the tropical instability waves has been one of the most detailed studies so far. Highly consistent estimates of their phase speed, wavelength, and periods have been obtained (0.59 m/s, 1600±200 km and 33±3 days respectively), and also the relative power of the waves with latitude. As a comparison, Busalacchi et al (1994) described the waves as having periods between 20-30 days, and a westward phase speed of ~45 cm/s. Giese et al (1994) measured a phase speed of 46 cm/s at 30 to 40 day periods. Legeckis reported wavelengths of 800-1200 km, periods around 20-30 days, and phase speed estimates of 40 cm/s, and Harvey et al (1993) a 25 day oscillation of 1000 km wavelength, with a phase speed of 50 cm/s. All of these authors find values for the phase speed lower than those obtained here using three different methods of analysis, although the in situ measurements provide the closest phase speeds to ours. The periods reported are also widely varying, although Busalacchi et al's (1994) and Legeckis's (1977) highest and Giese et al's (1994) lowest values correspond quite well to those obtained in this work. For a more detailed acocunt of the instruments used and the analysis methods, please refer to section 4.5/

The rôle of these waves in the ocean-atmosphere system is still not understood, but they may have important implications for Kelvin and Rossby wave energy transferral, and hence may ultimately play a key part in the El Nino phenomenon. Their generation mechanism is not well understood. It is known that they occur on current boundaries (the South Equatorial current/North Equatorial Counter-Current (NECC) boundary at ~5N), which suggests a current shear instability is responsible for their production. The instability waves are not always present or observable, however, tending to disappear from March through to May, corresponding to the months when the NECC is weak (Giese, 1994), again suggesting a current shear instability mechanism. Philander (1978) has carried out stability studies, and has come to the conclusion that this is indeed the case. The generation of these waves is also proceeded by the passage of a Rossby wave through the region. The Rossby wave may be having a destabilising effect on the current shear, thus initiating the instability. Recent results by Allen et al (1995) and Lawrence at al (1997) suggest that the instability waves may be phase locked to remotely forced Rossby waves, highlighting the importance of these waves.

7.7 Summary

Kelvin, Rossby, and tropical instability waves have been identified in TOPEX/Poseidon SLA data, and their propagation characteristics have been assessed. TOPEX/Poseidon provides an excellent tool for the study of such waves. The results obtained seem to improve upon previous studies of the waves made using other instruments. The altimeter allows a much wider and more spatially detailed study than would be possible using in situ techniques, and allows a dynamic description of the Pacific to be created. The period of data studied is unusual in that there was a persistant El Niño throughout 1992-1995, with no reversion to La Niña conditions.

These special circumstances have been fortuitous in providing many examples of Kelvin and Rossby wave activity, and are not typical.

A possible example of western boundary reflection has been described. Evidence for an eastern boundary Kelvin wave reflection has been given, and this result, which is contrary to previous studies, may have important implications for the further investigation of the El Niño phenomenon.

The results imply that neither the slow SST mode hypothesis nor the delayed action oscillator hypothesis are the definitive model for the equatorial Pacific. Features characteristic of both mechanisms have been observed in this study. It is concluded that both mechanisms are possible, the dominant mechanism at any one time depending on local ocean/atmosphere conditions.

A more thorough set of conclusions based on the dynamic description of the Pacific is difficult using the TOPEX/Poseidon altimeter alone, and a combination of accurate in situ wind data with TOPEX/Poseidon SLA data would be required.

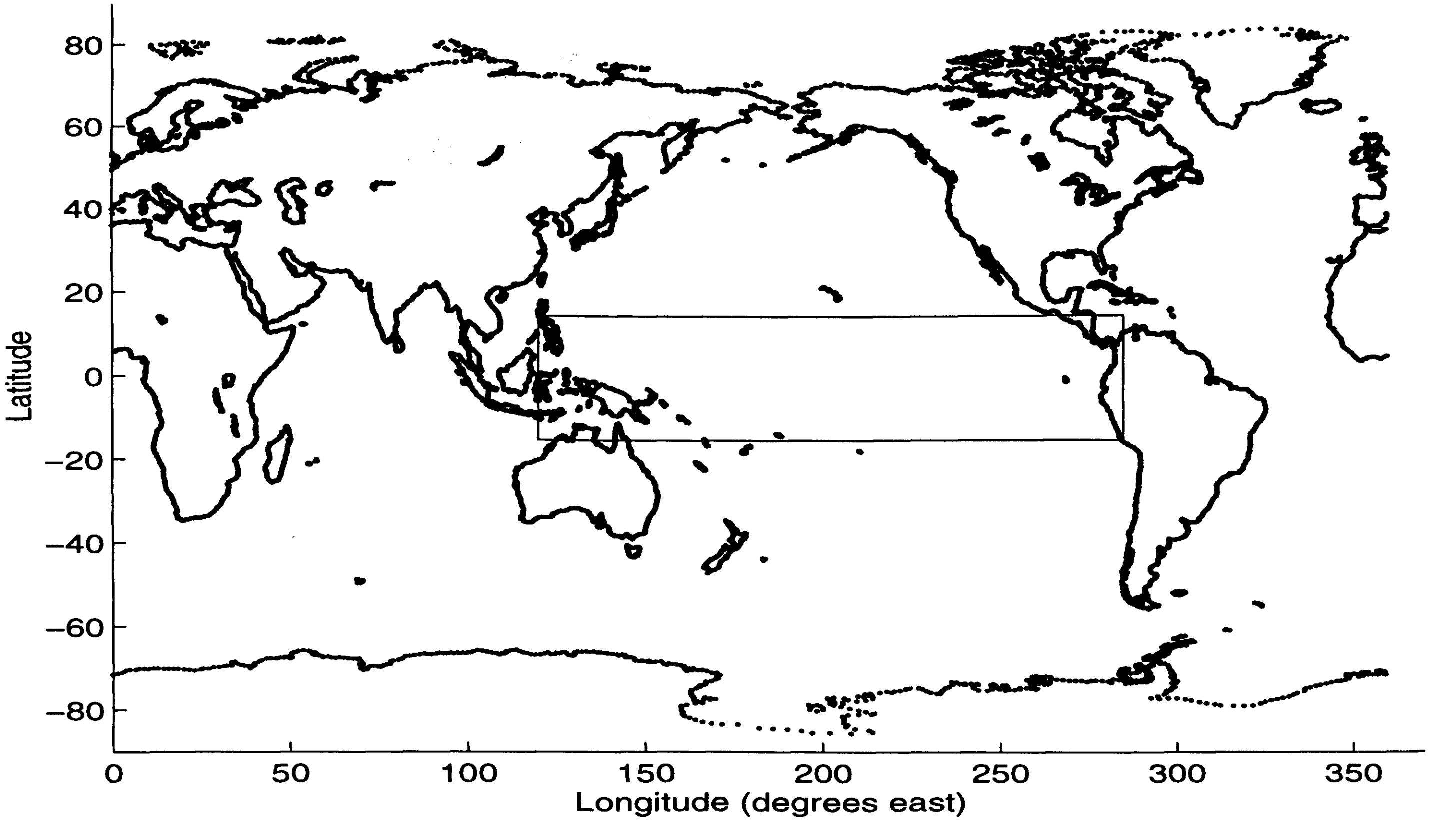

Figure 1: Schematic of the Pacific region under study (indicated by box)

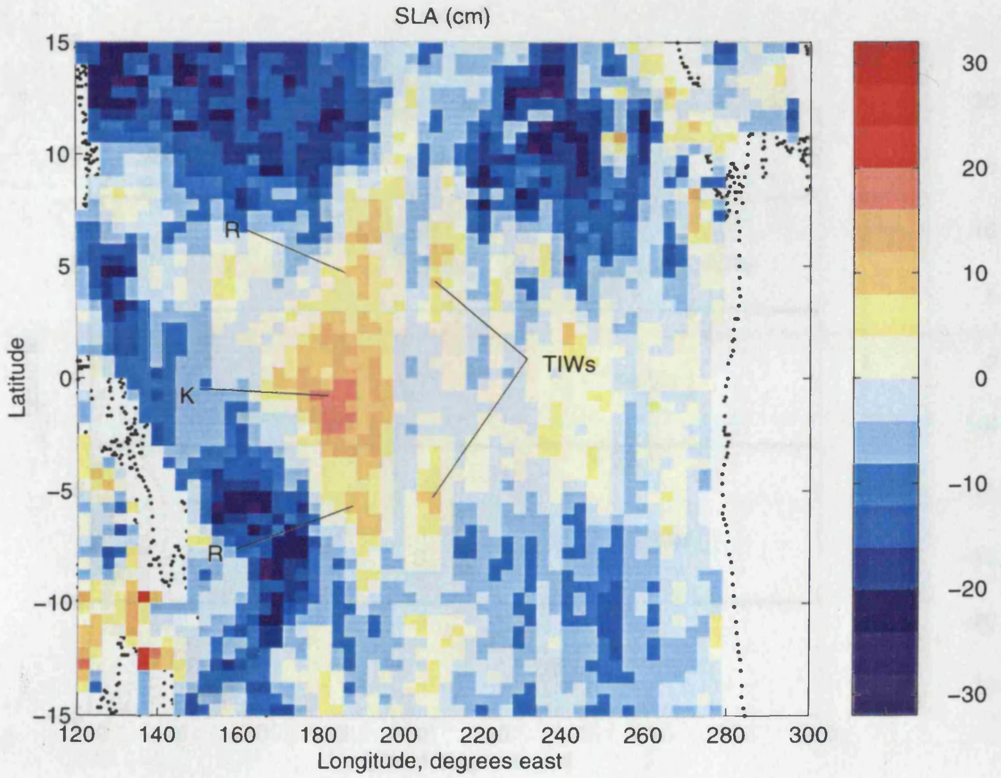

Figure 2: Spatial plot of SLA for cycle 11. Kelvin, Rossby and TIW signatures are indicated on the plot.

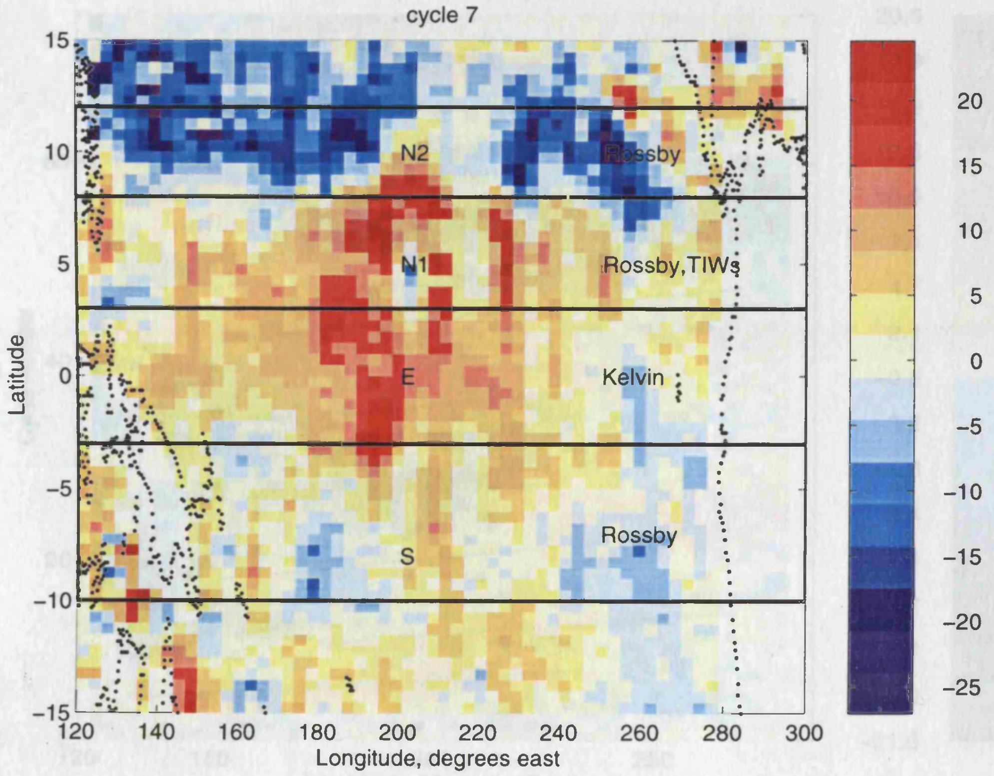

Figure 3: The SLA (cm) spatial plot for cycle 7. The N2, N1, E and S bands of variability are marked, with the main features to be found in each band indicated.

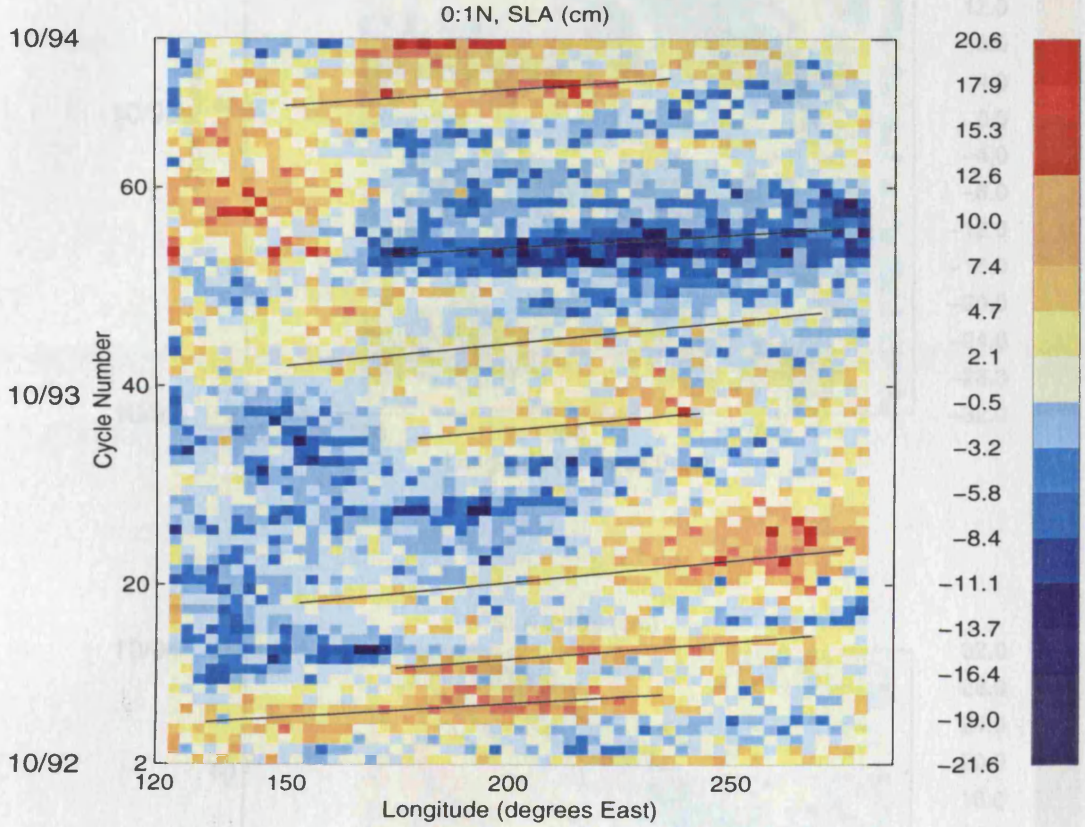

Figure 4: The time-longitude plot for the equatorial region 0° - 1°N (E band). Positive gradient black lines indicate downwelling (red) and upwelling (blue) Kelvin waves.

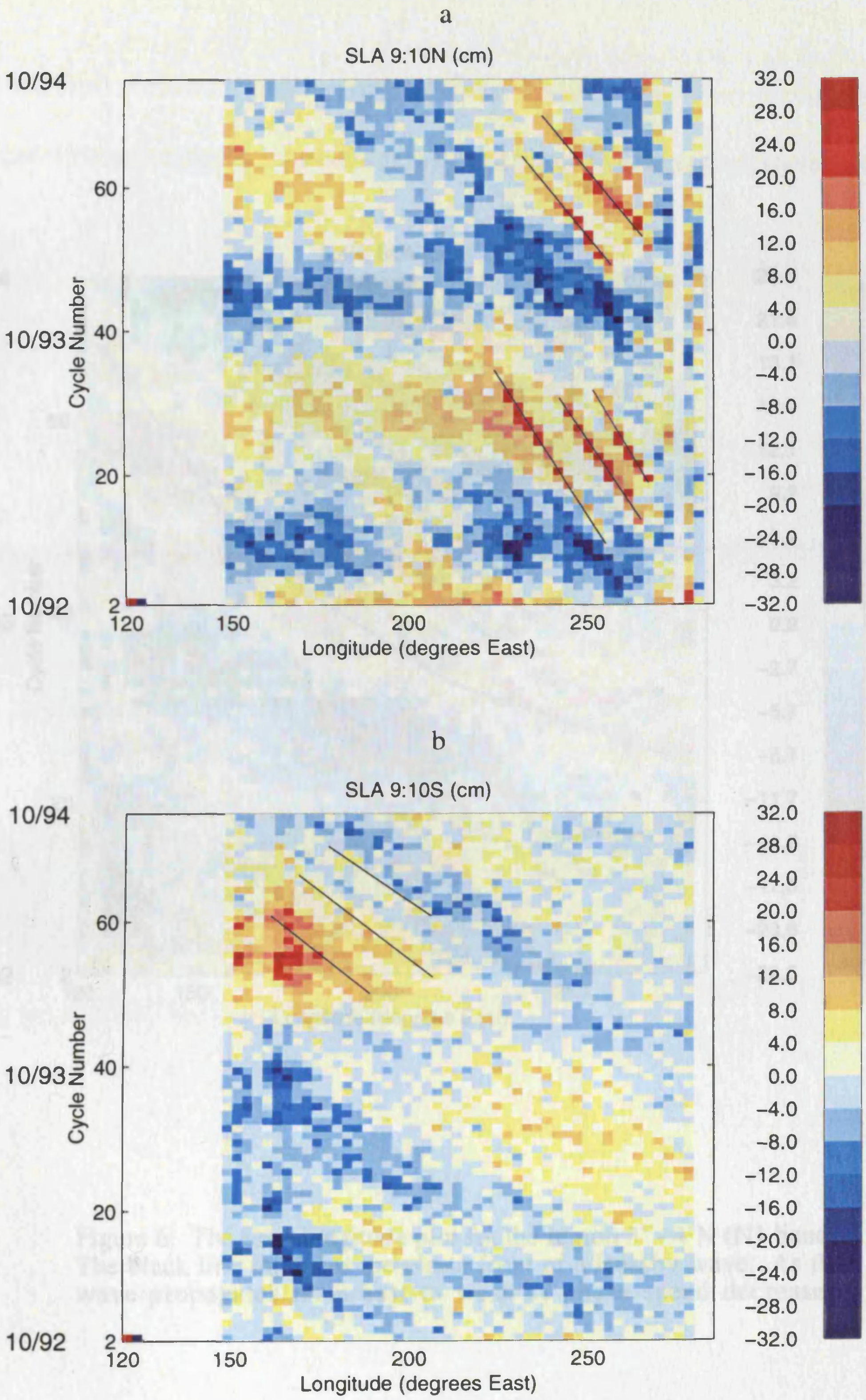

Figure 5: The time-longitude plots for a) 9°N-10°N (N2 band and b) 9°S-10°S (S band). Downwelling Rossby waves are indicated by black lines.

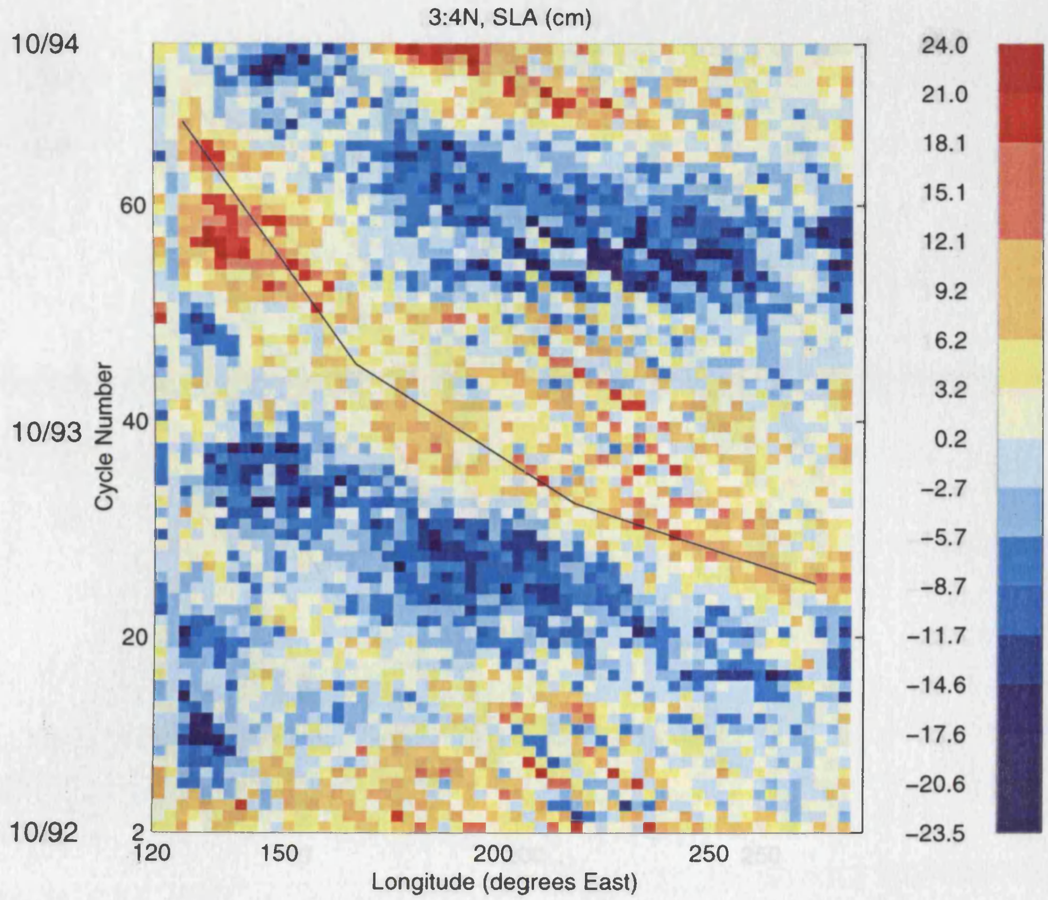

Figure 6: The time-longitude plot for the region 3° - 4°N (N1 band). The black line indicates the phase front of a Rossby wave. As the wave propagates from east to west its phase speed decreases.

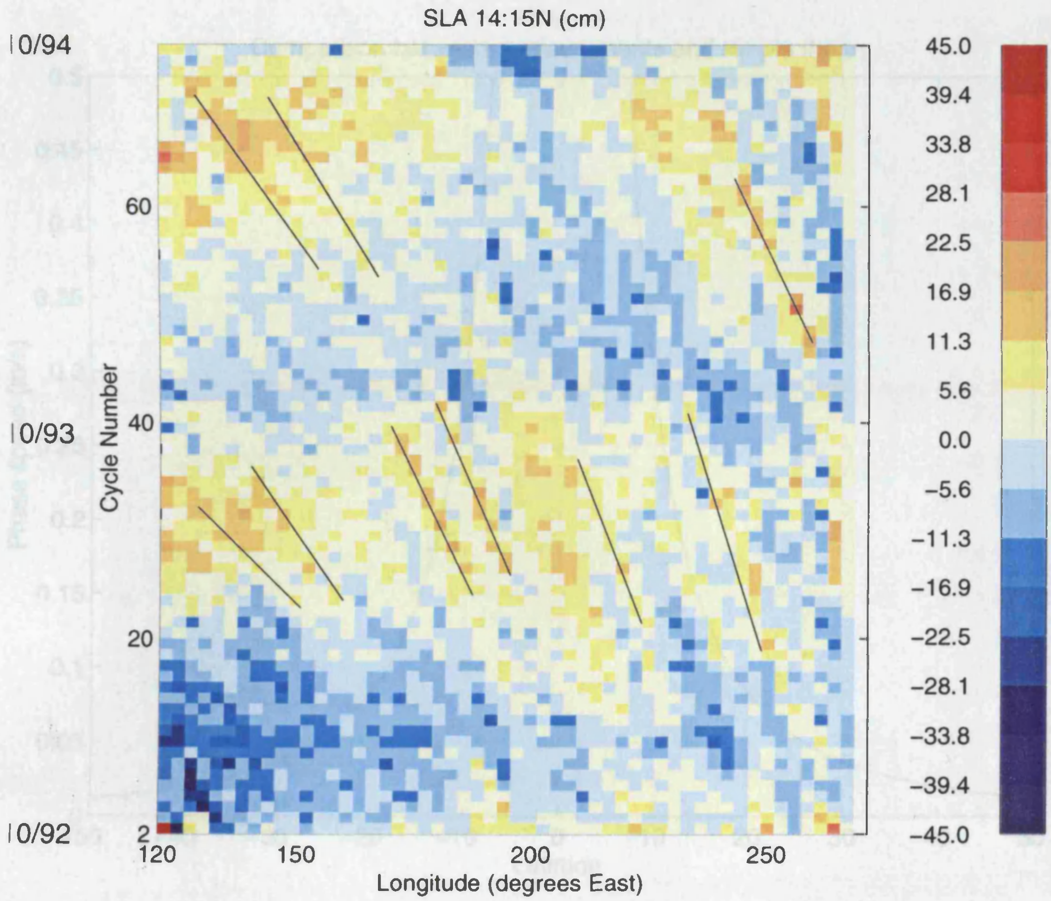

Figure 7: The time-longitude plot for 14°N-15°N (N2 band). Rossby waves are indicated by the black lines. The Rossby wave phase speed increases from east to west at this latitude.

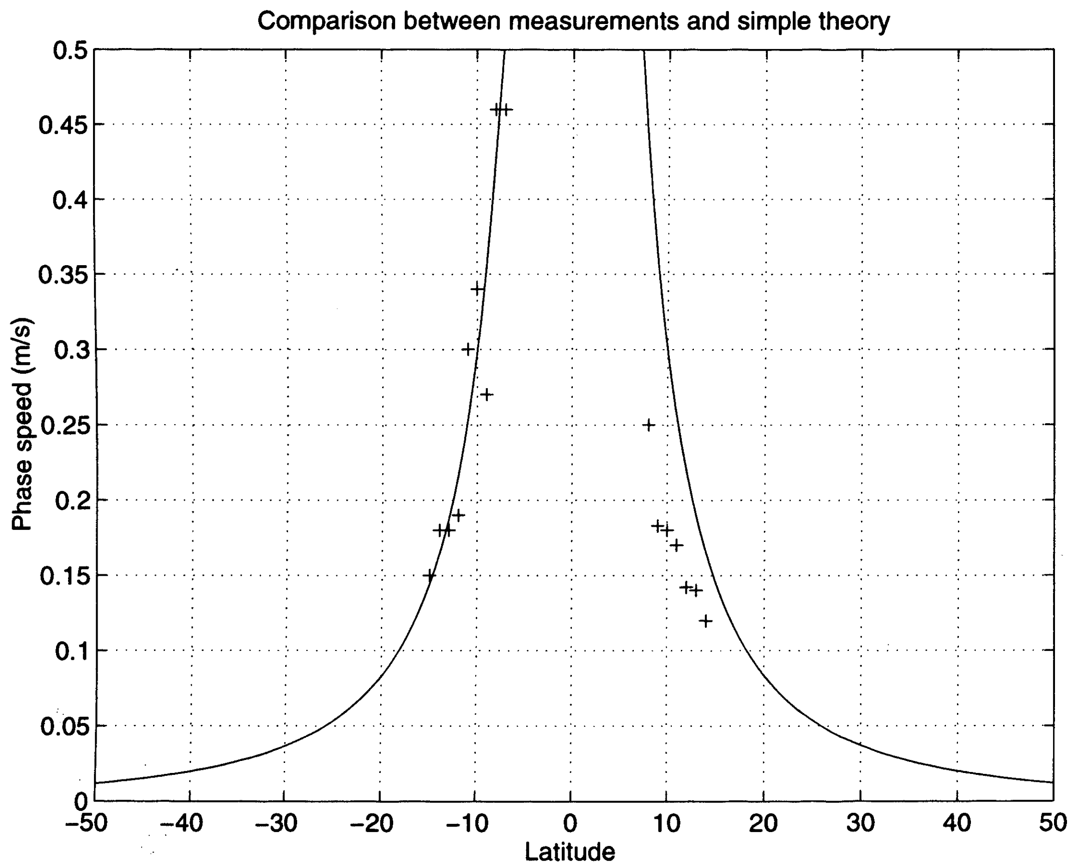

Figure 8: The comparison of Rossby wave phase speeds, measured by Topex/Poseidon (+'s), and a simple model (solid line).

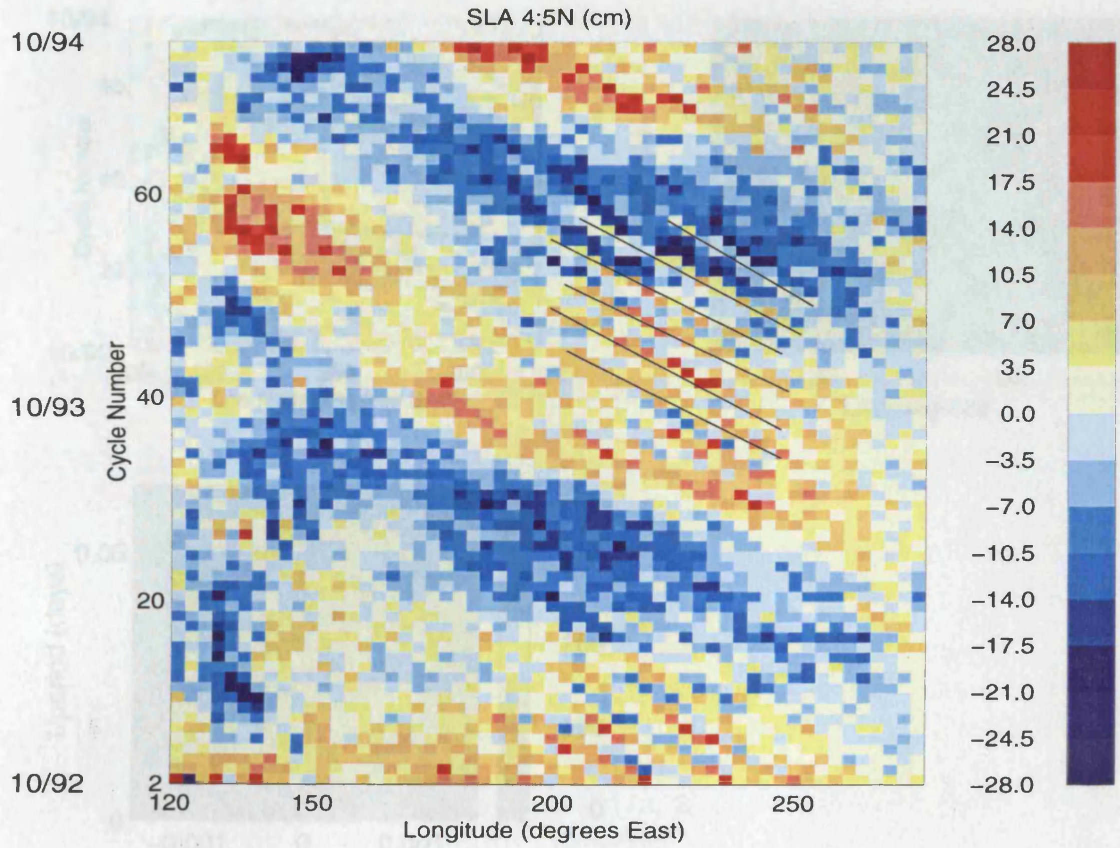

Figure 9: The time-longitude plot for 4°N - 5°N (N1band). A group of tropical instability waves is marked by black lines.

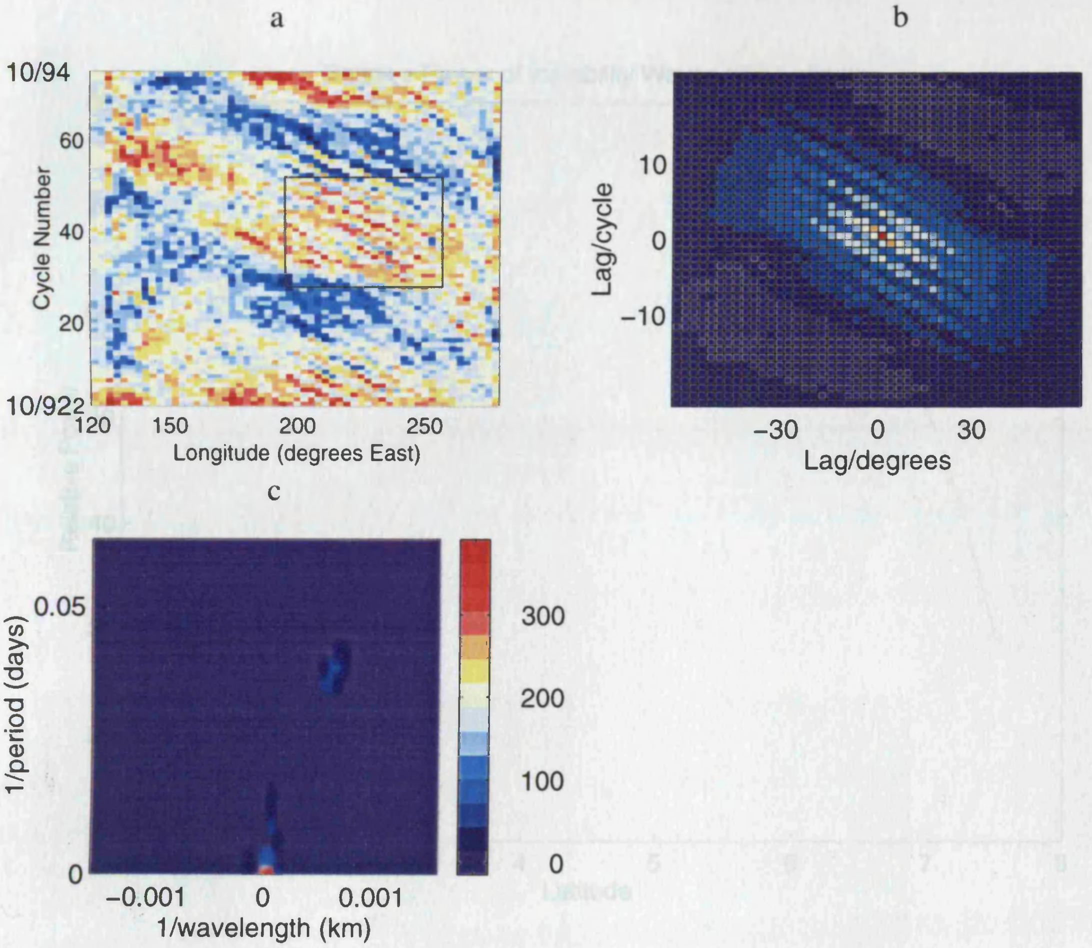

Figure 10: The steps involved in FFT analysis of the TIWs. a) An appropriate area is selected from a time-longitude plot b)the data is then autocorrelated, and finally c) the 2-dimensional (spatial and temporal) FFT is calculated.

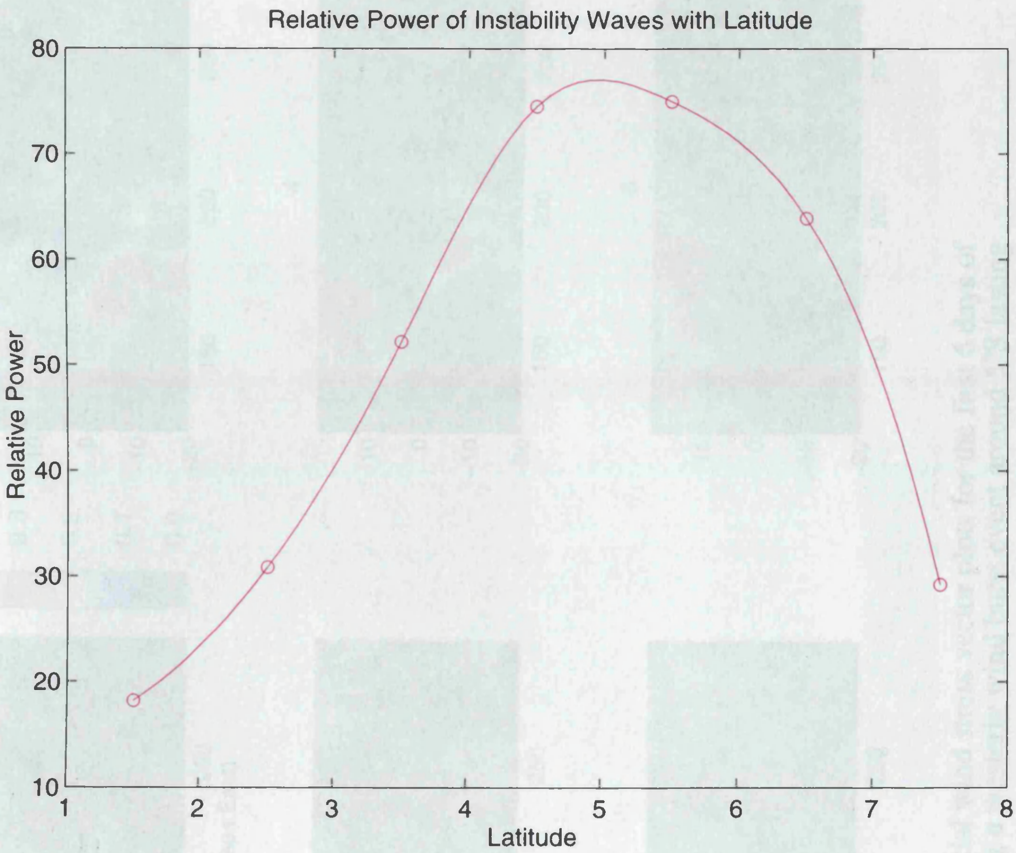

Figure 11: The relative power of tropical instability waves with latitude. The data is fitted by cubic spline interpolation, the peak in power lying just below 5°N

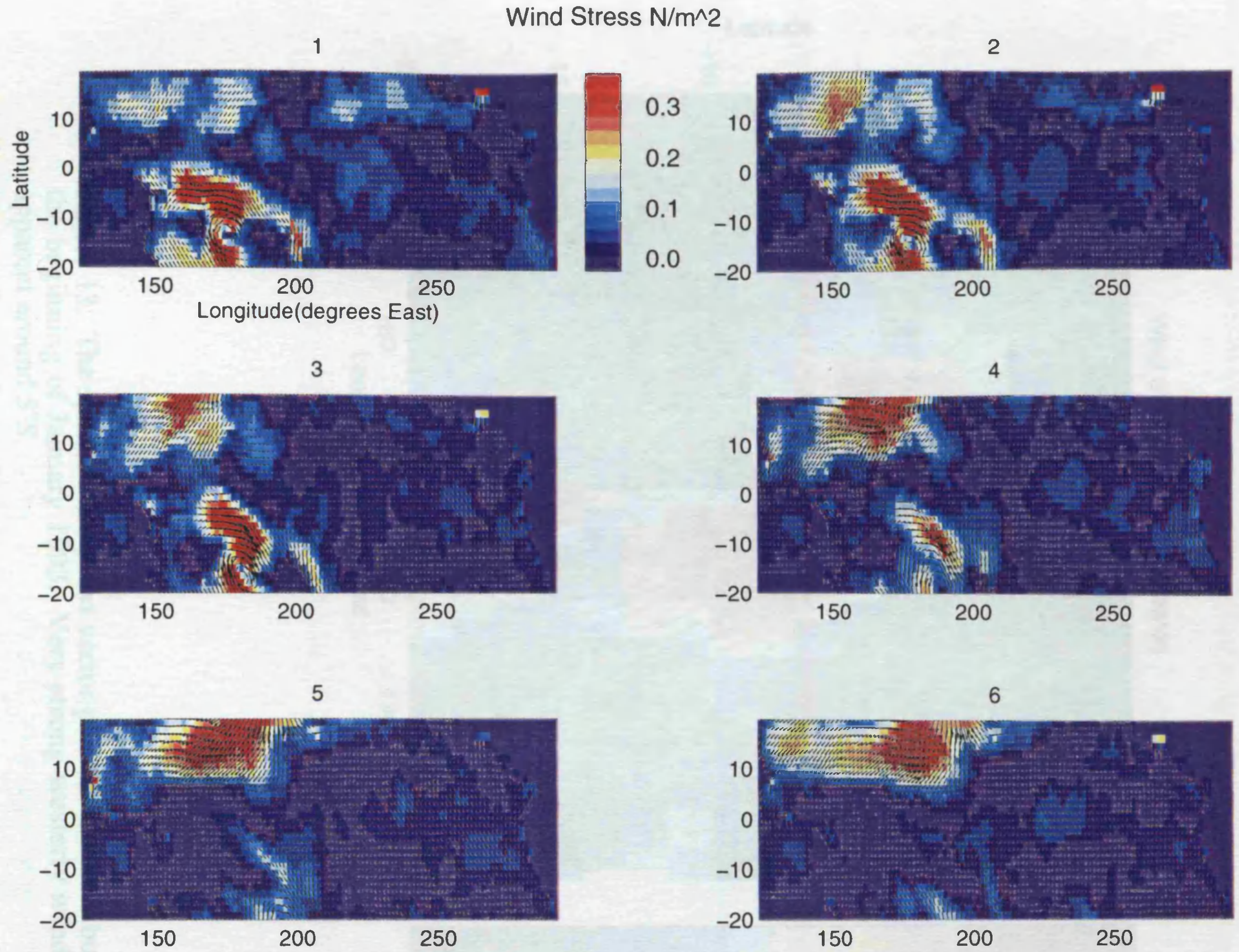

Figure 12: Spatial wind stress vector plots for the first 6 days of 1993, indicating a westerly wind burst event around 5°S lasting until day 5.

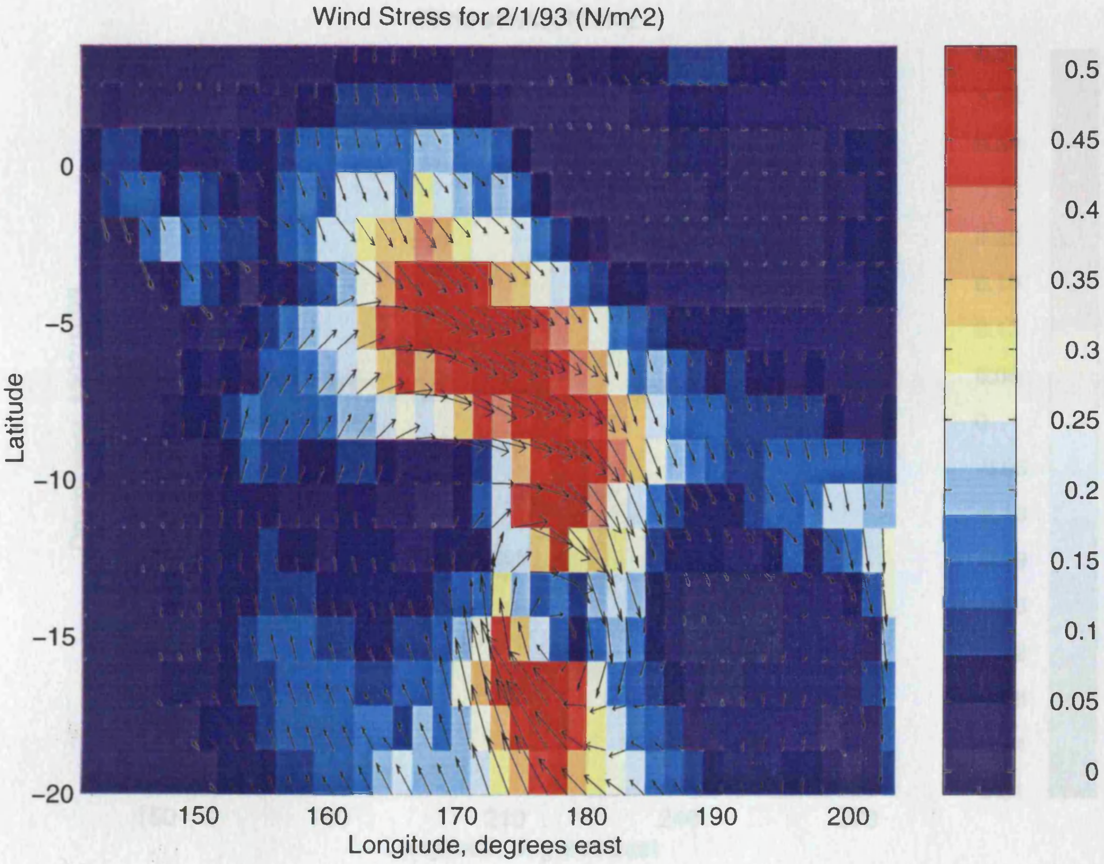

Figure 13: The spatial wind stress vector plot for the wind burst at the beginning of January 1993. Very strong westerly winds are apparent around 5°S.

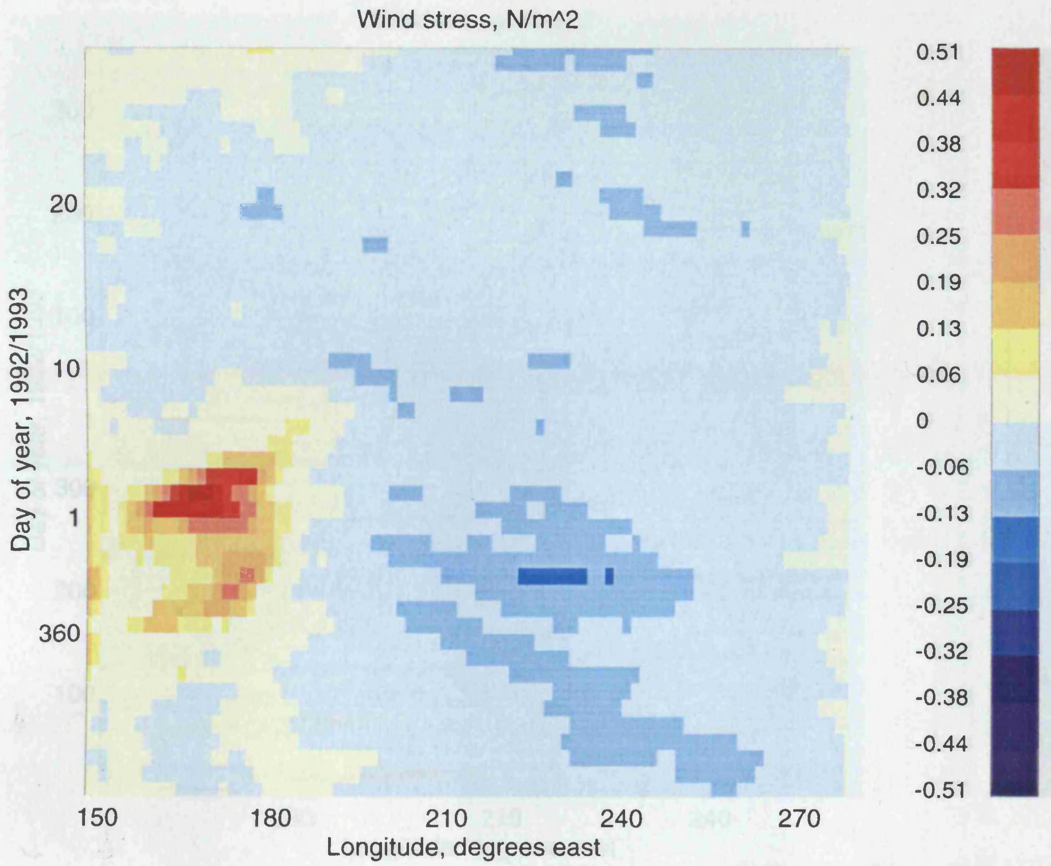

Figure 14: A time-longitude plot for the zonal wind stress at the end of 1992/beginning of 1993(averaged over latitude range 2S : 2N). Red colours indicate westerly wind stress, blue colours easterly wind stress.

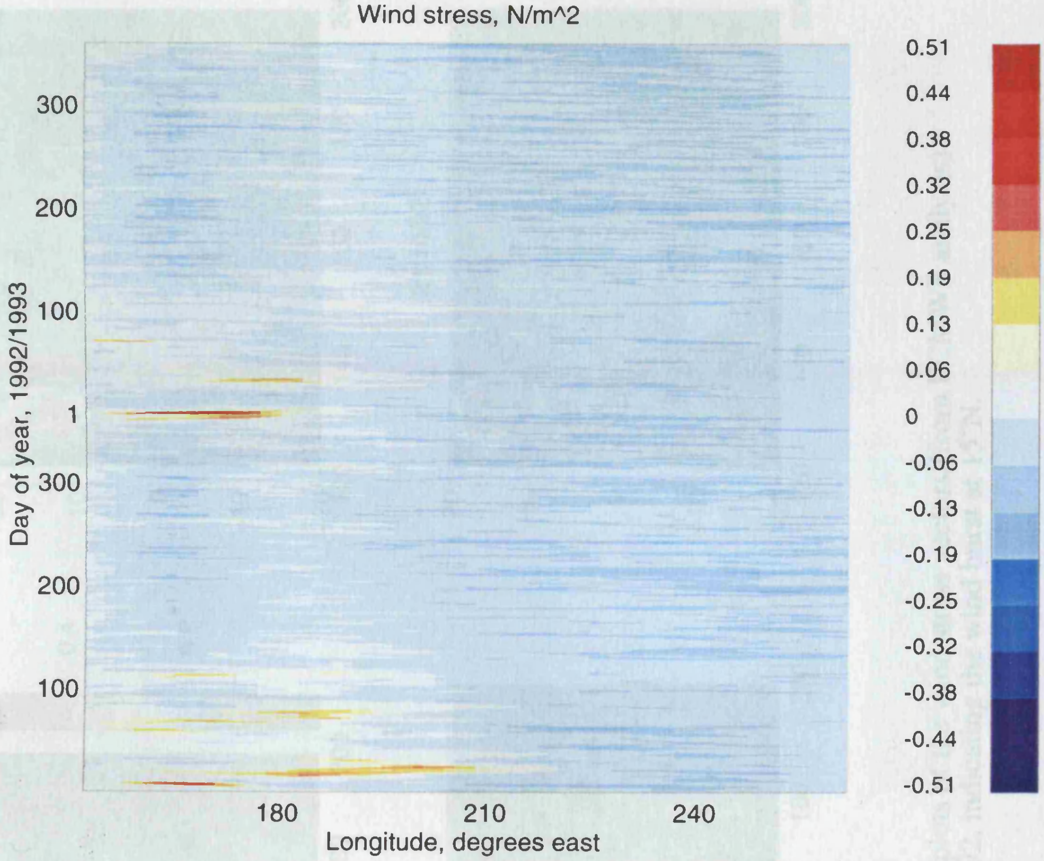

Figure 15: Time-longitude plot of zonal wind stress at 4°S. Red indicates a westerly wind stress, blue indicates an easterly wind stress.

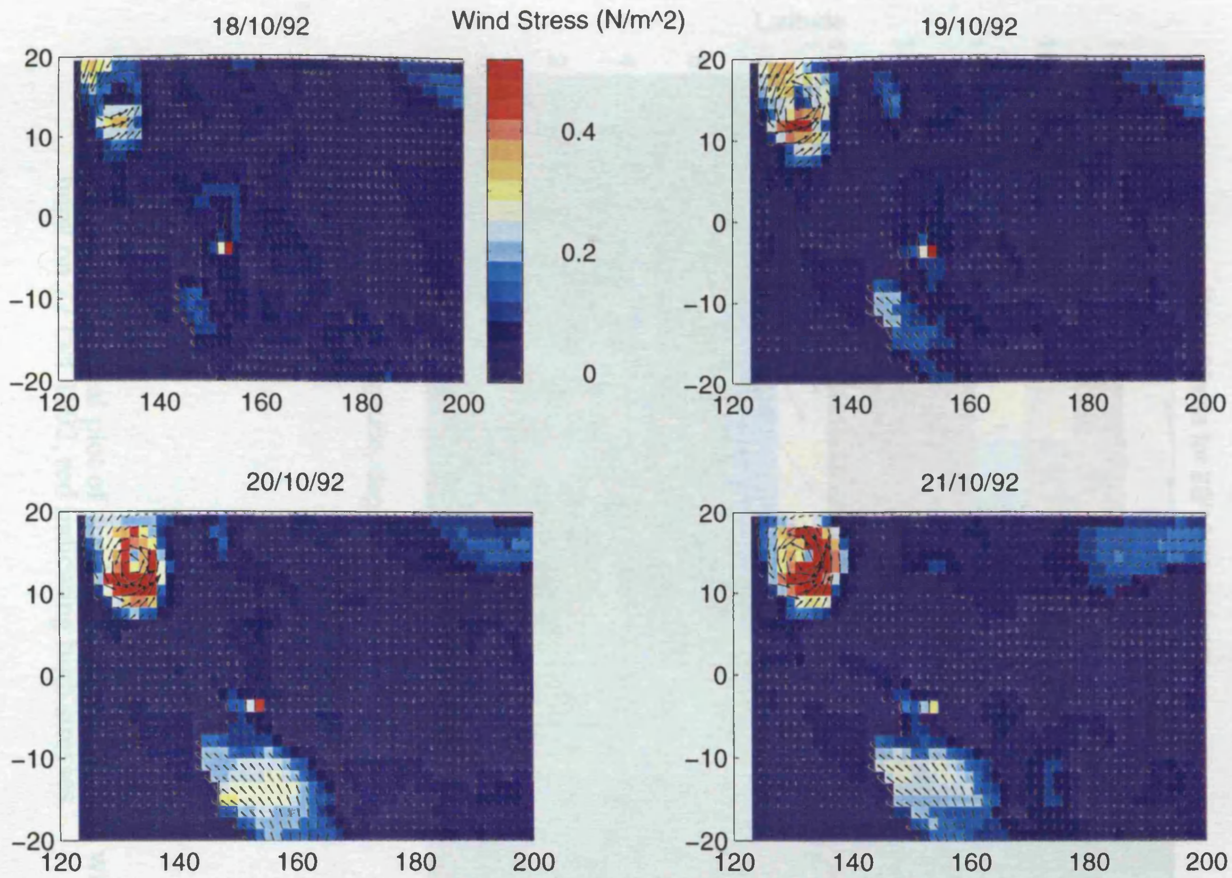

Figure 16: Spatial plots of the wind stress vectors (from ECMWF analysis) for 18 - 21 Oct 1992, indicating the wind burst at 15°N.

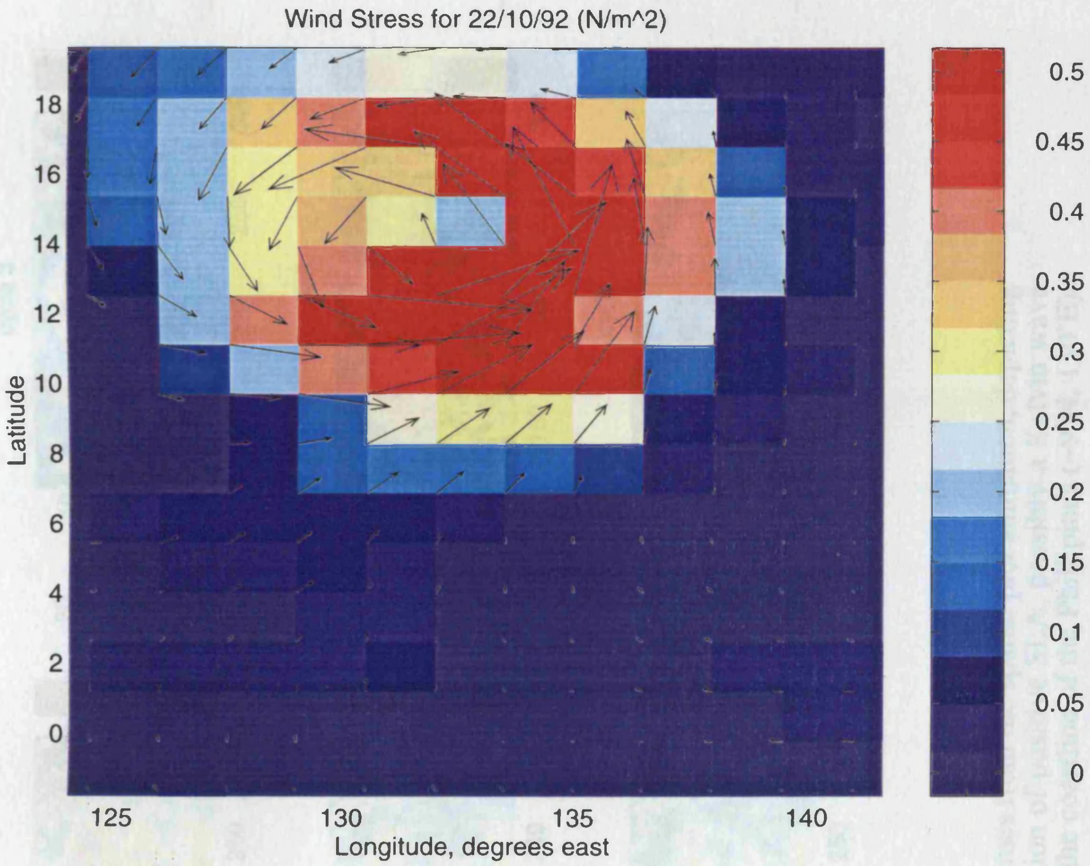

Figure 17: Spatial plot of wind stress vectors for the wind burst on 22 Oct 1992, red indicating high stresses.

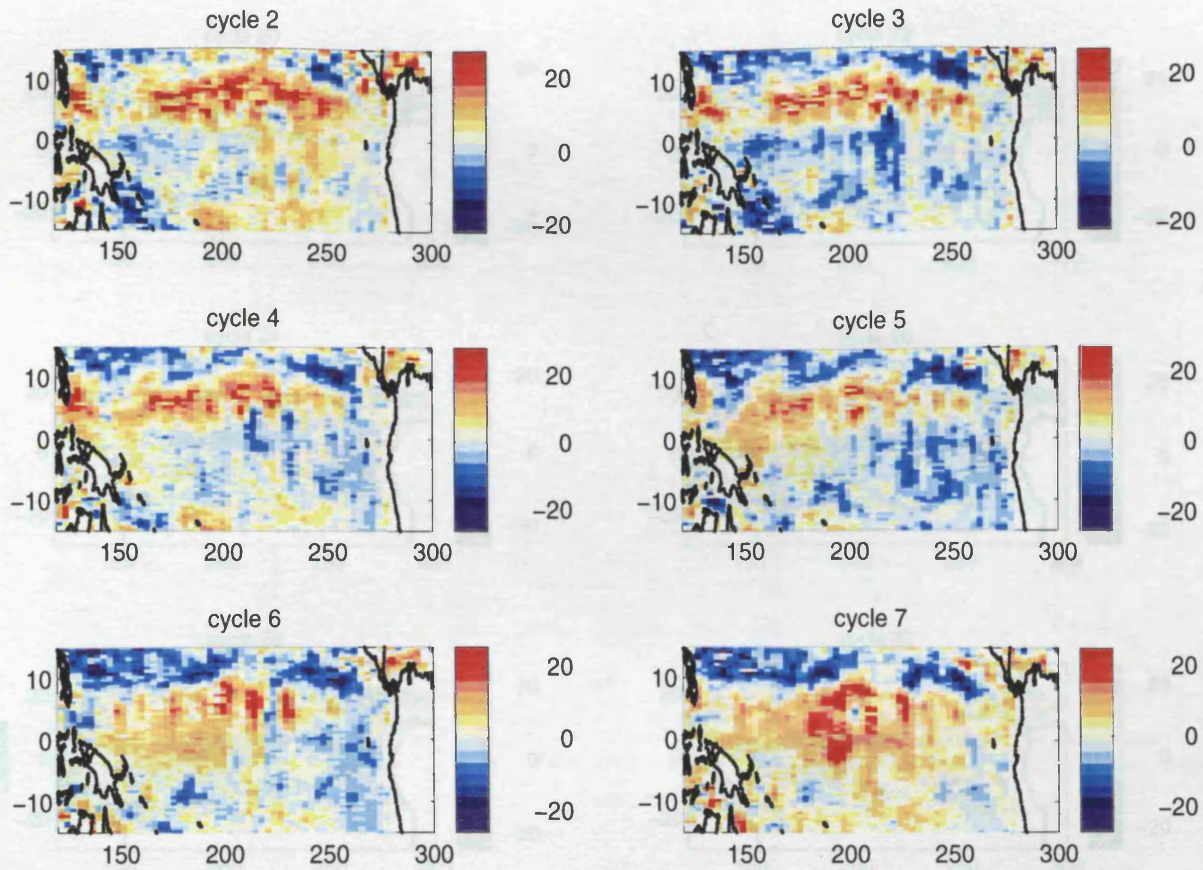

Figure 18: Six frames from the spatial plot animation, depicting cycles 2-7. A region of positive SLA, possibly a Kelvin wave is apparent along the coastline of the Phillipines (~9°N, 130°E).

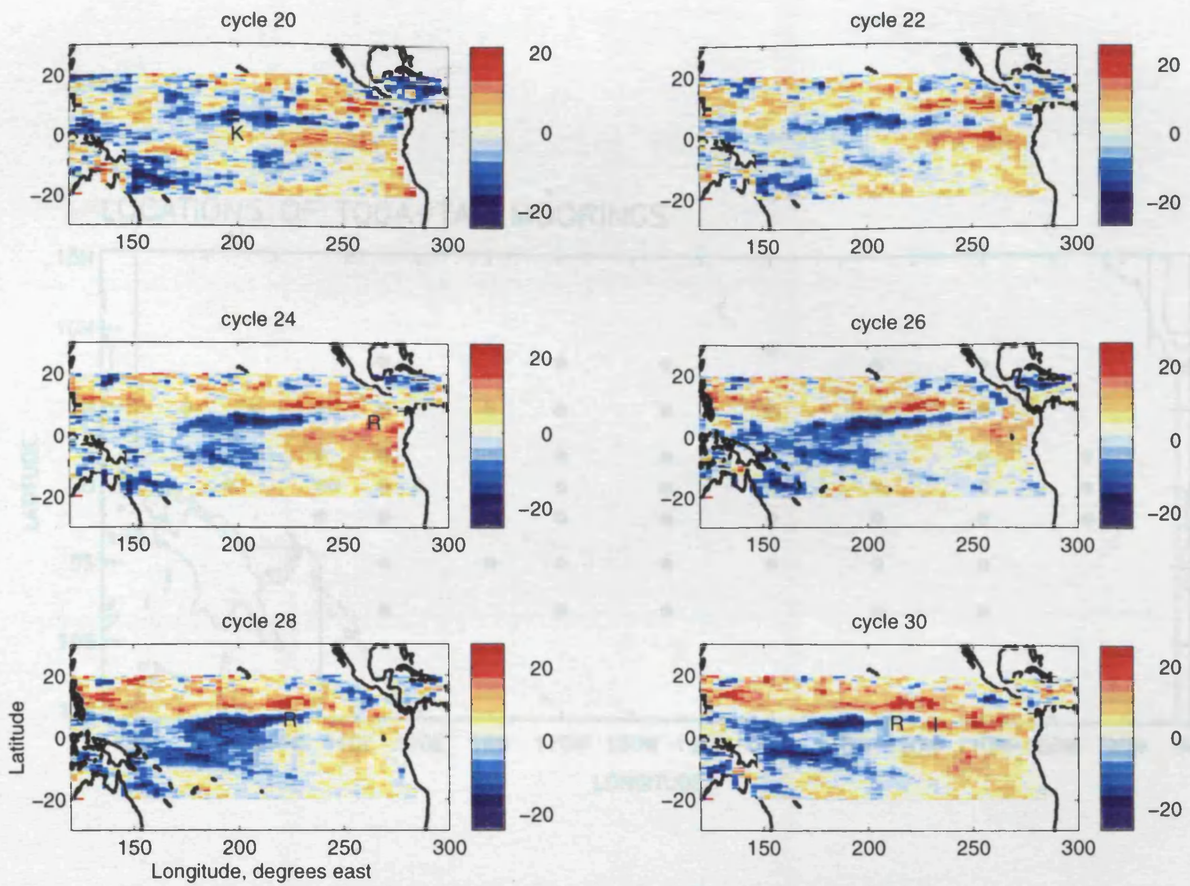

Figure 19: Six frames from the spatial plot animation, depicting the reflection of a Kelvin wave at the eastern boundary during cycles 20 to 30. Kelvin waves are indicated on cycle 20, Rossby waves on cycle 28, and TIWs on cycle 30.

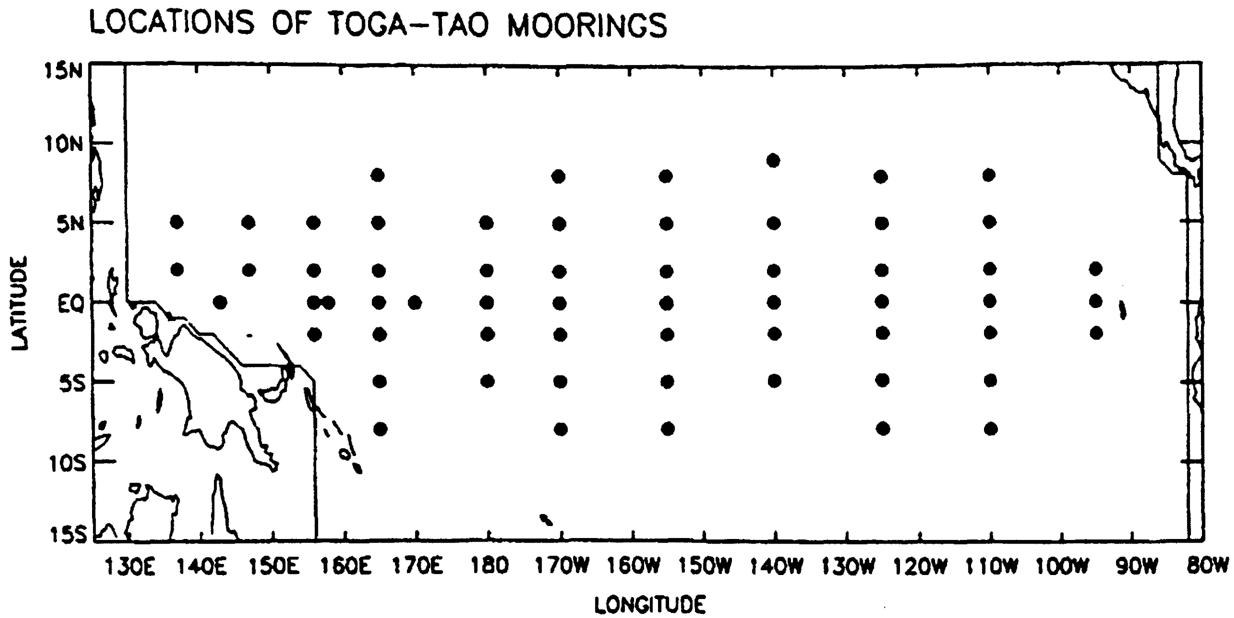

Figure 20: The Tropical Ocean and Global Atmosphere-Tropical Atmosphere Ocean (TOGA-TAO) array. (From Boulanger and Menkes, 1995).

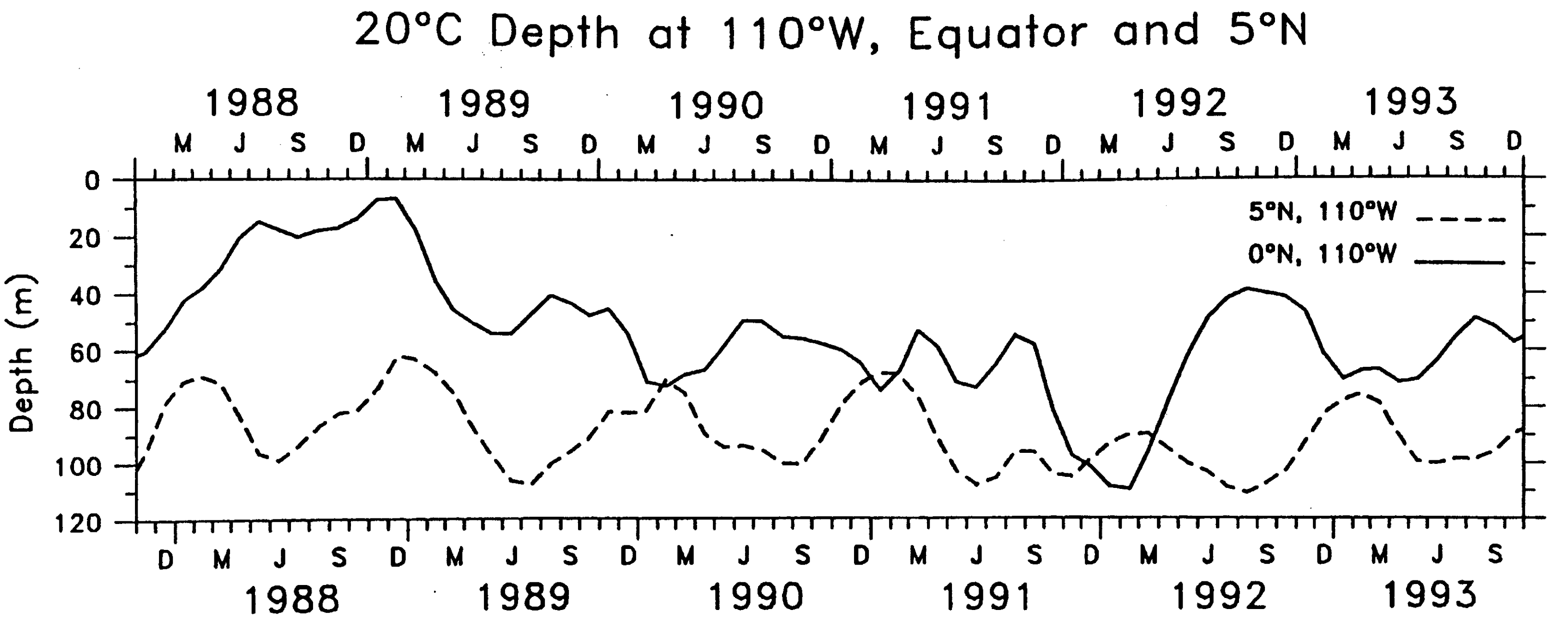

Figure 21: 20˚C depth at longitude 110˚W, and latitudes 0˚ and 5˚N. The solid line represents Kelvin wave activity, the dashed line Rossby wave activity (equatorial time series lagged 2 months to account for wave propagation)

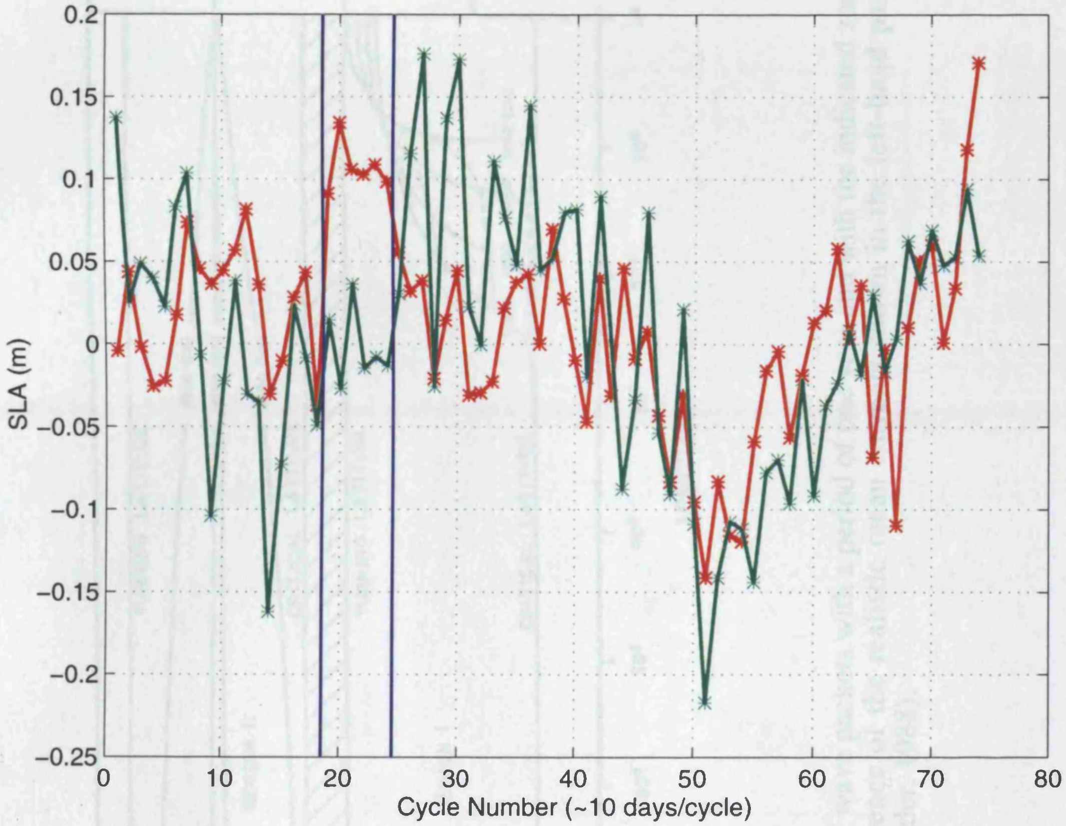

Figure 22: SLA time series for the longitude 250°E, and latitudes 0° N (red line) and 5°N (green line). There is a time lag of 2 months between the first appearance of the Kelvin wave and the Rossby wave response (indicated by the first and second vertical blue lines, respectively), consistent with an eastern boundary reflection.

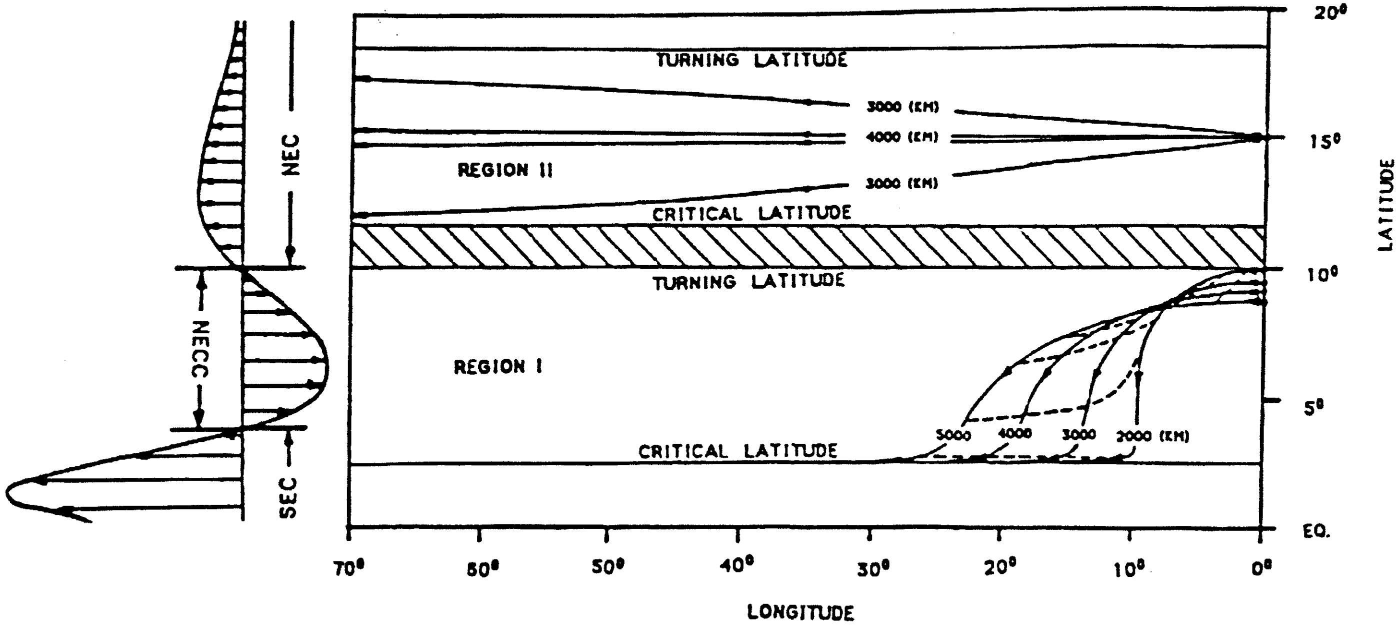

Figure 23: Ray paths of wave packets with a period of one year and with the indicated zonal wavelength in the presence of the realistic mean currents shown in the left-hand panel (from Chang and Philander, 1988).

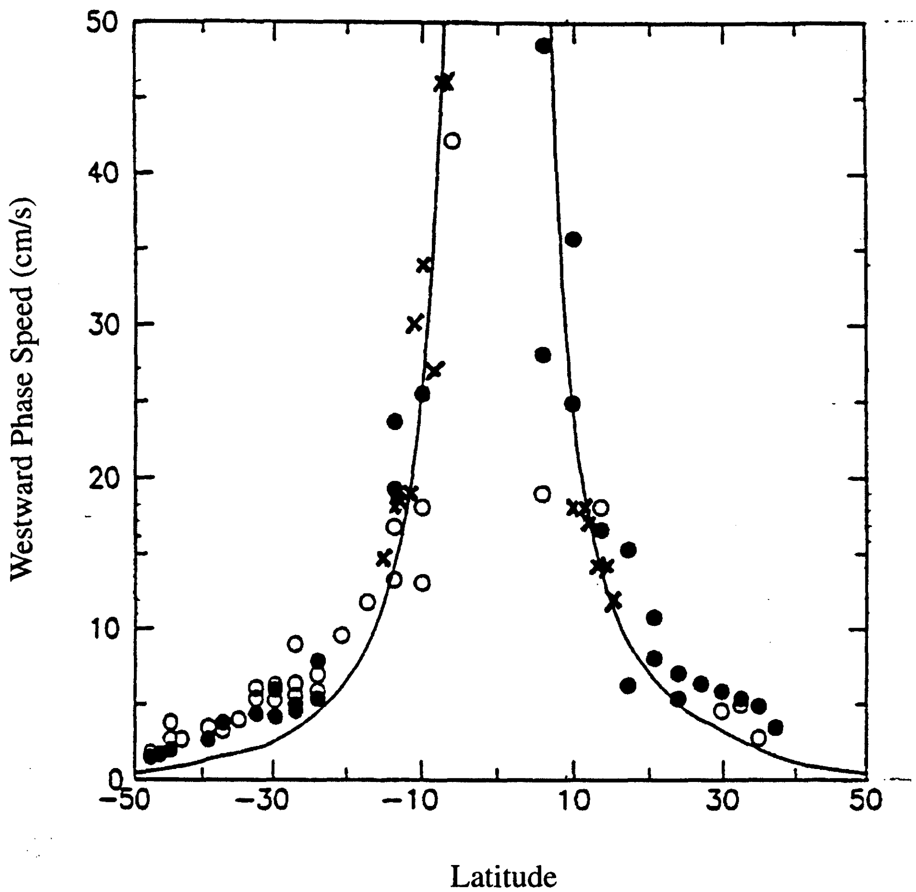

Figure 24: Comparison between the present study Rossby wave phase speeds (crosses), Chelton and Schlax (1996) phase speeds (circles), and linear theory (solid line) (after Chelton and Schlax, 1996).

Type of Wave	Initiation Cycle and Longitude	Termination Cycle and Longitude	Approximate Spatial Width (km, degrees longitude at equator)	Phase Speed (m/s)
Downwelling	3, 120E	10, 250E	10000, 90	2.90 ± 0.40
Downwelling	11, 170E	15, 280E	4500, 40	3.10 ± 0.30
Downwelling	19, 200E	28, 280E	7500, 70	2.70 ± 0.50
Upwelling	25, 120E	29, 205E	4000, 35	3.60 ± 0.20

Table 1: Kelvin wave propagation charateristics

Latitude Range	Amplitude (cm ±5cm)	Spatial Width (km)	Phase Speed (m/s)
14:15N	15	1000	0.12 ± 0.03
13:14N	25	1000	0.13 ± 0.03
12:13N	25	600	0.13 ± 0.03
11:12N	25	600	0.18 ± 0.03
10:11N	30	600	0.17 ± 0.03
9:10N	25	600	0.16 ± 0.03
8:9N	25	1000	0.22 ± 0.03
5:6S	15	2000	0.81 ± 0.20
6:7S	15	2000	0.51 ± 0.15
7:8S	10	-	0.36 ± 0.03
8:9S	8	-	0.34 ± 0.03
10:11S	8	2000	0.31 ± 0.03
11:12S	20	1200	0.22 ± 0.03
13:14S	15	1200	0.14 ± 0.03
14:15S	10	-	0.15 ± 0.03

Table 2: Rossby wave propagation charateristics

Latitude Range	Fourier Technique (± 0.01)	Best Fit Line To Plot (± 0.04)	Best Fit Line to Autocorrelation (± 0.02)
1:2N	0.55	0.59	0.57
2:3N	0.60	0.59	0.60
3:4N	0.60	0.58	0.58
4:5N	0.59	0.56	0.55
5:6N	0.59	0.57	0.60
6:7N	0.59	0.55	0.54
7:8N	0.59	0.53	0.60

Table 3: Tropical instability wave phase speeds

Cycle Number	Start Date
2	3/10/92
3	12/10/92
4	22/10/92
5	1/11/92
6	11/11/92
7	21/11/92
8	1/12/92
9	11/12/92
10	21/12/92
11	31/12/92
12	10/1/93
13	20/1/93
14	29/1/93
15	8/2/93
16	18/2/93
17	28/2/93
18	10/3/93
19	20/3/93
20	30/3/93
21	9/4/93
22	19/4/93
23	29/4/93
24	9/5/93
25	18/5/93
26	28/5/93
27	7/6/93
28	17/6/93
29	27/6/93
30	7/7/93
31	17/7/93
32	27/7/93
33	6/8/93
34	16/8/93
35	26/8/93
36	4/9/93
37	14/9/93
38	24/9/93
39	4/10/93
40	14/10/93
41	24/10/93
42	3/11/93
43	13/11/93
44	23/11/93
45	3/12/93
46	13/12/93
47	22/12/93
48	1/1/94
49	11/1/94
50	21/1/94

Cycle Number	Start date
51	31/1/94
52	10/2/94
53	20/2/94
54	2/3/94
55	12/3/94
56	22/3/94
57	1/4/94
58	10/4/94
59	20/4/94
60	30/4/94
61	10/5/94
62	20/5/94
63	30/5/94
64	9/6/94
65	19/6/94
66	29/6/94
67	9/7/94
68	19/7/94
69	28/7/94
70	7/8/94
71	17/8/94
72	27/8/94
73	6/9/94
74	16/9/94
75	26/9/94

Table 4: Topex/Poseidon cycle starting dates

Chapter 8: Conclusions and Future Work

This chapter aims to summarise and evaluate the work presented in the previous chapters, and to make suggestions for future work on these topics.

8.1 Overview

This thesis has utilised the TOPEX/Poseidon mission for both ionospheric and oceanic studies. Whilst at first appearing two quite distinct topics, the method of satellite radar altimetry knits the subjects together through concerns about accuracy - the ocean height could not be measured with any confidence without considering the delay on the radar pulse imposed by the ionosphere, and also through the similarity in the global extent of the key phenomena e.g. the equatorial features of both ionosphere and oceans (see Chapter 1).

Whilst the TOPEX mission relies on its dual frequency altimeter to correct for this delay, the Poseidon mission has to rely on either the Bent model or DORIS corrections. The Bent model has very similar limitations to the IRI, and the DORIS system accuracy is reduced over the Pacific Ocean region especially, due to a lack of ground receiving stations (AVISO, 1995). The TOPEX mission hence provides, in addition to its oceanographic mission, very important IEC data for the evaluation of existing empirical ionospheric models, as well as for the study of the ionosphere itself. As previously noted, the TOPEX mission is unique in being the only satellite borne dual frequency radar altimeter system. All other altimetry missions to date (e.g. Geosat, ERS-1, ERS-2) have to rely on empirical models to allow for the pulse delay due to the ionosphere. These empirical models are not perfect, and have been shown to be in considerable error, especially near high latitudes and the equatorial region (Beard and Robinson, 1994).

This work has utilised the unprecedented accuracy of TOPEX/Poseidon's oceanographic data to study the equatorial Pacific Ocean dynamics, and has also used the TOPEX mission's measurements of the ionospheric electron content with the aim of improving current empirical and adaptive models.

8.2 The Ionospheric Study

8.2.1 Integrated Electron Content Coherence (IEC)

The first ever quasi-global maps of coherence distance of the offset between measurements and mean model values of IEC are achievable using TOPEX data. The maps are very important to the implementation of adaptive models, describing the spatial scale over which data may be assimilated into the model. The offset coherence distance maps must be used in conjunction with ground based studies of temporal coherence distance in order to construct the space-time cell necessary for adaptive modelling. The maps also provide a new insight into the structure and variability of the ionosphere.

The maps exhibit a large well defined variation in spatial coherence distance with latitude and local time. This pattern of coherence has previously been unobservable due to the lack of a global data set. The results of the present study compare well with previous ground based techniques.

The important solar control of the ionosphere is apparent from the maps, with seasonal and diurnal structure a major feature. The role of upper atmosphere electrodynamics is well presented, also, with the equatorial fountain effect imposing its characteristic features onto the maps. They provide a detailed insight into the variability of the ionospheric electron content, which might well be extrapolated in suitable conditions to the F region critical frequency, *fo*F2. The maps have also revealed possible mid-latitude trough effects, a feature previously unobserved in terms of coherence distance, as well as a couple of unexplained features, again previously unobserved.

These maps will help lead to an improvement in current semi-empirical models by providing a means of producing adaptive models. As mentioned, the temporal coherence scale must be obtained from ground based studies at present, although a method of obtaining this parameter from dual frequency altimeter data should not be ruled out. More reliable models would provide an increase in the accuracy of sea surface height measurements made by single frequency altimeters.

8.2.2 Kp Dependence of Integrated Electron Content

The offset between TOPEX measurements of IEC and the monthly mean predictions produced by the IRI has been demonstrated to be partly dependent on the prevailing level of geomagnetic activity, exhibiting both latitudinal and seasonal structure.

The dependency is greatest in the equinoctial months. In the northern hemisphere the dependency is very low in both summer and winter, whereas in the southern hemisphere the dependency is negative for winter whilst positive for summer.

The dependency may be split into two regimes, a low-Kp dependency (Kp $\leq$ 5) and a high-Kp dependency (Kp > 5), which both exhibit latitudinal and seasonal structure. The low-Kp dependency switches from a negative dependence at high latitudes to a positive one at low latitudes. This shift in dependency may well have been missed or unobservable from ground based stations, again demonstrating the importance of the TOPEX ionospheric data.

Unfortunately predicting the ionospheric response to a geomagnetic storm is not a simple task. The response will consist of many mechanisms, both positive and negative, some of which have been discussed. Due to the superposition of these mechanisms, it is not possible to quantitatively examine their effect on the dependencies of the IEC offset on Kp, observed in the TOPEX data. However these dependencies appear significant, and as such could be used in future ionospheric models to allow for the geomagnetic effect on the IEC.

8.3 Study of the Equatorial Pacific Ocean Dynamics

Prior to satellite radar altimetry, in-situ instrumentation was the only method for collecting data on large scale wave activity. These in-situ methods were not able to resolve the waves very satisfactorily, due to the small amplitudes and large wavelengths involved.

The TOPEX/Poseidon sea level anomaly data has enabled the identification of Kelvin, Rossby and tropical instability waves in the equatorial Pacific Ocean, and also the calculation of their propagation characteristics. TOPEX/Poseidon provides an excellent tool for the study of such waves due to its unprecedented accuracy. The results obtained seem to improve upon previous studies of the waves made using other instruments. The altimeter allows a much wider and more spatially detailed study than would be possible using in situ techniques, and allows a dynamic description of the Pacific to be created.

An example of possible western boundary reflection has been described. Evidence for an eastern boundary Kelvin wave reflection has been given, and this result, which is contrary to previous studies, may have important implications for the further investigation of the El Niño phenomenon. The results imply that neither the slow SST mode hypothesis nor the delayed action oscillator hypothesis are the definitive model for the equatorial Pacific. Features characteristic of both mechanisms have been observed in this study. It is concluded that both mechanisms are possible, the dominant mechanism at any one time depending on local ocean/atmosphere conditions.

8.4 Future Work

TOPEX/Poseidon has presented, and continues to present, a very valuable data source for the study of not only the oceans but also the ionosphere as well. However limitations on the data are apparent in each of the areas studied, and a combination of such global data with more localised high time resolution data must be made in order to extract the maximum information from each data set.

8.4.1 Ionospheric Study

An evaluation of an adaptive model utilising the global coherence distance maps produced from TOPEX data is required. It is hoped that such a model would allow the inclusion of empirical data in a way that provides the maximum reduction in residual errors possible. The coherence distance calculated in this study has a direction along track - that is it makes an angle with the equator of around 70°. A technique to split the coherence distance into North-South and East-West components may be possible using the TOPEX data, and further investigation into this possibility should be made.

The adaptation and consequent evaluation of current empirical models to reflect the findings of the global Kp dependence of IEC is required. The inclusion of this study's results would improve the monthly mean behaviour of the IRI in an empirical way. Further work into the theoretical modelling of geomagnetic effects on the ionosphere also needs to be done, and indeed is currently underway under the supervision of the COSPAR and URSI working groups on the IRI (Bilitza, 1996).

On the question of improving the accuracy of the IRI, the requirements are the same as they have been since the IRI was created - that is a wider coverage of data stations for the CCIR maps. The CCIR maps are currently lacking in high latitude data, and the study of the coherence of IEC at high latitudes would require accurate model predictions of the mean conditions. The same complaint remains for southern hemisphere data, in that the majority of stations are based in northern hemisphere, and extrapolation over the southern ocean regions is necessary.

8.4.2 Equatorial Pacific Ocean Dynamics

There is great scope for future work in this field. The precise mechanism for the El Niño phenomenon is not yet understood, and whilst El Niño continues to wreak economic and natural disasters world wide the need for an accurate forecasting service is great.

The role of the tropical instability waves in the system has not been investigated at present, and future work in this field may produce some important implications for Kelvin and Rossby wave energy transferral. Recent work by Allen et al (1995) and Lawrence (1997) have hinted at such an effect, with the suggestion that phase locking between the instability waves and remotely forced Rossby waves may occur. More work is needed to explain the mechanism behind such a phase locking.

The generation mechanisms for Kelvin and Rossby waves also need to be investigated further, since they obviously play a crucial role in the dynamical El Niño system. However, since El Niño has global climatic effects through the ocean-atmosphere system, it is not illogical to recommend that future research should not just concentrate on the Pacific Ocean, but should be extended to include an in-depth study of both the Atlantic and Indian oceans also.

Whilst TOPEX/Poseidon provides an excellent instrument for the study of the ocean dynamics, a much more detailed picture could be built up if the altimeter data were used in conjunction with ground based instruments with higher temporal resolution. More accurate wind data is also required, especially near the eastern boundary, where current wind stress analysis tends to be unreliable.

An important future project can be envisaged whereby TOPEX SLA data utilising the dual frequency ionospheric correction is compared to TOPEX data processed using an empirical model for the ionospheric correction. This would ascertain the importance of the ionospheric error on measurements of currents, and indeed detailed studies of propagating features, in a more quantitative way.

8.5 Concluding Remarks

The research presented in this thesis has covered both the realms of ionospheric science and oceanography. The ionosphere is a crucial factor in the measurement of sea surface height from space, and the importance of correcting for the delay it imposes has been discussed, as has the variability of that delay and the difficulty in modelling it accurately. Results from the TOPEX mission, which utilises a dual frequency system to correct for the delay, have shown a vast improvement over previous altimeter missions, with the identification of dynamical features important to the El Niño phenomenon.

References

Abdu, M.A., Sobral, J.H.A., Depaula, E.R. and Batista, I.S.
Magnetospheric Disturbance Effects on the Equatorial Ionization Anomaly (EIA) - An Overview
JATP, 53, no.8, 757, 1991

Allen, M.R., S.P.Lawrence, M.J.Murray, C.T.Mutlow, T.N.Stickdale, D.T.Llewellyn-Jones, and D.L.T.Anderson
Control of Instability Waves in the Pacific
Geosphy.Res.Lett., 22, 2581-2584, 1995

Anderson, D.L.T, and J.P.McCreary
Slowly Propagating Disturbances in a Coupled Ocean-Atmosphere Model
J.Atmos.Sci, 42, 615-629, 1985

Appleton, E.V.
Wireless Studies of the Ionosphere
Journal Inst.Elec.Eng, 71, 642, 1932

AVISO, 1992
AVISO User Handbook: Merged TOPEX/Poseidon Products
AVI-NT-02-101-CN, Edition 2.1

AVISO, 1995
AVISO User Handbook: Sea Level Anomaly Files
AVI-NT-011-312-CN, Edition 1

Babcock, R.R., and Evans, J.V.
Effects of Geomagnetic Disturbances on Neutral Winds and Temperatures in the Thermosphere observed over Millstone Hill
JGR, 84, 5349, 1979

Battisti, D.S
Dynamics and Thermodynamics of a Warming Event in a Coupled Tropical Atmosphere-Ocean Model
J.Atmos.Sci, 45, 2889-2919, 1988

Beard, R., Robinson, T.R.
A Comparison between Electron Content Deduced from the IRI and that Measured by the TOPEX Dual Frequency Altimeter
Adv.Space.Res., 16, no.1, 155, 1995

Beard, R., Robinson, T.R. and Angell, J.P. Remote Sensing of the Ionosphere by the Dual-Frequency Radar Altimeter.
Proceedings of the 9th IEE Antennas and Propagation Symposium, Eindhoven, Holland, 1995.

Bent, R.B., Llewellyn, S.K., and P.E.Schmid
Description and Evaluation of the Bent Ionospheric Model
DBA Systems, Melbourne, Floride, 1972, B26740

Bent, R.B., Llewellyn, S.K., Nesterczuk, G., and P.E.Schmid
The Development of a Highly Successful Worldwide Empirical Ionospheric Model and its Use in Certain Aspects of Space Communications and Worldwide Total Electron Content Investigations
Proceedings of the Symposium on the Effect of the Ionosphere on Space Systems and Communications, Arlington, Virginia, 1975

Bhuyan, P.K. and T.R.Tyagi
Spatial Correlation of the Ionospheric Electron Content at Low Latitudes for Solar Minimum
Proceedings of the Internationsl Beacon Satellite Symposium on Radio Beacon Contribution to the Study of Ionization and Dynamics of the Ionosphere and To Corrections to Geodesy and Technical Workshop, Oulu, Finland, 1986

Bhuyan, P.K. and T.R.Tyagi
Low-latitude Features of Annual and Semi-annual Periodicities in IEC in the Indian Zone
Proceedings of the International Symposium on Beacon Satellite Studies of the Earth's Environment, New Delhi, India, 1983

Bhuyan, P.K., L.Singh, and T.R.Tyagi
Simultaneous Observations of IEC from Two Geostationary Satellites and their Spatial Correlation
Indian Journal of Radio and Space Physics, 13, 185, 1984

Bhuyan, P.K., and M.Bhattacharyya
Spatial Correlation of TEC at Two Midlatitude Locations 11000 km Apart
Indian Journal of Radio and Space Physics, 22, 397-400, 1993

Bjerknes, J.
Atmospheric Teleconnections from the Equatorial Pacific
Mon. Weather. Rev., 97, 163-172, 1969

Bjerknes, J.
Large-Scale Atmospheric Response to the 1964-65 Pacific Equatorial Warming
J.Phys.Oceans., 2, 212-217, 1972

Boulanger, J and C.Menkes
Propagation and Reflection of Long Equatorial Waves in the Pacific Ocean During the 1992-1993 El Nino
JGR vol.100, no.C12, pp.25,041-25,059, 1995

Boulanger,J and L.Fu
Evidence of Boundary Reflection of Kelvin and First-mode Rossby Wave from TOPEX/POSEIDON Sea Level Data
JGR Vol.101, No.C7, pp. 16,361-16,371, 1996

Busalacchi, A, K.Takeuchi, and J.J. O'Brien
Interannual Variability of the Equatorial Pacific, Revisited
J.Geophys.Res, 88, 7551-7562, 1983

Busalacchi, A, M.McPhaden, and J.Picaut
Variability in Equatorial Pacific Sea Surface Topography During the Verification Phase of the Topex/Poseidon Mission
JGR , Vol.99, No.C12, pp.24,725-24,738, 1994

Canby, T.Y.
El Niño's Illwind
National Geographic, 165, no.2, 144, 1984

Cane, M.A.
Comments on "the Fast-Wave Limit and Interannual Oscillations"
J.Atmos.Sci., 20, 1947-1949, 1992

Chandra, S. and Herman, J.R.
F-region Ionization and Heating During Magnetic Storms
Planet.Space.Sci, 17, 841, 1969

Chelton, D.B.
The Sea State Bias in Altimeter Estimates of Sea Level from Collinear Analysis of TOPEX data
JGR, 99, 24995, 1994

Chelton,D.B and M.G.Schlax
Global Observations of Oceanic Rossby Waves
Science , V.272, No.5259, pp. 234-238, 1996

Cheny, B, Miller, L, Agreen, R, Doyle, N, and Lillibridge, J
TOPEX/Poseidon: The 2 cm Solution
JGR, 99, C12, 24555-24564, 1994

Cippolini, P. , D.Cromwell, and G.D.Quartly
Variability of Rossby Wave Propagation n the North Atlantic from Topex/Poseidon Altimetry
Proceedings of the IEEE International Geoscience and Remote Sensing Symposium (IGARSS '96), Lincoln, Nebraska, 1996

Davies, K.
Ionospheric Radio
Peter Peregrinus Ltd., London, 1990

Delcroix, T, J.Picaut, and G.Eldin
Equatorial Kelvin and Rossby Waves Evidenced in the Pacific Ocean Through Geosat Sea Level and Surface Current Anomalies
JGR 1991, Vol.96, Supplement, pp 3249-3262

Delcroix, T, J.Boulanger, F.Masia, and C.Menkes
Geosat-derived Sea Level and Surface Current Anomalies in the Equatorial Pacific during the 1986-1989 El Niño and La Nina
JGR Vol.99, No.C12, pp.25,093-25,107, 1994

T.Delcroix
Equatorial Wave Sequence Associated with Warm Pool Displacements During the 1986-1989 El Nino - La Nina
JGR V.100, n0.C9, pp.18,393-18,408, 1995

Donatelli, D.E. and Allen, R.S
Temporal Variability of Ionospheric Refraction Correction.
Proceedings of the Symposium on the Effect of the Ionosphere on Space and Terrestrial Systems, Arlington, Virginia, 1978

Donatelli, D.E., and R.S.Allen
Temporal Variability of Ionospheric Refraction Correction
Proceedings of the Symposium on the Effect of the Ionosphere on Space and Terrestrial Systems, Arlington, Virginia, 1978

Donatelli, D.E., and R.S.Allen
Time Cells for Adaptive Prediction of Total Electron Content
Radio Science, 16, 261, 1981

Du Penhoat, Y, and M.Cane
Effect of Low-Latitude Western Boundary Gaps on the Reflection of Equatorial Motions
JGR, 96, 3307-3322, 1991

Duing, W., Hisard, P., Katz, E., Knauss, J., Meinke, J., Miller, L., Moroshkin, K., Philander, G., Rybnikov, A., Voigt, K. and Weisberg, R.
Meanders and Long Waves in the Equatorial Atlantic
Nature, 257, 280, 1975

Dulong, D.D.
Reduction of the Uncertainty of Radar Range Correction
ADA 046 166 AFGL-TR-77-0125

Dunbar, R.B, G.M.Wellington, M.W.Colgan, and P.W.Glynn
Eastern Pacific Sea Surface Temperature Since 1600 A.D. the $\Delta^{18}O$ record of climate variability in Galapagos Corals
Paleoceanography, 9,291-315, 1994

Emery, W.J., and L.Magaard
Baroclinic Rossby Waves as Inferred from Temperature Fluctuations in the Eastern Pacific
J.Mar.Res., 34, 365-385, 1976

Eriksen,C.C.
Moored Observations of Deep Low-Frequency Motions in the Central Pacific Ocean: Vertical Structure and Interpretation as Equatorial Waves
J.Phys.Oceans., 15, 1085-1113, 1985

Eriksen, C.C, M.B.Blumenthal, S.P.Hayes, and P.Ripa
Wind-generated Equatorial Kelvin Waves Observed across the Pacific Ocean,
J.Phys.Oceans, vol.13, No.9, pp. 1622-1640, 1983

Essex, E.A.
Ionospheric Total Electron Content at Southern Mid-latitudes during 1971-1974
J.Atmos.Terr.Phys., 40, 1019, 1978

Feen, M.M, V.L.Pisacane, and M.Sturmanis
Prediction Techniques for the Effect of the Ionosphere on Ranging from Satellites
Proceedings of the Symposium on the Effect of the Ionosphere on Space Systems and Communications, Arlington, Virginia, 1975

Fejer, B.G., Gonzales, C.A., Farley, D.T., Kelley, M.C. and Woodman, R.F.
Equatorial Electric Fields During Magnetically Disturbed Conditions 1.The Effect of the Interplanetary Magnetic Field
JGR, 84, 5797, 1979

Fu, L, Christensen, E, Lefebvre, M, and Menard, Y
TOPEX/Poseidon Mission Overview
JGR, 99, C12, 1994

Gaspar, P., Ogor, F., Le Traon, P.Y. and Zanife, O.Z.
Estimating the Sea State Bias of the TOPEX and Poseidon Altimeters from Cross Over Differences
JGR, 99, 24981, 1994

Gautier, T.N., and Zacharisen, D.H.
Use of Space and Time Correlation in Short-Term Ionospheric Predictions
Conference Record, First Annual IEEE Communications Convention, 1965

Georges, T.M.
Effects of Ionospheric Motions and Irregularities on HF Radio Propagation
Proceedings of the 2nd ESRIN-ESLAB Sumposium, Low Frequency Waves and Irregularities in the Ionosphere, Frascati, Italy, 1968

Giese, B, and D.Harrison
Eastern Equatorial Pacific Response to Three Composite Westerly Wind Types
JGR Vol.96, Supplement, pp.3239-3248, 1991

Giese, B., J.A.Carton, L.J.Holl
Sea-level Variability in the Eastern Tropical Pacific as Observed by Topex and Tropical Atmosphere-Ocean Experiment
JGR, 1994, Vol.99, No.C12,pp.24739-24748)

Gill, A.E.
Atmosphere-Ocean Dynamics
Academic Press, 1981

Gill, A.E.
An Estimation of Sea-Level and Surface-Current Anomalies During the 1972 El Niño and Subsequent Thermal Effects
J.Phys.Oceanogr., 13, 586-606, 1983

Gill,A.E, and A.J.Clarke
Wind-induced Upwelling, Coastal Currents, and Sea Level Changes
Deep Sea Research, 21, 325-346, 19

Goel, M.K. and Rao, B.C.N
Theoretical Calculations on the Changes in the Ionospheric Composition and Temperature Profiles During Storms
JATP, 43, 111, 1981

Harrison, D.E, and A.P.Graig
Ocean Model Studies of Upper-Ocean Variability at 0°, 160°W during the 1982-1983 ENSO: Local and Remotely Forced Response
J.Phys.Oceanog.,23, 425-451, 1993

Harvey, R.R., and W.C.Patzert
Deep Current Measurements Suggest Long Waves in the Eastern Equatorial Pacific
Science, 193, 883-884, 1976

Hayes, S.P., P.Chang, and M.J.McPhaden
Variability of the Sea Surface Temperature in the Eastern Equatorial Pacific During 1986-1988
JGR, 96, 10,553-10,566, 1991

Ho, C.M., Wilson, B.D., Mannucci, A.J., Lindqwister, U.J., and D.N.Yuan
A Comparative Study of Ionospheric Total Electron Content Measurements Using Global Ionospheric Maps of GPS, TOPEX radar, and the Bent Model
Radio Sci., 32, No.4, 1499-1512, 1997

Houminer, Z., and H.Soicher
Improved Short-Term Predictions of *foF2* Using GPS Time Delay Measurements
Radio Science, Vol.31, No.5, 1099-1108, 1996

Huang, T.X.
Average Horizontal Gradients and Spatial Correlation of Mid-latitude Total Electron Content at Solar Minimum
Proceedings of the International Symposium on Beacon Satellite Studies of the Earth's Environment, New Delhi, India, 1983

Huang, Y.N.
Spatial Correlation of the Ionospheric Total Electron Content at the Equatorial Anomaly Crest
JGR, 89, 9823, 1984

Johanson, J.M., Buonsanto, M.J., and Klobuchar, J.A.
The Variability of Ionospheric Time Delay
Proceedings of the Symposium on the Effect of the Ionosphere on Space and Terrestrial Systems, Arlington, Virginia, 1978

Jones, W.B. and Gallet, R.M., The Representation of Diurnal and Geographic Variations of Ionospheric Data by Mathematical Methods
Telecomms. J., 29, 129, 1962
Telecomms. J., 32, 18, 1965

Kane,R.P.
Day-to-Day Variability of Ionospheric Electron Content at Mid-Latitudes
JGR, 80, 3091, 1975

Katz, A.H., M.D.Grossi, R.S.Allen, and D.E.Donatelli
Adaptive Correction of the Effect of the Ionosphere on Range Determination by Terrestrial Radars
Proceedings of the Symposium on the Effect of the Ionosphere on Space and Terrestrial Systems, Arlington, Virginia, 1978

Kessler, W.
Can Reflected Extra-equatorial Rossby Waves Drive ENSO?
Journal of Physical Oceanography, Vol.21, pp.444-452, 1991

Kessler, W.S, and M.J.McPhaden
The 1991-1993 El-Nino in the Central Pacific
Deep-Sea Research Part II - Tropical Studies in Oceanography, 42, no.2-3, pp.295-333, 1995

Kessler, W, J.McPhaden, and K.Weickmann
Forcing of Intraseasonal Kelvin Waves in the Equatorial Pacific
JGR , Vol 100, No.C6, pp 10,613-10,631, 1995

Kilworth, P.D., Chelton, D.B., and R.A.DeSzoeke
The Speed of Observed and Theoretical Long Extratropical Planetary Waves
J. Phys.Ocean., 1997, Vol.27, No.9, 1946-1966

Kivelson, M.G., and C.T.Russell (Editors)
Introduction to Space Physics
Cambridge University Press, 1996

Klobuchar, J.A., and J.M.Johanson
Correlation Distance of Mean Daytime Electron Content
AFGL-TR-77-0185, Air Force Surveys in Geophysics, No.373, 1978

Klobuchar, J.A.
Present State of Ionospheric Time Delay Prediction
Proceedings of the Satellite Beacon Symposium, Warszawa, Poland, 1980

Knox, R., and D.Halpern
Long Range Kelvin Wave Propagation of Transport Variations in Pacific Ocean Equatorial Currents
J.Mar.Res., 40 (Suppl.), 329-339, 1982

Knox, A.
Equatorial Ocean Response to Impulsive Wind
Further Progress in Equatorial Oceanography:A Report of the U.S. TOGA Workshop on the Dynamics of the Equatorial Oceans, Honolulu, HI, 1986

Lawrence, S.P., M.R.Allen, T.N.Stockdale, C.T.Mutlow, and D.T.Llewellyn-Jones
Toprical Pacific Sea-Surface Temperature in an Ocean General Circulation Model and as Measured by the Along-Track Scanning Radiometer
Proceedings of the second ERS-1 symposium, Space at the Service of our Environment, ESA publication SP-361, 523-528, 1994

Lawrence *et al* 1997, in press.

Le Traon , P.Y, M.C Rouquetm and C.Bossier
Spatial Scales of Mesoscale Variability in the North Atlantic as Deduced From Geosat Data, J.Geophys.Res, 95, 20, 267-20, 285, 1990

Le Traon, P. Y., P Gaspar and P. Vincent
Global Statistical Analysis of Topex/Poseidon Data
JGR, 99, 24619-24631, 1994

Legeckis, R.
Long Waves in the Eastern Equatorial Pacific Ocean : A View from a Geostationary Satellite
Science, 197, 1179-1181, 1977

Leigh, R.P., Robinson, T.R. and Lester, M.
Ionospheric Corrections for Radar Altimetry.
Proceedings of IGARSS '88 Symposium, Edinburgh, Scotland, 1988 Publisher ESA Publications Division.

Leigh, R.P.
Ionospheric Corrections for SHF Satellite Radar Altimetry.
Ph.D. Thesis, University of Leicester, England, 1989

Lukas, R., S.P.Hayes, and K.Wyrtki, Equatorial Sea Level Response During the 1982-1983 El Niño
J.Geophys.Res., 89, 10425-10430, 1984

Lukas, R., and E.Firing
The Annual Rossby Wave in the Central Equatorial Pacific Ocean
J.Phys.OCeanogr., 15, 55-67, 1985

Madden, R.A. and Julian, P.R.
Description of Global-Scale Circulation Cells in the Tropics with a 40-50 day Period
J.Atmos.Sci., 29, 1109, 1972

Mannucci, A.J., Wilson, B.D., and C.D.Edwards
A New Method for Monitoring the Earth's Ionospheric Total Electron Content Using the GPS Global Network
Proceedings of the Sixth International Technical Meeting of the Satellite Division of the Institute of Navigation, pp.1323-1333, Inst.of Navig., Alexandria, Va., 1993

Marth, P.C., Jensen, J.R., Kilgus, C.C., Perschy, J.A., MacArthur, J.C., Hancock, D.W., Hayne, G.S., Purdy, C.L., Rossi, L.C. and Koblinsky, C.J.
Prelaunch Performance of the NASA Altimeter for the T/P project
IEEE Transcactions on Geoscience and Remote Sensing, Vol 31, No.2, March 1993

Martyn, D.F.
Electric Currents in the Ionosphere III. Ionization Drift due to Winds and Electric Fields
Phil.Trans.Royal Soc., A246, 306, 1954

McCreary, J.P.
Eastern Tropical Ocean Response to Changing Wind Systems: With application to El Niño
J.Phys.Ocean., 6, 632-645, 1976

McPhaden, M
The Interaction of Equatorial Wave Modes and Mean Currents
Further Progress in Equatorial Oceanography:A Report of the U.S. TOGA Workshop on the Dynamics of the Equatorial Oceans, Honolulu, HI, 1986

McPhaden, M
Monthly Period Oscillations in the Pacific North Equatorial Counter current
JGR , Vol.101, No.C3, pp.6337-6359, 1996

Mendillo, M., Buansanto, M.J. and Klobuchar, J.A.
Distortions of the Winter Nighttime Ionosphere at L=4
JGR, 82, 3223, 1977

Meyers, G.
On the Annual Rossby Wave in the Tropical North Pacific Ocean
J.Phys.Oceanogr., 9, 663-674, 1979

Miller, L, R.E.Cheney, and B.C.Douglas, GEOSAT Altimeter Observations of Kelvin Waves and the 1986-87 El Niño
Science, 239, 52-54, 1988

Neelin, J.D
A Hybrid Coupled General Circulation Model for El Niño Studies
J.Atmos.Sci, 47, 674-693, 1990

Neelin, J.D
The Slow Sea Surface Temperature Mode and the Fast-Wave Limit: Analytic Theory for Tropical Interannual Oscillations and Experiments in a Hybrid Coupled Model
J.Atmos.Sci., 48, 584-606, 1991

Nisbet, J.S., Tyrnov, O.F., Zintchenko, G.N. and Ross, W.J.
Limits on the Accuracy of Correction of Trans-ionospheric Propagation Errors by Using Ionospheric Models Based on Solar and Magnetic Indices and Local Measurements.
Radio Science 16: 127, 1981

Okano, S. and Kim, J.S.
Thermospheric Temperatures During the July 5, 1978 Storm - A Possible Existence of the Nonthermal Atomic Oxygen
J.Geomag.Geoelectr., 38, 189. 1986

Papoulis, A.
Probability, Random Variables and Stochastic Processes
McGraw Hill, 1965

Penhoat.Y, T.Delcroix, and J.Picaut
Interpretation of Kelvin/Rossby Waves in the Equatorial Pacific from Model-Geosat Data Intercomparison During the 1986-1987 El Nino
Oceanologica Acta , Vol.15, No.15, pp.545-554, 1992

Philander, S.G.H.
Instabilities of Zonal Equatorial Currents: II
J.G.R., 83, 3679-3682, 1978

Philander, S.G.H.
Tropical Oceanography
Adv.in Geophysics, 28, no.PA, 461, 1985

Philander, S.G.H.
El Niño, La Niña, and the Southern Oscillation
Academic Press, 1990

Pond, S. and G.L.Pickard
Introductory Dynamical Oceanography,
Pergamon Press, 1989

Prölss, G.W.
Magnetic Storm Associated Perturbations of the Upper Atmosphere: Recent Results Obtained by Satellite-Borne Gas Analysers
Rev.Geophys.Space.Phys., 18, 183, 1980

Prölss, G.W.
On Explaining the Local Time Variation of Ionospheric Storm Effects
Ann.Geophysicae, 11, pp.1-9, 1993

Qiao and Weisberg
Tropical instability Wave Kinematics - Observations from the Tropical Instability Wave Experiment
JGR, Vol.100, No.C5, pp.8677-8693, 1995

Quegan, S., Bailey, G.J., Moffet, R.J., Heelis, R.A., Fuller-Rowell, T.J., Rees, D., Spiro, R.W.
A Theoretical Study of the Distribution of Ionisation in the High-Latitude Ionosphere and the Plasmasphere: First Results on the Mid-Latitude Trough and the Light-Ion Trough
JATP., 44, p.619, 1982

Rawer, K. and Bilitza, D.
Electron Density Profile Description in the International Reference Ionosphere
JATP, 51(9/10), 781-790, 1989

Richmond, A.D.
Thermospheric Heating in a Magnetic Storm: Dynamo Transport of Energy from High to Low Latitudes
JGR, 84, 5259, 1979

Ripa, P., and S.P.Hayes
Evidence for Equatorial Trapped Waves at the Galapagos Islands
JGR, 86, 6509-6516, 1981

Risbeth, H.
Research Notes: The F-layer Dynamo
Planet.Space Sci., 19, 263, 1971

Risbeth, H.
F-region Storms and Thermospheric Circulation
JATP, 37, 1055, 1975

Risbeth, H., Fuller-Rowell, T.J., and Rees, D.
Diffusive Equilibrium and Vertical Motion in the Thermosphere During a Severe Magnetic Storm: A Computational Study
Planet.Space.Sci., 35, pp.1157-65, 1987

Rush, C.M.
An Ionospheric Observation Network for Use in Short-Term Propagation Predictions
Telecommunications Journal, 43, 544, 1976

Russell, C.T. and R.L.McPherron
The Magnetotail and Substorms
Space.Sci.Rev., 11, 111-122

Sarachik, E
The Role of the Ocean in Interannual Climate Variability
Further Progress in Equatorial Oceanography:A Report of the U.S. TOGA Workshop on the Dynamics of the Equatorial Oceans, Honolulu, HI, 1986

Schopf, P
Coupled Dynamics of the Tropical Ocean-Atmosphere System
Further Progress in Equatorial Oceanography:A Report of the U.S. TOGA Workshop on the Dynamics of the Equatorial Oceans, Honolulu, HI, 1986

Schopf, P.S. and M.J.Suarez
Vacillations in a Coupled Ocean Atmosphere Model
J.Atmos.Sci, 45, 549-566, 1988

Seager, R
Modelling Tropical Sea Surface Temperature: 1970-87
J.Phys.Ocean., 29?, 419-434, 1989

Soicher, H.
Spatial Correlation of Transionospheric Signal Time Delays.
IEEE Transactions on Antennas and Propagation AP-26, 311, 1978

Soicher, H., J. A. Klobuchar, and P.H.Doherty
Spatial Variability of Total Electron Content in the Eastern Mediterranean Region
Radio Science, 19, 757, 1984

Sojka, J.J., and Schunk, R.W
Theoretical Study of the Seasonal Behaviour of the Global Ionosphere at Solar Maximum
J.Geophys.Res., 83, p.4255, 1978

Sojka, J.J., Schunk, R.W., and Whalen, J.A.
The Longitude Dependence of the Dayside F region Trough: A Detailed Model-Observation Comparison
JGR, 95, A9, pp.15,275-15,280, 1990

Spiro, R.W., Heelis, R.A., and Hanson, W.B.
Ion Convection and the Formation of the Mid-Latitude F-region Ionization Trough
JGR, 83, 4255

Stirling, D.L., Hanson, W.B., Moffett, R.J. and Baxter, R.G.
Influence of Electromagnetic Drifts and Neutral Air Winds on some Features of the F2 Region
Radio Science, 4, 1005, 1969

Tanaka, T. and Hirao, K.
Effects of an Electric Field on the Dynamical Behaviour of the Ionospheres and its Application to the Storm Time Disturbance of the F-layer
JATP, 35, 1443, 1973

Tanaka, T.
Severe Ionospheric Disturbances Caused by the Sudden Response of Evening Sub-Equatorial Ionospheres to Geomagnetic Storms
JGR-Space Physics, 86, no.NA13, 1335, 1981

Titheridge, J.E.
Determination of Ionospheric Electron Content from the Faraday Rotation of Geostationary Satellite Signals
Planet.Spa.Sci., 20, 353, 1972

Torr, M.R., Torr, D.G., Roble, R.G. and Ridley, E.C.
The Dynamic Repsonse of the Thermosphere to the Energy Influx Resulting from Energetic O+ Ions
JGR, 87, no.NA7, 5290, 1982

Trenberth, K.E., and T.J.Hoar
Geophys.Res.Lett, 23, 57, 1986

Walker, G.O.
Longitude Structure of the F-region Equatorial Anomaly - A Review
JATP, 43, no.8, 763, 1981

Walker, G.T.
Correlation in Seasonal Variations of Weather IX. A Further Study of World Weather
Mem.Indian.Meteorol.Dept., 24, 275, 1924

Walker, G.T.
World Weather
Q.J.R.Meteorol.Soc., 54, 79, 1928

Walton, E.K. and Bowhill, S.A.
Seasonal Variations in the Low Latitude Dynamo Current System Near Sunspot Maximum
JATP, 41, 937, 1979

Weisberg, R
Observations Pertinent to Instability Waves in the Equatorial Oceans
Further Progress in Equatorial Oceanography:A Report of the U.S. TOGA Workshop on the Dynamics of the Equatorial Oceans, Honolulu, HI, 1986

Whalen, J.A.
Daytime F-layer Trough Observed on a Macroscopic Scale
JGR, 92, pp.2571-6, 1987

White, W.B
Secular Variability in the Baroclinic Structure of the Interior North Pacific from 1950-1970
J.Mar.Res., 35, 587-607, 1977

White, W.B., and C.Tai
Reflection of Interannual Rossby Waves at the Maritime Western Boundary of the Tropical Pacific
JGR, Vol.97, No.C9, pp.14,305-14,322, 1992

Wyrtki, K
El Niño - The Dynamic Response of the Equatorial Pacific Ocean to Atmospheric Forcing
J.Phys.Oceans, 5, 572-584, 1975

Yeh, K.C. and V.H.Gonzales
Note on the Geometry of the Earth Magnetic Field Useful to Faraday Effect Experiments
JGR, 65, 3209, 1960

Zheng, Q, X.Yan, C.Ho, and C.Tai
Observatio of equatorially trapped waves in the Pacific using Geosat altimeter data
Deep-Sea Research Part-1 Oceanographic Research Papers , 42, No.5, pp.797-817, 1995

Zou.J, and M.Latif
Modes of Ocean Variability in the Tropical Pacific as Derived from Geosat Altimetry
JGR Vol.99, no.C5, pp 9963-9975, 1994